3D GEOMECHANICAL CHARACTERIZATION OF RESERVOIRS OF ‘‘BETA’’ AND ‘‘FUJA’’ FIELDS, OFFSHORE NIGER DELTA, NIGERIA, USING AN INTEGRATED APPROACH

BY

AGOHA, CHIDIEBERE CHARLES

[B.Tech., M.Sc. (FUTO)]

20154988608

A DISSERTATION SUBMITTED TO THE POSTGRADUATE SCHOOL

FEDERAL UNIVERSITY OF TECHNOLOGY, OWERRI

IN PARTIAL FULFILLMENT OF THE REQUIREMENTS FOR THE AWARD OF THE DEGREE OF DOCTOR OF PHILOSOPHY (Ph.D) IN

GEOPHYSICS

DECEMBER, 2021

CERTIFICATION

This is to certify that this work ''3D Geomechanical Characterization of Reservoirs of ''Beta'' and ''Fuja'' Fields, Offshore Niger Delta, Nigeria, using an Integrated Approach'' was carried out by I, AGOHA, CHIDIEBERE CHARLES (20154988608) in partial fulfillment for the award of the degree of Doctor of Philosophy (Ph.D) in Applied Geophysics in the Department of Geology of the Federal University of Technology, Owerri.

.....
Prof. A.I. Opara
(Supervisor)

15/12/2021
Date

.....
Prof. O.C. Okeke
(Co-supervisor)

15/12/2022
Date

.....
Prof. C.N. Okereke
(Co-supervisor)

15-12-2021
Date

.....
Prof. A.I. Opara
(Head of Department)

15/12/2021
Date

.....
Prof. C.C.Z. Akaolisa
(Dean SOPS)

23/11/22
Date

.....
Prof. C. C. Eze
(Dean, Postgraduate School)

.....
Date

.....
Prof. H.O. Aboh
(External Supervisor)

15/12/2021
Date

ii

DEDICATION

This dissertation is dedicated to my late father, Mr. David Ihebirinachi Agoha, who against all odds laid the foundation for my academic exploits. He will remain my hero.

ACKNOWLEDGEMENTS

I owe the motivation I had throughout this research and the entire doctoral degree programme to Prof. Alexander Iheanyichukwu Opara whose spontaneous criticism brought out the strength to focus. I highly appreciate his efforts. I am also grateful to my co-supervisors; Professor Osita Christopher Okeke and Prof. Chikwendu Njoku Okereke for their contributions and advice. I will not forget my very committed postgraduate lecturers of the Department of Geology; Professor Alexander I. Selemo, Professor Casmir Zanders Akaolisa, Professor Samuel Okechukwu Onyekuru, Dr. Diugo Okereke Ikoro, Dr. Ikechukwu Onyema Njoku, Dr. Sabinus Ikechukwu Ibeneme and others for their efforts. I am also grateful to the Dean of Postgraduate School (Prof. C.C. Eze), the Associate Dean (Prof. C.O. Nweke), the Schedule Officer (Mr. E.E. Nwafor) and other staff of FUTO Postgraduate School for their respective contributions.

I am deeply and truly indebted to my parents for their kind contributions to the success of this research. I owe my appreciation to my late father, Mr. David Ihebirinachi Agoha who laid the foundation for my academic exploits, he is my hero. Special thanks also go to my mother Adazion (Mrs.) Rosemary Ada Agoha whose contributions to my success have been timely and constant. I am indeed very grateful to my lovely wife Mrs. Uloma Chidiebere Agoha whose all round support and encouragement have been my driving force throughout this research.

I want to thank in a very special way my good friends and course mates, Mr. Chukwuebuka Nnamdi Onwubuariri of BGP/CNPC and Dr. Osaki Lawson Jack who assisted in obtaining the data and also contributed in no small measure in the realization of this project, may God

Almighty bless you abundantly. I am also thankful to Mr. Promise Nkwocha who also contributed in making this project a reality.

Finally, I am grateful to the numerous authors whose texts and journals were consulted in one way or another in the course of this research, I thank you all.

TABLE OF CONTENTS

Title page…….....i

Certification…….....ii

Dedication…….iii

Acknowledgements……...iv

Table of Contents…….vi

List of Tables……xii

List of figures……..xv

Abstract……...xxvii

CHAPTER I

INTRODUCTION

1.1 Background Information……1

1.2 Problem statement……..4

1.3 Aim and objectives of the study…….5

1.3.1 Aim…….5

1.3.2 Objectives……...5

1.4 Justification of study…….....6

1.5 Scope of study …….....7

CHAPTER II

LITERATURE REVIEW

2.1 Review of previous studies……..9

2.2 Location of study area……15

2.3 Geology of the study area……...17

2.3.1 Lithology…….21

2.3.2 Basin Architecture……...26

2.3.3 Niger Delta petroleum system…….27

2.3.4 Distribution of petroleum……29

2.3.5 Reservoir rock…….31

2.3.6 Traps and seals……32

2.3.7 Fault sealing in the Niger Delta Basin…….33

2.3.8 Petroleum generation and migration……...34

2.4 Theoretical framework……...37

2.4.1 Introduction…….37

2.4.2 Mechanical properties of rocks……...37

2.4.3 Stress and strain……...38

2.4.4 Elasticity……..40

2.4.5 Hooke's law…….41

2.4.6 Elastic properties…….42

2.4.6.1 Bulk modulus……...43

2.4.6.2 Young's modulus…….45

2.4.6.3 Poisson's ratio……..46

2.4.6.4 Shear or rigidity modulus…….48

2.4.7 Compressional and shear wave velocities……...49

2.4.7.1 Compressional body waves……..50

2.4.7.2 Shear body waves…….50

2.4.8 Inelastic properties……..51

2.4.8.1 Formation strength……...51

2.4.8.2 Fracture gradient……...54

2.4.9 Mohr diagram……..54

2.4.9.1 Mohr-Coulomb equation……..56

2.4.10 Pressure…….57

2.4.10.1 Terzaghi relationship……..58

2.4.10.2 Relating pore pressure to velocity……..60

2.4.11 Stress…….61

2.4.12 Interpretation of seismic data……65

2.4.12.1 Seismic velocity…….67

2.4.12.2 Relating rock porosity and velocity……69

2.4.13 Petrophysical properties……70

2.4.13.1 Porosity and grain size……...70

2.4.13.2 Permeability……...71

2.4.14 Well logging……..71

2.4.14.1 Spontaneous potential log……..72

2.4.14.2 Gamma ray log……...73

2.4.14.3 Sonic log……74

2.4.14.4 Resistivity log……74

2.4.14.5 Density log……75

2.4.14.6 Neutron porosity log……...76

2.4.15 Artificial neural network……...77

2.4.15.1 Weights and biases…….....80

CHAPTER III

MATERIALS AND METHODS

3.1 Materials……81

3.2 Methods…….....82

3.2.1 Determination of dynamic elastic properties……...83

3.2.1.1 Determination of Poisson's ratio……..83

3.2.1.2 Determination of shear or rigidity modulus…….84

3.2.1.3 Determination of bulk modulus……84

3.2.1.4 Determination of bulk compressibility…….84

3.2.1.5 Determination of Young's modulus…….85

3.2.2 Determination of dynamic inelastic property……..85

3.2.2.1 Unconfined or uniaxial compressive strength……..85

3.2.3 Determination of petrophysical properties……..86

3.2.3.1 Determination of total porosity (density)…….86

3.2.3.2 Determination of effective porosity…….86

3.2.3.3 Determination of volume of shale……87

3.2.3.4 Determination of permeability…….……87

3.2.4 Determination of reservoir pore pressure, total vertical stress, maximum and minimum horizontal stresses……88

3.2.5 Modeling with empirical linear and non-linear equations……...91

3.2.6 Modeling with artificial neural network model……...92

CHAPTER IV

RESULTS AND DISCUSSION

4.1 Results and interpretation……...96

4.1.1 Reservoir delineation……...…96

4.1.1.1 Beta Field…….....99

4.1.1.2 Fuja Field…….....99

4.1.2 Rock elastic, inelastic and petrophysical properties, pore and effective pressures, total vertical stress, maximum and minimum horizontal stresses…….100

4.1.2.1 ‘‘Beta’’ Field ……100

4.1.2.2 ‘‘Fuja’’ Field ……109

4.1.3 Cross plots of rock elastic and inelastic properties, petrophysical properties, and Effective pressure……...119

4.1.3.1 ‘‘Beta’’ Field ……119

4.1.3.2 ‘‘Fuja’’ Field ……132

4.1.4 3D geomechanical models….....144

4.1.4.1 ‘‘Beta’’ Field ……145

4.1.4.2 ‘‘Fuja’’ Field ……151

4.1.5 Comparative assessment of geomechanical characteristics of ‘‘Beta’’ and ‘‘Fuja’’ reservoirs…….....157

4.1.5.1 Reservoir delineation…….....157

4.1.5.2 Rock elastic and inelastic properties, petrophysical properties and effective pressure……...158

4.1.5.3 Cross plots of rock elastic and inelastic properties, petrophysical properties and effective pressure……163

4.1.5.4 3D geomechanical models……..171

4.1.6 Modeling with empirical linear and non-linear methods……..173

4.1.6.1 Linear and quadratic models……..174

4.1.6.2 Power models….....185

4.1.6.3 Logarithmic models.....192

4.1.6.4 Exponential models.....200

4.1.7 Modeling with artificial neural network.....209

4.2 Discussion……229

CHAPTER V

CONCLUSION AND RECOMMENDATIONS

5.1 Summary……..231

5.2 Conclusion……234

5.3 Recommendations……235

5.4 Contribution to knowledge……...236

References…….....237

Appendix……....252

LIST OF TABLES

Table 2.1: Stratigraphic succession in the Niger Delta by Obaje, 2009……...24

Table 4.1: Average values of the elastic, inelastic and petrophysical properties, effective and pore pressures for sand and shale within Beta reservoirs.…….....101

Table 4.2: Estimated values of pore pressure, total vertical stress, maximum and minimum horizontal stresses within Beta reservoirs……..102

Table 4.3: Average values of the elastic, inelastic and petrophysical properties, effective and pore pressures for sand and shale within Fuja reservoirs.……..110

Table 4.4: Estimated values of pore pressure, total vertical stress, maximum and minimum horizontal stresses within Fuja reservoirs……..111

Table 4.5: The parameters and their respective average values in sand and shale units of the two reservoirs…….161

Table 4.6: Mean values of total vertical stress, maximum and minimum horizontal stresses within Beta and Fuja reservoirs…….....163

Table 4.7: Statistical table of linear model of first degree for UCS versus bulk density…...174

Table 4.8: Statistical table for linear model of second degree (quadratic model) for UCS versus bulk density…….175

Table 4.9: Statistical table of linear model of first degree for UCS versus sonic……...177

Table 4.10: Statistical table of linear model of second degree (quadratic model) for UCS

versus sonic……177

Table 4.11: Statistical table of linear model of first degree for permeability versus bulk Density……...180

Table 4.12: Statistical table of linear model of second degree (quadratic model) for permeability versus bulk density……...180

Table 4.13: Statistical table of linear model of first degree for V_s versus sonic……182

Table 4.14: Statistical table of linear model of second degree (quadratic model) for V_s versus sonic……182

Table 4.15: Statistical table of power model for UCS versus bulk density……185

Table 4.16: Statistical table for power model for UCS versus sonic…….186

Table 4.17: Statistical table of power model for permeability versus bulk density……...189

Table 4.18: Statistical table of power model for shear wave velocity versus sonic……...190

Table 4.19: Statistical table of logarithmic model for UCS versus bulk density……...193

Table 4.20: Statistical table of logarithmic model for UCS versus sonic……..194

Table 4.21: Statistical table of logarithmic model for permeability versus bulk density…...197

Table 4.22: Statistical table of logarithmic model for shear wave velocity versus sonic transit time……..198

Table 4.23: Statistical table of exponential model for UCS versus bulk density……...201

Table 4.24: Statistical table of exponential model for UCS versus sonic transit time……...202

Table 4.25: Statistical table of exponential model for permeability versus bulk density…..205

Table 4.26: Statistical table of exponential model for shear wave velocity versus sonic transit time……..206

LIST OF FIGURES

Fig. 1.1: Diagram showing deformation and stresses in the reservoir and their surroundings..4

Fig. 1.2: Reservoir Geomechanics through the Life of a Field……..4

Fig. 2.1: Prospectivity/Licence map of parts of the Niger Delta basin showing location of the study fields……...16

Fig. 2.2: Base maps of the study fields showing drilled Wells as well as seismic inline and crossline geometry……17

Fig. 2.3: Map of Niger Delta showing the different depositional belts……20

Fig. 2.4: Map of Nigeria showing major geological formations……..21

Fig. 2.5: Regional geological map of the Niger Delta Basin, Nigeria…….24

Fig. 2.6: Map of Niger Delta showing the structural elements……25

Fig. 2.7: Schematic map showing the location of lobes of the early Niger delta basin prolific oil centres, and shale prone areas……29

Fig. 2.8: Subsurface depth to top of the Niger delta oil kitchen……...34

Fig. 2.9: The elasticity path of an earth model…….39

Fig. 2.10: Illustration of Young's modulus……..44

Fig. 2.11: Illustrating Shear or Rigidity modulus…….47

Fig. 2.12: Mohr circle diagram with the Mohr-Coulomb-Griffith failure criterion envelop...54

Fig. 2.13: Illustration of the Terzaghi relationship……...58

Fig. 2.14: (a) The normal and shear stress components on an infinitesimal cube.
(b) A second-order stress tensor……...61

Fig. 2.15: Andersonian's classification scheme for types of faulting regimes…….63

Fig. 2.16: Generalized world stress map……..64

Fig. 2.17: A time-migrated seismic section from the Niger delta……65

Fig. 2.18: 3D seismic volume of a time-migrated seismic data from the Niger Delta…….66

Fig. 2.19: Gamma ray, density, neutron porosity, and sonic log signatures from an oil well, offshore Niger delta…….76

Fig. 2.20: An artificial neural network showing the input, hidden and output neurons……...78

Fig. 3.1: ANFIS structure…….....92

Fig. 3.2: Project workflow……94

Fig. 4.1: Delineation and correlation of reservoirs for Beta 1, Beta 2, Beta 3, and Beta 4 wells using gamma ray log……96

Fig. 4.2: Delineation and correlation of reservoirs for Fuja 1, Fuja 2, Fuja 3, and Fuja 4 wells using gamma ray log……96

Fig. 4.3: Inline 6985 of the seismic data showing penetrated wells and fault patterns within Beta Field reservoir……..97

Fig. 4.4: Inline 7001 of the seismic data showing penetrated wells and fault patterns within Fuja Field reservoir……...97

Fig. 4.5: Crossline and inline of seismic data from Fuja Field showing penetrated wells and reservoir top…….98

Fig. 4.6a: Logs of Beta 1 well showing elastic, inelastic and petrophysical properties of the reservoir rock……..102

Fig. 4.6b: Logs of Beta 1 well showing elastic, inelastic and petrophysical properties of the reservoir rock……..102

Fig. 4.6c: Logs of Beta 2 well showing elastic, inelastic and petrophysical properties of the reservoir rock…….103

Fig. 4.6d: Logs of Beta 2 well showing elastic, inelastic and petrophysical properties of the reservoir rock……..103

Fig. 4.6e: Logs of Beta 3 well showing elastic, inelastic and petrophysical properties of the

reservoir rock……..104

Fig. 4.6f: Logs of Beta 3 well showing elastic, inelastic and petrophysical properties of the reservoir rock……..104

Fig. 4.6g: Logs of Beta 4 well showing elastic, inelastic and petrophysical properties of the reservoir rock……..105

Fig. 4.6h: Logs of Beta 4 well showing elastic, inelastic and petrophysical properties of the reservoir rock……..103

Fig. 4.7a: Logs of Fuja 1 well showing elastic, inelastic and petrophysical properties of the reservoir rock……...111

Fig. 4.7b: Logs of Fuja 2 well showing elastic, inelastic and petrophysical properties of the reservoir rock……...111

Fig. 4.7c: Logs of Fuja 3 well showing elastic, inelastic and petrophysical properties of the reservoir rock……...112

Fig. 4.7d: Logs of Fuja 4 well showing elastic, inelastic and petrophysical properties of the reservoir rock……...112

Fig. 4.7e: Logs of Fuja 1 well showing elastic and petrophysical properties of the reservoir rock……..113

Fig. 4.7f: Logs of Fuja 2 well showing elastic and petrophysical properties of the reservoir rock……..114

Fig. 4.7g: Logs of Fuja 3 well showing elastic and petrophysical properties of the reservoir rock……..115

Fig. 4.7h: Logs of Fuja 4 well showing elastic and petrophysical properties of the reservoir rock……..116

Fig. 4.8a: Cross plot showing trend line of unconfined compressive strength against Poisson's ratio for Beta 1 well……...119

Fig. 4.8b: Cross plot showing trend line of unconfined compressive strength against shear modulus for Beta 3 well……119

Fig. 4.8c: Cross plot showing trend line of unconfined compressive strength against sonic transit time for Beta 3 well……120

Fig. 4.8d: Cross plot showing trend line of unconfined compressive strength against total porosity for Beta 4 well……..120

Fig. 4.8e: Cross plot showing trend line of unconfined compressive strength against measured depth for Beta 2 well……..121

Fig. 4.8f: Cross plot showing trend line of unconfined compressive strength against compressional wave velocity (V_P) for Beta 1 well……..121

Fig. 4.8g: Cross plot showing trend line of unconfined compressive strength against shear wave velocity (V_S) for Beta 3 well……122

Fig. 4.8h: Cross plot showing trend line of unconfined compressive strength against volume of shale for Beta 1 well……..122

Fig. 4.8i: Cross plot showing trend line of unconfined compressive strength against Young's modulus for Beta 1 well……..123

Fig. 4.8j: Cross plot showing trend line of Young's modulus against measured depth for Beta 2 well……..123

Fig. 4.8k: Cross plot showing trend line of bulk modulus against compressional wave velocity (V_P) for Beta 1 well……..124

Fig. 4.8l: Cross plot showing trend line of Poisson's ratio against total porosity for Beta 3 well……..124

Fig. 4.8m: Cross plot showing trend line of total porosity against sonic transit time for

Beta 2 well……..125

Fig. 4.8n: Cross plot showing trend line of unconfined compressive strength against effective porosity for Beta 1 well……...125

Fig. 4.8o: Cross plot showing trend line of unconfined compressive strength against permeability for Beta 2 well……...126

Fig. 4.8p: Cross plot showing trend line of Effective/differential pressure against measured depth for Beta 4 well……..126

Fig. 4.8q: Cross plot showing trend line of Effective/differential pressure against total porosity for Beta 1 well……..127

Fig. 4.8r: Cross plot showing trend line of Effective/differential pressure against unconfined compressive strength for Beta 1 well……..127

Fig. 4.8s: Cross plot showing trend line of compressional wave velocity against effective porosity for Beta 1 well……...128

Fig. 4.8t: Cross plot showing trend line of permeability against bulk density for Beta 1 well…….128

Fig. 4.8u: Cross plot showing trend line of unconfined compressive strength against bulk density for Beta 1 well……...129

Fig. 4.8v: Cross plot showing trend line of shear wave velocity against sonic transit time for Beta 1 well……129

Fig. 4.9a: Cross plot showing trend line of unconfined compressive strength against Poisson's ratio for Fuja 3 well……131

Fig. 4.9b: Cross plot showing trend line of unconfined compressive strength against shear modulus for Fuja 3 well……132

Fig. 4.9c: Cross plot showing trend line of unconfined compressive strength against sonic transit time for Fuja 3 well……132

Fig. 4.9d: Cross plot showing trend line of unconfined compressive strength against total porosity for Fuja 2 well……..133

Fig. 4.9e: Cross plot showing trend line of unconfined compressive strength against measured depth for Fuja 4 well……..133

Fig. 4.9f: Cross plot showing trend line of unconfined compressive strength against compressional wave velocity (V_P) for Fuja 4 well…….134

Fig. 4.9g: Cross plot showing trend line of unconfined compressive strength against shear wave velocity (V_S) for Fuja 2 well……134

Fig. 4.9h: Cross plot showing trend line of unconfined compressive strength against volume of shale for Fuja 1 well……..135

Fig. 4.9i: Cross plot showing trend line of unconfined compressive strength against Young's modulus for Fuja 2 well……...135

Fig. 4.9j: Cross plot showing trend line of Young's modulus against measured depth for Fuja 3 well…….....136

Fig. 4.9k: Cross plot showing trend line of bulk modulus against compressional wave velocity (V_P) for Fuja 1 well……...136

Fig. 4.9l: Cross plot showing trend line of Poisson's ratio against total porosity for Fuja 3 well……..137

Fig. 4.9m: Cross plot showing trend line of sonic transit time against total porosity for Fuja 3 well……..137

Fig. 4.9n: Cross plot showing trend line of unconfined compressive strength against effective porosity for Fuja 1 well……...138

Fig. 4.9o: Cross plot showing trend line of unconfined compressive strength

against permeability for Fuja 4 well……...138
Fig. 4.9p: Cross plot showing trend line of Effective/differential pressure against measured depth for Fuja 1 well……..139
Fig. 4.9q: Cross plot showing trend line of Effective/differential pressure against total porosity for Fuja 1 well……..139
Fig. 4.9r: Cross plot showing trend line of effective pressure against unconfined compressive strength for Fuja 2 well…….140
Fig. 4.9s: Cross plot showing trend line of compressional wave velocity against effective porosity for Fuja 1 well……...140
Fig. 4.9t: Cross plot showing trend line of permeability against bulk density for Fuja 1 well…….141
Fig. 4.9u: Cross plot showing trend line of unconfined compressive strength against bulk density for Fuja 1 well……....141
Fig. 4.9v: Cross plot showing trend line of shear wave velocity against sonic transit time for Fuja 1 well……142
Fig. 4.10a: 3D geomechanical model with inserted map showing the spatial distribution of Young's modulus across the Beta reservoir top…….144
Fig. 4.10b: 3D geomechanical model with inserted map showing the spatial distribution of Poisson's ratio across the Beta reservoir top……..145
Fig. 4.10c: 3D geomechanical model with inserted map showing the spatial distribution of bulk modulus across the Beta reservoir top……...146
Fig. 4.10d: 3D geomechanical model with inserted map showing the spatial distribution of shear modulus across the Beta reservoir top……..147
Fig. 4.10e: 3D geomechanical model with inserted map showing the spatial distribution of UCS across the Beta reservoir top……..148

Fig. 4.10f: 3D geomechanical model with inserted map showing the spatial distribution of bulk compressibility across the Beta reservoir top……149

Fig. 4.11a: 3D geomechanical model with penetrated wells and inserted map showing the spatial distribution of Young's modulus across the Fuja reservoir top……...150

Fig. 4.11b: 3D geomechanical model with penetrated wells and inserted map showing the spatial distribution of Poisson's ratio across the Fuja reservoir top…….151

Fig. 4.11c: 3D geomechanical model with penetrated wells and inserted map showing the spatial distribution of bulk modulus across the Fuja reservoir top……...152

Fig. 4.11d: 3D geomechanical model with penetrated wells and inserted map showing the spatial distribution of shear modulus across the Fuja reservoir top…….153

Fig. 4.11e: 3D geomechanical model with penetrated wells and inserted map showing the spatial distribution of UCS across the Fuja reservoir top……154

Fig. 4.11f: 3D geomechanical model with penetrated wells and inserted map showing the spatial distribution of bulk compressibility across the Fuja reservoir top……155

Fig. 4.12a: Relationship between unconfined compressive strength and effective porosity in Beta Field (green) and Fuja Field (red)……..162

Fig. 4.12b: Relationship between unconfined compressive strength and Young's modulus in Beta Field (green) and Fuja Field (red)…….163

Fig. 4.12c: Relationship between effective/differential pressure and depth in Beta Field (green) and Fuja Field (red)……164

Fig. 4.13a: Relationship between unconfined compressive strength and total porosity for Beta Field (green) and Fuja Field (red)……..165

Fig. 4.13b: Relationship between Young's modulus and depth for Beta Field (green) and Fuja Field (red)……...166

Fig. 4.13c: Relationship between unconfined compressive strength and permeability for

Beta Field (green) and Fuja Field (red)……..167

Fig. 4.13d: Relationship between effective pressure and total porosity in Beta Field (green) and Fuja Field (red)……168

Fig. 4.13e: Relationship between effective pressure and unconfined compressive strength in Beta Field (green) and Fuja Field (red)……..169

Fig. 4.14a: Comparison between the geomechanical models of UCS for Beta Field (top) and Fuja Field (bottom)……..170

Fig. 4.14b: Comparison between the geomechanical models of Poisson's ratio for Beta Field (top) and Fuja Field (bottom)……171

Fig. 4.15: Comparative analysis of actual and predicted output of UCS versus bulk density with linear and quadratic models……174

Fig. 4.16: Comparative analysis of actual and predicted output for UCS versus sonic with the linear and quadratic models…….176

Fig. 4.17: R-square values for UCS versus bulk density and UCS versus sonic from linear and quadratic models……..177

Fig. 4.18: Comparative analysis of the actual and predicted output for permeability versus bulk density with the linear and quadratic models…….179

Fig. 4.19: Comparative analysis of actual and predicted output for shear wave velocity versus sonic with the linear and quadratic models…….181

Fig. 4.20: R-square values for permeability versus bulk density and shear wave velocity versus sonic from linear and quadratic models……..182

Fig. 4.21: Comparative analysis of actual and predicted output for UCS versus bulk density with power model……..184

Fig. 4.22: Comparative analysis of actual and predicted output for UCS versus sonic with power model……...185

Fig. 4.23: R-square values for UCS versus bulk density and UCS versus sonic from power model……...186

Fig. 4.24: Comparative analysis of actual and predicted output for permeability versus bulk density with power model……..187

Fig. 4.25: Comparative analysis of actual and predicted output for shear wave velocity versus sonic with power model……..189

Fig. 4.26: R-square values obtained for permeability versus bulk density and shear wave velocity versus sonic from power model……..190

Figure 4.27: Comparative analysis of actual and predicted output for UCS versus bulk density with logarithmic model……..192

Fig. 4.28: Comparative analysis of actual and predicted output for UCS versus sonic with logarithmic model……..193

Fig. 4.29: R-square values obtained for UCS versus bulk density and UCS versus sonic from logarithmic model……..194

Figure 4.30: Comparative analysis of the actual and predicted output for permeability versus bulk density with logarithmic model……..195

Fig. 4.31: Comparative analysis of actual and predicted output for shear wave velocity versus sonic transit time with logarithmic model……...197

Fig. 4.32: R-square values obtained for permeability versus bulk density and shear wave velocity (V_s) versus sonic transit time from logarithmic model……...198

Fig. 4.33: Comparative analysis of the actual and predicted output for UCS versus bulk density with exponential model……..200

Fig. 4.34: Comparative analysis of actual and predicted output for UCS versus sonic

transit time with exponential model……...201
Fig. 4.35: R-square values obtained for UCS versus bulk density and UCS versus sonic transit time from exponential model……..202
Fig. 4.36: Comparative analysis of the actual and predicted outputs for permeability versus bulk density with exponential model…….203
Fig. 4.37: Comparative analysis of actual and predicted output for shear wave velocity versus sonic transit time with exponential model……..205
Fig. 4.38: R-square values obtained for permeability versus bulk density and shear wave velocity versus sonic transit time from exponential model……..206
Fig. 4.39: Statistical parameters indicating degree of prediction for UCS versus bulk density……....208
Fig. 4.40: ANN structure and outcome of ANN simulation for UCS versus bulk density…208
Fig. 4.41: Training performance of artificial neural network for UCS versus bulk density..209
Fig. 4.42: R-square value of the various ANN segments for UCS versus bulk density…….210
Fig. 4.43: Comparative analysis of actual and predicted output for UCS versus bulk density with ANN model……211
Fig. 4.44: Statistical parameters indicating degree of prediction for UCS versus sonic……211
Fig. 4.45: ANN structure and outcome of ANN simulation for UCS versus sonic……...212
Fig. 4.46: Training performance of artificial neural network for UCS versus sonic transit time……..213
Fig. 4.47: R-square value of the various ANN segments for UCS versus sonic transit time.214
Fig. 4.48: Comparative analysis of actual and predicted output for UCS versus sonic transit time with ANN model…….215
Fig. 4.49: R-square values obtained for UCS versus bulk density and UCS versus sonic transit time from ANN model…….216

Fig. 4.50: Statistical parameters indicating degree of prediction for permeability versus bulk density……217

Fig. 4.51: ANN structure and outcome of ANN simulation for permeability versus bulk Density……...217

Fig. 4.52: Training performance of artificial neural network for permeability versus bulk density……218

Fig. 4.53: R-square value of the various ANN segments for permeability versus bulk Density……...219

Fig. 4.54: Comparative analysis of actual and predicted output for permeability versus bulk density with ANN model……...220

Fig. 4.55: Statistical parameters indicating degree of prediction for shear wave velocity versus sonic……220

Fig. 4.56: ANN structure and outcome of ANN simulation for shear wave velocity versus Sonic…….....221

Fig. 4.57: Training performance of artificial neural network for shear wave velocity versus sonic……222

Fig. 4.58: R-square value of the various ANN segments for shear wave velocity versus sonic……223

Fig. 4.59: Comparative analysis of actual and predicted output for shear wave velocity versus sonic with ANN model……...224

Fig. 4.60: R-square values obtained for permeability versus bulk density and shear wave velocity versus sonic from ANN model……....225

ABSTRACT

The geomechanical characterization of the reservoirs of ‘‘Beta’’ and ‘‘Fuja’’ Fields, offshore Niger Delta has been carried out to mitigate well drilling and hydrocarbon exploitation challenges encountered in this environment. Well log data from 8 wells within the fields in addition to 3D reflection seismic data and core data from the fields were integrated to calculate rock elastic, inelastic and petrophysical properties, pore pressure, total vertical stress, as well as maximum and minimum horizontal stresses within the reservoirs from empirical equations, and generate 3D geomechanical models using Petrel and Microsoft Excel software. Cross plots between these rock properties were also obtained to ascertain the relationship between them in both fields. Using Matlab 2015 software, empirical linear and non-linear models and artificial neural network (ANN) model were used to model 4 parameter relationships and establish their prediction performances. Results revealed that all the rock elastic and inelastic properties have higher values in shale units than sand units within the reservoirs, while the petrophysical properties showed higher values in sand. In ‘‘Beta’’ Field, the average values of these properties in shale are 0.33, 13.70GPa, 13.30GPa, 5.12GPa, 0.07GPa^{-1}, 32.32GPa, 0.09, 0.07, and 0.022 mD; while in sand they are 0.30, 10.94GPa, 12.76GPa, 4.11GPa, 0.10GPa^{-1}, 25.19GPa, 0.25, 0.19, and 192.00mD. In ‘‘Fuja’’ Field, the average values of these properties in shale are 0.42, 6.08GPa, , 6.09Gpa, 2.84GPa, 0.016GPa^{-1}, 42.3GPa, 0.06, 0.04, and 0.110 mD; while in sand they are 0.39, 5.11GPa, 5.10GPa, 2.39GPa, 0.023GPa^{-1}, 39.0GPa, 0.16, 0.13 and 44.10mD for Poisson’s ratio, Young’s modulus, bulk modulus, shear modulus, bulk compressibility, unconfined compressive strength (UCS), total porosity, effective porosity, and permeability respectively. This implies larger vertical stress would be required to achieve deformation in the compacted shale than the unconsolidated highly porous sand. The cross plots reveal a definite relationship between these rock properties as shown by the increase in UCS with rock elastic properties and depth; and a decrease with total and effective porosity in both fields. From the generated geomechanical models, there will be lower mechanical rock failure around the NNE part of ‘‘Beta’’ Field and around the northeastern and parts of the eastern and western portions of ‘‘Fuja’’ Field due to the high values of elastic moduli and UCS observed in these areas. Stress estimations within the reservoirs in relation to the obtained elastic and rock strength parameters show that the reservoirs are stable. Also, results of parameter relationships modeling with ANN revealed that ANN can be utilized in the analysis and modeling of UCS versus bulk density, UCS versus sonic, and shear wave velocity versus sonic due to their high prediction performances (0.93214, 0.99953 and 0.69854 respectively). However, it cannot be used in the modeling and analysis of permeability versus bulk density due to its low prediction performance (0.13817). It is hoped that these findings will be invaluable in mitigating drilling and exploitation challenges within these fields.

KEYWORDS: Geomechanical Characterization, Reservoirs, Elastic Properties, Inelastic Properties, Petrophysical Properties, Empirical Equations, Artificial Neural Network, Cross Plots, Shale, Sand.

CHAPTER I

INTRODUCTION

1.1 Background Information

Geomechanics is the study of how rocks and soils deform, sometimes to failure, in response to changes of stress, pressure, temperature, and other parameters (Cook, 2015). It studies the mechanical response of rocks to the events that disturb their initial state (Mehrdad, 2015). Geomechanics is very relevant in modeling fluid movement and how fluid removal or injection leads to changes in permeability, fluid pressure, and in-situ rock stresses that can have significant effects on reservoir performance (Zoback, 1992).

In the petroleum industry, geomechanics is used to predict important parameters such as in-situ rock stresses, modulus of elasticity, leak-off coefficient and Poisson's ratio (Jaeger, Cook, & Zimmerman, 2007). Reservoir parameters that include formation porosity, permeability and bottom-hole pressure can be derived from geomechanical evaluation (Jaeger et al., 2007).

The geophysicist relies on various techniques to obtain reliable geomechanical models. The techniques that have evolved over the years are: coring, log analysis; well testing methods like hydraulic fracturing, and geophysical sonar methods such as acoustic emission (Jaeger et al., 2007). Reservoir geomechanical characterization is therefore the determination of geomechanical properties of the reservoir.

Geophysics in reservoir exploration and exploitation has evolved in role with rock mechanics assuming center stage in energy resources development and sustainability (Osaki, Uko, Iyeneomie, & Alabraba, 2019). This can be attributed to the array of problems encountered by operators during the life cycle of hydrocarbon reservoirs and at every stage of its well life. This is especially in unconventional plays like the offshore Niger Delta basin which

comprises deep water, high temperature, high pressure, and complexly faulted reservoirs that are usually characterized by low permeability and high stress changes during production. With the increasing requirement for hydrocarbon exploration and development in deep water, unconventional and other challenging environments, accurate geomechanical modeling has become ever more critical in ensuring safe and cost effective operations (Qiuguo, Zhang, Al-Ghammari, Mohsin, Jiroudi, & Al-Rawahi, 2013).

During hydraulic fracturing for permeability enhancement of a reservoir (an enhanced oil recovery technique), the fluid pressure can cause pre-existing dormant faults to be reactivated (De Souza, De Souza, Meurer, Naveira, Chaves, Frydman, & Pastor, 2014). This has a range of consequences including the shearing of casing, which can cut off production; the creation of additional fault compartments, which may isolate reserves; and the opening of unintended leakage pathways between adjacent formations, or worse yet, between the reservoir and the underlying formation (De Souza et al., 2014). Similarly, fluid pressure is reduced during hydrocarbon production from a reservoir. This reduction of pressure increases the effective stress due to overburden sediments and causes porous media compaction and surface subsidence (Okeke, 2010). This increase in effective stress can also cause dormant faults to be reactivated with its range of consequences (Ranjbar, Hassani & Shahriar, 2017). In other words, substantial depletion is likely to cause changes in situ stress field leading to reservoir compaction, induced seismicity, fault reactivation, reduction in permeability which are some of the geomechanical complications that can only be evaluated adequately with the peculiar benefits of the 3D numerical earth model that honours structural and stratigraphic constraints (Osaki, Uko, & Opara, 2018). A good knowledge of the reservoir rock strength helps in mitigating these production challenges in addition to predicting sand production for that reservoir.

This study is therefore aimed at determining the geomechanical properties of the reservoirs of the study fields, integrating seismic data, well logs, and core information. The benefits derivable from core description and interpretation stem from its contribution to reservoir geomechanical characterization and modelling (Zoback, 1992). It furnishes us with an understanding of causes of log responses; an understanding of both Sedimentological and Facies characterisation of the reservoir; a detailed knowledge of the reservoir characteristics that control fluid flow/movement within the reservoir and its zonation; an understanding of the reservoir quality and connectivity; provides information in support of a depositional model for predicting sand distribution and reservoir trends; and, finally and most importantly, it's for calibration and validation of elastic properties deduced from empirical methods (Zoback, 1992).

Attempts were made to determine the reservoir rocks strengths. This reservoir parameter will help operators apply a fluid pressure that will not exceed the reservoir rock strength during hydraulic fracturing operations for permeability enhancement purposes. It will also serve as an essential guide for operators in regulating fluid withdrawal pressure during hydrocarbon production, in addition to being a very important parameter for sand production prediction.

The study fields are offshore oilfields located in the offshore depobelt of the Niger Delta basin, Nigeria. Fuja field is situated within longitudes 7˚43′25.971″E and 7˚53′10.372″E, and latitudes 3˚47′35.715″N and 3˚56′7.466″N while Beta field is situated within longitudes 7˚19′14.338″E and 7˚29′57.122″E, and latitudes 3˚54′13.835″N and 4˚06′42.968″N.

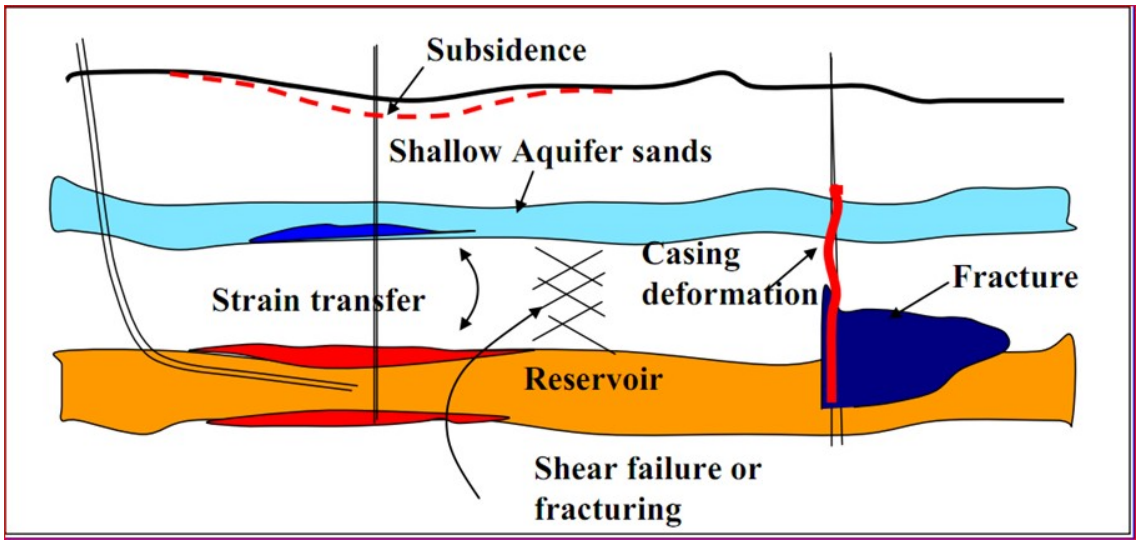


Fig. 1.1: Diagram showing deformation and stresses in the reservoir and their surroundings. (Source: Zoback, 1992).

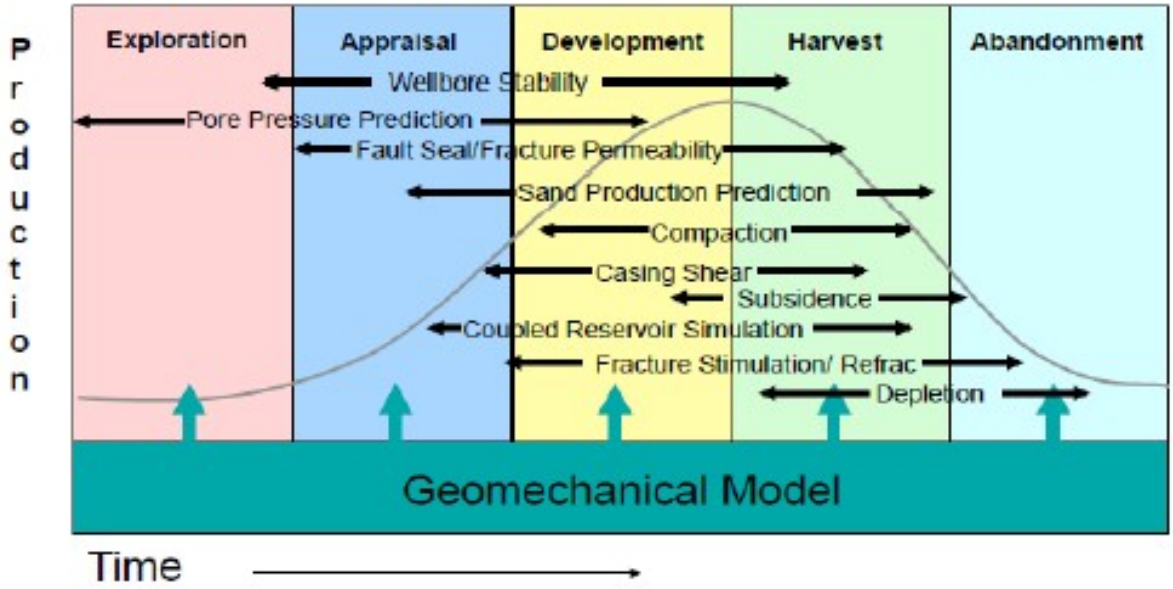


Fig. 1.2: Reservoir Geomechanics through the Life of a Field. (Source: Reservoir Geomechanics Stanford Online, 2016).

1.2 Problem Statement

The life cycle of a hydrocarbon reservoir is associated with a wide range of problems including fault reactivation, wellbore instability, casing collapse, sand production, perforation failure and hydraulic fracture initiation and propagation problems. This is especially true in

unconventional plays like the offshore Niger Delta which comprises deep water, high temperature, high pressure, and complexly faulted reservoirs that are usually characterized by low permeability and high stress changes during production. With the challenges of hydrocarbon exploration and development in deep water environments in addition to the operational challenges of drilling, there is the need to obtain accurate rock mechanical properties and a robust knowledge of the reservoir geomechanics. Accurate 3D geomechanical studies using an integrated approach is therefore very critical in ensuring safe and cost effective hydrocarbon exploration and exploitation.

1.3 Aim and Objectives of the study

1.3.1 Aim

This study is aimed at determining 3D geomechanical rock properties of the reservoirs of Beta and Fuja Fields by integrating 3D seismic data, core data, and well log data.

1.3.2 Objectives

i. To determine rock elastic properties of Poisson's ratio, bulk modulus, Young's Modulus, shear modulus, and bulk compressibility of the reservoirs.

ii. To determine rock inelastic property of Unconfined or Uniaxial Compressive Strength of the reservoirs.

iii. To estimate the petrophysical properties of the reservoirs including total porosity, effective porosity, permeability and volume of shale or shaliness.

iv. To calculate the pore pressure, total vertical stress, maximum horizontal and minimum horizontal stresses within the reservoirs.

v. To investigate the relationship between reservoir rock elastic, inelastic and petrophysical properties using cross plots.

vi. To generate 3D geomechanical models of the reservoirs using well logs, seismic, and core data.

vii. To carry out comparative assessment of the geomechanical characteristics of the reservoirs of the two fields.

viii. To model with empirical linear and non-linear equations, four different cross plots including UCS versus bulk density, UCS versus sonic, shear wave velocity versus sonic, and permeability versus bulk density and to estimate the performance prediction of the obtained models.

ix. To carry out modeling and optimization, with Artificial Neural Network (ANN), of the four cross plots stated above using Adaptive-Neuro Fuzzy Inference System (ANFIS) artificial model.

1.4 Justification of study

Due to the challenging nature of hydrocarbon exploration and exploitation in deepwater offshore Niger Delta consisting of reservoirs characterized by complex faults, high temperature, high pressure, and serious stress changes during production, quantitative estimation of reservoir geomechanical properties will mitigate drilling and production challenges encountered during the life cycle of hydrocarbon fields.

Several studies have been carried out on the geomechanical properties of rocks using 1D, 2D and 3D mechanical earth models for investigations (Osaki et al., 2018; Osaki et al., 2019; Ali, Mohammad, Gholam, & Mohammad, 2017; Grazulis, 2016; De Souza et al., 2014; Qiuguo et al., 2013; etc). Most of these studies in the Niger Delta are onshore and core data was not incorporated for investigation. This work, which is deep offshore, has the advantage of integrating 3D geomechanical model and core data from the study area and this revealed

more detailed geomechanical information about the reservoirs of the fields under investigation.

This work also has the advantage of modeling, with empirical linear and non-linear methods and artificial neural network, four different cross plots which will enable the seamless estimation of UCS and shear wave velocity data directly from bulk density and sonic data acquired from offshore Niger Delta and similar geologic environments without going to the field.

In addition, there is little information on the geomechanical characteristics of the reservoirs of the offshore Niger Delta where ‘‘Fuja’’ and ‘‘Beta’’ Fields are located. This study has therefore aided in bridging this information and knowledge gap particularly for the reservoirs of the fields under investigation.

1.5 Scope of study

This study will be limited to the analysis, determination of geomechanical rock properties, generation of 3D geomechanical models, and geomechanical interpretation of the reservoirs of the fields which lie between longitudes 7˚43′25.971″E and 7˚53′10.372″E, and latitudes 3˚47′35.715″N and 3˚56′7.466″N (‘‘Fuja’’ Field); and longitudes 7˚19′14.338″E and 7˚29′57.122″E, and latitudes 3˚54′13.835″N and 4˚06′42.968″N (‘‘Beta’’ Field). It will be limited to the information that can be derived from well log data obtained from eight different wells covering the two fields, 3D seismic data, and core data from the fields. The study will also be limited to the information that can be obtained from the modeling of four different cross plots including UCS versus bulk density, UCS versus sonic, shear wave velocity versus sonic, and permeability versus bulk density using empirical linear and non-linear methods and artificial neural network.

Due to the confidentiality agreement binding the collection of oilfield data, release of the exact coordinates of the fields is impossible, rather close coordinates have been released for the seismic sections.

CHAPTER II

LITERATURE REVIEW

2.1 Review of Previous Studies

The geomechanical characteristics of different formations in different geological provinces have been studied by various authors, each using one or a combination of the various datasets applied in geomechanical analysis. These datasets include; well log data, seismic data and core data. Independent research works have also been done by some researchers bothering on the use of geomechanical analysis to predict the stability or otherwise of rocks of the Earth's crust. The various authors in their separate works contributed in no small measure to the knowledge of the geomechanical characteristics or behaviour of the subsurface formations of the areas they studied. Nevertheless, there have been more extensive and intensive geological activities in most of these areas leading to renewed attempts at more detailed geomechanical studies in recent years. This, in addition to a better understanding of the geomechanical properties, has also led to a reduction in risk and cost of operations. Recent studies incorporating artificial neural network for analysis have also been reviewed.

Fredrich, Arguello, & Deitrick (2000) in the work ''Geomechanical Modeling of Reservoir Compaction, Surface Subsidence, and Casing Damage at the Belridge Diatomite Field'', used geomechanical modeling to characterize the Belridge diatomite field in California. They observed that, although water injection mitigated surface subsidence, it can increase the lateral gradients in effective stress that in turn can accelerate subsurface horizontal motions sufficient to result in well failure.

Horsrud (2001) estimated the mechanical properties of shale by using empirical correlations and generated a valuable database for shale properties through a testing program for North

Sea shale cores. Using these data, he developed empirical correlations for predicting shale mechanical properties. From his correlations, static mechanical properties of shale can be predicted from various data sources such as sonic wireline log, measurement while drilling (MWD) sonic, and acoustic measurements on cuttings and at various stages in the process of drilling a borehole.

In a study carried out in 2006 by Chang, Zoback, & Khaksar on empirical relations between rock strength and physical properties in sedimentary rocks, they summarized 31 empirical equations that relate unconfined compressive strength and internal friction angle of sedimentary rocks (sandstone, shale, limestone and dolomite) to physical properties (such as velocity, modulus, and porosity) and concluded that those equations can be useful when a range of geomechanical problems such as wellbore stability and in-situ stress measurements should be addressed without direct rock strength information available. However, due to the considerable scatter they observed between rock strength and individual physical property measurements, they recommended that local calibrations should be done before utilizing any of the empirical relationships presented.

Nygaard (2010) carried out the geomechanical analysis of Wabamun Area Carbon Dioxide sequestration Project, Canada and concluded that the lower sedimentary succession with the Nisku aquifer and Calmer cap rock is very competent and stiff using established dynamic deformation properties obtained from wireline logs.

Qiuguo et al. (2013) used 3D geomechanical model to predict wellbore stability for several planned developmental wells in Abu Butabul field, Oman. They recommended that a mud weight of 1.3 to 1.35g/cc was required to drill without significant borehole breakout in the area. According to them, the fracture initiation pressure gradient is as low as 1.5g/cc in the Al

Khalata formation, meaning hydraulic fractures might be induced, if the equivalent circulating density (ECD) exceeds that figure while drilling or tripping in the area.

Multi Layer Perceptron artificial neural networks and Kriging method were used by Secci, Foddis, Mazzella, Montisci, & Uras, in 2014 to carry out slope stability analysis by evaluating detrital layer depth within a test site located in countryside of Capoterra, South Sardinia, Italy. They compared between the results obtained with the multi layer perceptron artificial neural networks and kriging method and concluded that the two methods can be applied to implement a realistic and accurate representation of the depth and geomechanical properties of incoherent deposits.

De Souza et al. (2014) in the work ‘‘Integrated 3D Geomechanics and Reservoir Simulation; Optimize performance, avoid fault reactivation’’ in offshore Brazil, observed that the presence of faults had a significant impact on stress magnitudes and direction. They added that the risk of creating leakage pathways was far greater along theses faults. The 3D geomechanical modeling enabled them to identify areas of higher and lower risk of fault reactivation, allowing them to guide the placement of future injectors.

Abijah and Tse (2016) carried out an evaluation of the geomechanical characteristics of a field located onshore of the Niger Delta, Nigeria and concluded that the vertical stress increases vertically and laterally across the field due to variation in the density of sub-crustal materials, while the moduli of rigidity, bulk volume and matrix volume, bulk as well as grain compressibility decreases with depth. They added that there is an increase in elastic modulus of the rocks with depth due to increase in confining stress. According to them, mud weight window varies between 5.0 to 19.0ppg with depth across the field, while the direction of the

minimum horizontal stress was approximately 024˚ azimuth in a general NE-SW implying that fractures will form and propagate in an orthogonal plane in a NE-SW direction.

Grazulis (2016) analyzed stress and geomechanical properties in the Niobrara formation of Wattenberg field, Colorado, United States of America and observed that the largest fracture densities occur on either side of a central graben within the Wishbone section. He also observed from his analysis that the maximum horizontal stress direction within the formation is N65˚W.

Ali et al. (2017) prepared a geomechanical model for Bangestan reservoir in an oilfield in the south-west of Iran. From borehole failure observations from a formation micro scanner (FMS) image log, they observed the direction of minimum and maximum horizontal in-situ stresses to be N35˚E and N55˚W respectively. They also found the in-situ stress regime to be strike slip. For safe drilling at borehole breakout within the field, they recommended an optimum mud weight of 85.12pcf and 80.42pcf based on the Mohr-Coulomb and Mogi-Coulomb criteria respectively.

Ranjbar et al. (2017) used 3D geomechanical earth model to predict surface ground subsidence and reservoir compaction of Fahlian reservoir formation, Iran. In this study, they observed that the maximum amount of vertical and horizontal stresses on this formation is 110 and 94Mpa respectively. They also observed that ground subsidence is insignificant and the maximum value equals 29mm.

Osaki et al. (2018) carried out 3D geomechanical modeling of the reservoir of Emi-003 field, onshore Niger Delta; Nigeria and observed a marked increase of rock strength and elastic moduli with relative decrease in porosity. From their results, the mechanical failure in the NNW direction of the field will be relatively lower than other areas as analysed using the 3D

earth model. They concluded that a seismic-driven 3D geomechanical model can adequately analyze multiple well trajectories for optimal well placement and other reservoir applications during appraisal and development of a field.

Finisha, Haris, & Ronoatmojo (2018) carried out geomechanical modeling of reservoir rock using 2D seismic inversion and applied it to wellbore stability in the onshore of Northwest Java Basin, Indonesia. For next exploration wells within the basin, they recommended, from pressure and stress analysis, a drilling mud weight of between 8.5ppg and 10.7ppg from upper Cibulakan formation to Talang Akar formation.

Osaki et al. (2019) carried out the geomechanical characterization of a reservoir in part of Niger Delta, Nigeria, and concluded that the sandstone of the studied reservoir will fracture before the shale in a hydraulic fracturing process under the same fracture gradient while the shale will form a seal to the fracture growth. This is because the reservoir shale showed higher value of Poisson's ratio, Young's modulus, Bulk modulus, shear modulus, and uniaxial compressive strength.

Zorasi (2019) evaluated the petrophysical and geomechanical parameters of a marginal (Wabi) Field reservoir in north-central Niger Delta using seismic, core, wireline logs and DST in-situ stress measurements. He concluded from rock strength estimation in this field that the reservoir is stable but production of hydrocarbon from these zones may lead to subsidence. To mitigate for this futuristic event, he therefore recommended that reservoir pressure maintenance should be planned for. According to Zorasi (2019), if injection will be anticipated the appropriate pressure should be used not to fracture or cause fault reactivation in the wells.

Mahmoud, Elkatatny, Ali, & Moussa (2019) estimated static Young's modulus for sandstone formation using artificial neural network (ANN). They developed an ANN-based correlation model which was used to estimate static young's modulus from bulk density, compressional time, and shear time data with very high accuracy. They observed that the predicted static Young's modulus compared favourably with core-tested Young's modulus.

Son (2020) carried out geomechanical modelling by applying artificial neural networks in combination with geostatistics to solve the problem of minimum horizontal stress in Hai Thach - Moc Tinh field in Nam Con Son basin, Vietnam. He used artificial neural network to build a model of minimum horizontal stress estimation from relevant parameters such as true vertical depth, pore pressure and vertical stress, then combined with Kriging interpolation to obtain the distribution in space of the minimum horizontal stress estimation. He concluded that this method can estimate the minimum horizontal stress with a limited amount of available data without drilling new wells or finding empirical formulas for each survey area.

Finally, Nagham, Sameera, & Hazim (2020) in the work "Evaluation of geomechanical properties for tight reservoir using uniaxial compressive test, ultrasonic test, and well logs data", carried out in a field located in the west of the Persian Gulf Basin and to the east of the Arabic Continental Shield, reported the presence of vugges as shown by the Scanning Electron Microscope on some core samples from the reservoir. They concluded that these vugges were responsible for the initial high porosity, low unconfined compressive strength, and lower compressional and shear wave velocity of those samples when compared to others. They also added that the minerals contained in each sample, as indicated by the X-Ray Diffraction (XRD) results, give a descriptive analysis of the difference of the values of both

static and dynamic measured mechanical properties such as ultrasonic pulse travelling time, elastic properties, and unconfined compressive strength.

It is observed that in most of these studies, only 1D or 2D geomechanical models were employed for investigation. Few of the studies that employed 3D geomechanical models for their investigation either did not integrate core data or did not validate obtained results using any validation technique. In addition, most of these studies in the Niger Delta are onshore. This work, which is in the offshore depobelt, therefore has the advantage of integrating 3D geomechanical model and core data from the study area. This data combination guaranteed reliability of interpreted results and revealed much more detailed geomechanical information about the reservoirs of the fields under investigation. Core description and interpretation, among several other advantages, furnishes us with an understanding of both Sedimentological and Facies characterization of the reservoir which can be directly tied to the causes of log responses.

This study will also have the advantage of using empirical linear and non-linear methods and artificial neural network to obtain models which will enable the estimation of unconfined compressive strength and shear wave velocity data from bulk density and sonic data acquired from offshore Niger Delta and similar geologic environments without going to the field.

2.2 Location of study area

The two fields under investigation are offshore oilfields located within the eastern axis of the offshore depobelt of the Niger Delta Basin, Southern Nigeria. ‘‘Beta’’ Field is situated within longitudes 7˚19′14.338″E and 7˚29′57.122″E, and latitudes 3˚54′13.835″N and 4˚06′42.968″N; while ‘‘Fuja’’ Field is situated within longitudes 7˚43′25.971″E and 7˚53′10.372″E, and latitudes 3˚47′35.715″N and 3˚56′7.466″N.

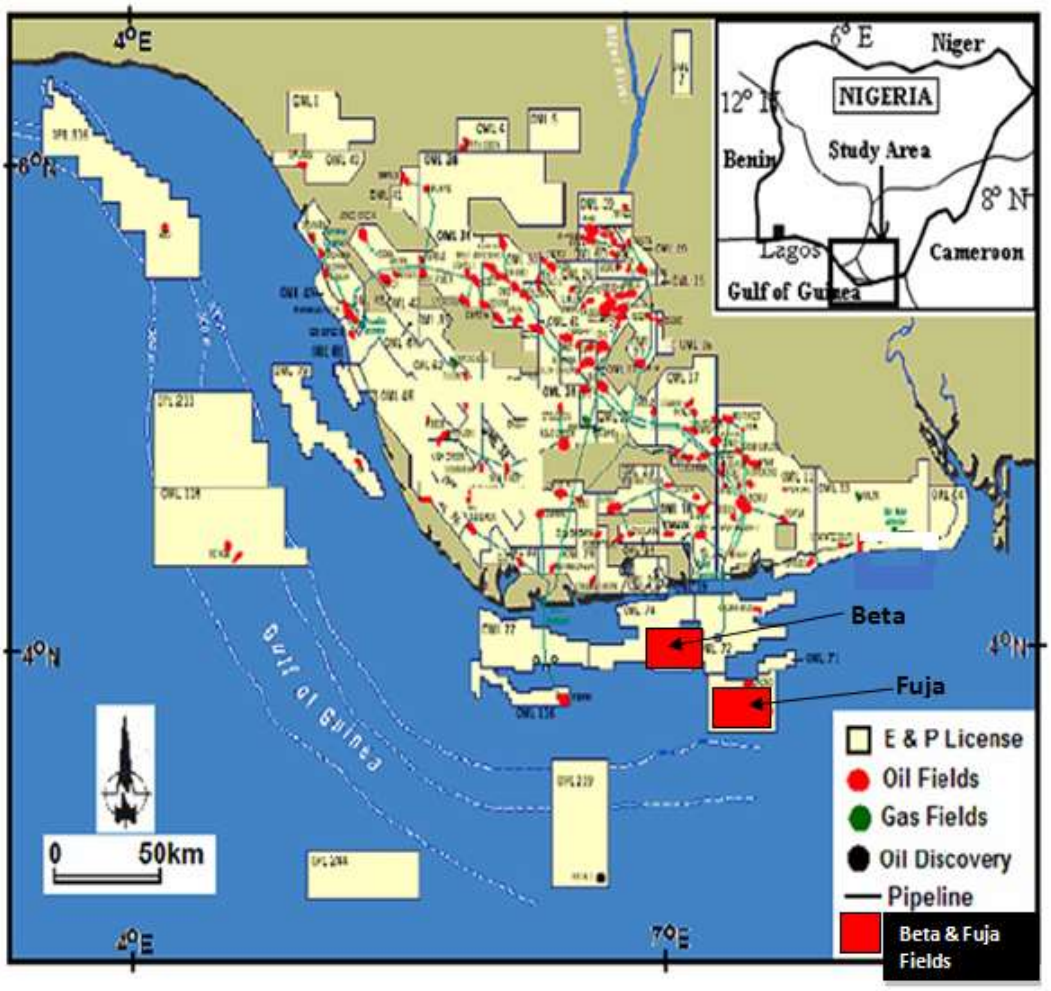


Fig. 2.1: Prospectivity/Licence map of parts of the Niger Delta basin showing locations of the study fields (modified from Nton and Esan, 2010).

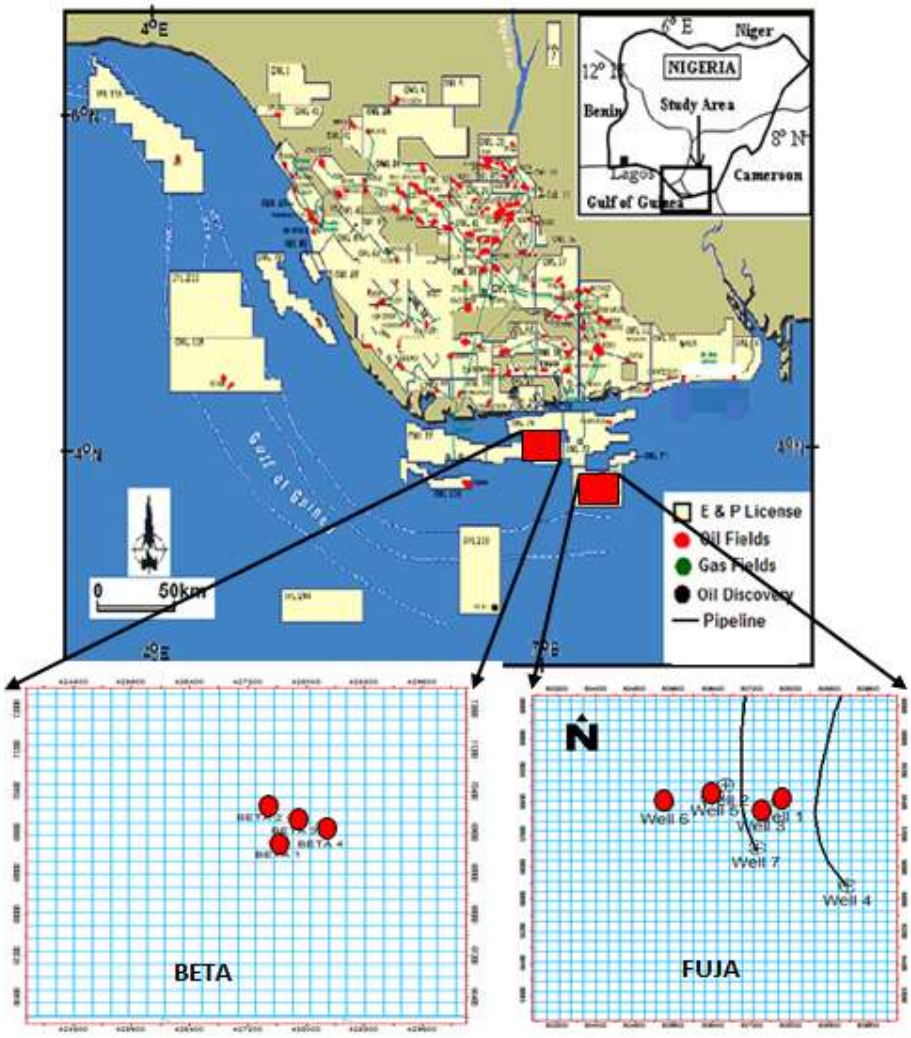


Fig. 2.2: Base maps of the study fields showing drilled wells as well as seismic inline and crossline geometry (modified from Nton and Esan, 2010).

2.3 Geology of the study area

The Niger Delta is located on the continental fringes of the Gulf of Guinea in the Equatorial West Africa between Latitude 4°N and 6°N, and Longitude 3°E and 9°E (Doust & Omatsola, 1990). It is classified among the most fertile hydrocarbon-producing Tertiary Deltas in the world that together accounts for about 2.5% of the present day basin area on earth (Whiteman, 1982). The Niger Delta is among the world's largest regressive sequence with a sedimentary thickness of over 12000m and occupies an area of about 7,500sqkm (Whiteman, 1982). The geology of the Tertiary Niger Delta has been described by several workers

including Short & Stauble (1967); Weber & Daukoru (1975); Weber (1987); Evamy, Harembourne, Kamerling, Knaap, Molley, & Rowlands (1978); Doust & Omatsola (1990) among others.

The Niger Delta province is a large arcuate wave and tide dominated delta, with sediments ranging in age from Eocene in the north to Quaternary in the south (Doust & Omatsola, 1990). The overall regressive sequence of clastic sediments was deposited in series of offlap cycles that were intermittently interrupted by period of sea level changes (Oresajo, Adekeye, & Haruna, 2015). This period resulted in minor although sometimes widespread, episodes or marine transgression. The Niger Delta is divided into three broad lithofacies units: the lower part consists of pre-dominantly undercompacted, over pressured marine shales, clays and silt stones with some turbidite sandstones called Akata Formation, followed by an alternation of paralic sandstones, shales and clay known as Agbada Formation which is turn followed by massive continental sandstones called Benin Formation (Short & Stauble, 1967).

The interaction between subsidence rate and sediment supply is believed to be the main control of the progradation of the delta. These are in turn modified by syn-sedimentation faulting (Evamy et al., 1978). Within the delta, several major growth fault bounded sedimentary units are present. These depobelts succeeded one another southward as the delta prograded through time (Evamy et al., 1978; Doust & Omatsola, 1990). Most of the extensional faulting occurs in the paralic part of the deltaic sequence and has strongly influenced the sedimentation pattern and the thickness distribution of sand and shale (Evamy et al., 1978).

As a sedimentary basin, the Niger Delta encompasses a region that is much larger than the geographical extent of the modern delta constructed by the Niger-Benue drainage systems

(Evamy et al., 1978). It embraces other deltas "which are not members of the Niger Delta, notably the Cross River Delta and extends into the continental margins of neighbouring Cameroon and Equatorial Guinea which therefore "have portions of the Niger Delta that contain hydrocarbons" (Evamy et al., 1978). Also, the Niger Delta sedimentary wedge contains major submarine parts that constitute a complex continental margin which projects pronouncedly into the Gulf of Guinea so that it overlaps the outlines of Africa and South America when both continents are fitted together along the 500 fathom Bathymetric contours (Evamy et al., 1978).

The Niger Delta has prograded towards the southwest from the Eocene epoch to the present; in the process, depobelts representing the highest active part of the delta at every stage of its development were formed (Doust & Omatsola, 1990). These Depobelts together make up one of the biggest regressive deltas around the world having an area of about 300,000 km^2 (Kulke, 1995), a sediment pile having a volume of 500,000 km^3 (Hospers, 1965), and a sediment succession having a thickness of above 10 km in the depocenter of the basin (Kaplan, Lusser, & Norton, 1994).

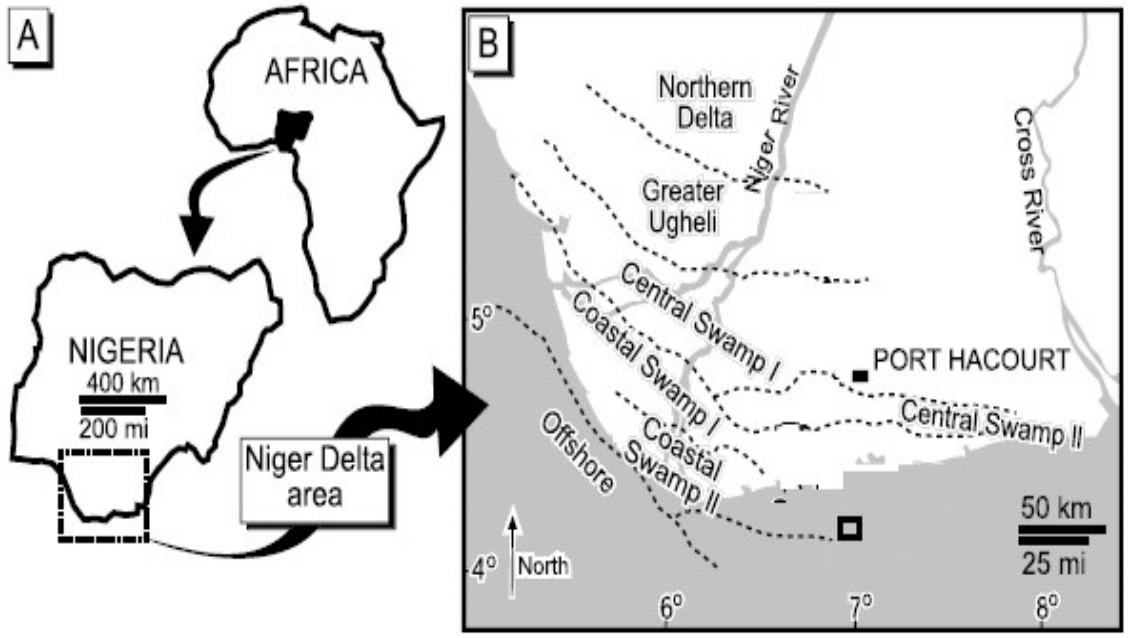


Fig. 2.3: Map of Niger Delta showing the different depositional belts (after Doust & Omatsola, 1990).

The geology of southern Nigeria as well as that of the southwestern Cameroon delineates the onshore part of the Niger Delta Province. The Benin Flank constitutes the northern boundary. This flank is a hinge line trending east-northeast in the southern part of the West Africa basement massif. Cretaceous outcrops located on the Abakaliki High and the Calabar Flank further east-south-east which is a hinge line bordering the adjacent Precambrian define the northeastern boundary. The Cameroon volcanic line define the offshore boundary of the province to the east, the offshore boundary is defined to the west by the eastern boundary of the Dahomey Basin, and to the south and southwest by the sediment thickness contour of about two kilometres or the bathymetric contour of about 4000 metres in locations having sediment thickness higher than two kilometres. This province, including the geologic range or extent of the Akata-Agbada Petroleum System of the Tertiary Niger Delta, covers an area of about 300,000 km^2.

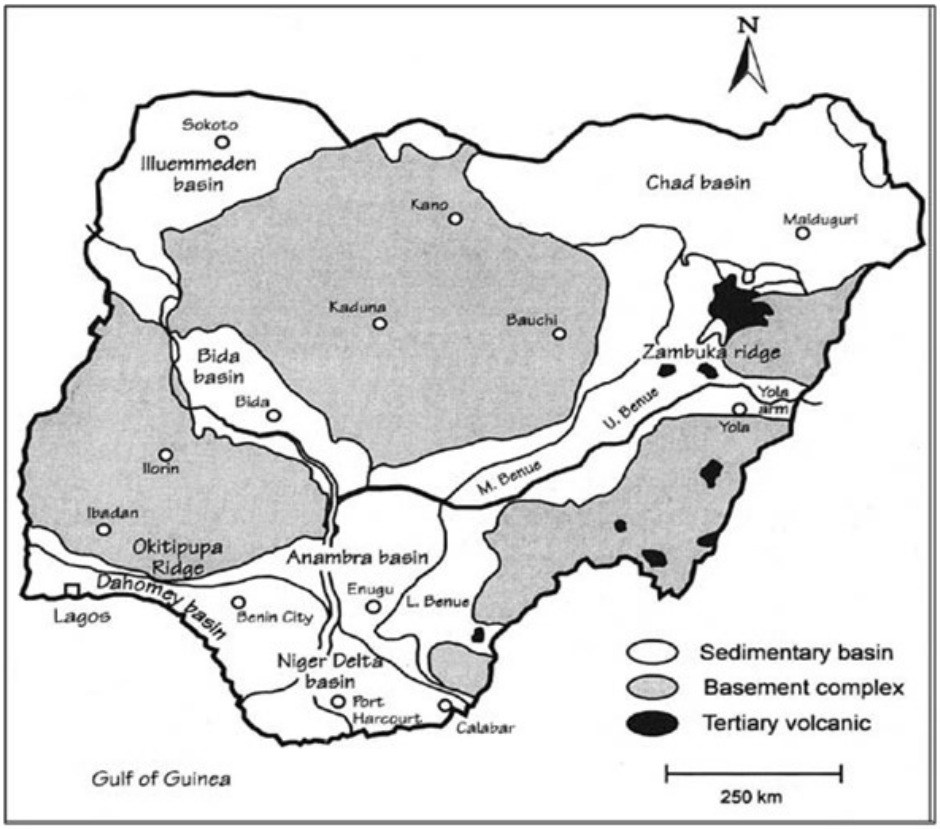


Fig. 2.4: Map of Nigeria showing major geological formations (Helmer & Hespanhol, 1997)

2.3.1 Lithology

The Niger Delta is the most recent and southernmost sub-basin located in the Benue-Abakaliki trough (Reijers, Petters, & Nwajide, 1997). Penetration has not gotten to the Cretaceous section underneath the Niger Delta Basin. Cretaceous rock lithologies that were deposited in the present Niger Delta basin can only be estimated or inferred from the outcrops of Cretaceous section found in the neighbouring basin towards the northeast known as the Anambra basin. There was a concave shoreline into the Anambra basin beginning from the Campanian through the Paleocene (Hospers, 1965), and this resulted in longshore drift cells that were convergent and which produced deltaic sedimentation dominated by tide during transgressions and deltaic sedimentation dominated by river during regressions (Reijers et al., 1997). Further offshore were deposited shallow marine rock fragments and. These are

represented in the Anambra basin by the Asu River shale which is Albian-Cenomanian in age, Eze-Aku and Awgu shales which are Cenomanian-Santonian in age and Nkporo group which are Campanian/Maastrichtian in age, among others (Nwachukwu, 1972; Reijers et al., 1997). Late Cretaceous shale distribution underneath the Niger Delta is not known.

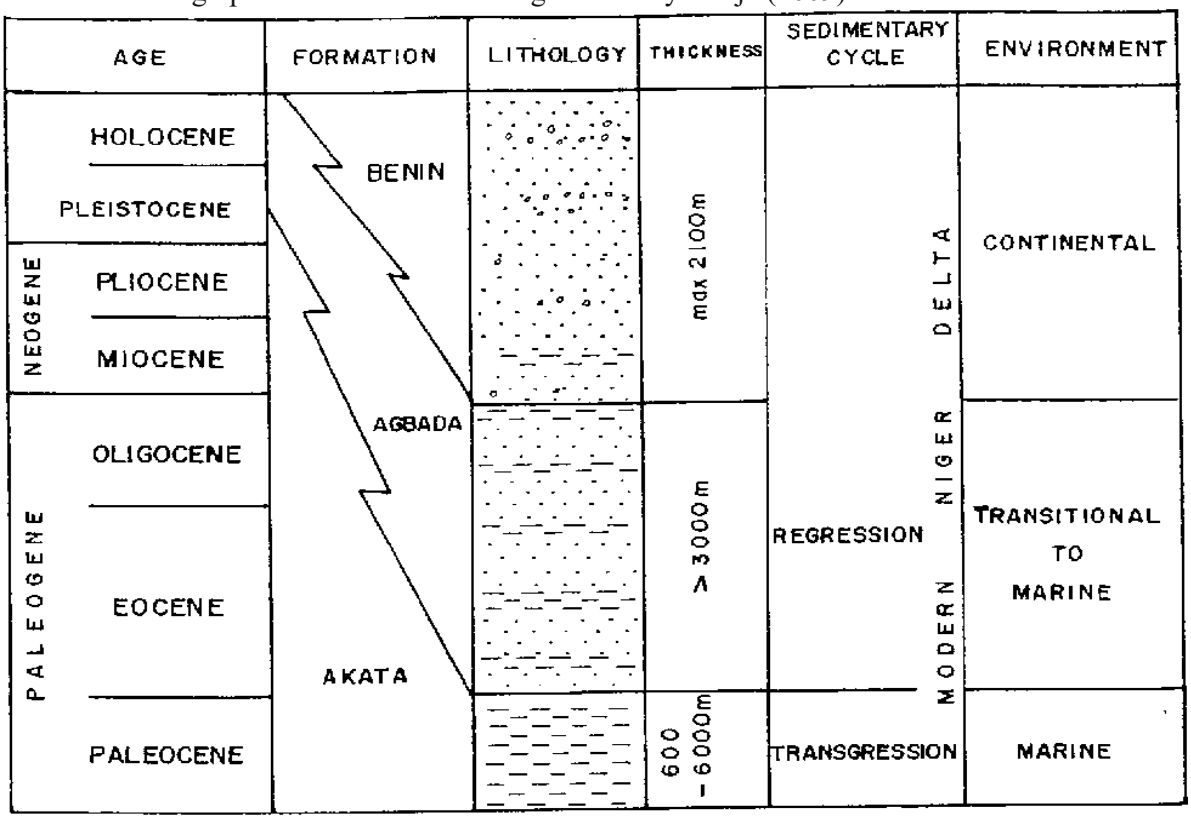
Imo shale was deposited in the Anambra Basin to the northeast and Akata Formation was deposited in the Niger Delta Basin to the southwest during the Paleocene as a result of a major marine transgression (called the Sokoto transgression by Reijers et al., 1997). The shape of the coastline was convexly curvilinear in the Eocene causing a switch in the longshore drift cells to divergent, and consequently resulting in sedimentation changing to being dominated by wave (Reijers et al., 1997). Paralic sedimentation started fully in the Niger Delta Basin at this time, and while the sediments moved south, the coastline gradually became more convex towards the sea. Currently, sedimentation in the delta is still dominated by wave and longshore drift cells are divergent (Burke, Dessauvagie, & Whiteman, 1972).

There are three distinct formations belonging to the Tertiary Niger Delta. These represent depositional Facies that are prograding and differentiated mainly by the ratio of sand and shale. Short & Stäuble (1967) discussed the type sections of these formations which are also summarized in a host of research papers including Avbobvo (1978); Doust & Omatsola (1990); Kulke, 1995; etc. The basal bed of the delta is called the Akata formation, it is of marine origin and is made up of sequences of thick shale which are the source rock for this delta, turbidite sands which are deep water potential reservoirs, and little quantities of silt and clay. Starting from the Paloecene and down to the recent, the Akata formation formed when there are lowstands, when organic matter from land areas and clays were moved to deep water environments characterized by lack of oxygen and low energy state (Stacher, 1995). Drilling has penetrated a small portion of this formation and it is roughly calculated that the Akata Formation is as thick as 7,000 meters (Doust & Omatsola, 1990). The entire Niger

Delta is underlain by this formation which is known to be overpressured. Deep sea fan sands called turbidite sands were deposited around the upper Akata Formation by turbidity currents during delta development (Burke et al., 1972).

Agbada Formation is the reservoir of the hydrocarbon within this basin. Deposition of this formation started in the Eocene epoch and continued to the Recent. This formation is made up of paralic sequence of sand and shale and has a thickness of over 3700 meters thick. It also represents the main deltaic part of the sequence. The clastics built up in three environments including delta front, delta topset, and fluvio-deltaic environments. The sand and shale units were deposited in almost equal proportions in the lower Agbada section; however, the upper Agbada section is mainly sand having only minor interbeds of shale. The Benin Formation, which is the third formation in this basin, overlies the Agbada Formation. It is a continental deposit of alluvial sands and upper coastal plain sands that are of Eocene to Recent in age. The Benin Formation is up to 2000m thick (Avbovbo, 1978).

Table 2.1: Stratigraphic succession in the Niger Delta by Obaje (2009)



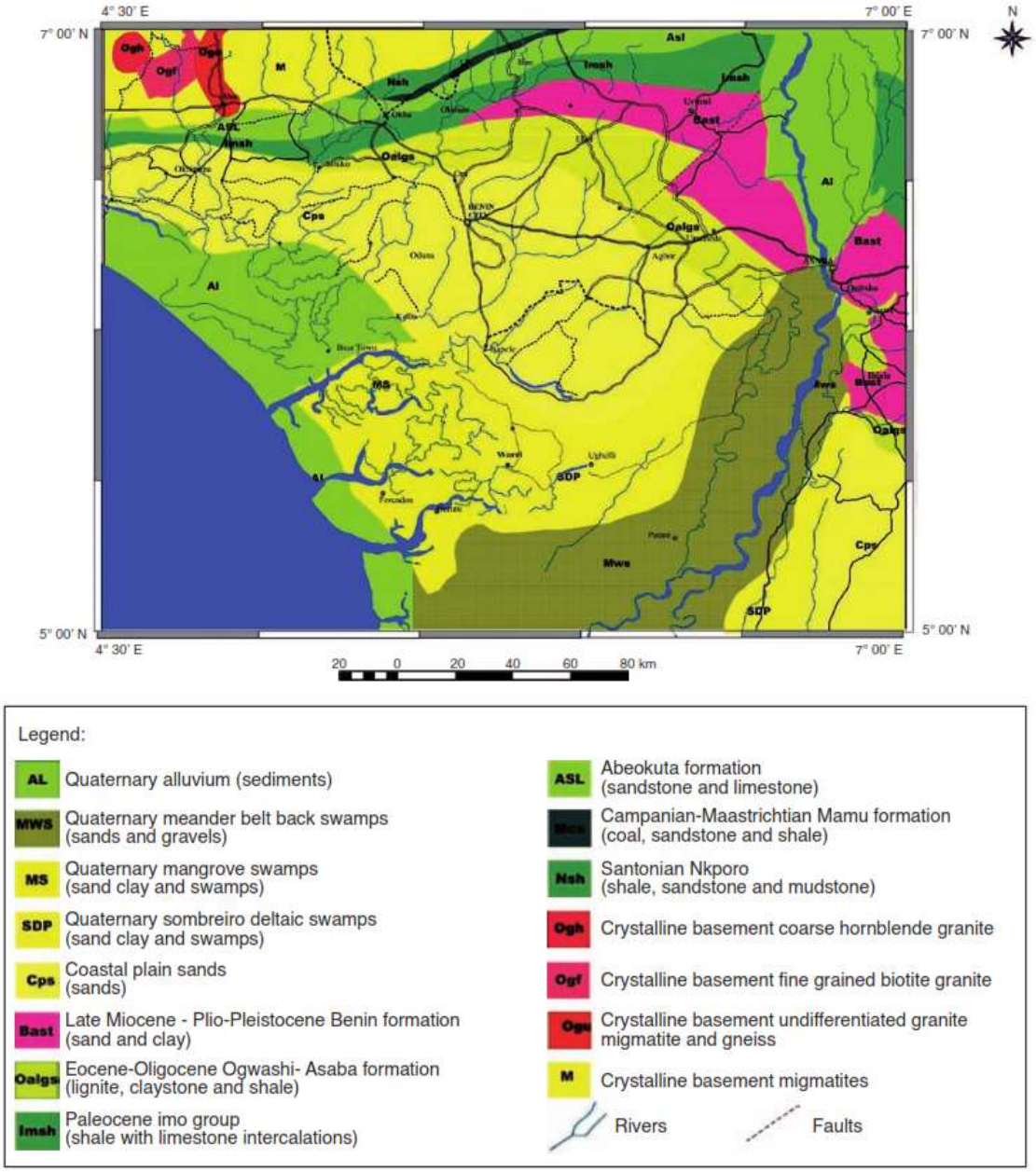


Fig. 2.5: Regional geological map of the Niger Delta Basin, Nigeria (after Okereke, 2012)

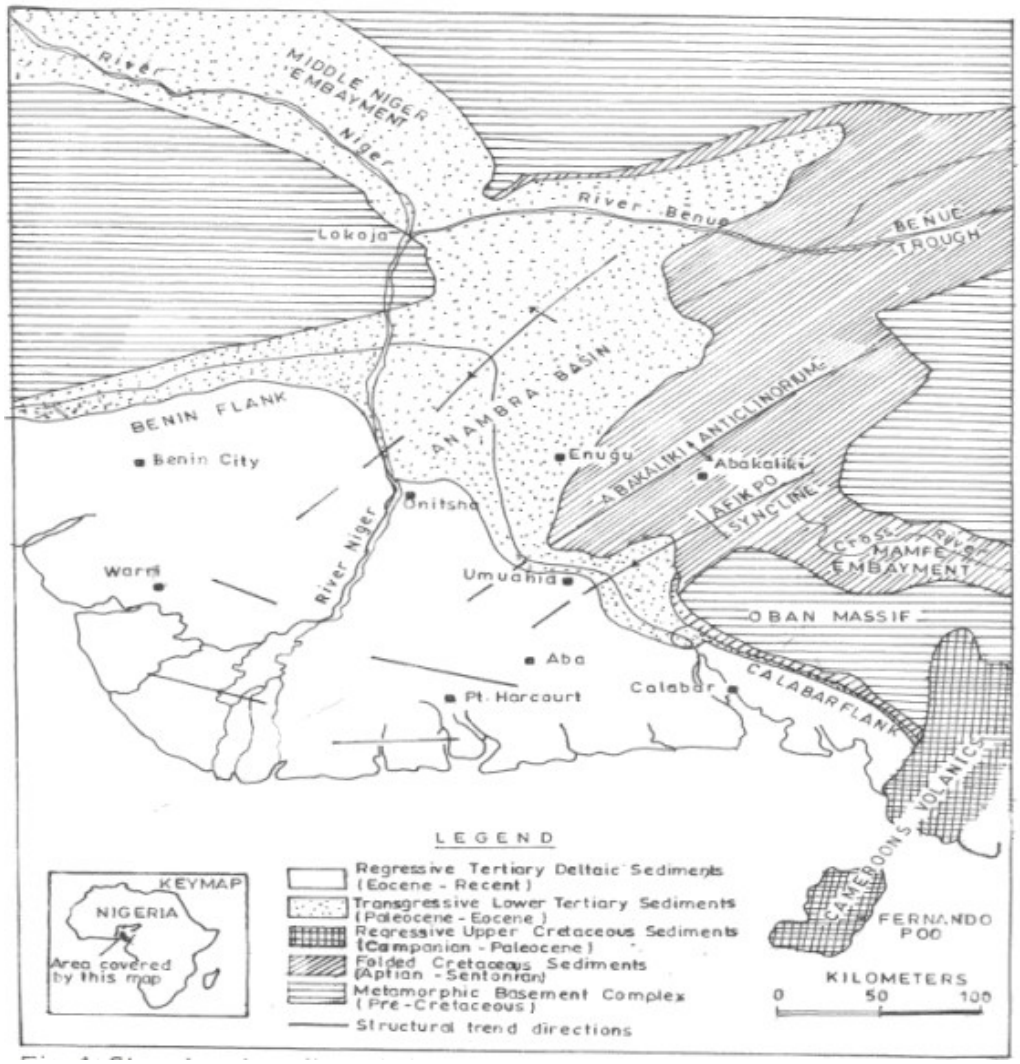


Fig. 2.6: Map of Niger Delta showing the structural elements (after Short & Stauble, 1967).

2.3.2 Basin Architecture

The Niger Delta is associated with five siliciclastic sedimentation cycles classified as off-lapping. Deposition of Akata, Agbada and Benin Formations took place in each of the five sedimentation cycles. These cycles which gave rise to the depobelts are between 30-60km wide and prograde towards the southwest over oceanic crust into the Gulf of Guinea (Stacher, 1995). The depobelts are defined by faults which are syn-sedimentary. The faults occurred due to diverse rates of sediment supply and subsidence (Doust & Omatsola, 1990). The

interaction of rates of supply and subsidence gave rise to deposition of distinct depobelts – when it was no longer possible to accommodate additional crustal subsidence of the basin, there was a shift towards the sea of the focus of sediment deposition, thereby forming another depobelt (Doust & Omatsola, 1990). Each depobelt is a unit separate from others and which represents a break in regional dip of the delta and is bounded towards the land area by growth faults and towards the sea by large counter-regional faults or growth fault of the next belt towards the sea (Evamy et al., 1978; Doust & Omatsola, 1990).

The depobelts generally recognized are five in number, each having its own sedimentation, deformation, and petroleum history. Three depobelt provinces were described by Doust & Omatsola (1990) based on structure. The northern delta depobelt province underlying relatively shallow basement and having rotational growth faults that happen to be the oldest, the growth faults are spaced evenly and their steepness increases towards the sea. Depobelts having well defined structures like deep rollover crests that tend to shift towards the sea for any particular growth fault characterize the central delta depobelt province. The most complex of the three provinces in terms of structures is the distal delta depobelt province. This is as a result of tectonics due to internal gravity on the contemporary continental slope.

2.3.3 Niger Delta Petroleum System

Petroleum occurs throughout the Agbada Formation in the Niger delta clastic wedge. Although the distribution of hydrocarbons is complex, there is a general tendency for the ratio of gas to oil to increase southward within individual depobelts (Doust, 1989). Stacher (1995) developed a hydrocarbon habitat model based on sequence stratigraphy of some petroleum-rich belts within the Niger delta area, and provides a short summary of basin, trap, reservoir, source rock, and hydrocarbon character. Gas to oil ratios within reservoirs were reported by Evamy et al. (1978), Ejedawe (1981) and Doust & Omatsola (1990). Reservoirs

occur along northwest-southeast “oil rich belts” and along a number of north-south trends in the Portharcourt area. Tuttle, Charpentier, & Brownfield (1999) suggested that belts roughly correspond to the change between the crust of the continent and that of the ocean within the axis of the highest limit of sediment thickness. Other authors have related oil-rich belts to structural or depositional controls, to an increase in the geothermal gradient, and shifts in deposition basinward within subsequent depobelts (Ejedawe, 1981; Weber, 1987; Doust & Omatsola, 1990; Haack, Sundaraman, & Dahl, 1997). Source rocks in the Niger delta might include the shales interbedded with sand within Agbada Formation, the shales of the Akata Formation and Cretaceous shales which are underlying (Evamy et al., 1978; Ekweozor, Okogun, Ekong, & Maxwell, 1979; Tuttle et al., 1999; Bustin, 1988; Doust & Omatsola, 1990). Reservoir intervals in the Agbada Formation have been interpreted to be deposits of highstand and transgressive systems tracts in proximal shallow ramp settings (Evamy et al., 1978). The reservoirs range in thickness from less than 45 feet to a few with thicknesses greater than 150 feet (Evamy et al., 1978). The most important reservoir units are reported by Kulke (1995) to be coastal barrier bars and point bars of distributary channels cut by channels filled with sand intermittently. Reservoirs may thicken toward down-thrown sides of growth faults (Weber & Daukoru, 1975). Reservoir units vary in grain size; fluvial sandstones tend to be coarser than the delta front sandstones. Point bar deposits fine upward; barrier bar sandstones tend to have the best grain sorting (Kulke, 1995). Most sandstone is unconsolidated with only minor argillaceous and siliceous cement (Kulke, 1995). Potential reservoirs in the external part of the delta complex include deep channel sands, sand bodies of lowstand and non-distal turbidite sandstones (Beka & Oti, 1995). Structural traps formed at the time of synsedimentary deformation of the Agbada Formation (Evamy et al., 1978; Stacher, 1995), and stratigraphic traps formed preferentially along the delta flanks (Beka &

Oti, 1995) define the most common reservoir locations within the Niger delta complex. The primary seal rocks are interbedded shales within the Agbada Formation.

2.3.4 Distribution of Petroleum

It is established that there is petroleum occurrence within the entire Agbada Formation of the Niger delta; however, several trends that are directional constitute a belt which is oil-rich, possessing the biggest field and least gas:oil ratio (Ejedawe, 1981; Evamy et al., 1978; Doust & Omatsola, 1990). The belt stretches from the offshore area of the northwest to the offshore area of the southeast and along several north-south trends in Portharcourt area. This is roughly equivalent to the transition between the crusts of the continent and the oceanic, and falls within the range of highest sedimentary thickness. This distribution of hydrocarbon was initially ascribed to timing of formation of trap in relation to migration of petroleum (earlier landward structures trapped earlier migrating oil). Evamy et al. (1978), however, pointed out that in several rollovers, there was a continuation of movement on the fault responsible for structure-building and resulting growth and was progressively relayed towards the south into the more recent portion of the section by consecutive crestal faults, ending by stating that there was no connection between petroleum distribution and growth along a fault. Five delta lobes which are fed by four separate rivers were related to the location of the areas rich in oil within the belt by Ejedawe (1981). He pointed out that the controlling agents are a rise in geothermal gradient in relation to the lowest gradient within the delta centre in addition to the generally higher age of sediments in the belt in relation to those further towards the sea. The most "maturity per unit depth" was given to the sediments in the belt by these factors. Weber (1987) stated that the belt rich in oil (golden lane) correspond with a concentration of rollover structures across depobelts with southern flanks that are short, and little southward paralic sequence. Doust & Omatsola (1990) suggested that distribution of petroleum is possibly connected to diversity of type of source rock (greater contribution from paralic sequences in

the west) and/or separation as a result of remigration. Haack et al. (1997) related the location of the belt rich in oil to source rocks that are oil-prone which are adjacently deposited to the delta lobes and suggested that accumulation of these source rocks was influenced by structural sub-basins of pre-Tertiary time connected to basement structures. Outside of the belt (central, easternmost, and northernmost parts of the delta), the gas-oil ratios (GOR) are high. The GOR within each depobelt increases seaward and along strike away from depositional centres. The causes for the distribution of GOR's are speculative and include remigration induced by tilting during the latter history of deposition within the down-dip portion of the depobelt, up-dip flushing of accumulations by gas generated at higher maturity, and/or heterogeneity of source rock type (Doust & Omatsola, 1990).

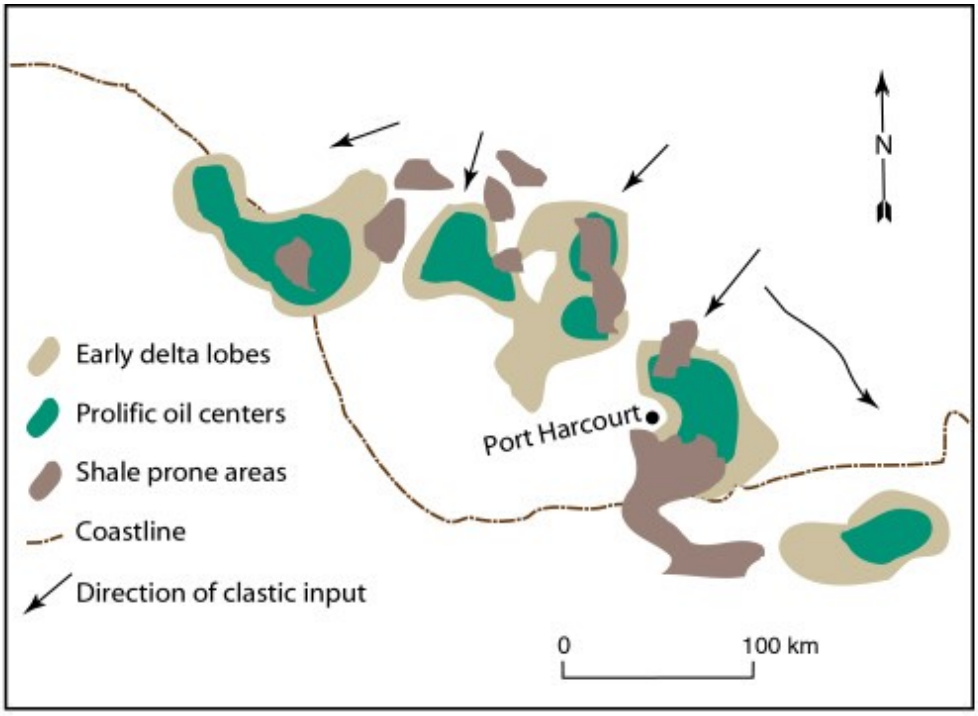


Fig. 2.7: Schematic map showing the location of lobes of the early Niger delta basin prolific oil centres, and shale prone areas (modified from Ejedawe 1981 and Reijers et al., 1997).

Stacher (1995) developed a hydrocarbon habitat model for the Niger delta using sequence stratigraphy. The model was constructed for the central portion of the delta, including some of the oil-rich belt, and correlates deposition of Akata Formation (the assumed source rock)

and the paralic sand and shale units in the Agbada Formation (the reservoir sand and seals) to sea level. Akata shale of pre-Miocene time was deposited in deep water at the time of lowstands and it underlies the system tracts of Miocene Agbada sequence. The Agbada Formation in the central portion of the delta fits a low depth ramp model with mostly highstand (sands bearing hydrocarbon) and transgressive (sealing shale) system tracts - third order lowstand system tracts were not formed. Faulting in the Agbada Formation provided pathways for petroleum migration and formed structural traps that, together with stratigraphic traps, accumulated petroleum. The shale in the transgressive system tract provided an excellent seal above the sands as well as enhancing clay smearing within faults.

2.3.5 Reservoir Rock

Petroleum in the Niger delta is produced from sandstone and unconsolidated sands predominantly in the Agbada Formation. Characteristics of the reservoirs in the Agbada Formation are controlled by depositional environments and by depth of burial (Evamy et al., 1978). Known reservoir rocks are Eocene to Pliocene in age, and are often stacked, ranging in thickness from less than 15meters to 10% having greater than 45 meters thickness (Evamy et al., 1978). The thicker reservoirs likely represent composite bodies of stacked channels (Doust & Omatsola, 1990). Based on reservoir geometry and quality, Kulke (1995) described the most important reservoir types as point bars of distributary channels and coastal barrier bars intermittently cut by sand-filled channels. Edwards & Santogrossi (1990) described the primary Niger delta reservoirs as Miocene paralic sandstones with 40% porosity, 2 darcys permeability, and a thickness of 100 meters. The lateral variation in reservoir thickness is strongly controlled by growth faults; the reservoir thickens towards the fault within the down-thrown block (Weber & Daukoru, 1975). The grain size of the reservoir sandstone is highly variable with fluvial sandstones tending to be coarser than their delta front counterparts; point bars fine upward, and barrier bars tend to have the best grain sorting. Much of this sandstone

is nearly unconsolidated, some with a minor component of argillo-silicic cement (Kulke, 1995). Porosity slowly decreases with depth because of the young age of the sediment and the coolness of the delta complex**.** In the outer portion of the delta complex, deep-sea channel sands, low-stand sand bodies, and proximal turbidites make possible reservoirs (Beka & Oti, 1995). Through greater part of the delta's history, three deep-water fans said to likely been active was described by Burke et al., (1972). The fans are comparatively smaller than those related with other big deltas. This is due to the fact that large quantity of the Niger-Benue sand is deposited on the delta top, and buried along with the non-distal parts of the fans as the location of the consecutive depobelts moves towards sea (Burke et al., 1972). The distribution, thickness, volume of shale, and pore volume/permeability characteristics of these fans are not well understood (Kulke, 1995).

2.3.6 Traps and Seals

Many of the traps known in the Niger delta oilfields are structural even though there also exist stratigraphic traps. It was during the synsedimentary deformation of Agbada Formation that the structural traps were developed (Evamy et al., 1978; Stacher, 1995). As discussed earlier, there is an increase in structural complexity from the north (older depobelts) down to the south (younger depobelts) due mainly to rising instability of the undercompacted and overpressured shale. Doust & Omatsola (1990) illustrated a variation of elements of structural trapping, including the ones connected with simple rollover features; channels that are clay filled, structures having several growth faults, structures having antithetic faults, and collapsed crest structures. Stratigraphic traps are as important as structural traps on the delta flanks (Beka & Oti, 1995). There is an occurrence of sandstone pockets between diapiric structures in this region. In the direction of the delta toe, this paralic series of sand and shale slowly grades to sandstone.

2.3.7 Fault Sealing in the Niger Delta Basin

Fault seals generally comprise two main types (though some minor types are known)– juxtaposition seals and fault gouge seals. Complete juxtaposition of a high sealing capacity rock layer (commonly shale or siltstone) against reservoir sandstone will form an effective hydrocarbon seal as long as the fault plane remains tightly closed and non dilatant and the seal rock is ductile during deformation (Doust & Omatsola, 1990). This is the simplest example of a fault seal. In other cases, deformed rock gouge material lying along the plane of a fault may seal or act as a flow barrier to hydrocarbons. Clay smears are known to form along fault planes in many delta regions where abundant ductile shales populate the stratigraphy (Doust & Omatsola, 1990). Clay smears have similar sealing properties to their parent ductile shale material and this means that depending on their continuity, they may seal hydrocarbons just as effectively as shale top seals (Doust & Omatsola, 1990). In Nigeria, clay smear seals are responsible for the retention of many commercial accumulations of oil and gas as well as substantial brine overpressures.

Fault gouge seals may also form when reservoir sands are themselves faulted, or faulted into contact with other sands. Under the correct conditions, the resulting cataclastic faults may act as capillary seals and flow barriers, commonly sealing columns of oil and gas several tens of meters in height under hydrostatic conditions. Diagenetic effects, such as quartz/calcite/salt precipitation, pressure solution and deposition of authiegenic clays, may enhance the sealing capacity of these faults. Older faults, which have not undergone tectonic reactivation, are likely to inherit these effects.

Three types of seals are recognized in the Niger delta basin, which include the following: (1) clay smears along faults, (2) interbedded sealing units juxtaposed against reservoir sands due to faulting, and (3) vertical seals produced by laterally continuous shale-rich strata (Doust &

Omatsola, 1990). Major erosion events of early to middle Miocene age formed canyons which filled with shale; these fills provide a top seal on the flanks of the delta for some important offshore fields (Doust & Omatsola, 1990). In summary, the primary seal rock in the Niger delta is the interbedded shale within the Agbada Formation. The shale provides three types of seals—clay smears along faults, interbedded sealing units against which reservoir sands are juxtaposed due to faulting, and vertical seals (Doust & Omatsola, 1990). On the flanks of the delta, major erosional events of early to middle Miocene age formed canyons that are now clay-filled. These clays form the top seals for some important offshore fields (Doust & Omatsola, 1990).

2.3.8 Petroleum Generation and Migration

Evamy et al. (1978) set the top of the present-day oil window in the Niger delta at the 240°F (115° C) isotherm. In the northwestern portion of the delta, the oil window (active source-rock interval) lies in the upper Akata Formation and the lower Agbada Formation**.** To the southeast, the top of the oil window is stratigraphically lower, up to 4000ft below the upper Akata/lower Agbada sequence (Evamy et al., 1978). Some researchers (Nwachukwu & Chukwura, 1986; Doust & Omatsola, 1990; Stacher, 1995) attribute the distribution of the top of the oil window to the thickness and sand/shale ratios of the overburden rock (Benin Formation and variable proportions of the Agbada Formation). The sandy continental sediment (Benin Formation) has the lowest thermal gradient (1.3 to 1.8°C/100 m); the paralic Agbada Formation has an intermediate gradient (2.7°C/100 m); and the marine, overpressured Akata Formation has the highest (5.5°C/100m) (Ejedawe, Coker, Lambeth-Aikhionabare, Alofe, & Adoh, 1984). Therefore, within any depobelt, the depth to any temperature is dependent on the gross distribution of sand and shale. If sand/shale ratios were the only variable, the distal offshore subsurface temperatures would be elevated because sand percentages are lower. To the contrary, the depth of the hydrocarbon kitchen is expected to be

deeper than in the delta proper, because the depth of oil generation is a combination of factors including temperature, time, and deformation related to tectonic effects (Beka & Oti, 1995).

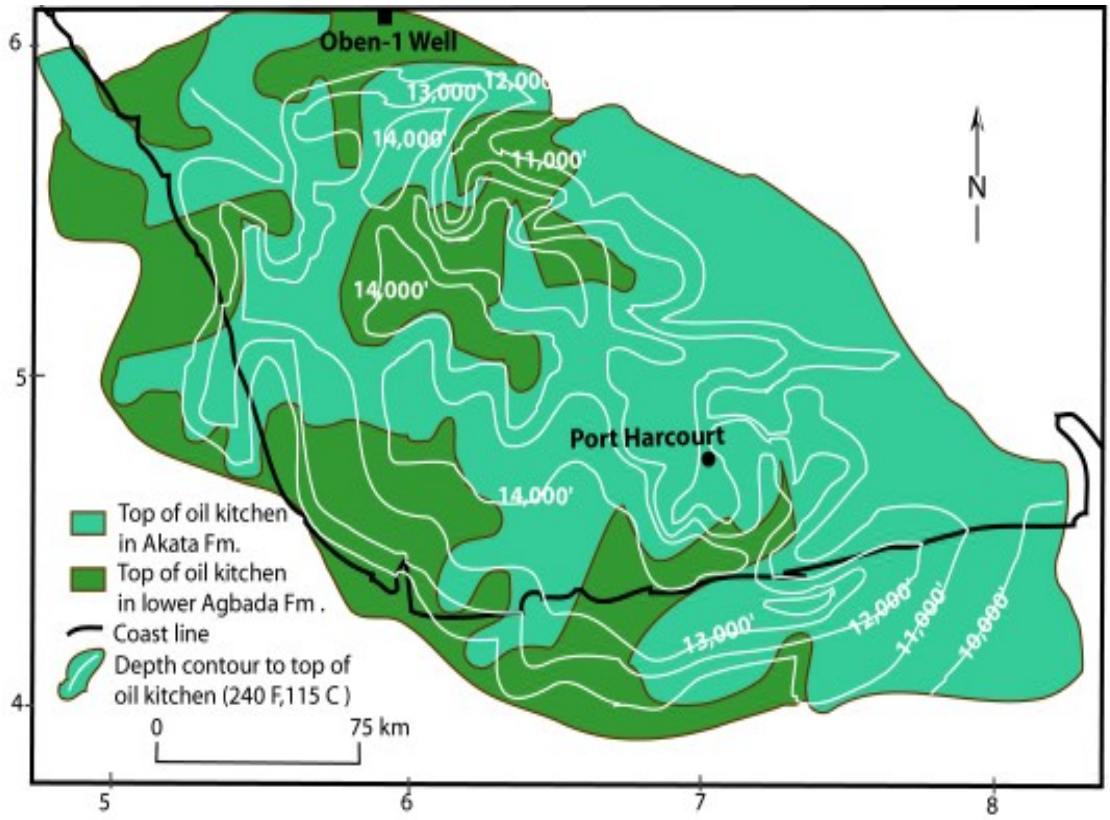


Fig. 2.8: Subsurface depth to top of the Niger delta oil kitchen showing where only the Akata Formation is in the oil window and where a portion of the lower Agbada is in the oil window. Contours are in feet (modified from Evamy, et al., 1978).

Evamy et al. (1978) argued that generation and migration processes occurred sequentially in each depobelt and only after the entire belt was structurally deformed, implying that deformation in the Northern belt would have been completed in the Late Eocene. The Akata/Agbada formational boundary in this region is currently at a depth of about 4,300 m, with the upper Akata Formation in the wet gas/condensation generating zone (vitrinite reflectance value >1.2) (Tissot & Welte, 1984). The lowermost part of the Agbada Formation here entered the oil window sometime in the Late Oligocene. The Northern Belt's Ajalomi-1 well about 25 km to the south of Oben-1 shows the Akata source rock first entering the oil window in the Oligocene after reservoir rock deposition (Stacher, 1995). Stacher assumed that migration overlapped in time with the burial and structural development of overlying reservoir sequences which occurred primarily across and up faults. Migration pathways were short as evidenced from the wax content, API gravity, and the chemistry of oils (Short & Stauble, 1967; Reed, 1969). Migration from mature, overpressured shales in the more distal portion of the delta may be similar to that described from overpressured shales in the Gulf of Mexico. Hunt (1990) related episodic expulsion of petroleum from abnormally pressured, mature source rocks to fracturing and re-sealing of the top seal of the overpressured interval. In rapidly sinking basins, such as the Gulf of Mexico, the fracturing/re-sealing cycle occurs in intervals of thousands of years. This type of cyclic expulsion is certainly plausible in the Niger delta basin where the Akata Formation is overpressured. Beka & Oti (1995) predicted a bias towards lighter hydrocarbons (gas and condensate) from the overpressured shale as a result of down-slope dilution of organic matter as well as differentiation associated with expulsion from overpressured sources.

2.4 Theoretical Framework

2.4.1 Introduction

Geomechanics can be defined as the scientific behaviour of rock and soil under stress. It is the study of how rocks deform, sometimes to failure, due to changes of stress, temperature, pressure, and other environmental factors (Whaley, 2019). Geomechanics is a branch of geophysics that applies to nearly all aspects of petroleum extraction from exploration to production down to abandonment. At the wellbore, geomechanics is important to understanding how drill bits remove rock, characterizing borehole stability, and designing and monitoring hydraulic fracturing stimulation programmes. Geomechanics is used to reduce risks and optimize rewards related to the mechanical failure of the reservoir, overburden, and underburden formations due to oil and gas exploration and production.

2.4.2 Mechanical Properties of Rocks

Mechanical properties of rocks are those physical properties which determine the mechanical behaviour of rocks under different conditions. This includes all the properties due to the static or dynamic action of solid bodies, liquids, or rocks. The elasticity and strength of rocks depend upon the magnitude and duration of such action. Included among the mechanical properties of rocks are acoustic properties, hydraulic and gas dynamic properties, and technological properties.

Frequently applied alternating loads give rise to elastic waves in the rocks. The properties characterizing the capacity to transmit these waves are known as ‘‘acoustic properties’’. Hydraulic and gas dynamic properties in rocks result from the action of liquids and gases either static or dynamic. Technological properties refer to the different conditions of breaking of rocks under different stress states. These include hardness, strength, rigidity, drillability, blastability, resistance to cutting, twistability, ductility, and malleability.

The mechanical properties of rocks can be quantitatively described by the knowledge of

(i) The rock compressive strength which is defined as the critical value of uniaxial compressive stress at which a rock breaks.

(ii) The rock tensile strength which is the critical value of uniaxial tensile stress at which a rock breaks.

(iii) Elastic constant which controls the amount of energy spent on breaking a rock either through drilling, blasting, or cutting. Also, the distribution of acoustic and shock waves in rocks depends on their elastic properties. These elastic properties are specified by the elastic moduli such as bulk modulus, shear or rigidity modulus, Young's or Stretch modulus, Poisson's ratio, Lame's constant, velocity of compressional and shear waves, and elastic impedance or acoustic impedance.

The two major categories of rock mechanical properties are elastic properties (Young's modulus, bulk modulus, shear modulus, Poisson's ratio, etc) and inelastic properties (Unconfined or Uniaxial compressive strength, formation strength, etc)

2.4.3 Stress and Strain

The generation of elastic waves involves the study of the stress and strain in the earth's materials or rocks. Since elastic waves are propagated through rocks, geophysicists study carefully the concepts of stress and strain in detail.

Stress is defined as the force per unit area of a given material. Thus, when a force is applied to a body, the stress is the ratio of force to the area on which the force is applied. If the force varies from point to point, the stress also varies and its value at any point is found by taking an infinitesimally small element of the area centred at the point and dividing the total force acting on this area by the magnitude of the area. If the force is perpendicular to the area, the stress is said to be a normal stress. When the force is tangential to the element of an area, the

stress is a shearing stress. However, when the force is neither parallel nor perpendicular to an element of an area, it can be resolved into components. Hence, any stress can be resolved into components of normal and shearing stress.

When external forces are applied to a body, balanced internal forces are set up within it. Stress is a measure of intensity of these balanced internal forces. The stress acting on any area of the surface within the body may be resolved into the components of normal stress perpendicular to the surface, and shear stress in the plane of the surface. At any point in the stressed body, three orthogonal directions can be defined on which the components of stress are wholly normal stresses; that is, no shearing act along them. These lengths define three orthogonal axes known as the principal axes of stress and the normal stress acting on these are known as ‘‘principal stresses’’. Each principal stress represents a balance of equal magnitude but oppositely directed towards components. The stress is said to be compressive if the forces are directed towards each other, and tensile if the forces are directed away from each other. If the principal stresses are all equal in magnitude within a body, the condition of stress is said to be hydrostatic, since this is the state of stress throughout a fluid body at rest. There are no shear stresses existing in a hydrostatic field since they cannot be sustained by a fluid body. A body subjected to stress may undergo a change of shape or size known as strain, up to a certain limiting value of stress known as the yield point/strength of the material.

Strain is the change in dimension and shape that occur when an elastic body is subjected to stresses. These changes which are called strains can be resolved into certain fundamental types. Therefore strain is defined as the relative or fractional change in the dimension or shape of a body when such body is subjected to serious stress. The elementary strain associated with such bodies includes normal strain, shearing strain, and simple rotations

about the three axes. The relative increase in length in the x, y, and z axes are referred to as normal strains. Mathematically, normal strains may be given as

$$\Sigma_{xx}=\frac{\partial u}{\partial x}\,;\ \Sigma_{yy}=\frac{\partial v}{\partial y}\,;\ \Sigma_{zz}=\frac{\partial w}{\partial z} \tag{2.1}$$

While shear strains are often given as

$$\Sigma_{xy}=\Sigma_{yx}=\frac{\partial v}{\partial x}+\frac{\partial u}{\partial y}\,;\ \Sigma_{yz}=\Sigma_{zy}=\frac{\partial w}{\partial y}+\frac{\partial v}{\partial z}\,;\ \Sigma_{zx}=\Sigma_{xz}=\frac{\partial u}{\partial z}+\frac{\partial w}{\partial x} \tag{2.2}$$

In equations 2.1 and 2.2, u, v and w are displacement vectors in the x, y and z directions, Σ_{xx}, Σ_{yy}, and Σ_{zz} are normal strains in the x, y and z directions, while Σ_{xy} and Σ_{yx}, $\Sigma_{yz}$and Σ_{zy}, and Σ_{zx} and Σ_{xz} are shear strains in the xy, yz, and zx axes respectively.

2.4.4 Elasticity

Elasticity is the property of resisting changes in size and shape by a body, and of returning to the original condition when the external force is removed. An elastic body is a body prone to reversible deformation.

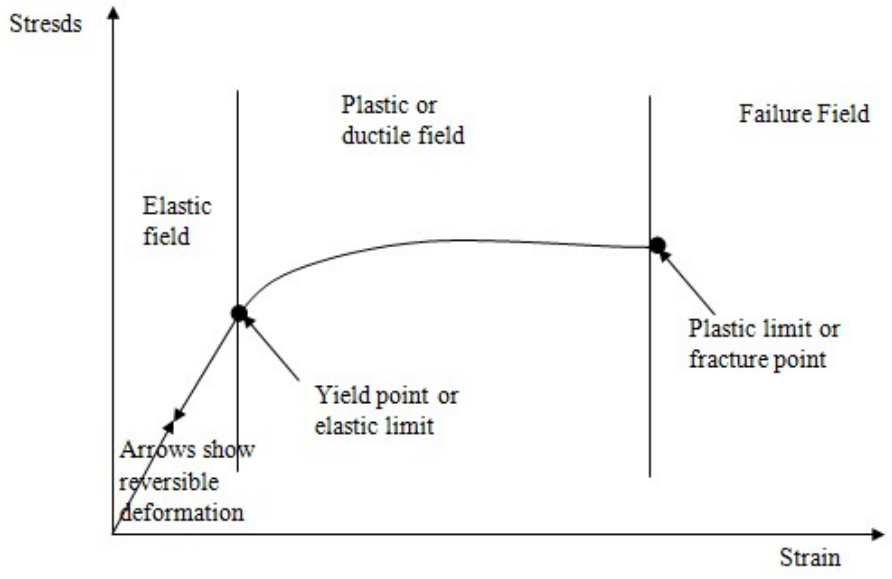


Fig. 2.9: The elasticity path of an earth model.

When a force is applied to a material, it may deform. This means that the particles of the material are displaced from their original positions. Provided the forces do not exceed a critical value, the displacements are reversible; the particles of the material return to their original positions when the force is removed, and no permanent deformation results. This is called elastic behaviour.

If a solid is deformed beyond a certain point known as elastic limit, it will not recover its original shape when the stress is removed. In this range, a small increase in applied stress causes a disproportionately large increase in strain. The deformation is said to be plastic. If the applied stress is removed in the plastic range, the strain does not return to zero, a permanent strain has been produced. If eventually the applied stress exceeds the strength of the material, failure occurs. In some rocks, failure can occur abruptly within the elastic range, this is called brittle behaviour.

2.4.5 Hooke's Law

In order to calculate the strains when the stresses are known, we must know the relationship between stress and strain. When the stresses are small, the relationship is given by Hooke's law. Hooke's law therefore states that ''a given strain is directly proportional to the stress producing it''. However, when several strains exist, each produced independent of the others; the total strain is the sum of strain produced by the individual stresses.

Although Hooke's law has a wide application, it does not hold for large stresses. For a given substance, when the stress is increased beyond the elastic limit, Hooke's law no longer holds and strains increase more rapidly. Hooke's law shows that all manner of deformations that take place in a solid body when the elastic limit (yield point) is not exceeded are all reversible. This shows that the elastic strength is reversible so that the removal of the stress is the removal of the strain.

If the yield point is exceeded, permanent strain results, that is, the strain becomes non-linear and partly irreversible and this is known as ‘‘plastic or ductile’’ strain. If the stress is increased still further, the body fail by fracture. The linear relationship between stress and strain in the elastic field is specified for any material by its various elastic moduli, each of which expresses the ratio of a particular type of stress to the resultant strain.

Hooke’s law can be written for an isotropic, elastic solid as

$$\sigma_{ij} = \lambda\theta\delta_{ij} + 2\mu e_{ij} \quad (2.3)$$

Where σ_{ij}= stress components, λ= Lame’s constant, θ = the dilatation (change in volume per unit volume), δ_{ij}=Kronecker delta such that $\delta=1$(i=j) and $\delta=0$ (i is not equal to *j*), μ=shear or rigidity modulus, and e_{ij}=strain components. The constant λ is related to the elastic constants defined physically. μ is the shear or rigidity modulus. The bulk and Young’s modulus can be expressed in both μ and λ.

2.4.6 Elastic Properties

A perfectly elastic body obeys the generalized Hooke’s law in which each component of stress is a linear function of the components of strain. Rock’s elastic properties include Poisson’s ratio, bulk modulus, shear modulus, Young’s modulus, etc. These elastic properties are interrelated such that anyone can be expressed in terms of two others. Evaluation of rock strength parameters and rock deformation behaviours are based on the analysis of rock mechanical behaviours and their relationship. The relationships between Poisson's ratio and other rock properties such as overburden pressure, bulk properties such as bulk compressibility, Young's modulus, modulus of rigidity, compressive and tensile strength, porosity, density, wave velocities, modulus of resilience, modulus of rupture, fractures, drill ability, and hardness is integral in the understanding of most of the questions in rock mechanics, which includes prediction of formation strength, determination of the magnitude

of in situ stresses, well stimulation, borehole and perforation stability, sand production and drawdown limits in unconsolidated formations.

A compact form of expressing all the stress-strain relationships is given by Hooke's law in equation 3 above. All the familiar elastic moduli may be expressed in terms of λ and μ by considering the application of special types of stress and by solving equation 3 above.

Depending on the mode of determination, we have the dynamic and the static elastic rock properties. Dynamic elastic rock properties are those elastic properties derived from well log (sonic and density) as an in-situ measurement. They can also be determined in the laboratory using high frequency acoustic pulses on core samples. Static elastic properties or constants on the other hand are derived in the laboratory from tri-axial stress-strain measurements (non-destructive) or the Chevron notch test (destructive).

2.4.6.1 Bulk Modulus (K)

Bulk modulus (K) expresses strain relationship in the case of a simple hydrostatic pressure (P) applied to a cubic element. It is the change in volume of a material under hydrostatic pressure. The resultant volume change or volume strain is change in volume divided by the original volume. Bulk modulus is therefore defined as the ratio of the volume stress applied to a cubic element to the volume strain.

$$\text{Bulk modulus} = \frac{\text{Volume Stress}}{\text{Volume strain}} = \frac{P}{\Delta v/v} \quad (2.4)$$

Bulk modulus or modulus of incompressibility is defined from the dilatation experienced by a body under hydrostatic pressure. It must be noted that the shear components of stress are zero for hydrostatic conditions ($\sigma_{xy}=\sigma_{yz}=\sigma_{zx}=0$) and the inward pressure (P, negative normal stress) is equal in all directions (that is $\sigma_{xx}=\sigma_{yy}=\sigma_{zz}=-P$). The bulk modulus is therefore the ratio of the hydrostatic pressure to the dilatation.

That is

$$K=\frac{-P}{\theta}, \text{ hence, } P=-k\,\theta \quad (2.5)$$

The inverse of equation 5, which is the inverse of the bulk modulus, often written as K^{-1} is called the modulus of compressibility. The bulk modulus describes the volumetric shape change of a material under the effects of the normal stresses σ_{xx}, σ_{yy}, σ_{zz}.

An expansion of the Hooke's law using Tensor analysis gives the following

$$\sigma_{xx}= \lambda\theta + 2\mu e_{xx}$$

$$\sigma_{yy}= \lambda\theta + 2\mu e_{yy}$$

$$\sigma_{zz}= \lambda\theta + 2\mu e_{zz} \quad (2.6)$$

Adding the three equations above and assuming hydrostatic conditions ($\sigma_{xx}=\sigma_{yy}=\sigma_{zz}=-P$) gives

$$\sigma_{xx}+\sigma_{yy}+\sigma_{zz}= 3\lambda\theta + 2\mu(e_{xx}+ e_{yy}+ e_{zz})$$

Therefore, $-3P = 3\lambda\theta + 2\mu\theta$; where $\theta = e_{xx}+ e_{yy}+ e_{zz}$

$$P = -(\frac{3\lambda\theta+2\mu\theta}{3}) = -(\frac{3\lambda\theta}{3} + \frac{2\mu\theta}{3})$$

$$P = -(\lambda\theta + \frac{2}{3}\mu\theta)$$

But $K=\frac{-P}{\theta}$

$$\text{Therefore, } K = \frac{(\lambda\theta + \frac{2}{3}\mu\theta)}{\theta} = (\lambda + \frac{2}{3}\mu) \quad (2.7)$$

This is the equation of the bulk modulus or modulus of incompressibility.

The bulk modulus can also be derived from density and sonic log information using the following equation (Osaki et al., 2018):

$$K = a\rho_b[\frac{1}{\Delta T_c^2} - \frac{4}{3T_s^2}] \quad (2.8)$$

Where a is a coefficient = 13464

ρ_b=Bulk density

T_C=Compressional sonic transit time in $\mu s/Ft$ and

T_s=Shear sonic transit time in $\mu s/Ft$.

K is in Gigapascal (GPa).

Bulk compressibility (C_b) is the inverse of the bulk modulus (K) or modulus of incompressibility and it is derived from the following equation:

$$C_b = \frac{1}{K} = \frac{3\Delta T_c^2 \, T_s^2}{a\rho_b[3T_s^2 - 4T_c^2]} \quad (2.9)$$

2.4.6.2 Young's Modulus (E)

Young's modulus or the modulus of elasticity describes the longitudinal strains on a material when a uniaxial normal stress is applied on the material. It is the ratio of uniaxial compressive (tensile) stress on a material to the resultant strain. It is derived from the principle of extensional deformations. In Young's modulus, each longitudinal strain is proportional to the corresponding stress component, that is, the stress in X direction is proportional or equal to the strain in that direction.

$$\sigma_{xx} = E\epsilon_{xx}$$

$$\sigma_{yy} = E\epsilon_{yy}$$

$$\sigma_{zz} = E\epsilon_{zz} \quad (2.10)$$

Where the constant of proportionality, E is the Young's modulus.

Consider a rod of original length, L and cross sectional area, A which is extended by an increment ΔL through an application of force to its ends as shown in the figure 2.10 below.

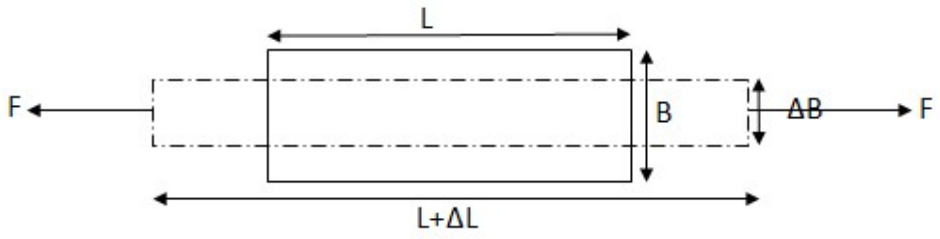


Fig. 2.10: Illustration of Young's modulus.

The relevant elastic modulus applicable to this form of deformation is the Young's modulus of elasticity, **E** defined as follows

Young's modulus, $E = \frac{\text{Longitudinal Stress}}{\text{Longitudinal Strain}}$

$$E = \frac{F/A}{\Delta L/L} \tag{2.11}$$

The extension of the rod in figure 2.10 above will be accompanied by the reduction in its diameter, that is, the rod will suffer both lateral and longitudinal strain. The ratio of the lateral strain to the longitudinal strain is called Poisson's ratio.

If one longitudinal stress only, say P_{11} is operative in a body (as in the stretching of a wire), Young's modulus, E is given as

$$E = \frac{P_{11}}{e_{11}} \tag{2.12}$$

In this case, applying equation 2.3 to equation 2.12 leads to the Young's modulus, E being given as

$$E = \frac{\mu(3\lambda+2\mu)}{\lambda+\mu} = \frac{9K\mu}{3K+\mu} \tag{2.13}$$

The Young's modulus or modulus of elasticity can also be derived from an equation involving a relationship between Young's modulus (E), Shear modulus (μ), and Poisson's ratio (σ) (Osaki et al., 2018) as stated below:

$$E = 2\mu\ (1 + \sigma) \tag{2.14}$$

Where μ=Shear modulus and σ =Poisson's ratio

2.4.6.3 Poisson's Ratio (σ)

The Poisson's ratio is the ratio of lateral strain to the longitudinal strain in a material subjected to longitudinal stress. The Poisson's ratio is the relation between the transverse

contraction stress and the longitudinal extension stress in the direction of the stretching forces. It is a measure of the change in shape of a rock under stress, that is, it is the geometric change of shape of a rock or material under uniaxial stress.

Normal materials have a positive Poisson's ratio and are one of the most important parameters related to vertical and horizontal stresses.

Poisson's ratio is an important mechanical property and can be used to predict geomechanical behaviour during well drilling and subsequent recovery processes. High instability, sand production and hydraulic fracturing are strongly influenced by resistance parameters, which may be related to its magnitude (Kumar, 1976).

Poisson's ratio = $\frac{\text{Lateral Strain}}{\text{Longitudinal Strain}}$

If only one longitudinal strain exists, the Poisson's ratio is given by

$$\sigma = \frac{-e_{zz}}{e_{11}} \tag{2.15}$$

Similarly, applying equation 2.3 to equation 2.15 gives the Poisson's ratio as

$$\sigma = \frac{\lambda}{2(\lambda+\mu)} = \frac{3K-2\mu}{6K+2\mu} \tag{2.16}$$

This parameter is critical in measuring compressional and shear rates (V_p and V_s) from seismic data or sonic well logs and then calculating the dynamic Poisson's ratio (σ_d) from Jones, Leddra, Goldsmith, & Edwards (1992) as:

$$\sigma_d = \frac{0.5(V_p^2 - 2V_s^2)}{(V_p^2 - V_s^2)} \tag{2.17}$$

The theoretical maximum value of σ is 0.5, where V_p= compressional wave velocity and V_s = shear wave velocity.

Velocity measurements are less destructive to rock mass, cheap and fast. Poisson ratio measurements reduce the risk of making incorrect predictions or inferences from certain data points. The Poisson frame ratio is determined by two independent factors, cracks and solid

rock (mineral compositions). In the presence of significant amounts of cracks, the Poisson ratio decreases considerably and the difference between the solid rocks is lost.

2.4.6.4 Shear or Rigidity Modulus (μ)

Shear or rigidity modulus is defined from the basic principle of shear deformation. It is a measure of the resistance of a rock or material to tensile shearing and is defined as the ratio of shear stress to shear strain. As in the case of longitudinal strains, each shear strain is proportional to the corresponding shear stress component, that is

$$\sigma_{xy} = \mu e_{xy}$$

$$\sigma_{yz} = \mu e_{yz}$$

$$\sigma_{zx} = \mu e_{zx} \qquad (2.18)$$

The proportionality constant, μ is the shear or rigidity modulus of the material. This elastic rock parameter describes a rock's tendency to shear (the deformation of shape at constant volume) when acted upon by opposing forces. The deformation of a solid material is small if the shear modulus is high. Shear modulus can be determined in the laboratory as a static modulus and can be determined dynamically using data from sonic and density logs.

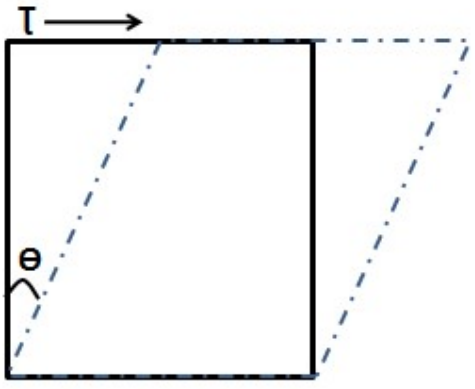


Fig. 2.11: Illustrating Shear or Rigidity modulus.

The shear modulus is defined as the ratio of shear stress to the resultant shear strain. Mathematically, it is given as

$$\mu = \frac{\text{Shea Stress } (\tau)}{\text{Shear Strain } (\text{Tan } \Theta)} = \frac{E}{2(1+\sigma)} \quad (2.19)$$

The Shear modulus (μ) can also be determined from the following empirical formular (Schlumberger 1989) :

$$\mu = \frac{a\rho_b}{\sigma(\Delta T_s)} \quad (2.20)$$

Where *a* is a coefficient=13464,

ρ_b=Bulk density,

σ=Poisson's ratio, and

T_s=Shear sonic transit time in$\mu s/Ft$.

μ is in Gigapascal GPa.

The above described four elastic parameters are interrelated such that anyone can be expressed in terms of two others as shown in equations 2.21 to 2.24 below:

i. The bulk modulus, $K = (\lambda + \frac{2}{3}\mu) = \frac{E}{3(1-2\sigma)}$ (2.21)

ii. The Young's modulus, $E = \frac{\mu(3\lambda+2\mu)}{\lambda+\mu} = \frac{9K\mu}{3K+\mu}$ (2.22)

iii. The Poisson's ratio, $\sigma = \frac{\lambda}{2(\lambda+\mu)} = \frac{3K-2\mu}{6K+2\mu}$ (2.23)

iv. And the Lame constant, $\lambda = K - \frac{2}{3}\mu = \frac{\sigma E}{(1+\sigma)(1-2\sigma)}$ (2.24)

2.4.7 Compressional and Shear Wave Velocities

When seismic energy is released suddenly at a point near the surface of the earth, part of the energy spreads out on the surface of the earth as seismic surface waves, analogous to the ripples on the surface of a pool of water into which a stone has been thrown. The remaining part of this seismic energy propagates through the body of the earth. These are called seismic

body waves. In seismology, two types of body waves are recognized and they are: Compressional or Primary body waves (called P-waves) and Shear or Secondary body waves (called S-waves).

2.4.7.1 Compressional Body Waves (P-Waves)

The compressional body waves passes through a medium as a series of compressions and dilatations. The equation of the compressional body wave in the X-direction is given as

$$\frac{\partial^2 \theta}{\partial t^2} = V_P{}^2 \frac{\partial^2 \theta}{\partial X^2} \tag{2.25}$$

Where θ is the displacement at time *t, X* is the distance from the origin, and V_P is the compressional or primary wave velocity.

In terms of the elastic constants, this velocity is given by

$$V_P{}^2 = \sqrt{\frac{\lambda+2\mu}{\rho}} = \sqrt{\frac{K+4/3\mu}{\rho}} = \sqrt{\frac{E-(1-\sigma)}{\rho(1-2\sigma)(1-\sigma)}} \tag{2.26}$$

ρ is the density.

The compressional wave is the fastest of all seismic waves. When an earthquake occurs, this wave is the first to arrive at a recording station. As a result, it is called the primary or P-wave. From equation 2.26 above, P-waves can travel through solids, liquids, and gases all of which are compressible (K is not equal to zero).

2.4.7.2 Shear Body Waves (S-Waves)

The equation of the shear wave is given as

$$\frac{\partial^2 N}{\partial t^2} = V_S{}^2 \frac{\partial^2 N}{\partial X^2} \tag{2.27}$$

Where V_S is the velocity of the shear wave given by:

$$V_S = \sqrt{\frac{\mu}{\rho}} = \sqrt{\frac{E}{2\rho(1+\sigma)}} \tag{2.28}$$

The only rock elastic property that determines the velocity of the shear wave is the rigidity or shear modulus μ. In liquids and gases, the shear modulus is zero (μ=0) and shear waves

cannot propagate. Shear waves from an earthquake travel slowly compared to the compressional waves and are recorded at an observation station as later arrivals. Hence, they are often referred to as secondary waves.

The compressional and shear wave velocities are very important parameters in the computation of the mechanical properties of rocks. The ratio of the compressional wave to the shear wave ($\mathbf{V_P/V_S}$) combined with formation density is used in the calculation of the elastic rock parameters of Poisson's ratio, Young's modulus, bulk modulus, and shear modulus.

2.4.8 Inelastic Properties

Inelastic properties of a rock or material are those properties that describe the inflexibility of that material when a load or stress is applied on it. The two inelastic rock properties are formation strength; which includes uniaxial compressive strength, tensile strength, shear strength, and cohesive strength; and fracture gradient. As in elastic rock properties, we also have dynamic and static inelastic properties depending on their mode of determination.

2.4.8.1 Formation Strength

The strength of a rock or material is the capability of that material to resist stress or pressure without fracturing or failing. The strength of a rock is determined by its makeup, mineralogy, character of particle contacts which are a result of post depositional compaction, digenesis, catagenesis, and tectonism which all depend on the geologic history of the formation. The compaction resulting from the stress conditions of the overburden layer causes the expulsion of fluids, the increase in contact with the grains, the apparent density, the Biot coefficient, the modulus of elasticity and rigidity; decrease in porosity and general increase in resistance. Burial diagenesis drives the sediment towards higher mechanical and chemical

thermodynamic stability reducing porosity and pore pressure as dictated by stress, permeability and compartmentalization.

The temporal and spatial variations in lithologies, sedimentation rate and structural configurations form compartments and induce heterogeneity able to cause time-dependent or non-time-dependent heterogeneity, resistance to rocks, mechanical properties and in situ constraints. (Fjær, Holt, Horsud, & Raaen, 2008).

Rock strength are determined from laboratory tests through uniaxial, triaxial and polyaxial compressive tests on cylindrical rock cores from the well section at depth of interest and secondarily from empirical correlations using wireline log data calibrated with core tested rock strength from the laboratory.

There are four major types of rock strength, uniaxial or unconfined compressive strength (UCS), Tensile strength, shear strength, and cohesive strength.

Unconfined or uniaxial compressive strength (UCS) is the capacity of a material to carry loads when acted upon under compression. It is the maximum value of the stress that can be applied to a rock without irreversible deformation or causing the rock to fracture completely under compression. Unconfined compressive strength of a rock (UCS), which measures the rock strength, is one of the most vital properties required to address various geomechanical problems which ranges from limiting wellbore instabilities during drilling to assessing sanding problems during production.

Tensile strength of a rock or material is the maximum amount of tensile stress that a rock or material withstands before fracturing. Rocks under tensile stress shows a decrease in the total volume per unit area and it is usually much lower than the uniaxial compressive strength of the same rock. Rocks are most likely to fail under tensile stress than compressional stress. As

such, it is very necessary to know the stress regime a rock will have to undergo prior to any design.

Shear strength is the ability of a rock or material to withstand shear stresses acting in opposite directions along a plane of weakness (fracture, fault, etc.) inclined at some angle to the forces. Shear strength is a product of the normal stress and the angle of friction of the material. Shearing forces tear the material along the plane of shearing e.g. rifting in tectonic environment where mantle upwelling below the crustal earth provide tension.

Finally, cohesive strength is a component of shear strength acting along the shear plain independent of the particle's internal friction. It is derived from tight interlocking of room crystals and grains (Blyth & Freitas, 2006). Rocks deform and fail even under constant stresses lower than the rock strength after a time delay. This is evident from wellbore deterioration with time as shear-failure-depicted breakouts increase greatly from dipmeter logs conducted hours later after drilling at the same depth. This is attributed to decrease in compressive strength of the rock as time exposure increases. Zoback (2007) have reported decrease in rock compressive strength caused by relaxation or creep under constant loading.

The following parameters are used to determine rock strength from geophysical logs:

1. Compressional wave velocity ($\mathbf{V_p}$) which is the reciprocal of interval transit time. This is directly measured.
2. Young's modulus (**E**), which is obtained from velocity and density measurements.
3. Porosity ($\boldsymbol{\phi}$), which is often gotten from measurement of density assuming rock matrix and fluid densities.

2.4.8.2 Fracture Gradient

Fracture gradient or fracture gradient pressure can be defined as the pressure at which a fracture closes. Formation breakdown pressure or fracture pressure is the pressure needed to cause fracturing of intact rocks. According to Nagel and Meng (2009), fracture breakdown pressure is dependent on the tensile strength of the rock, pore pressure and the maximum and minimum horizontal stresses.

Fracture gradient is used to identify the maximum mud weight for drilling safely without unintentionally fracturing the formation and causing loss of mud circulation and it is ideally the minimum horizontal stress magnitude. When fracture gradient is equal to the near wellbore hoop stress drilling is at high risk. The lower bound of the fracture gradient is the minimum horizontal stress under poro-elasticity.

2.4.9 Mohr Diagram

The state of stress and rock failure in a solid medium can be described by the Mohr circle diagram and the Mohr-Coulomb-Griffith failure criterion envelop as shown in figure 6 below. The Mohr circle is a 2D illustration of the stress tensor in the normal stress (horizontal axis) and shear stress (vertical axis) domains (Kamei, Nakata, & Lumley, 2015).

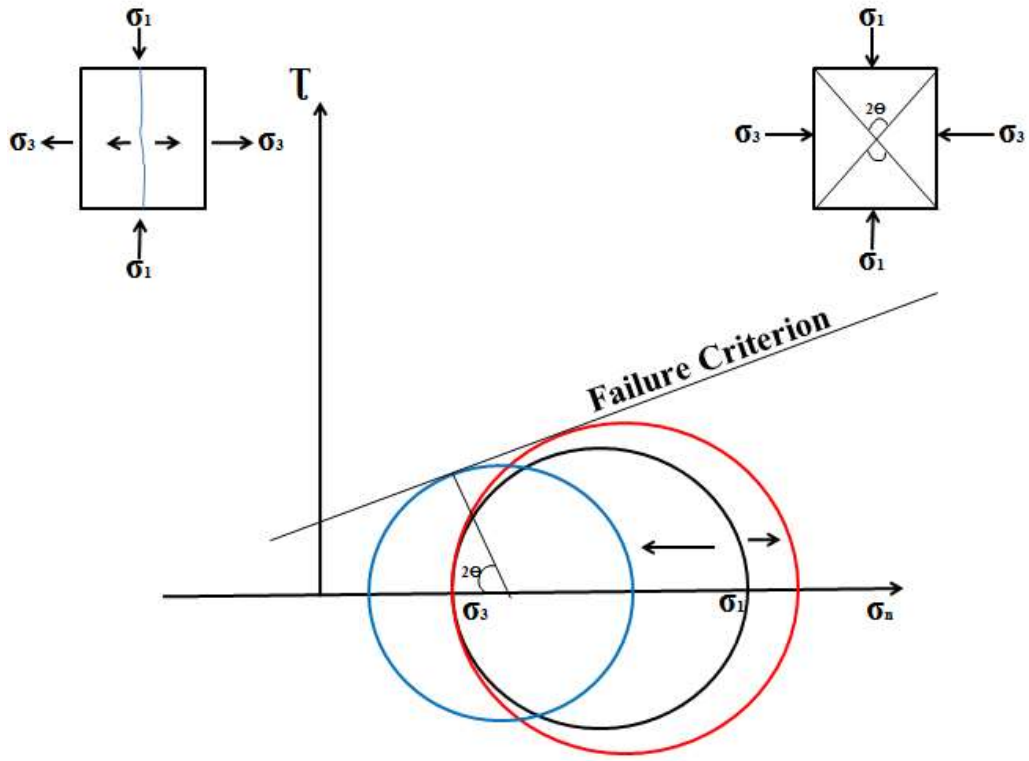


Fig. 2.12: Mohr circle diagram with the Mohr-Coulomb-Griffith failure criterion envelop.

In the Mohr diagram above, the horizontal axis is effective normal stress, while the vertical axis is effective shear stress. The black Mohr circle indicates an initial stable stress condition, and each point along the Mohr circle corresponds to the normal and shear stress values at various coordinate direction rotation angles. For example, the stress values along the horizontal axis describe the minimum and maximum principal stresses because the shear stress is zero. Remark that the stress values plotted in the Mohr circle diagram are effective stress values (that is, the applied stress minus the pore pressure). The resulting fracture mechanisms of pure shear failure (positive normal stress regime) and pure tensile failure (negative normal stress regime) are illustrated by the schematic insets in the figure 6 above.

Changing either the applied stress or the pore pressure (by fluid injection or withdrawal) can shift the initial stable Mohr circle towards the failure envelop. The cohesion or fracture strength of the rock is described by the intercept, while the sliding friction of the rock

material is related to the slope of the Mohr-Coulomb-Griffith failure envelop. When the Mohr circle touches the Mohr-Coulomb-Griffith failure envelop, the rock fails. The angle perpendicular to the failure envelop at that point where the Mohr circle touches the failure envelop gives the fracture angle of the rock failure. An increase in maximum principal stress, for instance long term tectonic deformation (red circle), or an increase in pore pressure, for instance water injection (blue circle) can induce failure in the rock.

2.4.9.1 Mohr-Coulomb Equation

The theory of Mohr-Coulomb represents a mathematical model that describes the response of brittle materials or rubble piles to shear stress and normal stress (Juvinal & Marshek, 1991). In general, this theory is applicable to materials for which the compressive strength far exceeds the tensile strength (Juvinal & Marshek, 1991). It is applied in geotechnical engineering to define shear strength of soils and rocks at different effective stresses, and in structural engineering to determine failure load in addition to the angle of fracture of a displacement fracture in concrete and similar materials (Juvinal & Marshek, 1991).

The Mohr-Coulomb failure criterion represents the linear envelope that is obtained from a plot of the shear stress of a material against the applied normal stress (Coulomb, 1776). This relation is expressed as

$$\tau = C + \sigma_n \tan\phi \qquad (2.29)$$

Where τ is the shear stress, σ_n is the normal stress; C is the intercept of the failure envelope with the τ-axis, $\tan\phi$ is the slope of the failure envelope or the coefficient of internal friction. The quantity C is called the cohesion or the inherent shear strength, and the angle ϕ is called the angle of internal friction. This shows that the Mohr-Coulomb criterion contains two constants related to the material. It is worthy of note that this criterion reduces to Tresca

criterion if ϕ equals zero, and is equivalent to Rankine model if ϕ equals ninety degrees. The Mohr-Coulomb criterion does not permit higher values of ϕ.

2.4.10 Pressure

Pressure is the amount of force applied perpendicular to the surface of an object per unit area. We have effective/differential pressure, formation or pore pressure, as well as overburden or lithostatic or total pressure.

Effective pressure, P_e, is the pressure caused by the weight of the rock matrix overlying the formation of interest and it is given by

$$P_e = \rho_g \, g \, z \tag{2.30}$$

Where ρ_g is the grain density, g is the acceleration due to gravity and z is the height of the column.

Overburden pressure (lithostatic or geostatic pressure) is the pressure exerted by the overlying pore fluid and rocks. This pressure increases with depth. It is expressed as

$$S = g\int\rho_b(z)dz \quad \text{and} \quad \rho_b = \phi\,\rho_f + (1-\phi)\rho_g \tag{2.31}$$

Where ρ_b is the depth dependent bulk density, ϕ is fractional porosity, ρ_f is pore fluid density and ρ_g is the density of the matrix (grain density).

Formation or pore pressure is therefore the pressure of fluid contained in pore space of rock. It is the pressure of fluid held within a rock, in gaps between particles (pores). This is the pressure exerted by the pore fluids and its unit is pounds per square inch (psi)

Pore pressure = normal pressure + over/underpressure

There are three categories of formation pressure and they are normal pressure, abnormal pressure, and subnormal pressure.

1. Normal formation pressure is the hydrostatic pressure of formation fluid extending from the surface to the surface formation being considered. Normal formation pressure is not a constant; its magnitude varies with the concentration of dissolved salts, type of fluid, gases present, and temperature gradient.

2. Abnormal formation pressure or overpressure is defined as any pore pressure that is greater than the hydrostatic pressure of the formation fluid occupying the pore space. It is sometimes called overpressure or geopressure. An abnormally pressured formation can often be predicted using well history, surface geology, downhole logs, or geophysical surveys.

Overpressure = pore pressure - normal pressure

3. Subnormal formation pressure or underpressure is defined as any formation pressure that is less than the corresponding fluid hydrostatic pressure at a given depth. Subnormally pressured formations have pressure gradients lower than fresh water or less than 0.433 psi/ft.

Formation pressure is determined in drilled wells or boreholes through logging.

2.4.10.1 Terzaghi Relationship

The Terzaghi's pressure relationship (net lithostatic stress or net overburden stress or net confining stress) states that ''the total stress on a rock unit is jointly supported by the pore fluid and the rock matrix'' (Terzaghi, 1943).

$$\sigma_{\text{total}} = \text{PP} + \sigma_{\text{effective}} \tag{2.32}$$

Where σ_{total} the total stress on the rock unit, PP is is the pore pressure, and $\sigma_{\text{effective}}$ is the effective stress on the rock.

The total or overburden pressure is the pressure due to the combined weight of the rock matrix and the fluids in the pore space overlying the formation of interest at a given depth (Ugwu, 2015). As stated in equation 30 above, the overburden pressure can be expressed as integral of density (Ugwu, 2015):

$$S = g \int_0^z \rho(z)dz \tag{2.33}$$

Where S is the overburden pressure, g stands for acceleration due to gravity, and ρ is the bulk density obtainable from a density log (Ugwu, 2015).

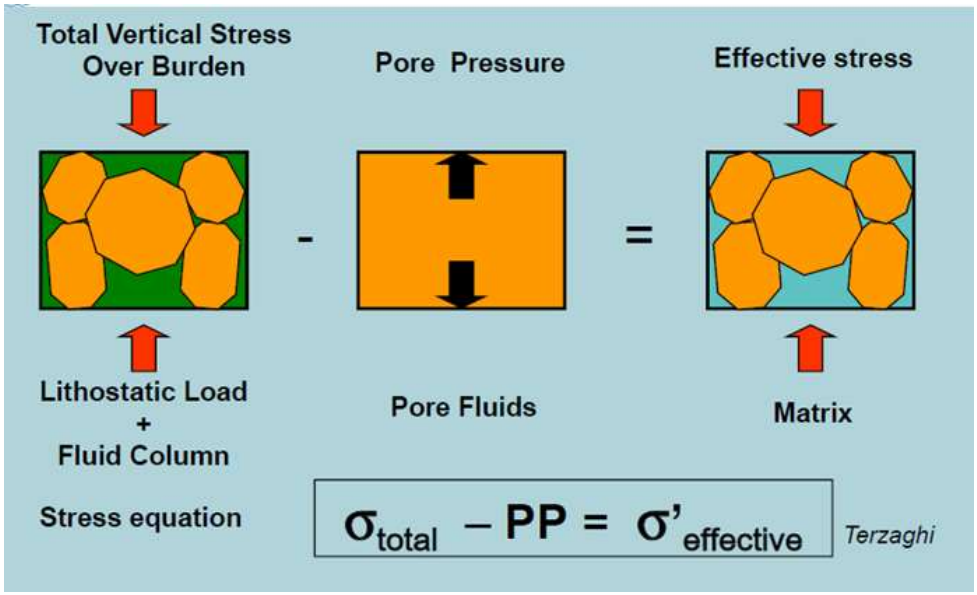


Fig. 2.13: Illustration of the Terzaghi relationship.

The effective vertical stress is the stress applied to the rock matrix.

$$\sigma_{effective} = \sigma_{total} - PP \tag{2.34}$$

2.4.10.2 Relating Pore Pressure to Velocity

Eaton's method

According to Eaton, 1975,

$$PP = P_{ob} - (P_{ob}-P_{hd}) \ (V_{int} \ / V_{norm}\, x)^3 \quad (2.35)$$

Where: PP = Pore pressure gradient (ppg or psi/ft), P_{ob} = Overburden pressure (ppg or psi/ft), P_{hd} = Hydrostatic pressure, V_{int} = seismic interval velocity (m/s), and V_{norm} = shale velocity at normal pressure (m/s).

This Eaton's method however, has limitations when applied in geological complicated areas such as formations with unloading effects (Ugwu, 2015). The method can only act to simulate unloading curves when the exponent in equation above becomes greater than 3 (Ugwu, 2015). The modified Eaton's method becomes:

$$PP = P_{ob} - (P_{ob}-P_{hd}) \ (V_{int} \ / V_{norm}\, x)^n \quad (2.36)$$

Where n describes the sensitivity of velocity to differential stress and depends on the Formation being studied.

Bowers method

PP = Total vertical stress – Effective stress σ (2.37)

Bower assumes an Effective stress σ–velocity relationship such that

$$\sigma = 1/a(V_{int} - V_{mudline})^{(1/b)} \quad (2.38)$$

Where: V_{int} = Interval velocity observed (m/s), a and b are calibration functions from known pressure zones (Bowers, 1995).

Tau compaction model

Sonic velocities are related to effective stress by scaling the interval transit time as:

$$\tau = (200- ITT)/(ITT- 150) \quad (2.39)$$

Then, $\tau = A \times \sigma^{B}_{eff} = A \times VES^{B}$ (2.40)

And $VES = S - \xi PP$ (2.41)

Where: ITT = Initial Travel Time, σ_{eff} = VES = *Vertical* Effective Stress, τ = tau, S = Overburden or lithostatic stress, PP = Pore pressure, ξ= Skempton factor or poroelastic coefficient, A and B are parameters determined from the behaviour of the sonic log data in the normally pressured zone where effective stresses are known.

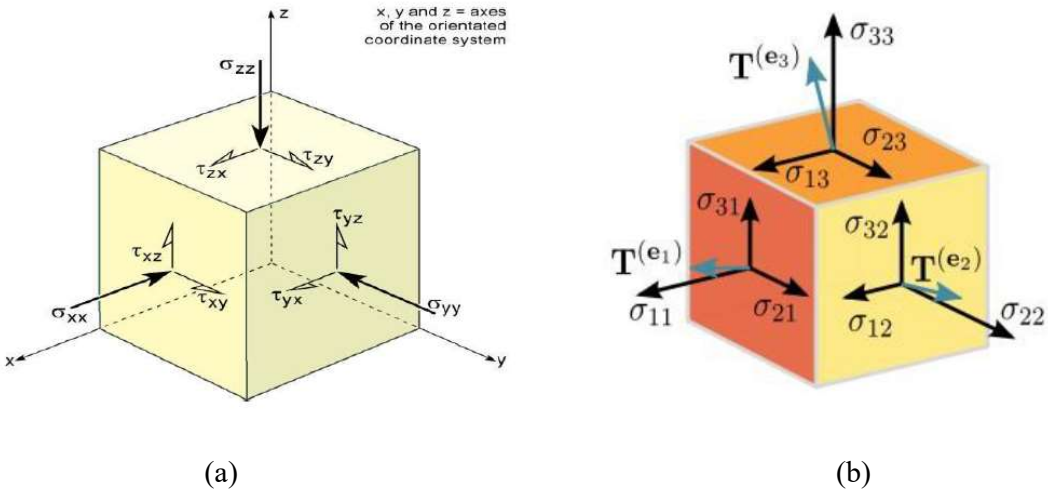
2.4.11 Stress

Stress can be described as the force which is acting over a given area. Sometimes, because stress is a tensor, stress tensor is employed in showing the amount of forces which is acting on a given surface in a continuous medium at a given point (Tingay, 2009; Zoback, 2007). Rocks exhibit anisotropic as well as isotropic properties. For rocks which are anisotropic, the rock property values estimated in various directions are different from each other. For rocks which are isotopic, the rock property values estimated in various directions are the same. A material whose response is independent of the applied stress is isotropic (Jaeger et al. 2007). The stresses acting on a homogenous isotropic body is described by continuum mechanics as a tensor of rank two with a total of nine components (Hudson & Harrison, 1997). Six out of these nine are shear stresses while three are normal stresses (Tiab & Donaldson, 2012). These define the stress state acting on a cubic element situated at any given depth as shown in equation 2.42.

$$S = \begin{matrix} \sigma_{11}\ \tau_{12}\ \tau_{13} \\ \tau_{21}\ \sigma_{22}\ \tau_{23} \\ \tau_{31}\ \tau_{32}\ \sigma_{33} \end{matrix} \quad (2.42)$$

The subscripts of the tensors of second order rank represent the direction of the components of force and the surface acted upon. It can then be said that stress components are

representative of the force which is acting in a definite direction on an area of known orientation. To effectively picture the stress condition in a reservoir at a given depth, description of the three normal and six shear stress magnitudes in addition to their orientation angles in 3D is very essential (Zoback, 2007).



(a) (b)

Fig. 2.14: (a) The normal and shear stress components on an infinitesimal cube. (b) The stress tensor, a second-order tensor (Hudson & Harrison, 1997).

All shear stresses become zero along some sets of axes where the normal stresses have their highest values. Three mutually- perpendicular planes describe these axes, normal stresses acting on these planes are referred to as principal stresses (Tiab & Donaldson, 2012). All stress states aid in comprehending the principal stresses. A representation of the principal stress tensor is stated as

$$S = \begin{matrix} \sigma_1 & 0 & 0 \\ 0 & \sigma_2 & 0 \\ 0 & 0 & \sigma_3 \end{matrix} \qquad (2.43)$$

where σ_1 represents the total vertical stress, σ_2 represents the maximum horizontal and σ_3 represents the minimum horizontal stress.

Three stress regimes can be identified if rock deforms or fails in shear (Anderson, 1951; Cerveny, Davis, Dudley, Kaufman, Knipe, & Krantz, 2004). These stress systems are related to the three fault system classifications by Anderson (1951). Faulting theory is applied as a base to explain the foundation of failure associated with faults. The state of stress is described by three mutually-perpendicular principal stresses (Twiss & Moores, 1992). This description was done by Anderson by applying a hypothesis that makes the assumption that one out of the principal stresses is the largest, then the intermediate and the least (i.e. $\sigma_1 > \sigma_2 > \sigma_3$).

The overburden load is always vertical and is initially identified because the remaining two are perpendicular as well as horizontal. This automatically describes the directions or inclinations of the two stresses which are horizontal (Cerveny et al, 2004; Economides & Nolte, 2000). This faulting theory by Anderson foretells the nature and type of fault that develops at an area to form in dual conjugate planes.

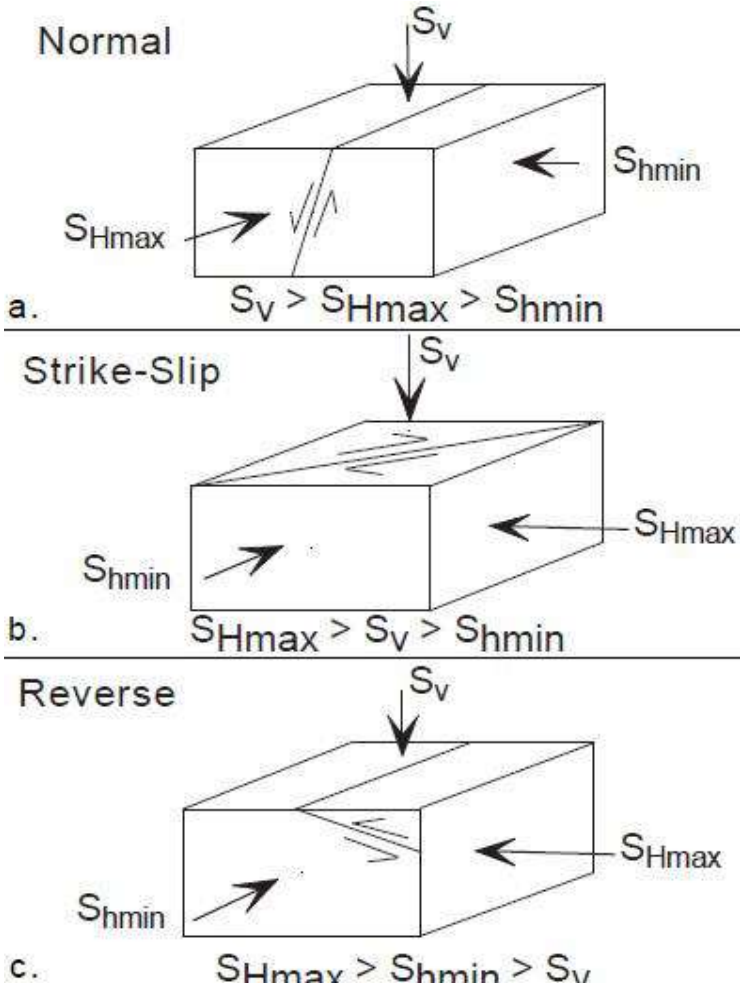


Fig. 2.15: Andersonian's classification scheme for types of faulting regimes (Zoback, 2016)

Geomechanics experts apply science and theory in evaluating the mechanical response of rocks of the subsurface inside the force fields operating in their physical surrounding (Sorough, 2013). Geomechanics involves the application of the principles of engineering to rock design mechanics and construction on/in the rock.

A good understanding of modern day tectonic stress is essential for several applications including improvement of wellbore stability to augment hydrocarbon recovery via induced/ natural fracture (Tingay, Muller, Reimaker, & Heidbach, 2005).

The study of global stress map gives an insight into the state of stress of the Earth. This reveal the forces generating local as well as regional stress fields as plate boundaries tectonics particularly at mid-oceanic ridges and zones of continental convergence (Tingay, 2009). Therefore, information on stress distribution, rock mass distribution and history of deformation are uncovered from modern day stress field knowledge, predominantly within sedimentary basins (Tingay et al., 2005). Hence, there are implications on petroleum exploration and exploitation of regional and local scale stresses.

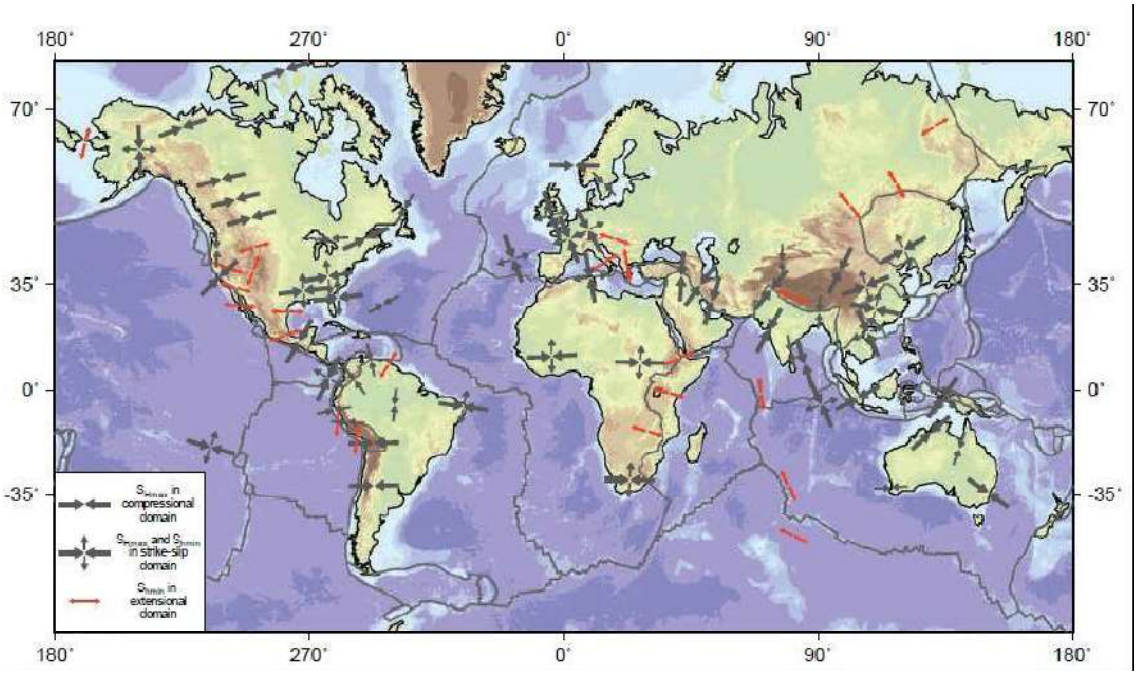


Fig. 2.16: Generalized world stress map (Zoback, 1992)

2.4.12 Interpretation of Seismic Data

The interpretation of reflection seismic data commences as soon as the acquired seismic data is fully processed. This involves the actual analyses of the seismic section. The seismic section is a graphical representation of the physical measurements of the subsurface displayed in two dimensions of space and time. In the interpretation of seismic data, the data are carefully and thoroughly examined, faults picked, horizons mapped and seismic maps

prepared. From the seismic section, seismic velocity which indicates the time rate of change of displacement is generated from the seismic section. The seismic velocity is a very important parameter in pore pressure and geomechanical evaluation. It is a property of the medium, which can be inferred from refraction time-distance curve, sonic logs, Normal Moveout, and in well shooting. Seismic velocities include; average velocity, root mean square velocity, stacking velocity, instantaneous velocity, interval velocity and normal move out velocity. These seismic velocities are measured in boreholes through sonic logs and also by surface seismic data acquisition method.

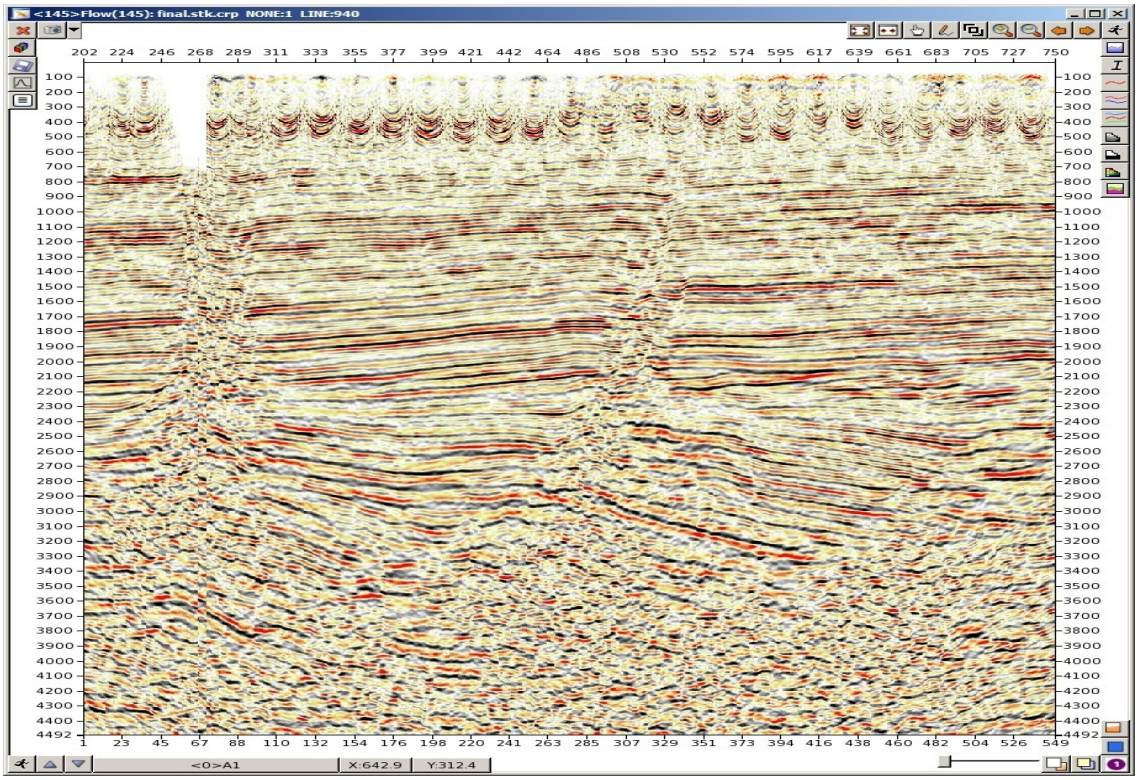


Fig. 2.17: A time-migrated seismic section from the Niger Delta (Agoha, 2018).

In reflection seismic data interpretation, 3-Dimensional (3D) seismic data is highly preferred and generally acceptable over 2-Dimensional seismic data. This is mainly due to the fact that 3D seismic data provides a volume of closely spaced three-dimensionally time-migrated data, and a highly enhanced signal-to-noise ratio (Gaarenstroom, 1984). This allows for a better and more robust interpretation of the data. 3D seismic volume also collapses subtle

diffractions from fault boundaries and other discontinuities or distorted images to their point of origin in a 3D manner (Gaarenstroom, 1984).

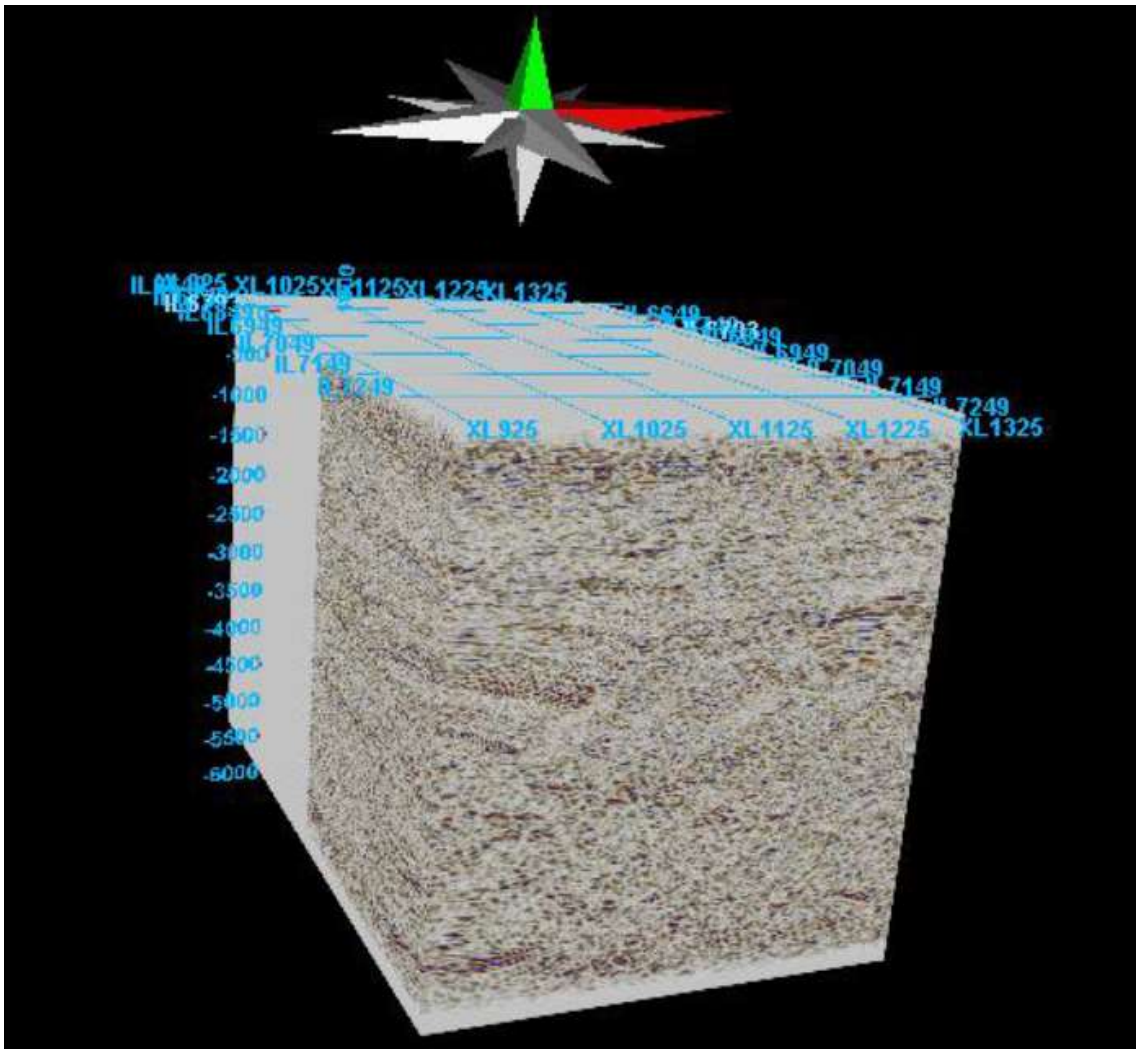


Fig. 2.18: 3D seismic volume of a time-migrated seismic data from the Niger Delta (Osaki, 2019)

2.4.12.1 Seismic Velocity

The velocity of P-waves in a homogenous solid is a function only of the elastic constants and the density. Several factors can influence velocity in fluid–filled sediments. These factors include: Porosity, grain size, pressure, compaction, pore space and micro-cracks, lithology, etc.

Pressure, compaction and depth

Differential or effective pressure is defined as the differences between overburden or lithostatic pressure and fluid or pore or formation pressure. Differential pressure is inversely related to porosity. Pressure and compaction increase with increase in depth of burial. Consequently, velocity increases with an increase in depth. In actual rocks the pore spaces are filled with a fluid whose elastic constant and density also affect the seismic velocity (Telford, Geldart, Sheriff, & Keys, 1976). The fluid is under a pressure which usually is different from that resulting from the weight of the overlying rocks. In this situation, the effective pressure on the granular matrix is the difference between the overburden and fluid pressures. Where formation fluids are under abnormal pressures approaching the overburden pressure, the seismic velocity is exceptionally low, a fact which is sometimes used to predict abnormal fluid pressure from velocity measurements (Telford et al., 1976).

Pore space and micro-cracks

Seismic velocity is dependent not only on rock type, porosity and depth of burial, but also on physical arrangement of the materials that surround the pores, the distribution and shape of pores. The presence of micro-cracks in rocks can reduce the velocity of the whole rock (Gardner, Gardner, & Gregory, 1974).

Lithology

Changes in seismic velocity as a result of change in lithology are caused by changes in porosity from one lithology to the other. The subsurface rock, during or after deposition may have been affected by both physical and chemical changes (Gardner et al., 1974).

Sorting and cementation

Sorting and type of cementing materials affect the porosity of a rock. With increased cementation and poor sorting, pore volume tends to decrease, resulting in reduced porosity and consequently affecting seismic velocity.

2.4.12.2 Relating Rock Porosity and Velocity

Nearly all proposed formulae for the determination of rock strength and elastic moduli from geophysical logs make use of either compressional velocity (V_p), transit time (μs/ft) or porosity (φ) (Horsrud, 2001; Kwasniewski, 1989; Lama & Vutukuri, 1978; and Carmichael, 1982).

It has been said that seismic velocities are affected by several factors such as lithology, interstitial fluid, porosity, depth, density, and so on. Lithology is an obvious factor affecting velocity (P-wave and S-wave). Pores are one of the weakest and the most deformable elements in rocks; hence porosity affects the velocity of the acoustic waves penetrating the rocks (Horsrud, 2001). Wyllie & Rose (1950) developed an equation showing the relationship between velocity and porosity.

$$\frac{1}{V} = \frac{\varphi}{V_f} + \frac{(1-\varphi)}{V_{ma}} \tag{2.44}$$

Where:

V = velocity of formation, V_f = velocity of the interstitial fluid, V_{ma} = velocity of rock matrix, and φ = Porosity. Equation 33 above is statistical and empirical. It makes no allowance for the structure of a rock matrix, the connectivity of the pore spaces, or past history, all of which might be expected to affect velocity (Sheriff & Geldart, 1995).

Porosity and grain size are discussed under petrophysical properties section.

2.4.13 Petrophysical Properties

These are the physical properties of rocks relating to the pore system and its fluid distribution and flow characteristics (Crain, 1986). Petrophysical properties of rocks include porosity (total, effective, etc), permeability, fractional flow, fluid saturation, lithology, etc. These properties are employed for lithology determination, net-pay determination, porosity determination, fluid contacts identification, water saturation determination, permeability determination, etc.

2.4.13.1 Porosity and Grain Size

Porosity is the ratio of the fraction of voids to the volume of rock in which they occur. One of the reasons for the broad range of velocity within any given rock is variation in porosity (Telford et al., 1976). Porosity is however directly related to the grain size. Rocks with high porosity will have low seismic velocity. The most important aspect in which rocks differ from homogenous solids is in having granular structure with voids between the grains. These voids are responsible for the porosity of rocks and porosity is the important factor in determining velocity (Telford et al., 1976). In summary, porosity appears to be the dominant variable in determining the velocity in sedimentary rocks and porosity in turn is determined principally by the existing differential pressure and the maximum depth of burial.

Total porosity is the ratio of the fraction of total voids to the volume of rock in which they occur while effective porosity is the ratio of the fraction of total interconnected voids to the volume of rock in which they occur.

2.4.13.2 Permeability

Permeability is a rock petrophysical property that characterizes the ability of a rock to transmit fluids. This property is dependent on the interconnectivity between the pore spaces or voids within a rock unit. The higher the permeability of a rock, the higher the ability of that rock to transmit fluids within its pores. Clay, for instance, is very porous sediment but has very low permeability as a result of the lack of connectivity between its pore spaces whereas sand and gravel, on the other hand, have very well interconnected pore spaces making them good water aquifers and hydrocarbon reservoirs. Permeability is measured in millidercy (mD).

The final form of the Darcy equation for horizontal linear flow of an incompressible fluid is established through a core sample of length L and cross sectional area A and is given as

$$Q = -\frac{KAdP}{\mu dL} \tag{2.45}$$

Where K is the permeability, μ is the viscosity of flowing fluid, Q is the volumetric flow rate in cm^3/sec and dP/dL is the pressure drop per unit length.

Glover (1997) gave a classification of the permeability of reservoir rocks. According to this classification, a permeability value of less than 10 millidarcy (mD) is classified as fair, between 10 and 100 millidarcy is classified as high, permeability values between 100 and 1000 millidarcy is classified as very high, while values greater than 1000 millidarcy are classified as exceptional.

2.4.14 Well Logging

Well logging denotes an operation wherein a continuous recording is made versus depth of the formations penetrated by a drill hole (Harald, 2012). This record is called a Log. Many types of well logs are recorded by means of appropriate downhole instrument called Sondes lowered into the borehole on the end of a cable. Some types of geophysical well logs can be

done during any phase of a well's history: drilling, completing, producing, or abandoning (Hilchie, 1990). Well logging is performed in boreholes drilled for the oil and gas, groundwater, mineral, and geothermal exploration, as well as part of environmental and geotechnical studies (Harald, 2012).

Wireline logging is employed by the oil and gas industry to generate a standard record of the properties of a rock of any given formation. Analyses of wireline logging can be used to infer such properties as hydrocarbon saturation, reservoir pressure, etc and also helps in making further decisions bordering on drilling and production. Logging tools developed over the years measure the natural gamma ray, electrical, acoustic, stimulated radioactive responses, electromagnetic, pressure, and other properties of the rocks and their contained fluids (Harald, 2012). Logs which are used to quantify the hydrocarbon in place can be classified into three groups namely reservoir thickness logs (gamma ray and spontaneous potential logs), porosity logs (density, neutron, and sonic logs), and resistivity logs (laterolog, induction, and micro-resistivity logs) (Selemo, 2008).

2.4.14.1 Spontaneous Potential (SP) Log

Spontaneous potential log is a recording versus depth of the difference between the potential of a moveable electrode in the borehole and the fixed potential of a surface electrode (Rider, 1986). It is one of the very important geophysical logs usually used in well analyses. Three factors necessary to generate SP currents are: a conductive fluid in the borehole, a porous and permeable bed surrounded by an impermeable formation, and a difference in salinity between the borehole fluid and the formation water (Selemo, 2008).

SP current originate principally through the electrochemical effects of salinity differences between the borehole fluid (mud filtrate) and the formation water (Selemo, 2008). These differences create spontaneous currents either when the fluids themselves come in contact

through a porous medium or when they come in contact through shale which acts as a semi permeable membrane (Selemo, 2008). In oil well logging, the potentials involve principally the boundaries of the shale units, especially shale-sand interfaces and the principal effect is the electrochemical potential which is normally less than 75mV (Telford, Geldart, & Sheriff, 1990).

2.4.14.2 Gamma Ray Log

The gamma ray log is basically a record of a formation's radioactivity. Gamma ray log usually reflects the shale content of sedimentary Formations since these radioactive elements are embedded in shale (Selemo, 2008). Clean sandstones and carbonates normally exhibit a low level of natural radioactivity while the clay minerals and fine particles in shale show higher levels of radioactivity due to absorption of the heavy radioactive elements (Selemo, 2008).

Natural radiation in rocks comes essentially from only three elemental sources: the radioactive elements of the thorium family, the uranium-radium family, and the radioactive isotope of potassium (Selemo, 2008). Each of these elements emits gamma rays, the number and energies of which are distinctive of each element (Selemo, 2008). When passing through matter, gamma rays experience successive Compton scattering collisions with atoms of the Formation material, losing energy with each collision (Schlumberger, 1987). After losing enough energy, the gamma ray is absorbed through photoelectric effect by the Formation's atom. Thus, natural gamma rays are gradually absorbed and their energies reduced as they pass through the Formation (Schlumberger, 1987). Hence, the rate at which the gamma ray is absorbed is dependent on the density of the Formation.

2.4.14.3 Sonic (Acoustic) Log

The sonic or acoustic log is a log that measures a formation's capacity to transmit sound waves. It shows a formation's interval transit time (the reciprocal of sonic velocity) (Selemo, 2008). Geologically, it varies with lithology and with rock texture, remarkably porosity (Rider, 1986). Two types of sound waves are propagated in an infinite medium and they are compressional or primary waves otherwise known as P-waves and shear or secondary waves otherwise known as S-waves. In a finite medium however (e.g. a borehole), guided or interface waves (e.g. Rayleigh waves, Stoneley waves) may be propagated (Selemo, 2008).

Sonic tools are comprised of transmitter transducers that convert electrical energy into mechanical energy, and receiver transducers that do the reverse (Selemo, 2008). At time 0, the transmitter emits a small shock wave that travels through the mud to the borehole wall where it is refracted through the formation (Selemo, 2008). Part of the energy travelling through the formation is in turn refracted back into the mud column and finds its way to the first receiver at time T_1 and to the second receiver at time T_2 (Selemo, 2008). The difference in the two times is denoted by Δt and represents the time it takes a compressional wave to travel through the formation a distance equal to the spacing between the two receivers (Selemo, 2008). The travel time Δt is measured in μs/m or μs/ft.

2.4.14.4 Resistivity Log

Resistivity log simply entails measurement of the resistivity of a given formation to the flow of electric current. Most rock materials are essentially insulators, while their enclosed fluids are conductors (Selemo, 2008). Hydrocarbons are not conductive but rather resistive. When a given formation is porous and contains salty water, the overall resistivity of that formation will be low because saltwater is conductive. On the other hand, if this same formation

contains hydrocarbon, its overall resistivity will be high (Rider, 1986). This is the basic principle applied in resistivity logs.

When a current is passed between two electrodes on a logging tool, the potential drop between them gives the resistivity (Selemo, 2008). The pores contained within a rock unit are principally filled with water called formation water. These pores may also be occupied by oil and natural gas (Selemo, 2008). The expression of the passive behaviour of a rock in the presence of an electric field is referred to as the formation resistivity factor. This resistivity factor is a function of both the volume of pores in a rock unit, called porosity, and the manner in which the pores are connected, called tortuosity (Selemo, 2008).

2.4.14.5 Density Log

This is a continuous record of a formation's bulk density. It gives information of the overall density of a rock including solid matrix and the fluid enclosed in the pores (Rider, 1986). It is used in rock porosity determination.

In density logging, a radioactive source applied to the borehole wall in a shielded sidewall skid, emits medium energy gamma rays into the formation (Schlumberger, 1989). These gamma rays may be thought of as high velocity particles that collide with the electrons of the formation. At each collision, a gamma ray loses some (but not all) of its energy to the electron and then continues with diminished energy (Selemo, 2008). This interaction is referred to as Compton scattering. The scattered gamma rays reaching the detector at a fixed distance from the source are counted as an indication of formation density (Telford, 1990). In other words, according to Selemo (2008), there is physical relationship between the attenuation of these gamma rays and the electron density of a formation (number of electrons per cubic centimeter). The electron density of a material is closely related to its true bulk

density which in turn depends on the density of the rock matrix material, the formation porosity, and the density of the fluids filling the pores (Selemo, 2008).

2.4.14.6 Neutron Porosity Log

Neutron logs are essentially used for the identification of porous Formation, and for the estimation of their porosities (Dresser Atlas, 1982). These logs give continuous records of a Formation's reaction to fast neutron bombardment, and they are expressed in terms of neutron porosity units which are related to a Formation's hydrogen index, a sign of its richness in hydrogen (Rider, 1986). Formations absorb neutrons rapidly when they contain abundance of hydrogen nuclei which in the geological context are supplied by water. Therefore, this log is a measure of a Formation's water content, either bound water or free pore water (Selemo, 2008). The quantity of hydrogen per unit volume or the richness in hydrogen of a Formation, indicated by the hydrogen index is converted directly to neutron porosity units (Selemo, 2008).

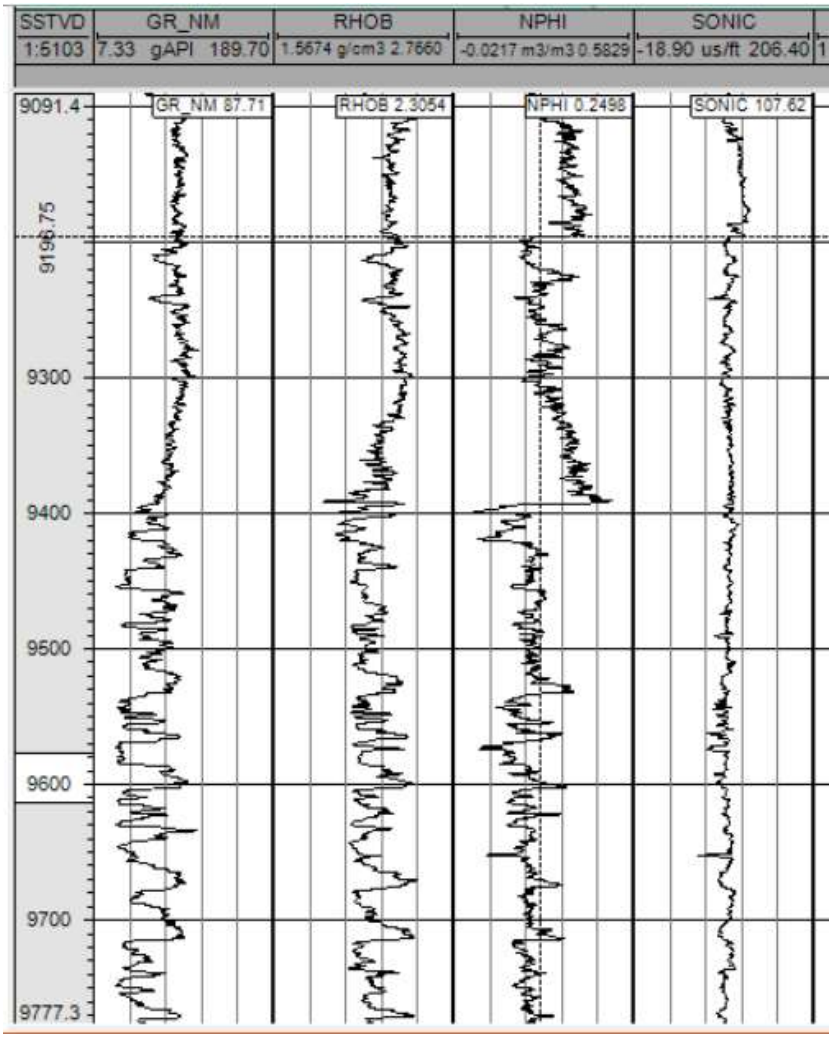


Fig. 2.19: Gamma ray, density, neutron porosity, and sonic log signatures from an oil well, offshore Niger Delta (Osaki, 2019).

2.4.15 Artificial Neural Network (ANN)

Artificial neural networks (ANNs) can be described as computer programmes which are inspired by the study of living matter and designed to replicate the manner in which the brain of humans carryout information processing (Dayhoff & DeLeo, 2001). ANNs are essentially an alternative approach to typical programmed computing and they are designed to operate like the human brain. ANNs are trained via experience and their knowledge is gathered by discovering the relationships and arrangements in data and not necessarily from computer

programming (Choudhury, Atteya, Dahal, Chetia, Choudhury, & Paradkar, 2018). In other words, the capacity to study a given data and generalize from it, that is to imitate the ability of humans to learn through experience, makes ANNs very useful in making the process of learning rules from various applications to be automated.

Apart from learning through experience, another important difference between ANNs and other computer programmes lies in the fact that the algorithms applied in ANNs data analysis are very flexible. This implies that in the process of data analysis, the algorithm can be changed (Choudhury et al., 2018). ANNs have the ability to efficiently deal with problems having more than two dimensions. From several single units, ANN is formed. The neural structure organized in layers is made up of artificial neurons connected with coefficients called weights. Neural computations are made possible by the connectivity of neurons in a network. A neuron is an excitable cell which makes communication with other cells through connections known as synapses. Well connected neurons in a network ensure a better prediction as output (Choudhury et al., 2018).

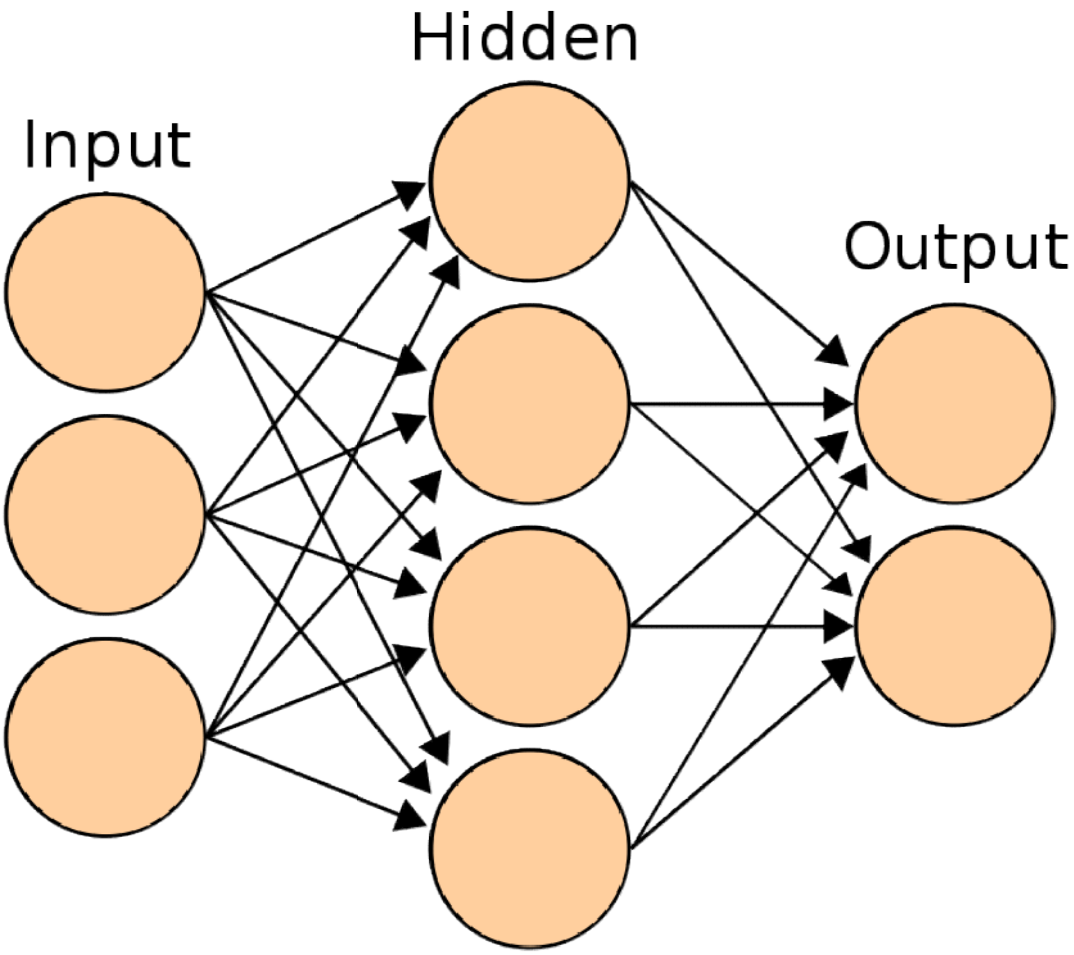


Fig. 2.20: An artificial neural network showing the input, hidden and output neurons.

The transfer functions of the neurons of a particular network goes a long way in determining, through the learning rule and the network architecture, the activity of that network. To achieve very successful results from ANNs modeling, prediction error must be minimized through inter-unit connections optimization during data training. The expected accuracy level is reached through trial and error. The neural network can be used to predict an output with new information as input if such network has been trained with much reduced prediction error (Choudhury et al., 2018).

In modeling with artificial neural network, the dataset is divided into three groups namely training dataset, validation dataset, and testing dataset. The splitting of the dataset depends on two factors; first, the overall number of samples in the data and second, the actual model to be trained. The training dataset is the sample of data used to train the model including weights and biases. It is the dataset used to fit the model. This is the dataset from which the model sees and learns. The validation dataset is used to carry out an evaluation of a given model. It is a dataset used to fine-tune the hyperparameters of a model. The test dataset on the other hand is used only when a model is trained completely. This dataset is used to give a neutral evaluation of a final model fit on the training dataset.

2.4.15.1 Weights and Biases

The weights and biases can be described as the learnable parameters of an artificial neural network model. A neural network consists of very basic units referred to as neurons. Every neuron in any layer of an artificial neural network is connected to another neuron in another layer of the network. The weights and bias are applied to the inputs when transmitting inputs between neurons. The strength of the connection between two neurons is controlled by weights; hence, the influence of the input on the resulting output is decided by the weights. The weights are used to adjust the input to a neuron when the desired information is not obtained. On the other hand, biases are constant. Biases are applied to the input along with the weights. Biases do not have incoming connections hence they are not in any way influenced by the previous layer. They however possess outgoing connections. The very essence of the bias unit is to ensure that there exists activation in any neuron even when the inputs to that neuron are zero.

CHAPTER III

MATERIALS AND METHODS

3.1 Materials

The materials used for this study are classified into two categories and they are: data and software.

The data used for this study includes 3D reflection seismic data volumes for the two fields; log suites comprising gamma ray log, sonic log, density log, and neutron porosity logs from eight different oil wells within the two fields; core data from the two fields; check-shot data for the two fields; Well reports from the study fields; and base maps for the two fields. These data were obtained from Monipulo Petroleum Limited.

The hardware and software employed in processing and analyzing the various dataset for this study includes a standard workstation, Petrel to simulation software, MS Excel software, and Matlab 2015 software.

Beta and Fuja Fields are offshore oilfields located within the eastern axis of offshore depobelt of the Niger Delta Basin. The stratigraphic sequence is also the well-known stratigraphy of the Niger Delta comprising undercompacted, over-pressured marine shales, clays, and siltstones with some turbidite sandstones called Akata Formation (Short and Stauble, 1967). This formation is the basal bed and source rock for the hydrocarbon in this delta. The Akata Formation is overlain by an alternation of paralic sandstones, shales, and clay known as the Agbada Formation. The Agbada Formation is the reservoir rock for the hydrocarbon in this delta and it is overlain by massive continental sandstones called Benin Formation (Short and Stauble, 1967).

3.2 Methods

The methodology utilized in this study is broken down into eleven important stages/steps. The first stage involved importing the datasets into Petrel and MS Excel software and saving them in text delimited format. The datasets were also quality-checked at this stage.

The second stage is stratigraphic correlations using well logs to identify the reservoirs of interest for the two fields. In other words, this was carried out in order to identify the sand and shale units of the reservoirs we are working on. Because we apply different sonic transit times, different density information, and in some cases different empirical formulas for sand and shale, we therefore need to know the units clearly. This was achieved by correlating the eight wells used for this study with the aid of Petrel software.

The third stage involved carrying out well-to-seismic tie to ensure that the well logs and the seismic data are in agreement. This is a calibration step that has to do with the generation of a synthetic seismogram from well data and comparing it to actual seismic data collected over the area. The synthetic seismogram is generated by convolving the reflectivity derived from digitized acoustic and density logs with the wavelet derived from seismic data. By comparing marker beds or other correlation points picked on well logs with major reflections on the seismic section, interpretations of the data can be improved. This ensures robustness or goodness of fit, that is, that interfaces and intervals interpreted on the seismic section match those same markers and units in the well penetration with a high level of accuracy.

Horizon and fault picking was also carried out at this stage for the purpose of generating depth structure maps. The depth structure maps were generated with the aid of Petrel software using the well logs and seismic data. These maps were generated for a better understanding of the area of interest.

The fourth stage involved reservoirs structure delineation for the two fields using seismic data and well log data. This was done by identifying surfaces of interest from the eight wells used for this study on a well correlation panel. The reservoir boundary and geometry was delineated using the seismic data. This allowed us to determine the structure or geometry of the reservoirs laterally and in terms of depth. The 3D seismic volume also aided in building the 3D geomechanical model of the reservoirs. With just well logs, we can only obtain 1D geomechanical model.

Generation of dynamic elastic and inelastic as well as petrophysical properties of the reservoirs of the two fields make up the fifth stage of the methodology. The elastic rock properties include Poisson's ratio (σ), shear or rigidity modulus (μ), bulk modulus (K), bulk compressibility (C_b), and Young's modulus (E). The inelastic rock property determined in this study is the unconfined or uniaxial compressive strength (UCS) of the reservoirs. Pore pressure (P_p) in sand and shale units of the reservoirs, total vertical stress (S_v), maximum horizontal stress (Sh_{max}), and minimum horizontal stress (Sh_{min}) within the reservoirs of the two fields were also calculated using bulk density and appropriate empirical equations.

3.2.1 Determination of Dynamic Elastic Properties

These dynamic elastic rock properties were derived with appropriate empirical equations, using sonic log, compressional and shear travel times along with density log data.

3.2.1.1 Determination of Poisson's Ratio (σ)

In the determination of dynamic Poisson's ratio (σ), compressional (V_p) and shear (V_s) wave velocities were determined from sonic log. Thereafter, dynamic Poisson's ratio was calculated using equation 2.17.

With the results obtained, a Poisson's ratio log with depth of each of the wells was then generated using Petrel software. Note that compressional wave velocity (V_p) was obtained from sonic data using the equation $V_p = \frac{304878}{sonic/1000}$ in km/s. The shear wave velocity (V_s) was computed from the compressional wave velocity (V_p) using the Greenberg & Castagna (1992) velocities for sand and shale beds given by: $V_s = 0.80416V_p - 0.85588$ (for sand beds) and $V_s = 0.76969V_p - 0.86735$ (for shale beds).

3.2.1.2 Determination of Shear or Rigidity Modulus (μ)

In the determination of dynamic shear or rigidity modulus (μ), the formation bulk density (ρ_b) was determined from density log while the shear sonic transit time (ΔT_s) in $\mu s/Ft$ was determined from sonic log. The dynamic shear or rigidity modulus was then calculated in Gigapascal (GPa) using the empirical relation of equation 2.20. As in Poisson's ratio, with the results obtained, a shear or rigidity modulus log with depth of each of the wells was then generated using Petrel software.

3.2.1.3 Determination of Bulk Modulus (K)

In the determination of the dynamic bulk modulus (K), the formation bulk density (ρ_b) was determined from density log while the compressional and shear sonic transit times (T_c and T_s) in $\mu s/Ft$ were computed from sonic log. The dynamic bulk modulus was then calculated in Gigapascal (GPa) using the empirical formular in equation 2.8.

With the results obtained from the equation of bulk modulus, a bulk modulus log with depth of each of the wells was then generated.

3.2.1.4 Determination of Bulk Compressibility (C_b)

This is the inverse of the dynamic bulk modulus (K) or modulus of incompressibility and it was calculated from equation 2.9.

Similarly, with the obtained results, a bulk compressibility log with depth of each of the wells was then generated.

3.2.1.5 Determination of Young's Modulus (E)

The dynamic Young's modulus or modulus of elasticity (E) was calculated from an equation involving a relationship between Young's modulus (E), Shear modulus (μ), and Poisson's ratio (σ) as stated in equation 2.14.

The obtained dynamic Young's modulus results was then used to generate a Young's modulus log with depth of each of the eight wells in the two fields with the aid of Petrel software.

3.2.2 Determination of Dynamic Inelastic Property

The dynamic inelastic rock property (the unconfined compressive strength) was also determined with appropriate empirical equations, using sonic log information.

3.2.2.1 Unconfined or Uniaxial Compressive Strength

From sonic log, compressional sonic transit time (T_C) was determined. This transit time was then used to calculate the unconfined compressive strength using the empirical equations suitable for the Niger Delta which is our study terrain.

For the sandstone units, the unconfined compressive strength (UCS) was calculated using the equation by McNally (1987) given as:

$$UCS = 1200\exp^{(-0.036\Delta_c)} \quad (3.1)$$

The above equation is suitable for calculating UCS for fine grained consolidated and unconsolidated sandstone units with all porosity ranges (Abijah & Tse, 2016).

For the shale units, the unconfined compressive strength was calculated using the below equation by Lal (1999) which is suitable for calculating UCS for high porosity Tertiary shales like those of the Niger Delta:

$$UCS = 10\left(\frac{304.8}{\Delta T_c^{-1}}\right) \quad (3.2)$$

Where ΔT_c is the change in compressional sonic transit time in $\mu s/Ft$. Note that Compressional sonic transit time (T_c) was obtained from the reciprocal of compressional wave velocity (V_p) given as: $T_c = \frac{1}{V_p}$, while shear sonic transit time (T_s) was obtained from the reciprocal of shear wave velocity (V_s) given as: $T_s = \frac{1}{V_s}$.

3.2.3 Determination of Petrophysical Properties

The reservoir petrophysical properties determined in this study are the total porosity, the effective porosity, the permeability and the volume of shale or shaliness.

3.2.3.1 Determination of Total Porosity

This was determined using the equation according to Schlumberger (1989). It is the total porosity of the average density of the pore fluid and the densities of the rock. The equation is given by $\emptyset_D = \frac{(\rho_{ma} - \rho_b)}{(\rho_{ma} \quad \rho_{fl})}$ (3.3)

Where $\emptyset_D$= total density porosity, ρ_{ma}= density of rock matrix (2.65g/cm^3), ρ_b = bulk density derived from density log, and ρ_{fl} = density of fluid occupying pore spaces (1.1g/cm^3 for water, 0.9g/cm^3 for oil, and 0.74g/cm^3 for gas).

3.2.3.2 Determination of Effective Porosity

The effective porosity was calculated by applying the volume of shale equation by Asquith & Gibson, (1982) as stated below:

$$\emptyset_{eff} = \frac{(\rho_{ma} - \rho_b)}{(\rho_{ma} \quad \rho_{fl})} - \frac{V_{sh}(\rho_{ma} - \rho_{sh})}{(\rho_{ma} \quad \rho_{fl})} \quad (3.4)$$

Where $\emptyset_{eff}$= shale-corrected density porosity, V_{sh}= volume of shale, ρ_{sh} = density of shale (2.30g/cm^3), ρ_{ma}= density of rock matrix (2.65g/cm^3), and ρ_{fl} = density of fluid occupying pore spaces.

3.2.3.3 Determination of Volume of Shale

The shaliness or volume of shale was calculated using the equation according to Larionov (1969), given as:

$$V_{sh} = 0.083(2^{3.7I_{gr}} - 1) \quad (3.5)$$

Where I_{gr} is the gamma ray or shale index given as:

$$I_{gr} = \frac{GR_{log} - GR_{min}}{GR_{max} - GR_{min}} \quad (3.6)$$

GR_{log}= gamma ray reading from log, GR_{min}= minimum gamma ray reading (sand baseline), GR_{max}= maximum gamma ray reading, and V_{sh}= volume of shale.

3.2.3.4 Determination of Permeability

Permeability was calculated using the porosity equation from Adiela, Ayodele, & Okafor, (2017) given as:

$$K = \frac{0.136\emptyset^{4.4}}{(S_{wirr})^2} \quad (3.7)$$

Where Ø is the effective porosity and S_{wirr} is the irreducible water saturation.

S_{wirr} is determined using the equation also by Adiela et al. (2017) given by

$$S_{wirr} = \left(\frac{F}{2000}\right)^{1/2} \quad (3.8)$$

where F is the formation factor obtained from $F = \frac{a}{\emptyset^m}$, where a is the tortuosity factor given as 0.62, Ø is the effective porosity, and m is the cementation factor given as 2.15.

3.2.4 Determination of Reservoir Pore Pressure, Total Vertical Stress, Maximum and Minimum Horizontal Stresses

Pore pressure is the pressure exerted by a fluid column or pore water from sea level or surface of the Earth down to the depth of the formation. Pore pressure was estimated using the equation by Jones et al. (1992) and Omar (2015) given by

$$P_p = \int_0^h \rho_f g h \, dh \tag{3.9}$$

$$P_p = 1 \text{ x } 1000 \text{ x g x h x } 0.3048 \text{ x } 0.0001450378 \text{ psi} \tag{3.10}$$

Where P_p is the pore pressure, ρ_f is formation fluid density, g is acceleration due to gravity, and h is the depth in feet.

Total vertical stress (S_v) is the stress acting on the reservoir rock as a result of the load of the overlying strata (Jones et al., 1992). Total vertical stress was calculated using the equation by Jones et al. (1992) and Omar (2015) given as:

$$S_v = \rho_b \text{ x } 1000 \text{ x g x h x } 0.3048 \text{ x } 0.000145037738 \text{ psi.} \tag{3.11}$$

From Terzaghi pressure relationship, effective pressure is obtained from the difference between total vertical stress or overburden pressure and pore pressure at every depth.

The maximum horizontal stress (Sh_{max}) is one of the principal stresses, in addition to total vertical stress and the minimum horizontal stress, acting on a formation at depth. Numerous empirical relations exist that can be used to calculate the maximum and minimum horizontal stresses. In this study, the poroelastic model expressed by Ostadhassan, Zong, & Zamrian, (2012); and Holbrook & Maggiori (1993) was used. It is given by

$$Sh_{max} = \frac{\boldsymbol{\sigma}}{(1-\boldsymbol{\sigma})}(S_v - \alpha P_p) + \alpha P_p + \frac{E_{sta}}{(1-\sigma^2)} \mathcal{E}_y + \sigma \mathcal{E}_x \text{ in megapascals} \tag{3.12}$$

Where σ is the Poisson's ratio, S_v is the total vertical stress, α is the Biot constant, P_p is the pore pressure, E_{sta} is the static Young's modulus, $\mathcal{E}_y$ and $\mathcal{E}_x$ are strain at maximum and minimum horizontal stress directions.

The strain in the maximum and minimum horizontal directions was determined using the following relations by Kidambi & Kumar (2016).

$$\mathcal{E}_y = \frac{S_v\sigma}{E_{sta}}\left(\frac{1}{1-\sigma} - 1\right) \quad (3.13)$$

$$\mathcal{E}_x = \frac{S_v\sigma}{E_{sta}}\left(1 - \frac{\sigma^2}{1-\sigma}\right) \quad (3.14)$$

Static Young's modulus (E_{sta}) was obtained from the relationship by Seyed & Aghighi (2015) expressed as

$$E_{sta} = 0.731 \text{ x } E_{dyn} - 2.337 \quad (3.15)$$

where 0.731 and 2.337 are Seyed and Aghighi constants determined from laboratory experiment on core.

Minimum horizontal stress (Sh_{min}) was calculated using the equation by Ahmed *et al* (1991) expressed as

$$Sh_{min} = \frac{\boldsymbol{\sigma}}{(1-\boldsymbol{\sigma})}(S_v - \alpha P_p) + \alpha P_p \text{ in megapascals} \quad (3.16)$$

Where the parameters are as defined above. The Biot constant (α) is estimated from Schlumberger (1985) equation expressed as

$$\alpha = 1 - \frac{K_b}{K_r} \quad (3.17)$$

where K_b is the material bulk modulus and K_r is the bulk of the rock constituents.

Validation and upscaling of reservoir properties with core data for the fields to ensure that the lithologies interpreted by the well logs are accurate and at the correct depths constitute the

sixth stage of the research methodology. At this stage, the core data was used to validate the well log and seismic reflection information.

Estimation of the relationship between rock elastic properties, inelastic property, petrophysical properties and effective pressure using cross plots constitute stage seven of the research methodology. At this stage, a graphical evaluation of the relationship between the unconfined compressive strength, elastic properties, petrophysical properties and effective pressure of the reservoirs of the study fields using cross plots was carried out. This assisted in validating or otherwise the assertion by Wong & David (1997) and Horsrud (2001) that there is a definite link between rock elastic parameters, depth, and unconfined compressive strength.

3D geomechanical modeling and horizontal extrapolation of derived properties with reservoir geometry in simulation was carried out in stage eight of this study. This is the spatiotemporal distribution of the geomechanical properties of the reservoir rock. This stage involved modeling in three dimensions, with the aid of Petrel software, the geomechanical properties of the reservoirs of the study fields by integrating 3D seismic volume, core data, well log data, and all the calculated parameters. The 3D models of the elastic and inelastic parameters were constructed using stochastic methods to reduce ambiguities associated with estimates for which data is limited to well locations alone. Variogram modelling and calculations were carried out to checkmate the distribution of the parameters outside wells. Sequential Gaussian simulation with collocated co-kriging algorithm was used in the transformation of pillar grids of the parameters.

Stage nine of the research methods of this study involved the comparative analysis of the geomechanical characteristics of the reservoirs of the two fields. Here, we carried out a

detailed comparison of the geomechanical properties calculated for the reservoirs of the two different fields.

Modeling with Empirical linear and non-linear equations of four different cross plots which includes UCS versus bulk density, UCS versus sonic, shear wave velocity versus sonic, and permeability versus bulk density make up stage ten of the research methodology.

3.2.5 Modeling with Empirical Linear and Non-Linear Equations

MATLAB 2015 was used to obtain models for the four cross plots stated above using linear, quadratic, power, logarithmic and exponential regression techniques. The performance prediction of the linear and non-linear models utilized in this study was then carried out and analyzed. To achieve this, the UCS, bulk density, sonic transit time, shear wave velocity, and permeability data from the two fields were imported from Excel spreadsheet to MATLAB-file. The UCS from ‘‘Beta’’ well and the UCS from ‘‘Fuja’’ well was then merged. This was also done for the other four parameters. Curve fitting tool was used to carry out the cross plotting between the parameters and generate the empirical linear and non-linear equations. The prediction performance of each regression technique was obtained and comparative analysis performed with statistical parameters. The schematics for each technique (Cook & Weisberg, 1982) are outlined in the equations shown below:

For linear model: $y = a_o + a_1 x$ (3.18)

For quadratic model: $y = a_o + a_1 x + a_2 x^2$ (3.19)

For power model: $y = a_o x^{a_1}$ (3.20)

For logarithmic model: $y = a_o \log (a_1 x)$ (3.21)

For exponential model: $y = a_o e^{a_1 x}$ (3.22)

Where y is the dependent variable, x is the independent variable and a_o, a_1, and a_2 are the regression coefficients.

The statistical parameters used in determining the prediction performance of the models from comparative analysis (Devore, 2012) are outlined below;

Sum of squares error (SSE): $SSE = \sum(y_p - y)^2$ (3.23)

Sum of squares regression (SSR): $SSR = \sum(y_p - y_m)^2$ (3.24)

Sum of squares total (SST): $SST = SSE + SSR$ (3.25)

R-squared statistics (coefficient of determination): $R^2 = \frac{SSE}{SST}$ (3.26)

Where y_p is the predicted dependent variable, y is the actual or measured dependent variable and y_m is the mean of the measured dependent variable data.

Finally, stage eleven involves modeling and optimization with Artificial Neural Network model of the same four cross plots modelled with empirical equations which includes UCS versus bulk density, UCS versus sonic, shear wave velocity versus sonic, and permeability versus bulk density.

3.2.6 Modeling with Artificial Neural Network (ANN)

Adaptive-Neuro Fuzzy Inference System (ANFIS) artificial intelligence model in MATLAB 2015 software was used in carrying out the modeling and optimization of the data. ANFIS is a familiar cross-breed intelligent system that puts together ANN and fuzzy logic to generate a dependable predicting system. The method is well able to construct a network having input and output and made up of many nodes through which data processing through if-then algorithms are possible. Such algorithms are applied mainly to determine the faults of models that are not precise by carrying out a careful review of the data patterns observed from the

preceding patterns. ANFIS uses the neural training method to modify the membership function and other parameters (Maiti & Tiwari, 2014).

To achieve this, data normalization of the dependent and independent variables was done using the model in equation 3.27 by Codd (1970). Data normalization is a method of structuring a data, mainly a relational data, in accordance with a series of normal forms in order to minimize data redundancy and increase data integrity. The normalized data were then imported into the ANFIS model. The architectural structure of the ANFIS model used in this study is shown in figure 3.1.

$$X_{norm} = \frac{X}{X_{max}} \tag{3.27}$$

Where X represents dependent or independent variable data.

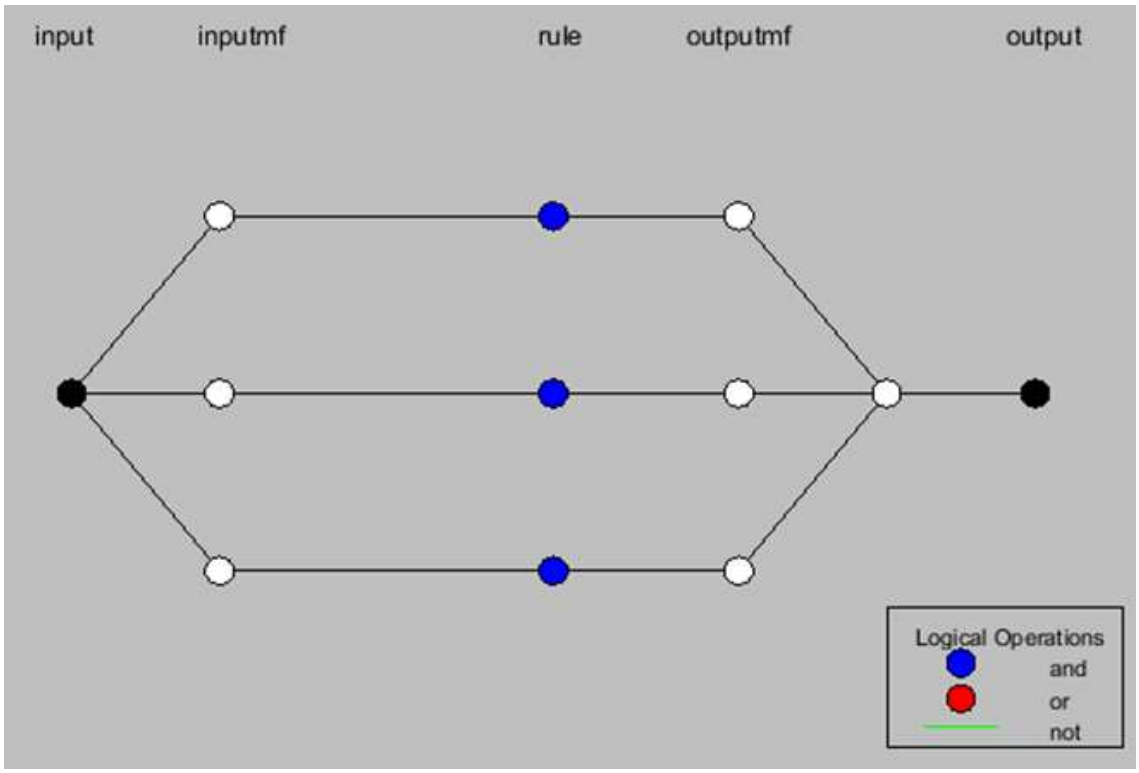


Fig. 3.1: ANFIS structure

In modeling with artificial neural network, the input layer of the network is composed of 1 neuron corresponding to either bulk density or sonic transit time, depending on the parameter relationship being modelled. The output layer is composed also of 1 neuron corresponding to unconfined compressive strength (UCS), permeability or shear wave velocity depending on the parameter relationship being modelled. The hidden or intermediate layer is composed of 10 neurons determined by means of trial and error. The Levenberg-Marquardt algorithm was used to train the network.

The statistical parameters used in determining the prediction performance of ANFIS prediction and optimization are the same parameters utilized for the empirical models.

Below is a breakdown of the general research methods:

(i) Seismic and well log data importation into Petrel and MS Excel Software.

(ii) Lithological correlations using well logs.

(iii) Well-to-Seismic tie, horizon and fault picking.

(iv) Reservoirs structure delineation using 3D seismic data.

(v) Calculation of elastic, petrophysical, and inelastic properties of the reservoirs of the fields. Estimation of reservoir effective and pore pressures, total vertical stress, maximum and minimum horizontal stresses within the reservoirs of the two fields.

(vi) Validation and upscaling of reservoir properties with core data for the fields.

(vii) Investigation of the interrelationship between rock elastic, inelastic and petrophysical properties using cross plots.

(viii) 3D geomechanical modeling and horizontal extrapolation of derived properties with reservoir geometry in simulation.

(ix) Comparative assessment of the geomechanical characteristics of the reservoirs of the two fields.

(x) Modeling with empirical linear and non-linear equations of four different cross plots and carrying out performance prediction of the obtained models.

(xi) Modeling and optimization with Artificial Intelligence.

The project workflow showing the key steps taken to achieve desired results is shown in figure 3.2.

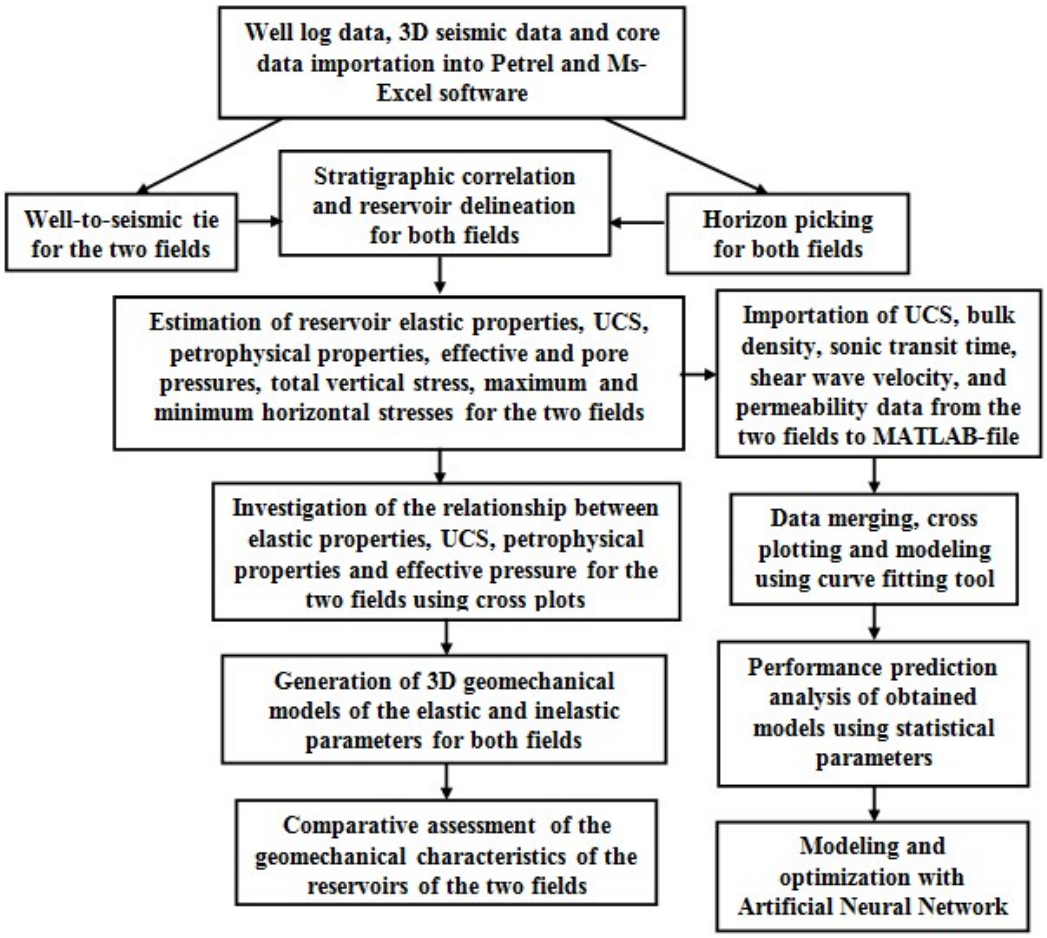


Fig. 3.2: Project workflow

CHAPTER IV

RESULTS AND DISCUSSION

4.1 Results and Interpretation

The results obtained from the study of the geomechanical properties of the reservoirs of the fields under investigation are presented in this chapter. It includes results on reservoir delineation for the two fields; rock elastic, inelastic, petrophysical properties and reservoir effective pressure; interrelationship between rock elastic, inelastic, petrophysical properties and effective pressure using cross plots; 3D geomechanical modeling of the reservoirs, and comparative analysis of the geomechanical characteristics of the reservoirs of the two fields. Also presented are results of modeling with empirical linear and non-linear models and artificial neural network model of UCS versus bulk density, UCS versus sonic transit time, permeability versus bulk density and shear wave velocity versus sonic transit time.

4.1.1 Reservoir Delineation

Reservoir delineation was done using gamma ray and sonic logs by initially identifying surfaces of interest in Beta 1, Beta 2, Beta 3 and Beta 4 wells (for Beta Field) and Fuja 1, Fuja 2, Fuja 3 and Fuja 4 wells (for Fuja Field) on a well correlation panel. For Beta Field, this fell between 8,860ft and 10,220ft in the central part of the field while for Fuja Field, it fell between 9,100ft and 9,860ft also around the central part of the field.

Figure 4.1 shows the delineation and correlation of reservoir horizons for Beta 1, Beta 2, Beta 3, and Beta 4 wells using gamma ray and sonic logs while figure 4.2 shows the delineation and correlation of reservoir horizons for Fuja 1, Fuja 2, Fuja 3, and Fuja 4 wells using gamma ray and primary wave velocity (V_P) logs.

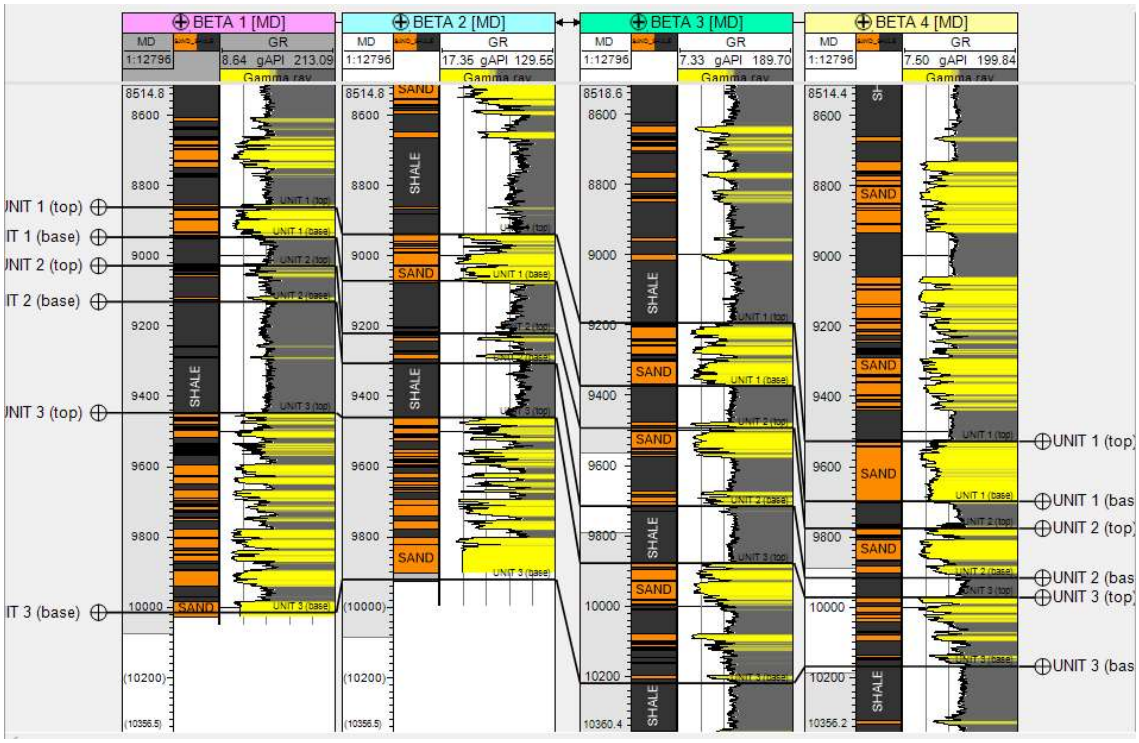


Fig. 4.1: Delineation and correlation of reservoirs for Beta 1, Beta 2, Beta 3, and Beta 4 wells using gamma ray log.

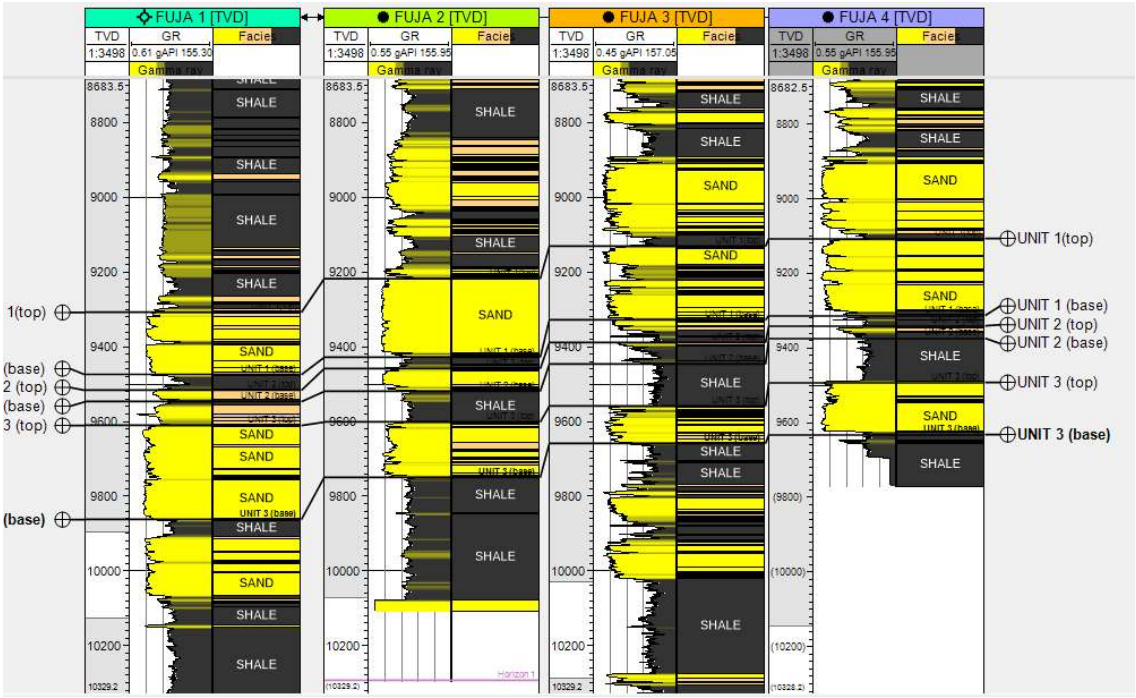


Fig. 4.2: Delineation and correlation of reservoirs for Fuja 1, Fuja 2, Fuja 3, and Fuja 4 wells using gamma ray log.

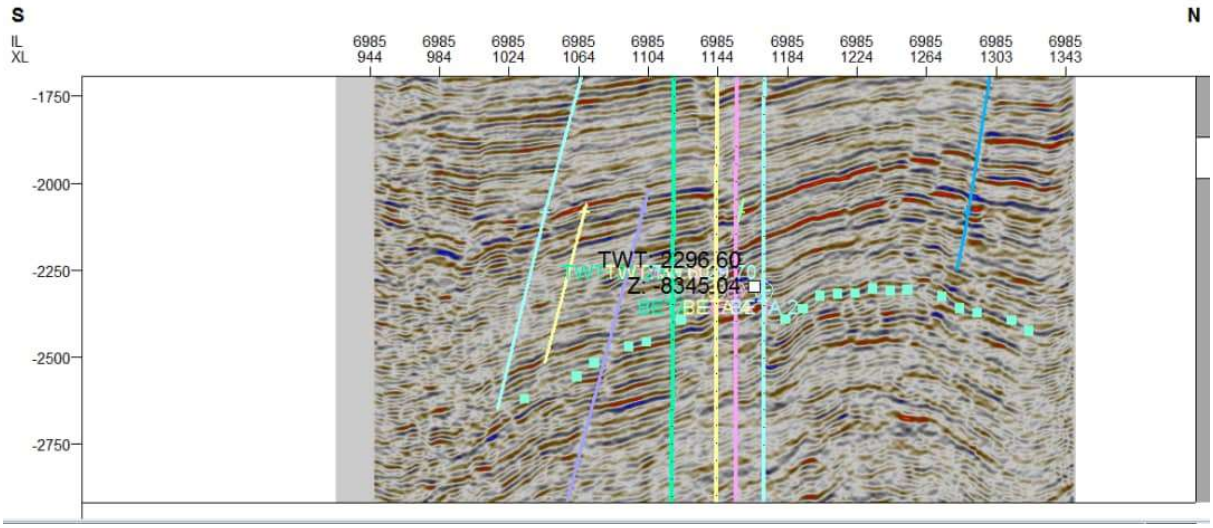


Fig. 4.3: Inline 6985 of the seismic data showing penetrated wells and fault patterns within Beta Field reservoir.

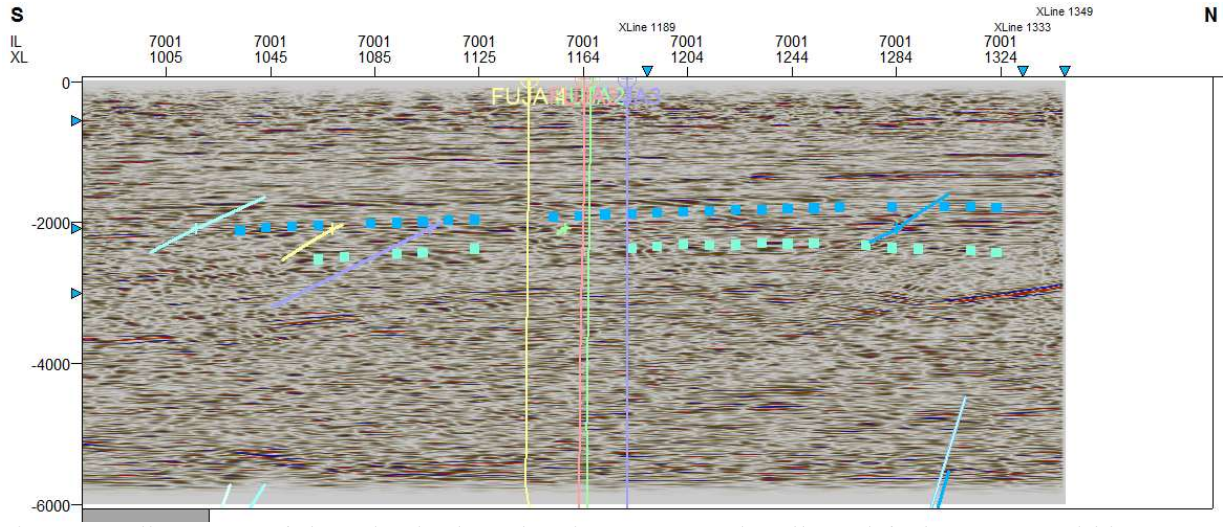


Fig. 4.4: Inline 7001 of the seismic data showing penetrated wells and fault patterns within Fuja Field reservoir.

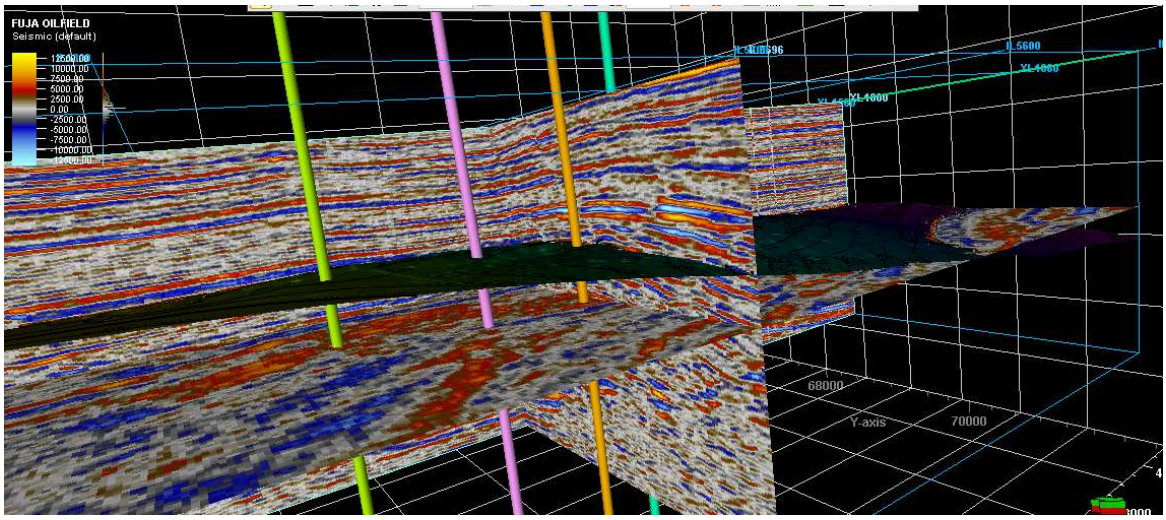


Fig. 4.5: Crossline and inline of seismic data from Fuja Field showing penetrated wells and reservoir top.

4.1.1.1 Beta Field

From results of reservoir delineation using well log data, the reservoir range in interval from a depth of 8,860ft to a depth of 10,220ft. The lithological and stratigraphic investigation of the reservoir reveals that the geological units are mainly sand and shale, with an increasing tendency towards high sand/shale ratio across the four wells as can be seen in figure 25. The reservoir lithology show a paralic sequence of sandstone intercalated with shale and the depth describes a formation with shale and sandstone units deposited in almost equal proportion with the sandstone unconsolidated. According to Doust & Omatsola (1990), this validates the formation of interest to be Agbada Formation of the Niger Delta.

4.1.1.2 Fuja Field

In a similar manner, results of reservoir mapping/delineation in the Fuja Field using well log data revealed that the reservoir range in interval from a depth of 9,100ft to a depth of 9,860ft almost around the central portion of the field. The geological units are mainly sand and shale with Fuja 1 well showing an increasing tendency towards high sand/shale ratio, Fuja 2 having sand and shale deposited almost in equal proportion, while Fuja 3 and 4 wells show an

increasing tendency towards high sand/shale ratio as can be seen in figure 26 above. This is according to the lithological and stratigraphic investigation of the reservoir. There is also a paralic sequence of sandstone intercalated with shale lithology-wise within this reservoir. This also validates the formation of interest to be Agbada Formation of the Niger Delta according to Doust & Omatsola, (1990).

4.1.2 Rock Elastic, Inelastic and Petrophysical Properties, Pore and Effective Pressures, Total Vertical Stress, Maximum and Minimum Horizontal Stresses

The elastic, inelastic and petrophysical properties of the rocks of the reservoirs of the two fields were calculated using the empirical relationships as presented in the materials and method section.

4.1.2.1 Beta Field

From the results obtained from Beta Field reservoir, Young's modulus has an average value of 10.94GPa for sand and 13.70GPa for shale, bulk modulus has 12.76GPa for sand and 13.30GPa for shale, shear modulus gave 4.11GPa for sand and 5.12GPa for shale, Poisson's ratio has 0.30 for sand and 0.33 for shale, bulk compressibility has $0.10GPa^{-1}$ for sand and $0.07GPa^{-1}$ for shale, unconfined compressive strength (UCS) has 25.19GPa for sand and 32.32GPa for shale, total porosity has 0.25 for sand and 0.09 for shale, effective porosity has 0.19 for sand and 0.07 for shale, permeability has 192.00mD for sand and 0.022 mD for shale and finally effective pressure has 14,964psi for sand and 12,730psi for shale.

Table 4.1 shows the average values of the Poisson's ratio, Young's modulus, shear modulus, bulk modulus, bulk compressibility, UCS, total porosity, effective porosity, permeability and effective pressure for sand and shale units within Beta Field reservoir, while Table 4.2 shows

estimated values of pore pressure, total vertical stress, maximum and minimum horizontal stresses within Beta reservoirs.

Table 4.1: Average values of the elastic, inelastic and petrophysical properties, effective and pore pressures for sand and shale within Beta reservoirs.

S/N	**PROPERTY**	**AVERAGE FOR SAND**	**AVERAGE FOR SHALE**
1.0	Young's Modulus	10.94±1.52 GPa	13.70±1.90 GPa
2.0	Bulk Modulus	12.76±2.12 GPa	13.30±2.01 GPa
3.0	Shear Modulus	4.11±1.03 GPa	5.12±1.27 GPa
4.0	Poisson's Ratio	0.30±0.02	0.33±0.03
5.0	Bulk Compressibility	0.10±0.03 GPa^{-1}	0.07±0.014 GPa^{-1}
6.0	UCS	25.19±14.15 GPa	32.32±17.52 GPa
7.0	Total Porosity	0.25±0.07	0.09±0.02
8.0	Effective Porosity	0.19±0.09	0.07±0.01
9.0	Permeability	192.00±53.9 mD	0.022±0.016 mD
10.0	Pore Pressure	13,683±390.3 psi	15,662±279.5 psi
11.0	Effective Pressure	14,964±746.9 psi	12,730±611.8 psi

Table 4.2: Estimated values of pore pressure, total vertical stress, maximum and minimum horizontal stresses within Beta reservoirs.

PARAMETER	**MINIMUM (psi)**	**MAXIMUM (psi)**	**AVERAGE (psi)**
Pore pressure (P_p) (Sand)	13,228.9	14,184.6	13,683±390.3
Pore pressure (P_p) (Shale)	15,111.6	16,015.0	15,662±279.5
Total vertical stress (S_v)	27,755.9	29,431.6	28,392±629.0
Maximum horizontal stress (Sh_{max})	24,671.9	26,161.4	25,537±440.6
Minimum horizontal stress (Sh_{min})	20,045.9	21,256.2	20,781±330.5

The geophysical logs of the four Beta wells showing elastic, inelastic and petrophysical properties as well as effective pressure of the reservoir rock depicted by gamma ray, shear modulus, bulk modulus, Young's modulus, unconfined compressive strength, bulk compressibility, effective porosity, total porosity, sonic velocity, Poisson's ratio, density, effective pressure, compressional wave velocity, shear wave velocity, permeability, and volume of shale are presented in figure 4.6(a-h).

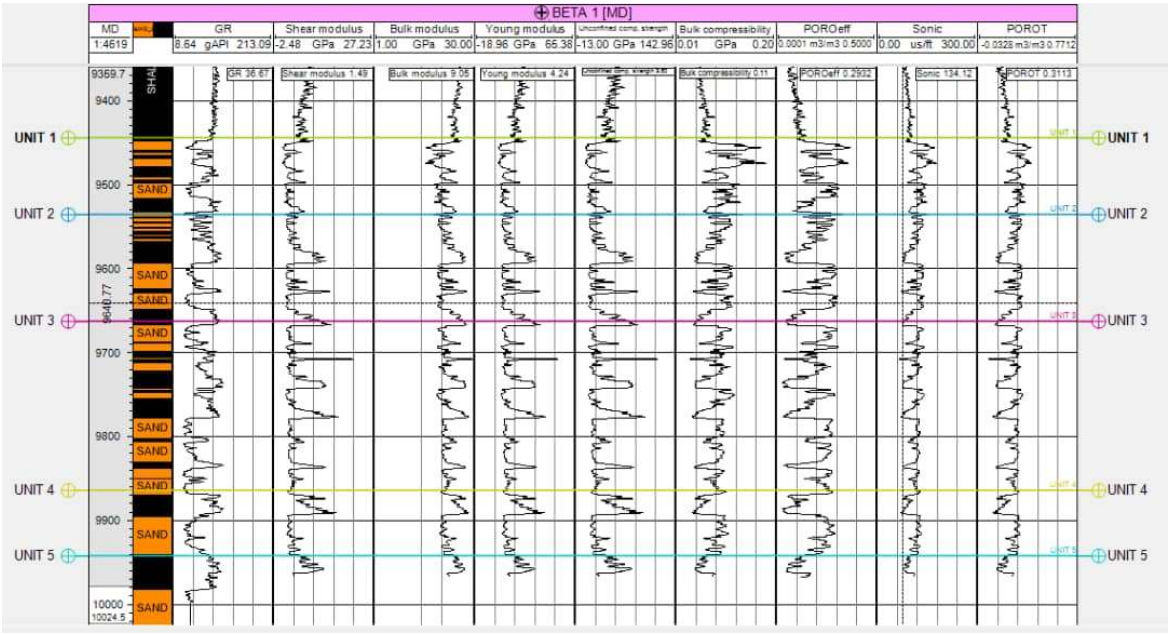


Fig. 4.6a: Logs of Beta 1 well showing elastic, inelastic and petrophysical properties of the reservoir rock depicted by gamma ray, shear modulus, bulk modulus, Young's modulus, unconfined compressive strength, bulk compressibility, effective porosity, sonic, and total porosity.



Fig. 4.6b: Logs of Beta 1 well showing elastic, inelastic and petrophysical properties of the reservoir rock depicted by gamma ray, Poisson's ratio, density, total porosity,V_p, V_s, permeability, volume of shale, and unconfined compressive strength.

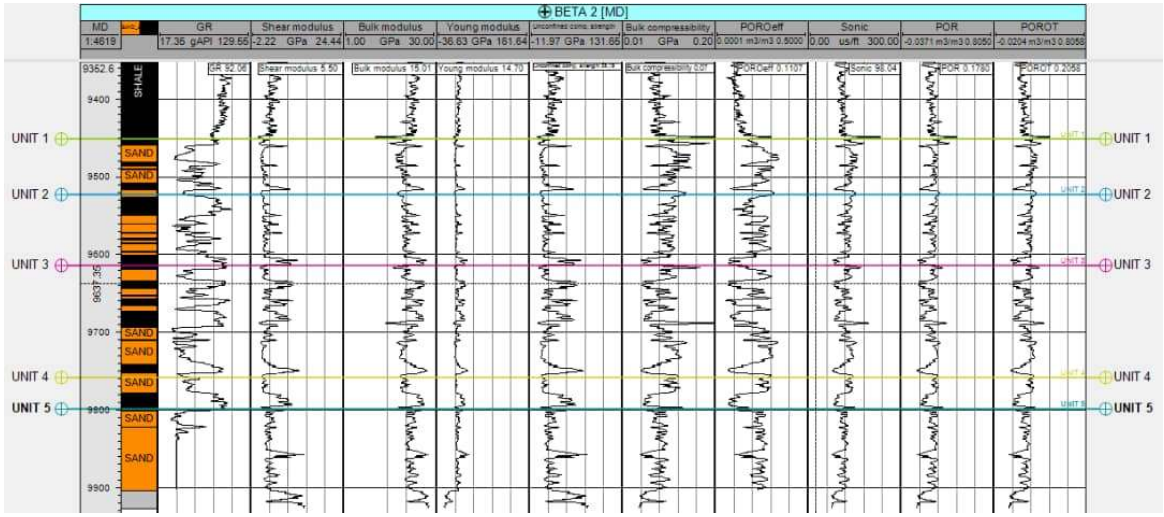


Fig. 4.6c: Logs of Beta 2 well showing elastic, inelastic and petrophysical properties of the reservoir rock depicted by gamma ray, shear modulus, bulk modulus, Young's modulus, unconfined compressive strength, bulk compressibility, effective porosity, sonic, and total porosity.

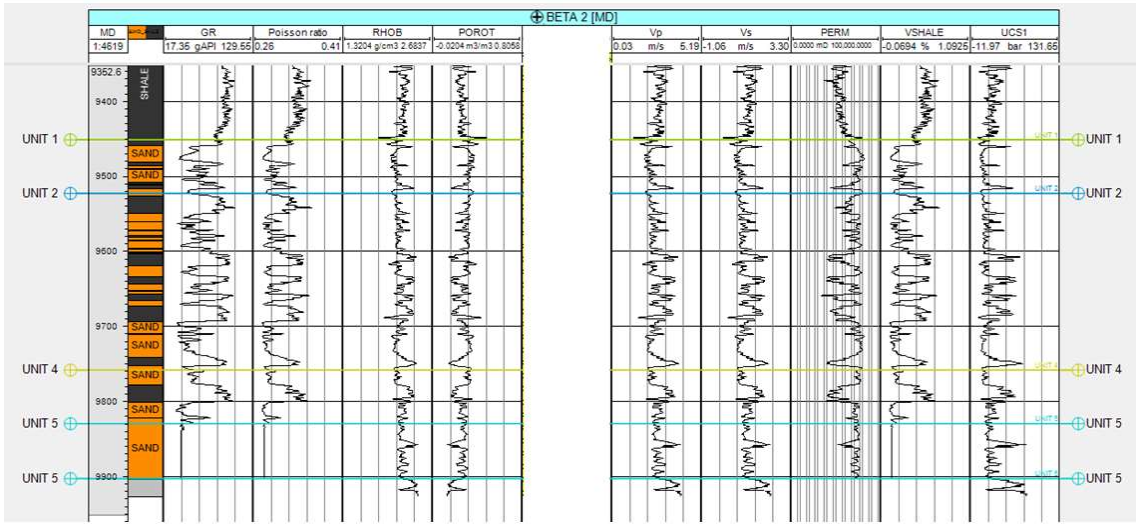


Fig. 4.6d: Logs of Beta 2 well showing elastic, inelastic and petrophysical properties of the reservoir rock depicted by gamma ray, Poisson's ratio, density, total porosity, V_p, V_s, permeability, volume of shale, and unconfined compressive strength.

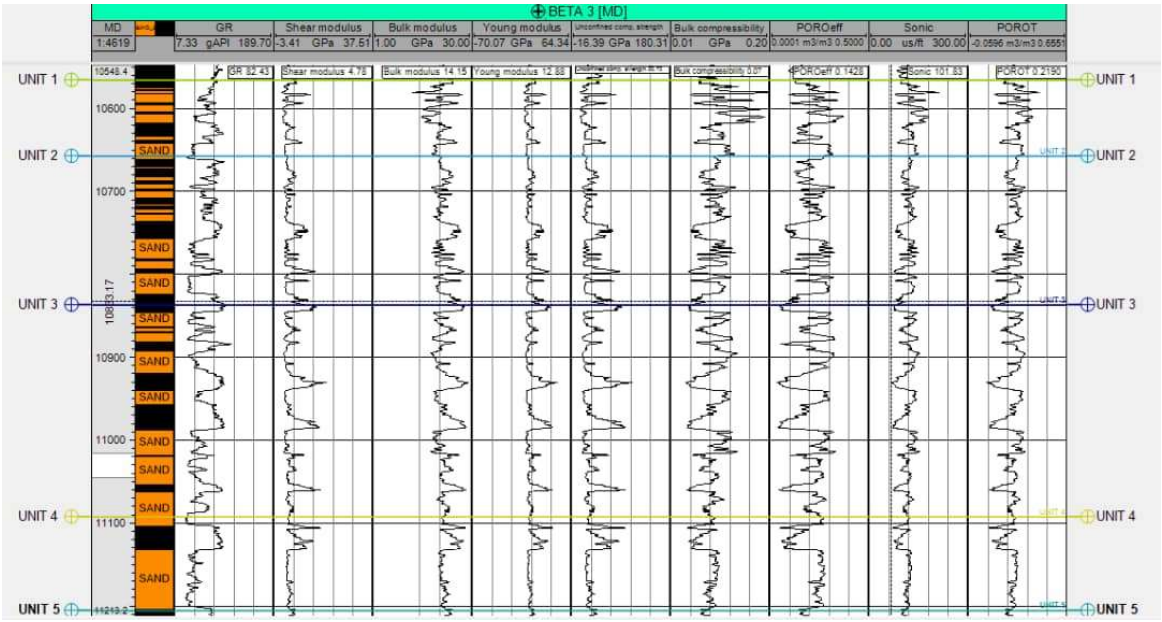


Fig. 4.6e: Logs of Beta 3 well showing elastic, inelastic and petrophysical properties of the reservoir rock depicted by gamma ray, shear modulus, bulk modulus, Young's modulus, unconfined compressive strength, bulk compressibility, effective porosity, sonic, and total porosity.

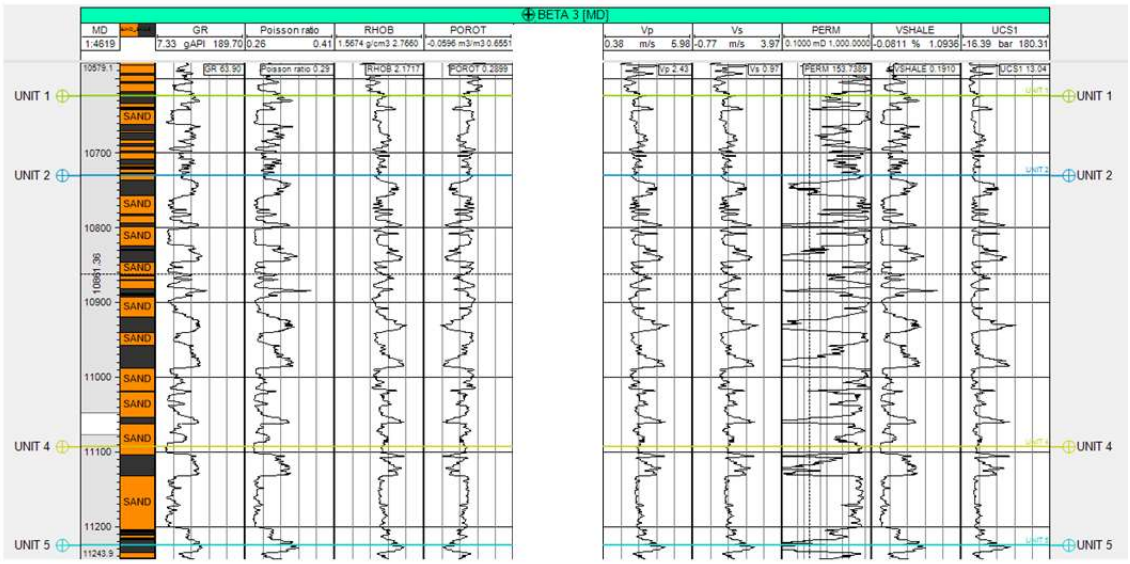


Fig. 4.6f: Logs of Beta 3 well showing elastic, inelastic and petrophysical properties of the reservoir rock depicted by gamma ray, Poisson's ratio, density, total porosity, V_p, V_s, permeability, volume of shale, and unconfined compressive strength.

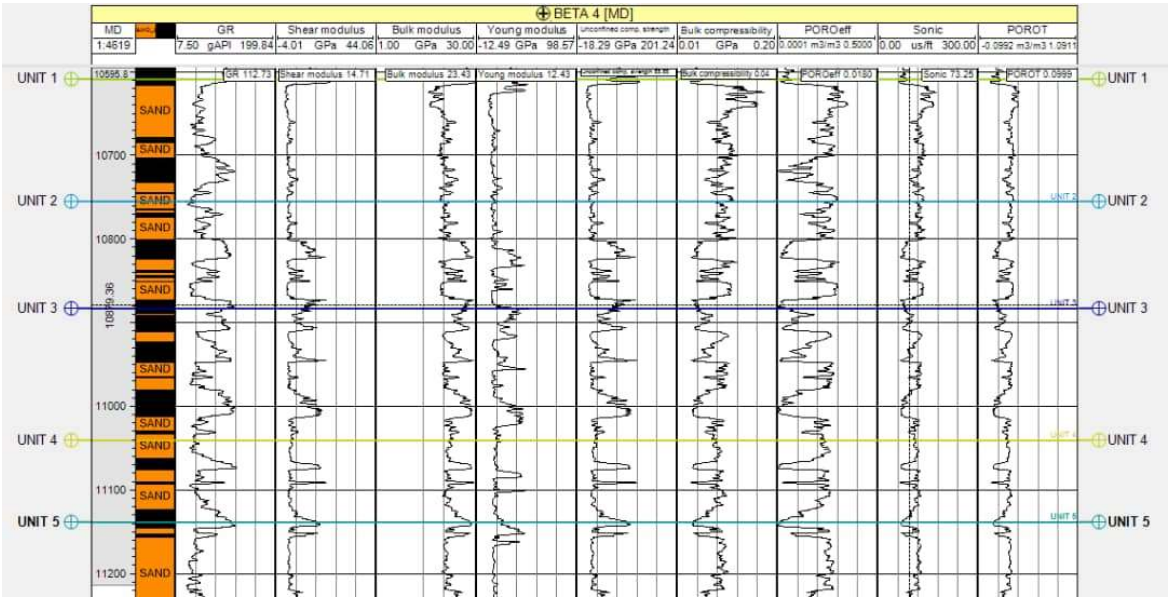


Fig. 4.6g: Logs of Beta 4 well showing elastic, inelastic and petrophysical properties of the reservoir rock depicted by gamma ray, shear modulus, bulk modulus, Young's modulus, unconfined compressive strength, bulk compressibility, effective porosity, sonic, and total porosity.

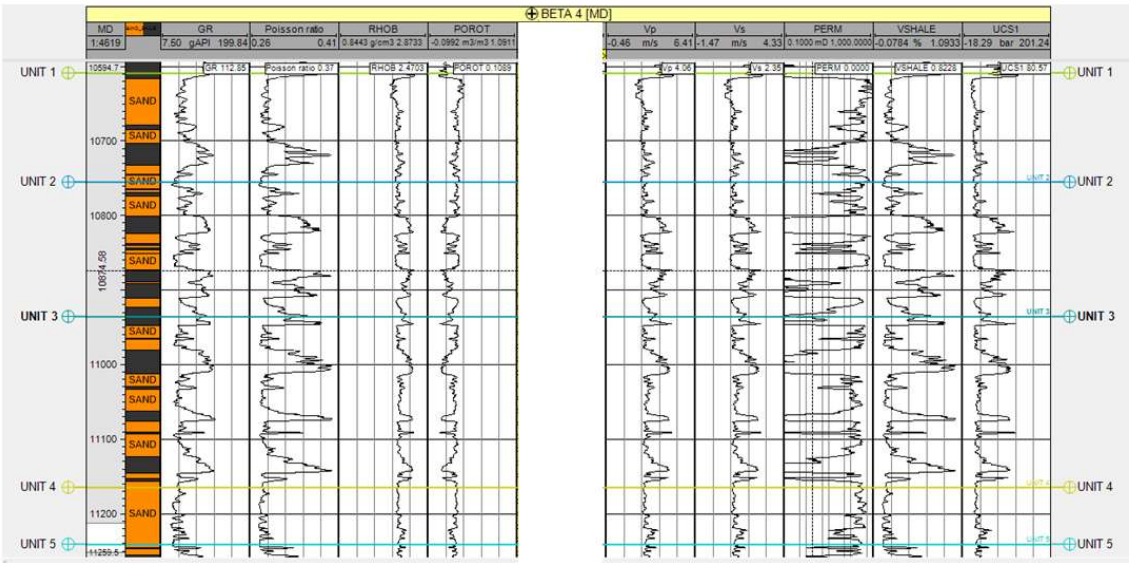


Fig. 4.6h: Logs of Beta 4 well showing elastic, inelastic and petrophysical properties of the reservoir rock depicted by gamma ray, Poisson's ratio, density, total porosity, V_p, V_s, permeability, volume of shale, and unconfined compressive strength.

Results of the evaluation of reservoir rock dynamic elastic (Young's modulus, bulk modulus, shear modulus, and Poisson's ratio), inelastic (unconfined compressive strength) and petrophysical properties (total porosity, effective porosity, permeability and volume of shale)

show a noticeable variation in the average values of these properties between sand and shale within the reservoirs. While the average values of the elastic and inelastic parameters are higher in shale, the average values of the petrophysical properties in addition to bulk compressibility are higher in sand. In shale, the average Poisson's ratio is 0.33, Young's modulus is 13.70GPa, bulk modulus is 13.30GPa, shear modulus is 5.12GPa, bulk compressibility is $0.07GPa^{-1}$, unconfined compressive strength is 32.32GPa, total porosity is 0.09, effective porosity is 0.07, and permeability is 0.022 mD. However, for sand, the average Poisson's ratio is 0.30, Young's modulus is 10.94GPa, bulk modulus is 12.76GPa, shear modulus is 4.11GPa, bulk compressibility is $0.10GPa^{-1}$, unconfined compressive strength is 25.19GPa, total porosity is 0.25, effective porosity is 0.19, and permeability is 192.00mD as presented in table 4.1. This implies that the shale is stronger and more ductile than the sand and is an indication that the sandstone of the studied reservoir will more rapidly deform than the shale under the same stress conditions while the shale will very likely form a seal to the fracture growth. The shale represents more stable rock unit.

Results of the estimation of reservoir pore pressure indicate that pore pressure is higher in shale units than sand units within the reservoirs of this field. The shale units are slightly overpressured. For the reservoirs of this field, the mean pore pressure value in shale is 15,662psi while the mean value of this pressure in sand is 13,683psi. There is a general increase in pore pressure with depth within the reservoirs due to the progressive increase in overburden fluid column. This higher pore pressure observed in shale is attributable mainly to compaction disequilibrium and other underlying causes (Opara, 2010).

On the other hand, effective pressure is lower in shale than sand because pore pressure is higher in shale than sand. According to Terzaghi pressure relationship which states that

effective pressure is the difference between total vertical pressure and pore pressure, when formation pore pressure is high, effective pressure becomes consequently low and vice versa.

Analysis of the three principal stresses of total vertical stress, maximum and minimum horizontal stresses show that the total vertical stress is greater than the maximum horizontal stress which in turn is greater than the minimum horizontal stress throughout the depth extent of the reservoirs ($S_v > Sh_{max} > Sh_{\min}$). These stresses are therefore not in equilibrium. According to Abijah and Tse (2016), this implies a normal fault stress regime within the field. The two principal horizontal stresses ought to be equal (Maleki et al., 2014) but because of tectonic activities and active faults within the Niger Delta, this is not possible. Changes in the magnitude of vertical stress and pore pressure also contribute to the observed differences in the magnitudes of the horizontal stresses. The total vertical stress increased generally with depth of burial due to increase in overburden weight. There were slight variations in the bulk densities of the rocks with increasing depth but these were not significant enough to alter the trend of the vertical stress field.

The difference between vertical stress and minimum horizontal stress (S_v-$Sh_{\min}$) called differential stress is slightly high; hence, deformation within the reservoirs will likely be by shear failure rather than tensile failure (Wilson & Cosgrove, 1982). From the results however, the magnitude of these principal stresses are very much lower than the estimated elastic properties and rock compressive strength. This directly implies that the reservoir rocks are stable.

According to the work by Adewole & Healy (2013) using borehole breakout data and multi-arm caliper logs to quantify in situ horizontal stress in the Niger Delta Basin, there is a diverse range of principal horizontal stress orientations including ENE-WSW, NNW-SSW,

NW-SE, N-S, and E-W. These diverse orientations can be attributed to the existence of multiple sources of stress within the Niger Delta region (Adewole & Healy, 2013).

4.1.2.2 Fuja Field

From the results obtained from Fuja Field reservoir, Young's modulus has an average value of 5.11GPa for sand and 6.08GPa for shale, bulk modulus has 5.10GPa for sand and 6.09GPa for shale, shear modulus gave 2.39GPa for sand and 2.84GPa for shale, Poisson's ratio has 0.39 for sand and 0.42 for shale, bulk compressibility has 0.023 GPa^{-1} for sand and 0.016 GPa^{-1} for shale, unconfined compressive strength (UCS) has 39.0 GPa for sand and 42.3 GPa for shale, total porosity has 0.16 for sand and 0.06 for shale, effective porosity has 0.13 for sand and 0.04 for shale, permeability has 44.10 mD for sand and 0.110 mD for shale and finally effective pressure has 14,945psi for sand and 12,973psi for shale.

The average values of the Poisson's ratio, Young's modulus, shear modulus, bulk modulus, bulk compressibility, UCS, total porosity, effective porosity, permeability and effective pressure for sand and shale units within Fuja Field reservoirs are shown in table 4.3, while estimated values of pore pressure, total vertical stress, maximum and minimum horizontal stresses within Fuja reservoirs are shown in Table 4.4.

.

Table 4.3: Average values of the elastic, inelastic and petrophysical properties, effective and pore pressures for sand and shale within Fuja reservoirs.

S/N	PROPERTY	AVERAGE FOR SAND	AVERAGE FOR SHALE
1.0	Young's Modulus	5.11±1.53 GPa	6.08±1.96 GPa
2.0	Bulk Modulus	5.10±1.48 GPa	6.09±1.57 GPa
3.0	Shear Modulus	2.39±0.88 GPa	2.84±1.21GPa
4.0	Poisson's Ratio	0.39±0.08	0.42±0.07
5.0	Bulk Compressibility	0.023±0.013 GPa^{-1}	0.016±0.006 GPa^{-1}
6.0	UCS	39.0±5.30 GPa	42.3±8.70 GPa
7.0	Total Porosity	0.16±0.06	0.06±0.024
8.0	Effective Porosity	0.13±0.024	0.04±0.009
9.0	Permeability	44.10±17.4 mD	0.110±0.04 mD
10.0	Pore Pressure	13,248±821.3 psi	15,220±746.2 psi
11.0	Effective Pressure	14,945±891.2 psi	12,973±608 psi

Table 4.4: Estimated values of pore pressure, total vertical stress, maximum and minimum horizontal stresses within Fuja reservoirs.

PARAMETER	**MINIMUM (psi)**	**MAXIMUM (psi)**	**AVERAGE (psi)**
Pore pressure (P_p) (Sand)	11,841.2	15,872.9	13,248±821.3
Pore pressure (P_p) (Shale)	12,860.9	17,759.3	15,220±746.2
Total vertical stress (S_v)	23,622.0	32,935.0	28,193±1,682.5
Maximum horizontal stress (Sh_{max})	20,997.4	29,275.6	26,237±1,406.8
Minimum horizontal stress (Sh_{min})	17,060.4	23,786.4	21,532±1,225.7

The geophysical logs of the four Fuja wells showing elastic, inelastic and petrophysical properties as well as effective pressure of the reservoir rock depicted by gamma ray, density, compressional wave velocity, shear wave velocity, shear modulus, bulk modulus, unconfined compressive strength, Young's modulus, total porosity, permeability, volume of shale, effective pressure, Poisson's ratio, sonic, effective porosity, and bulk compressibility are presented in figure 4.7(a-h) below.

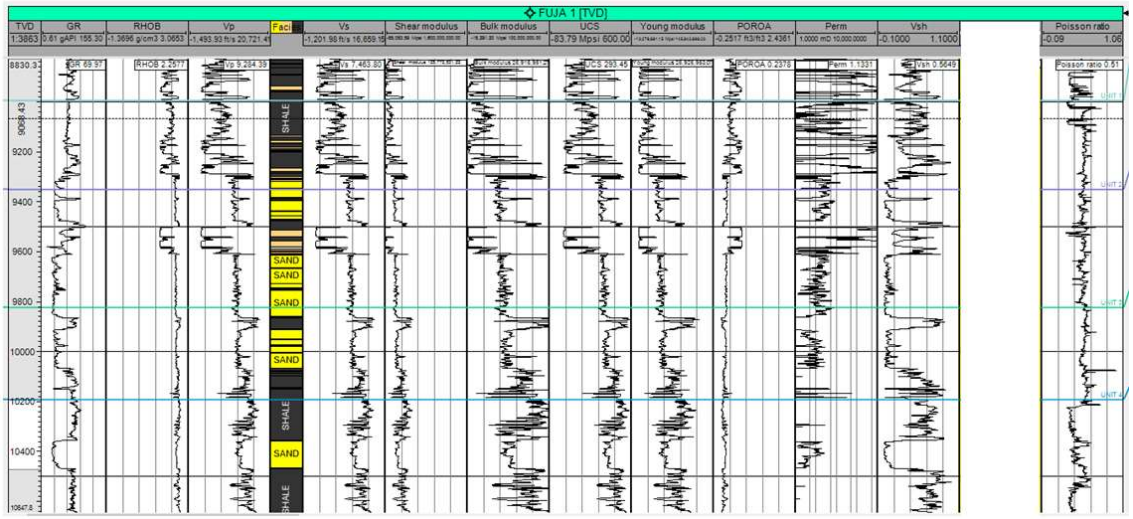


Fig. 4.7a: Logs of Fuja 1 well showing elastic, inelastic and petrophysical properties of the reservoir rock depicted by gamma ray, density, V_p, V_s, shear modulus, bulk modulus, unconfined compressive strength, Young's modulus, total porosity, permeability, volume of shale and Poisson's ratio.

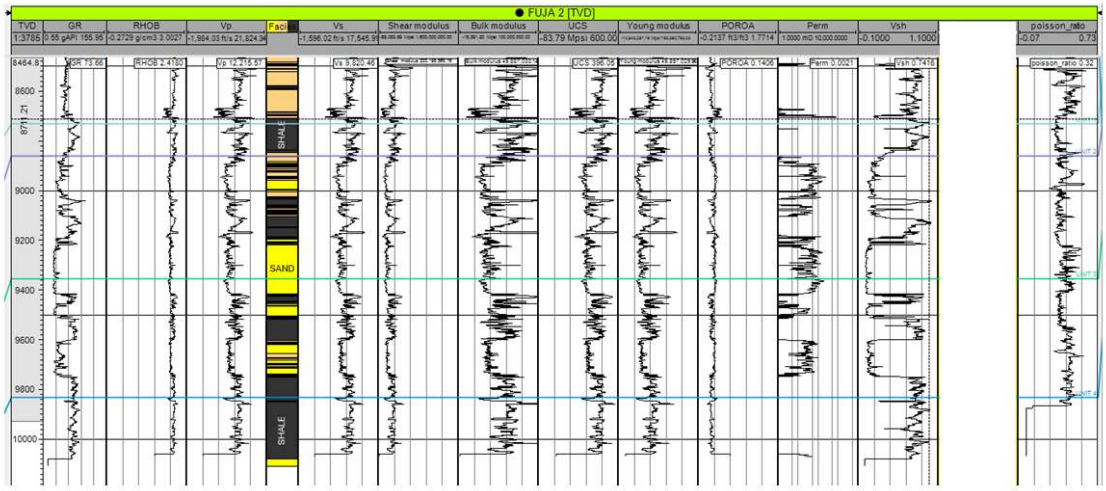


Fig. 4.7b: Logs of Fuja 2 well showing elastic, inelastic and petrophysical properties of the reservoir rock depicted by gamma ray, density, V_p, V_s, shear modulus, bulk modulus, unconfined compressive strength, Young's modulus, total porosity, permeability, volume of shale, and Poisson's ratio.

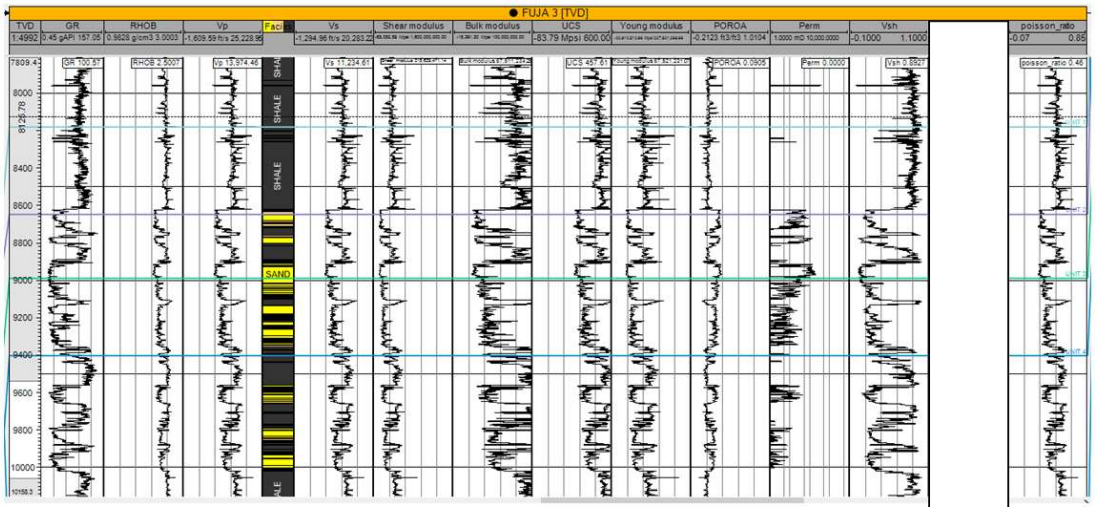


Fig. 4.7c: Logs of Fuja 3 well showing elastic, inelastic and petrophysical properties of the reservoir rock depicted by gamma ray, density, V_p, V_s, shear modulus, bulk modulus, UCS, Young's modulus, total porosity, permeability, volume of shale, and Poisson's ratio.

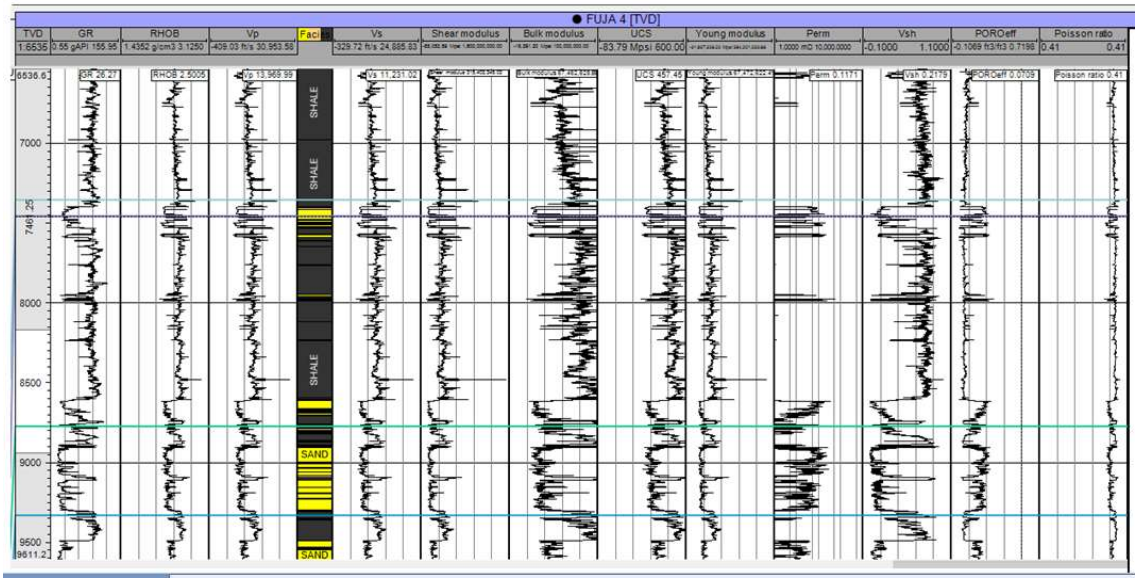


Fig. 4.7d: Logs of Fuja 4 well showing elastic, inelastic and petrophysical properties of the reservoir rock depicted by gamma ray, density, V_p, V_s, shear modulus, bulk modulus, UCS, Young's modulus, permeability, volume of shale, effective porosity, and Poisson's ratio.

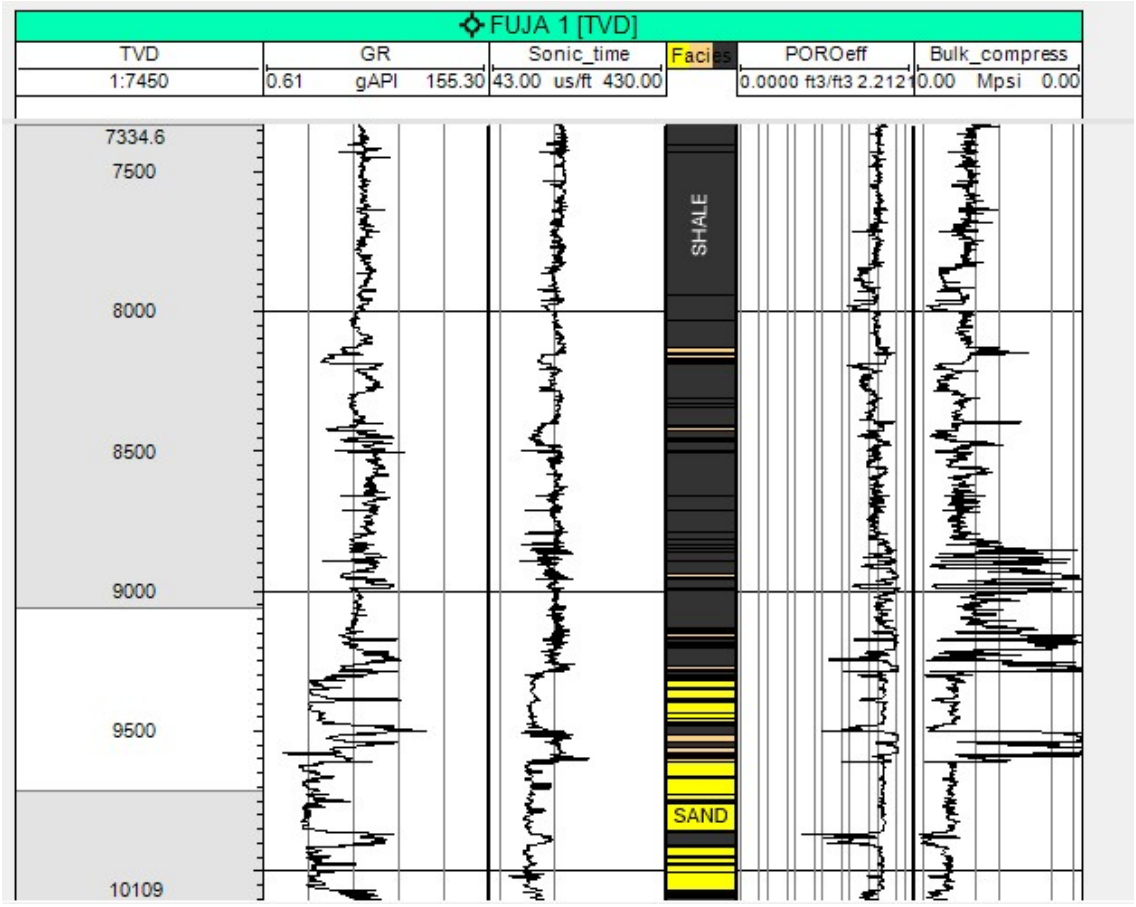


Fig. 4.7e: Logs of Fuja 1 well showing elastic and petrophysical properties of the reservoir rock depicted by gamma ray, sonic, effective porosity, and bulk compressibility.

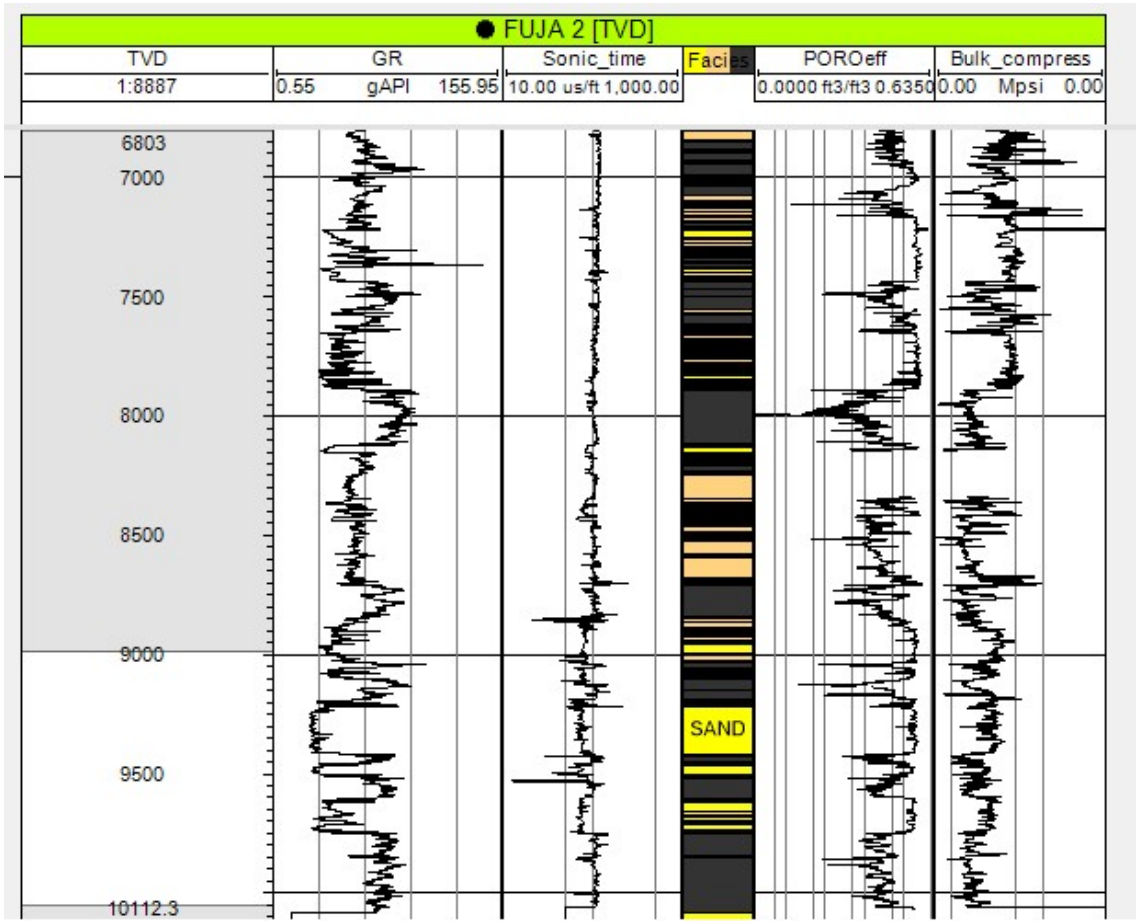


Fig. 4.7f: Logs of Fuja 2 well showing elastic and petrophysical properties of the reservoir rock depicted by gamma ray, sonic, effective porosity, and bulk compressibility.

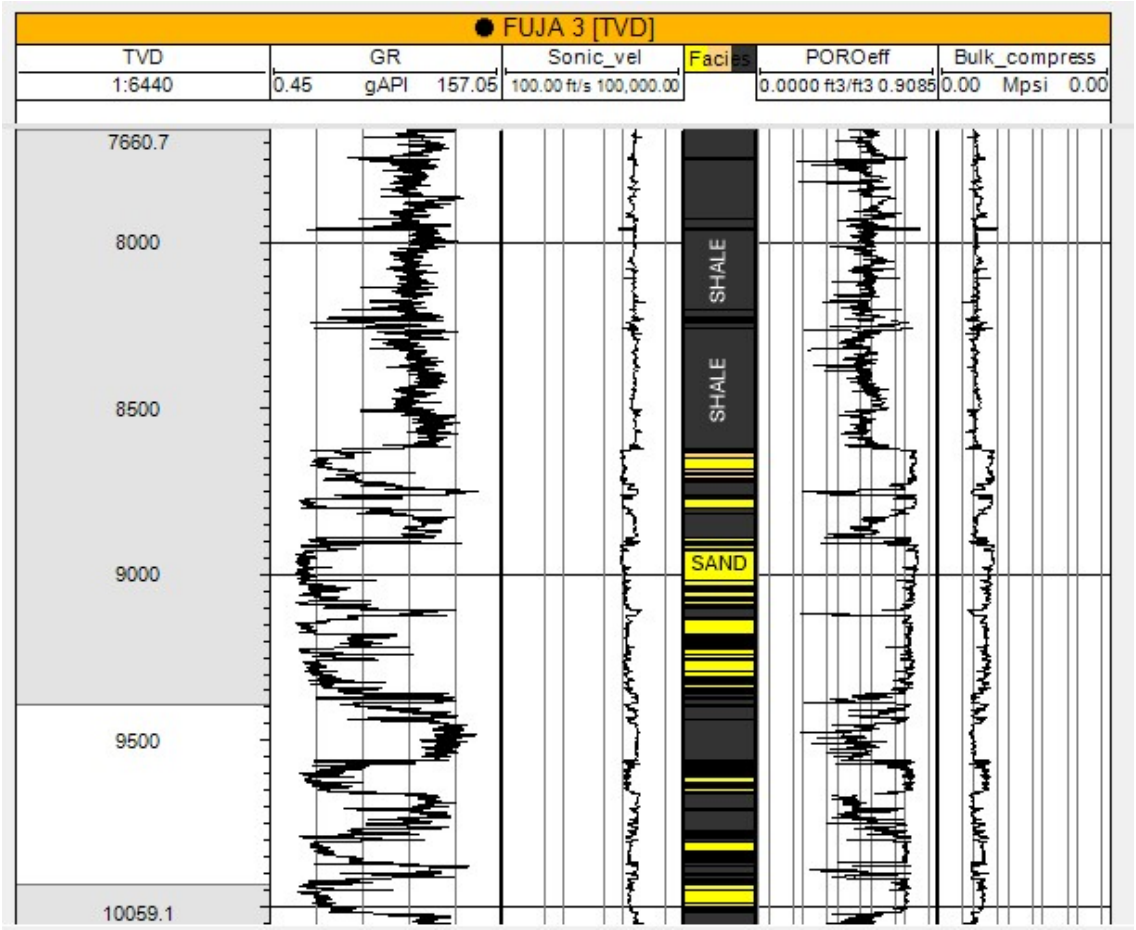


Fig. 4.7g: Logs of Fuja 3 well showing elastic and petrophysical properties of the reservoir rock depicted by gamma ray, sonic, effective porosity, and bulk compressibility.

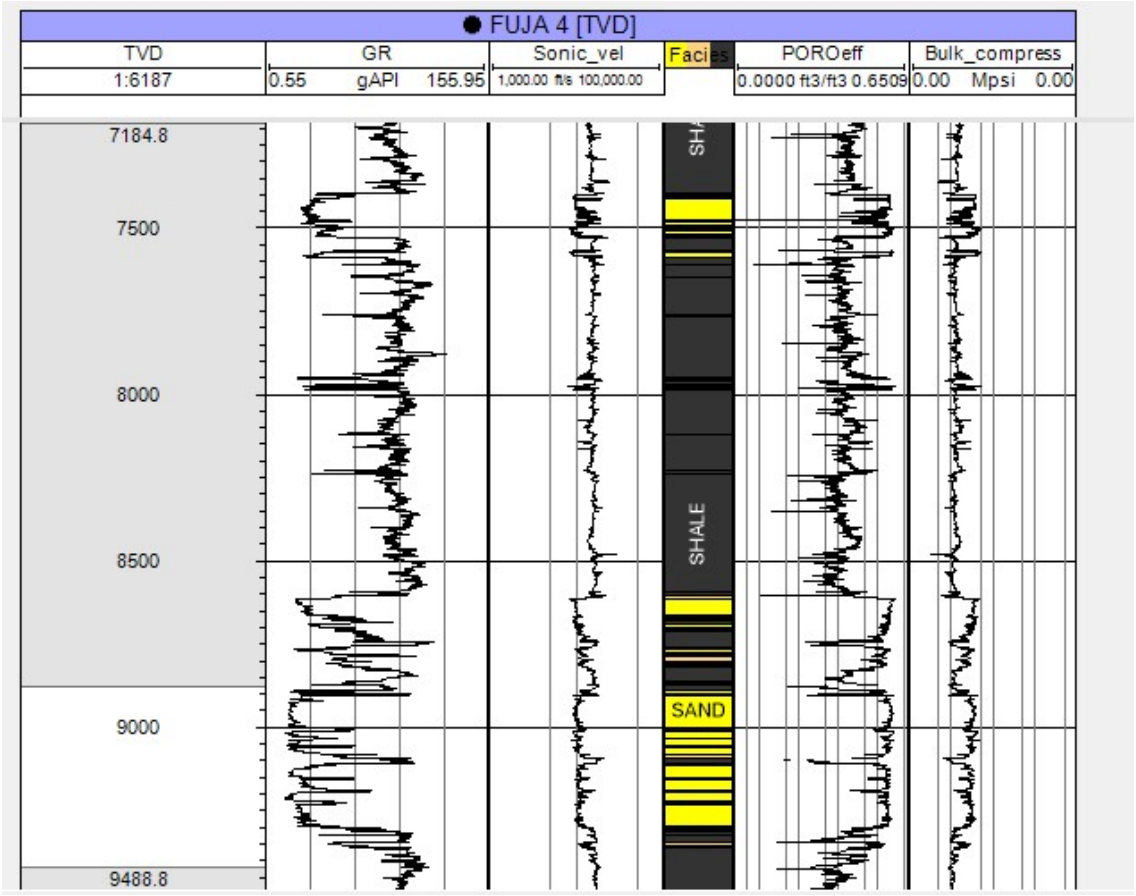


Fig. 4.7h: Logs of Fuja 4 well showing elastic and petrophysical properties of the reservoir rock depicted by gamma ray, sonic, effective porosity, and bulk compressibility.

Results obtained from the evaluation of reservoir rock dynamic elastic, inelastic and petrophysical properties show a noticeable variation in the average values of these properties between sand and shale within this reservoir. Just as in Beta Field, the average values of the elastic (Young's modulus, bulk modulus, shear modulus, and Poisson's ratio) and inelastic (unconfined compressive strength) parameters are higher in shale while the average values of the petrophysical properties (total porosity, effective porosity, and permeability) and bulk compressibility are higher in sand. In shale, the average Poisson's ratio is 0.42, Young's modulus is 6.08 GPa, bulk modulus is 6.09 GPa, shear modulus is 2.84GPa, bulk compressibility is 0.016 GPa^{-1}, unconfined compressive strength is 42.3 GPa, total porosity is 0.06, effective porosity is 0.04, and permeability is 0.110 mD. However, for sand, the

average Poisson's ratio is 0.39, Young's modulus is 5.11GPa, bulk modulus is 5.10 GPa, shear modulus is 2.39 GPa, bulk compressibility is 0.023 GPa^{-1}, unconfined compressive strength is 39.0 GPa, total porosity is 0.16, effective porosity is 0.13, and permeability is 44.10 mD as presented in Table 4.3. Again, this is an indication that the shale is more ductile and stronger than the sand and is a pointer to the fact that the sandstone of the studied reservoir will more likely deform than the shale under the same pressure conditions and the shale will very much likely form a seal to the growth of the resultant fracture.

There is also a general increase in pore pressure with depth within the reservoirs of this field due to the progressive increase in overburden fluid column. Results show that pore pressure is also higher within the shale units than sand units of the reservoirs, in other words, the shale is slightly overpressured with pressures approaching 18,000psi at deeper sections. This is attributable mainly to compaction disequilibrium and other underlying causes (Opara, 2010).

Analysis of the three principal stresses operative within the reservoirs of this field also show that the total vertical stress is greater than the maximum horizontal stress which in turn is greater than the minimum horizontal stress throughout the depth extent of the reservoirs ($S_v > Sh_{max} > Sh_{\min}$). There is disequilibrium between these stresses and this implies a normal fault stress regime within the field (Abijah and Tse 2016). Because of tectonic activities and active faults within the Niger Delta, the two principal horizontal stresses are not equal. The total vertical stress also increased generally with depth of burial in this field due to increase in overburden weight.

The differential stress which is the difference between vertical stress and minimum horizontal stress (S_v-$Sh_{\min}$) is also slightly high in this field and this implies that deformation within

the reservoirs will likely be by shear failure rather than tensile failure according to Wilson and Cosgrove (1982). In this field, because the magnitudes of these principal stresses are very much lower than the estimated elastic properties and rock compressive strength, the reservoir rocks, just like in Beta Field, are stable.

4.1.3 Cross Plots of Rock Elastic, Inelastic, Petrophysical Properties and Effective Pressure

The interrelationship between rock elastic, inelastic, petrophysical properties and effective pressure was investigated for the two fields to verify the suggestion by Horsud (2001) and Wong and David (1997) that there is a definite link between the rock elastic parameters, depth and the compressive rock strength (UCS) of a reservoir.

4.1.3.1 Beta Field

Cross plots of rock elastic, inelastic and petrophysical properties as well as effective pressure for Beta Field are shown in Figure 4.8(a-v) below. They include cross plots between UCS and Poisson's ratio, UCS and shear modulus, UCS and sonic transit time, UCS and total porosity, UCS and measured depth, UCS and compressional wave velocity, UCS and shear wave velocity, UCS and volume of shale, UCS and Young's modulus, Young's modulus and depth, bulk modulus and compressional wave velocity, Poisson's ratio and total porosity, porosity and sonic transit time, UCS and effective porosity, UCS and permeability, effective pressure and depth, effective pressure and porosity, effective pressure and UCS, compressional wave velocity (V_P) and effective porosity, permeability and bulk density, UCS and bulk density, and finally shear wave velocity and sonic transit time.

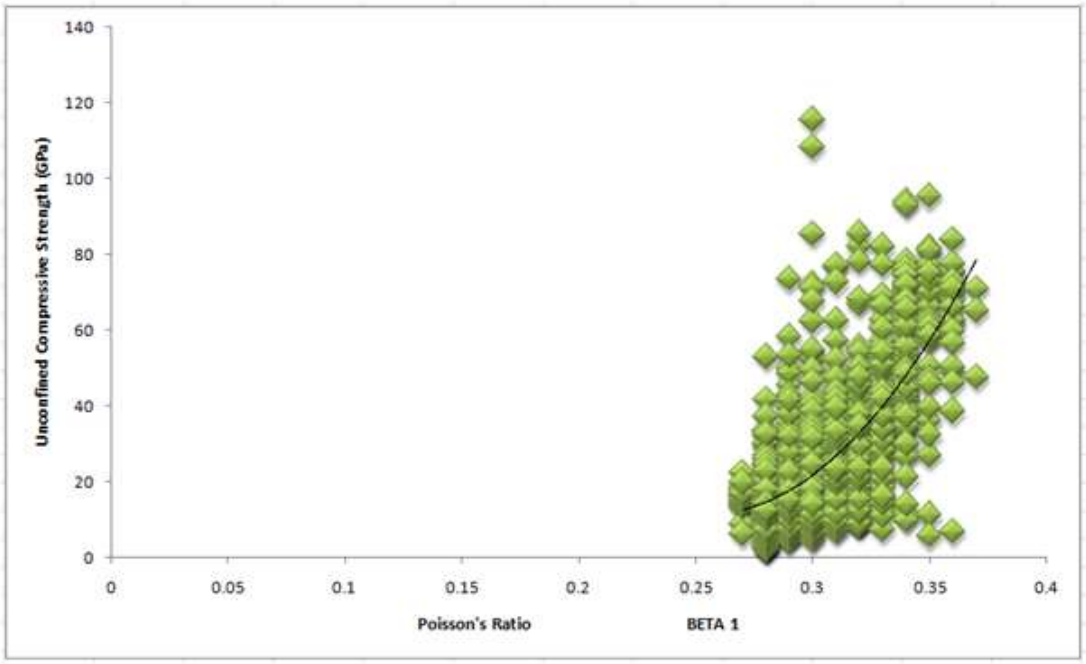


Fig. 4.8a: Cross plot showing trend line of unconfined compressive strength against Poisson's ratio for Beta 1 well.

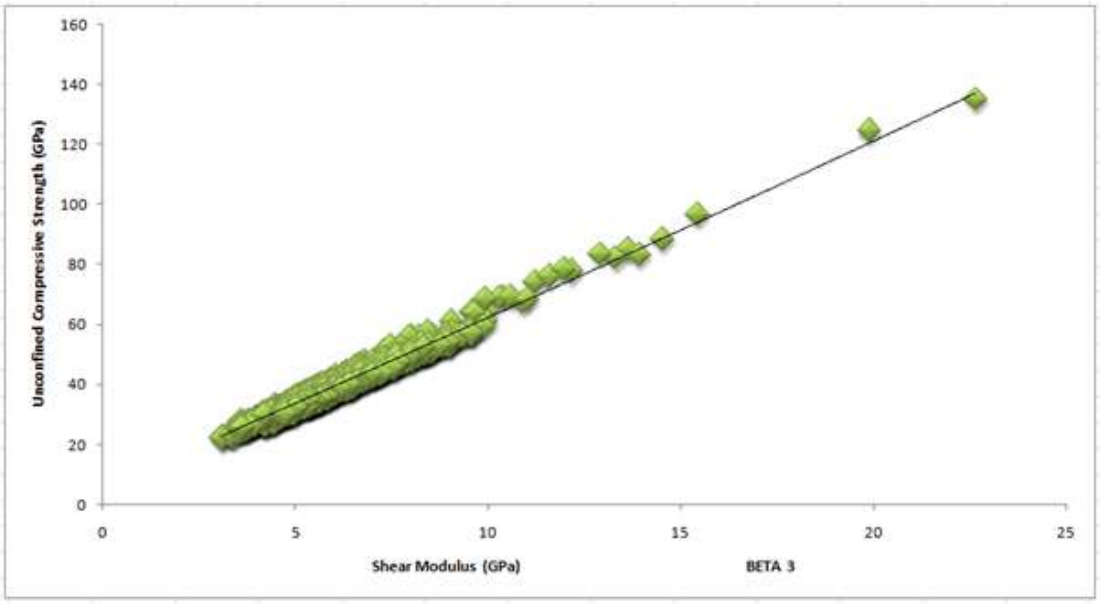


Fig. 4.8b: Cross plot showing trend line of unconfined compressive strength against shear modulus for Beta 3 well.

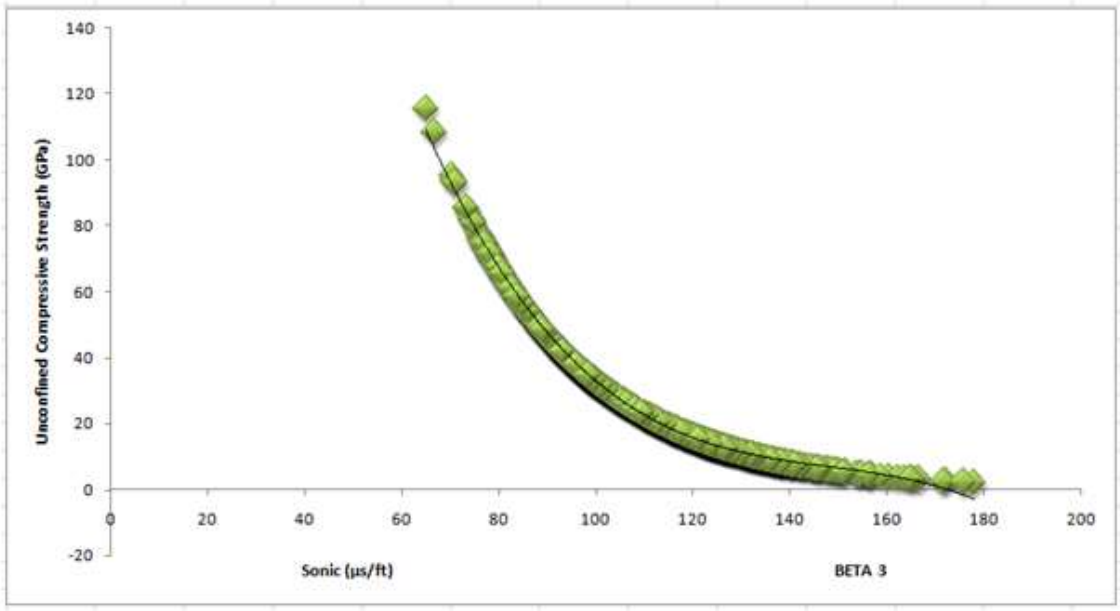


Fig. 4.8c: Cross plot showing trend line of unconfined compressive strength against sonic transit time for Beta 3 well.

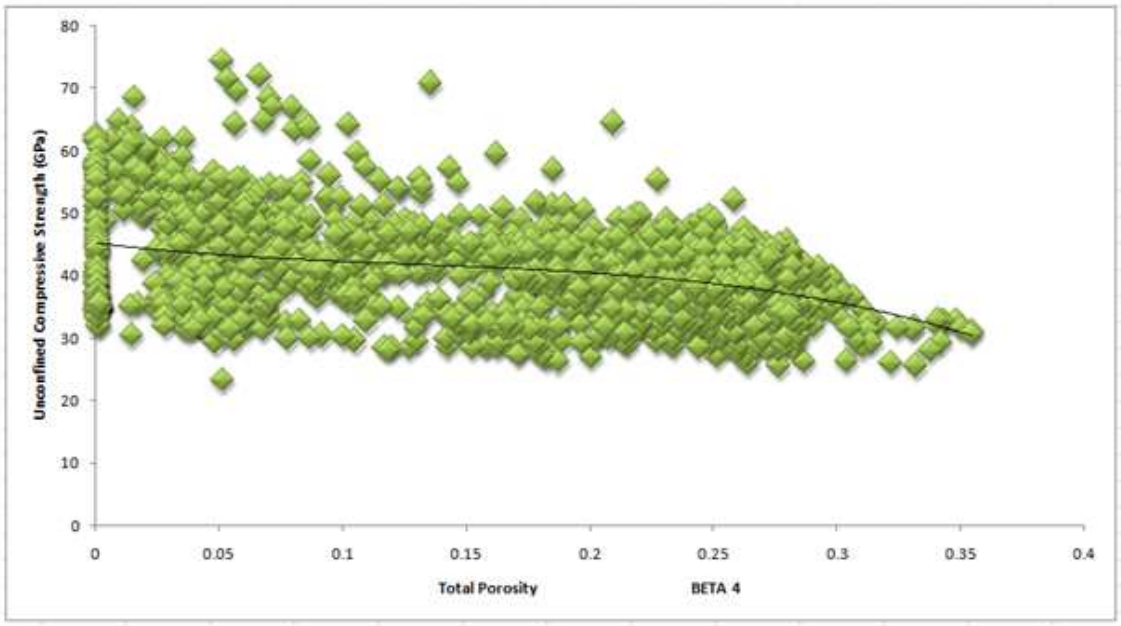


Fig. 4.8d: Cross plot showing trend line of unconfined compressive strength against total porosity for Beta 4 well.

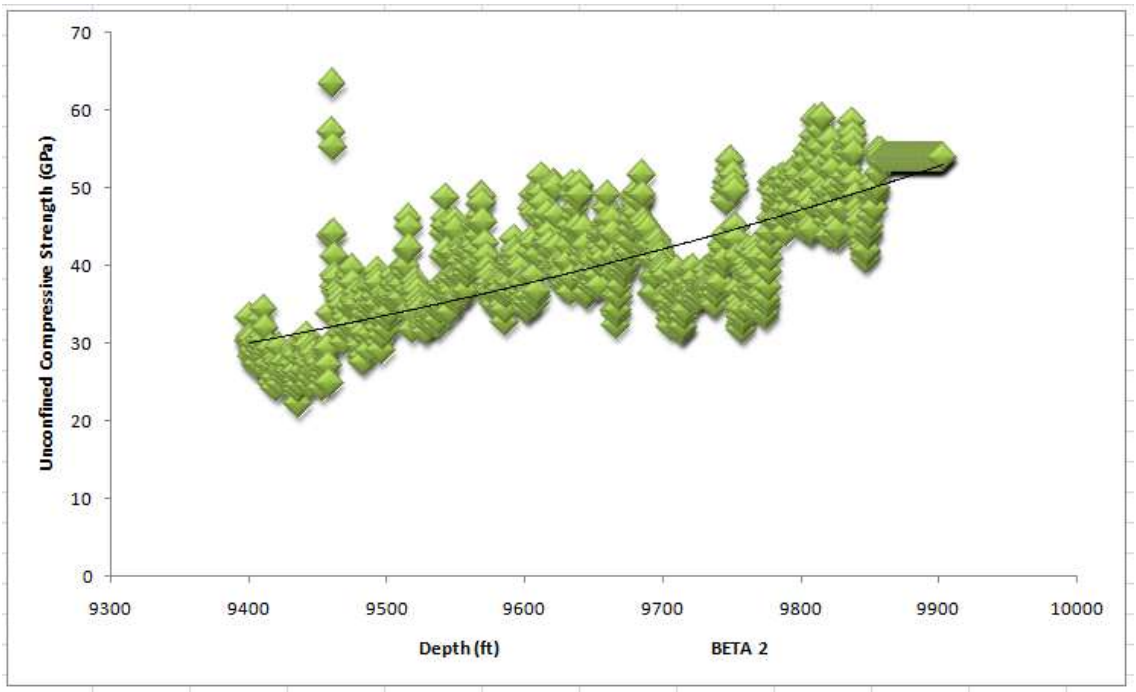


Fig. 4.8e: Cross plot showing trend line of unconfined compressive strength against measured depth for Beta 2 well.

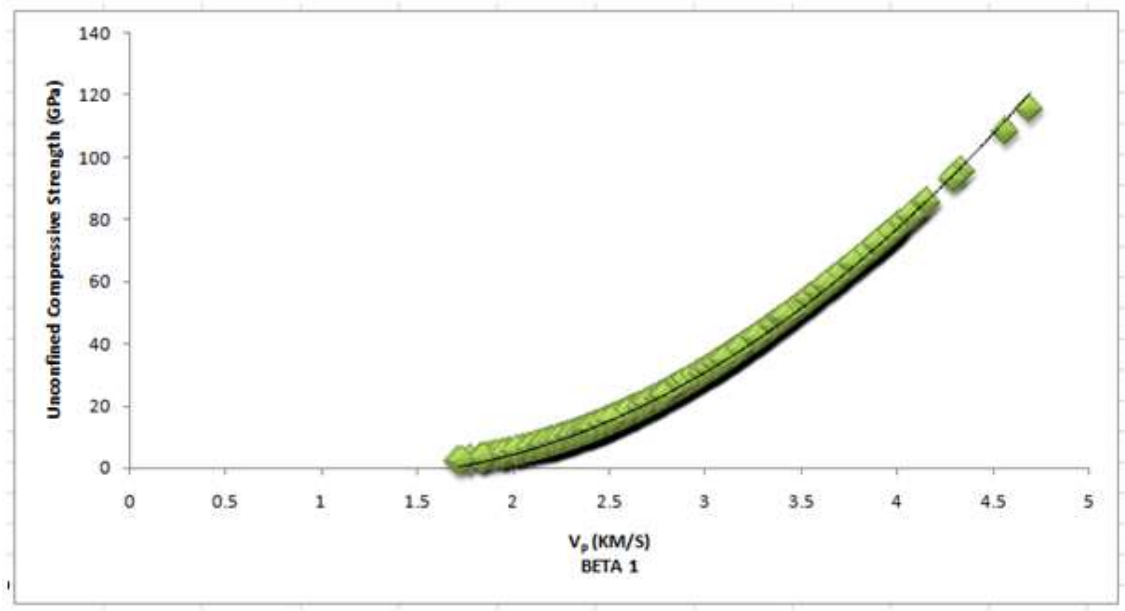


Fig. 4.8f: Cross plot showing trend line of unconfined compressive strength against compressional wave velocity (V_P) for Beta 1 well.

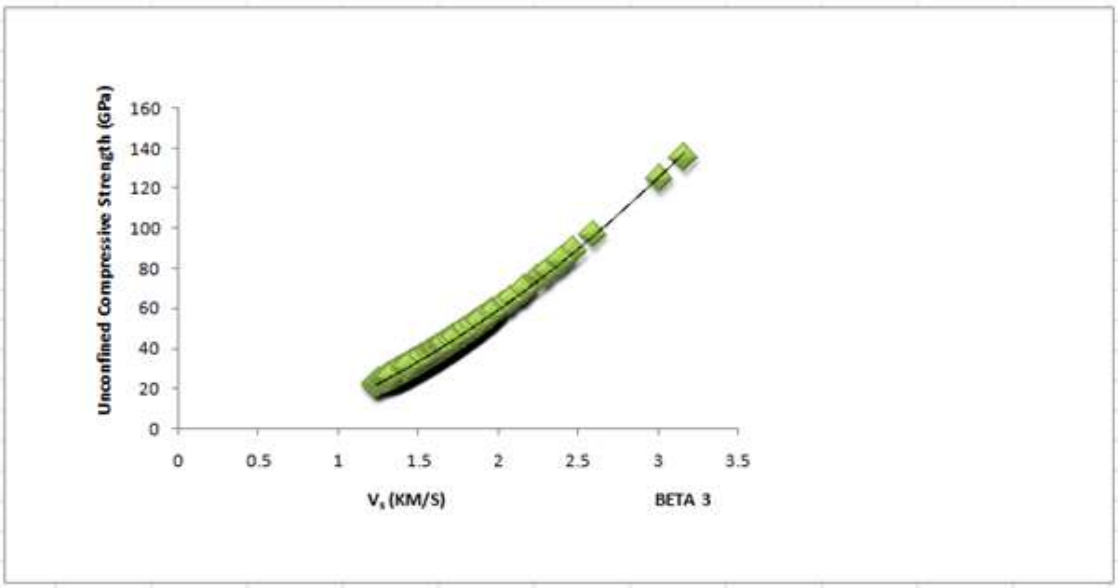


Fig. 4.8g: Cross plot showing trend line of unconfined compressive strength against shear wave velocity (V_S) for Beta 3 well.

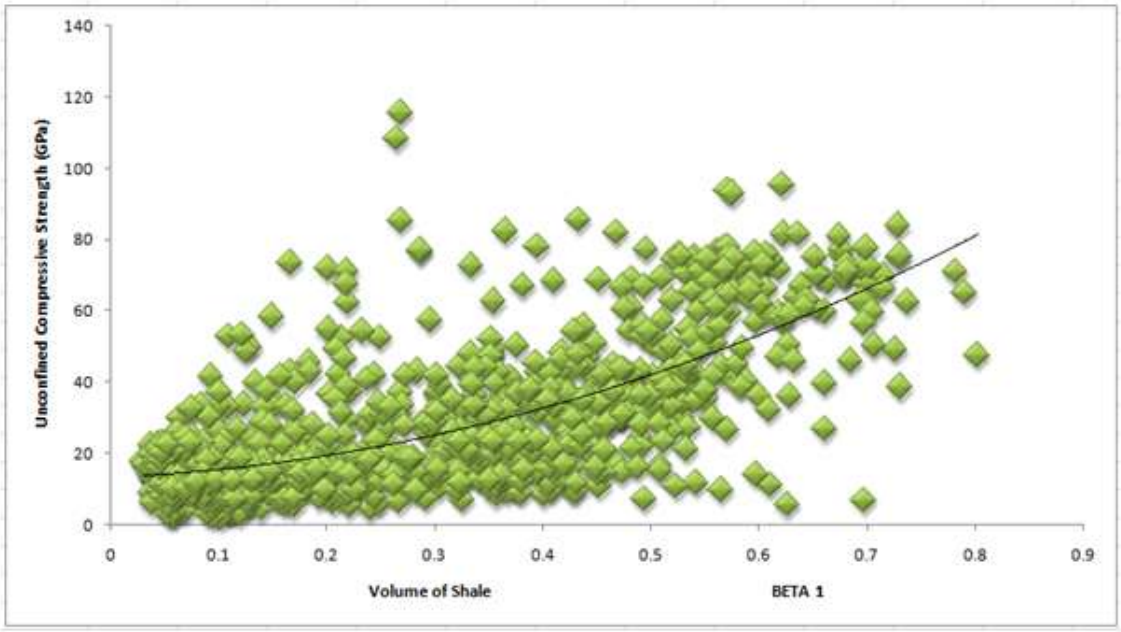


Fig. 4.8h: Cross plot showing trend line of unconfined compressive strength against volume of shale for Beta 1 well.

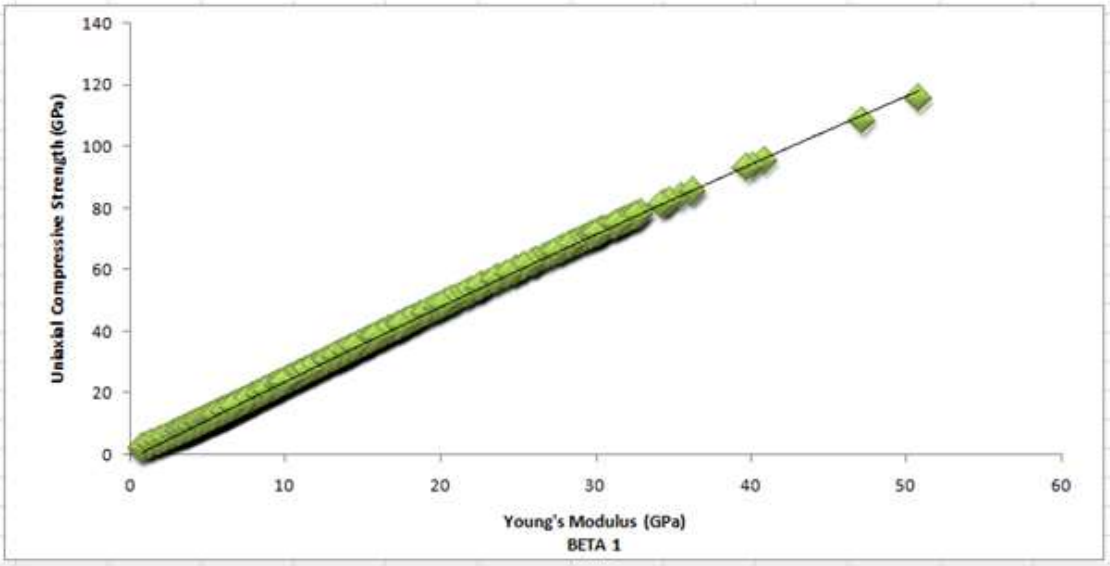


Fig. 4.8i: Cross plot showing trend line of unconfined compressive strength against Young's modulus for Beta 1 well.

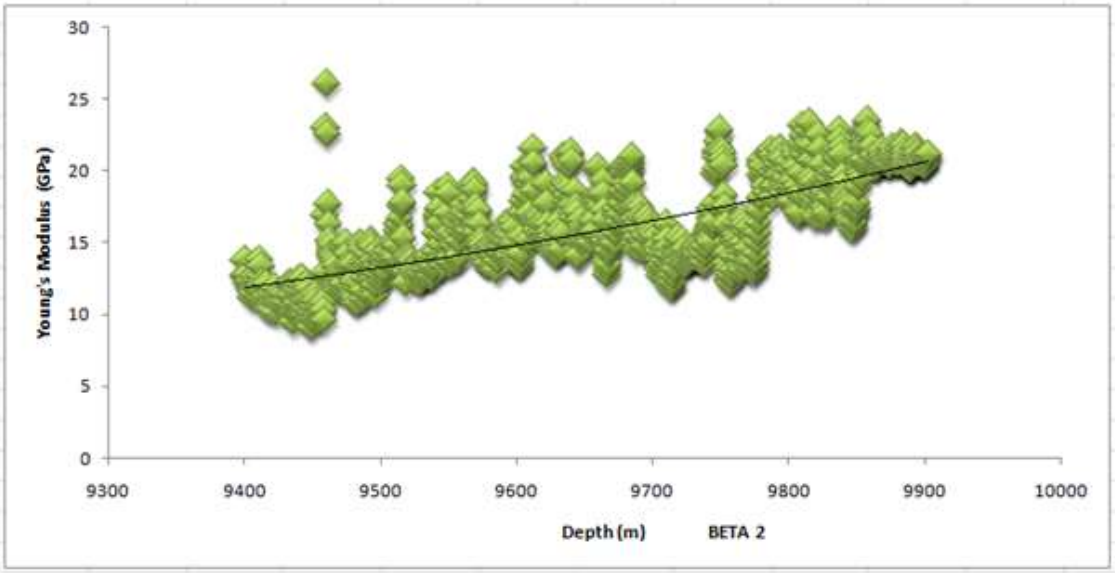


Fig. 4.8j: Cross plot showing trend line of Young's modulus against measured depth for Beta 2 well.

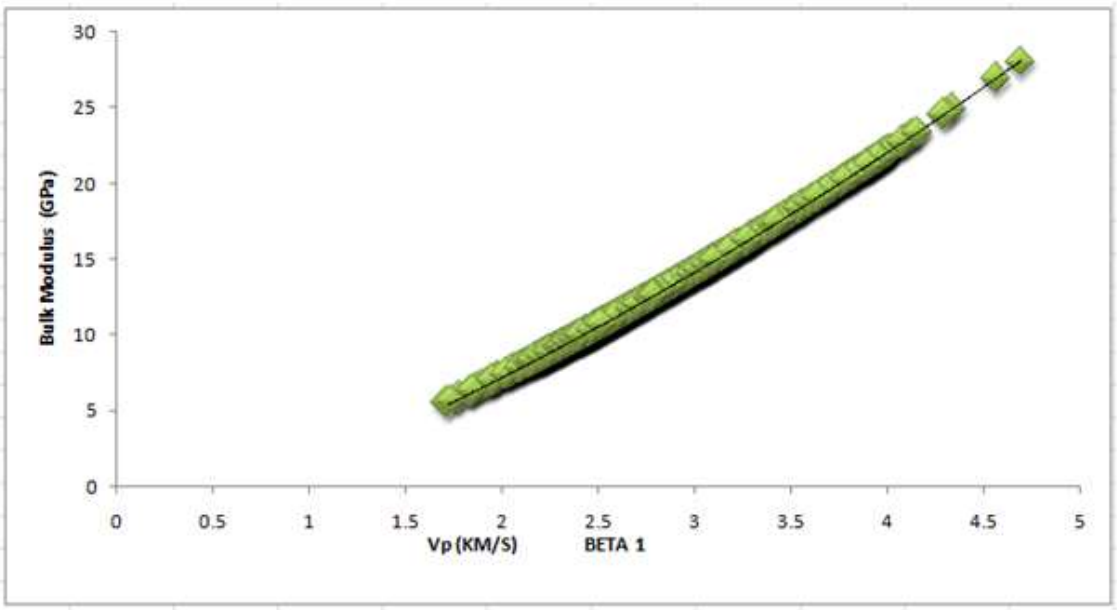


Fig. 4.8k: Cross plot showing trend line of bulk modulus against compressional wave velocity (V_P) for Beta 1 well.

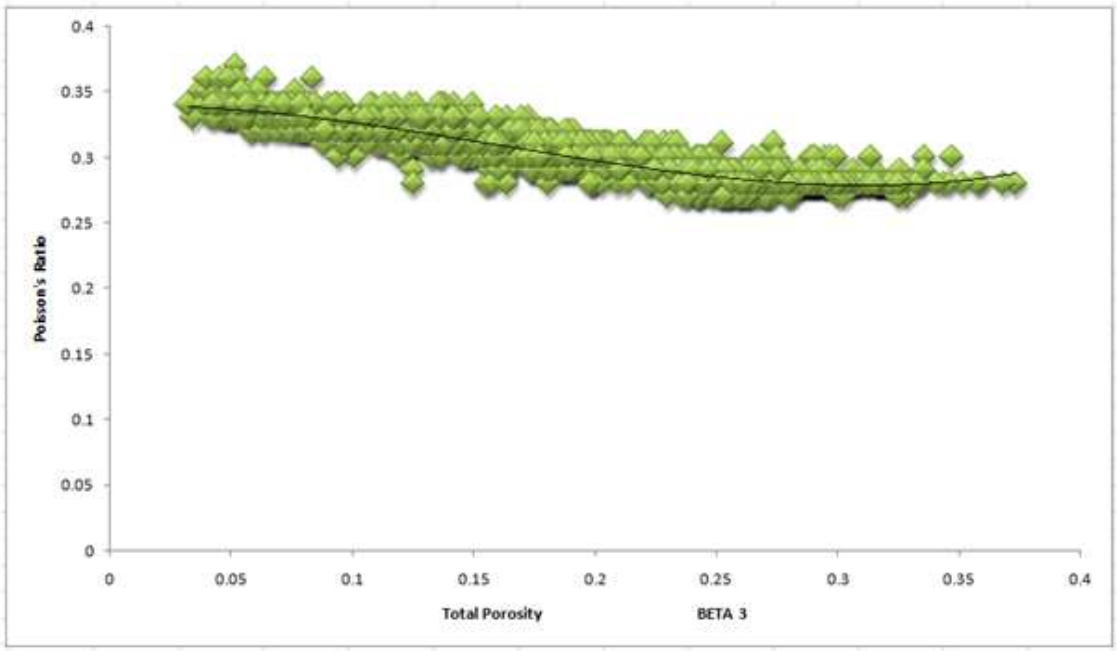


Fig. 4.8l: Cross plot showing trend line of Poisson's ratio against total porosity for Beta 3 well.

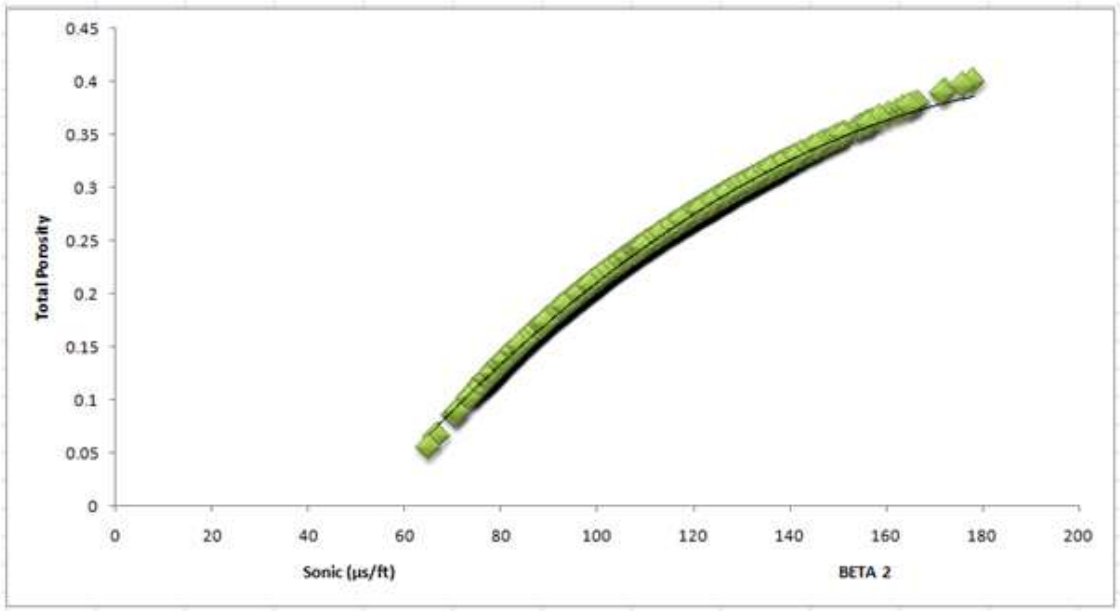


Fig. 4.8m: Cross plot showing trend line of total porosity against sonic transit time for Beta 2 well.

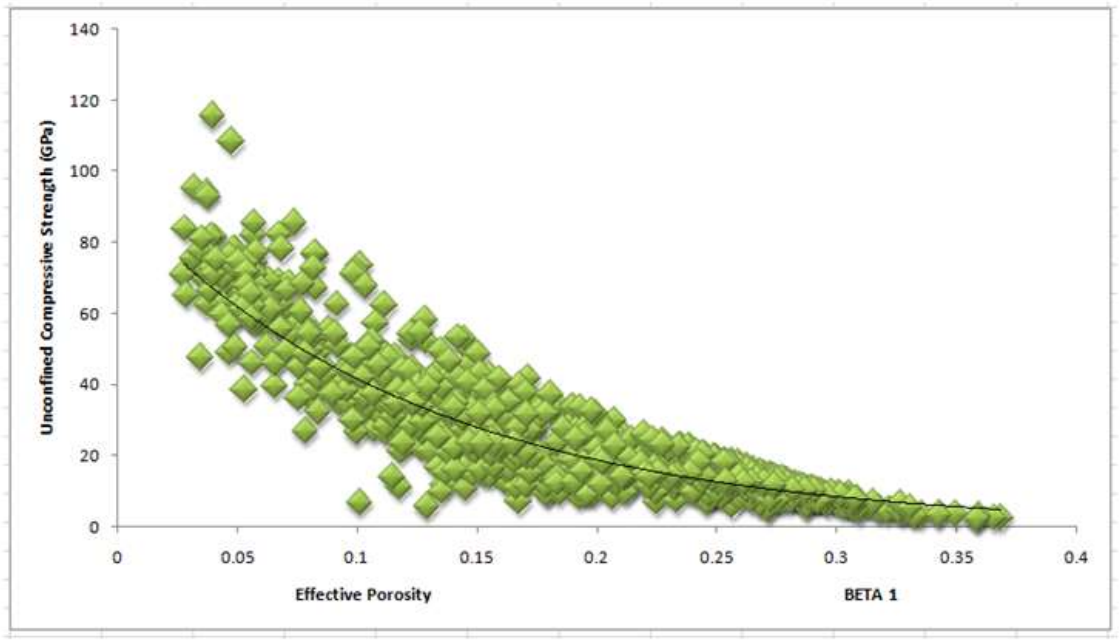


Fig. 4.8n: Cross plot showing trend line of unconfined compressive strength against effective porosity for Beta 1 well.

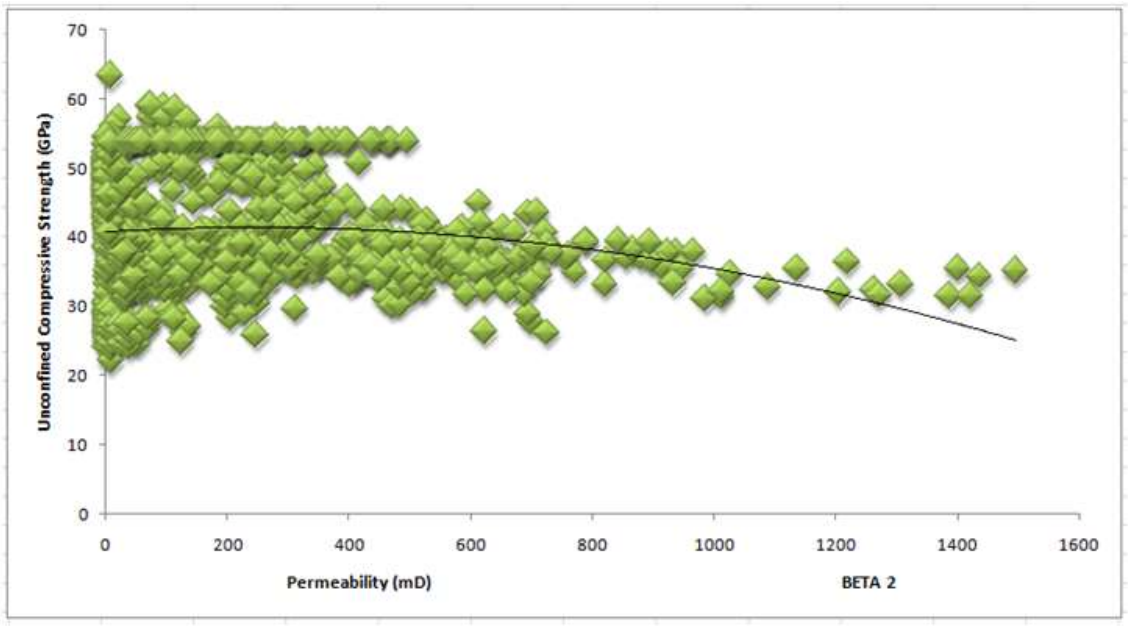


Fig. 4.8o: Cross plot showing trend line of unconfined compressive strength against permeability for Beta 2 well.

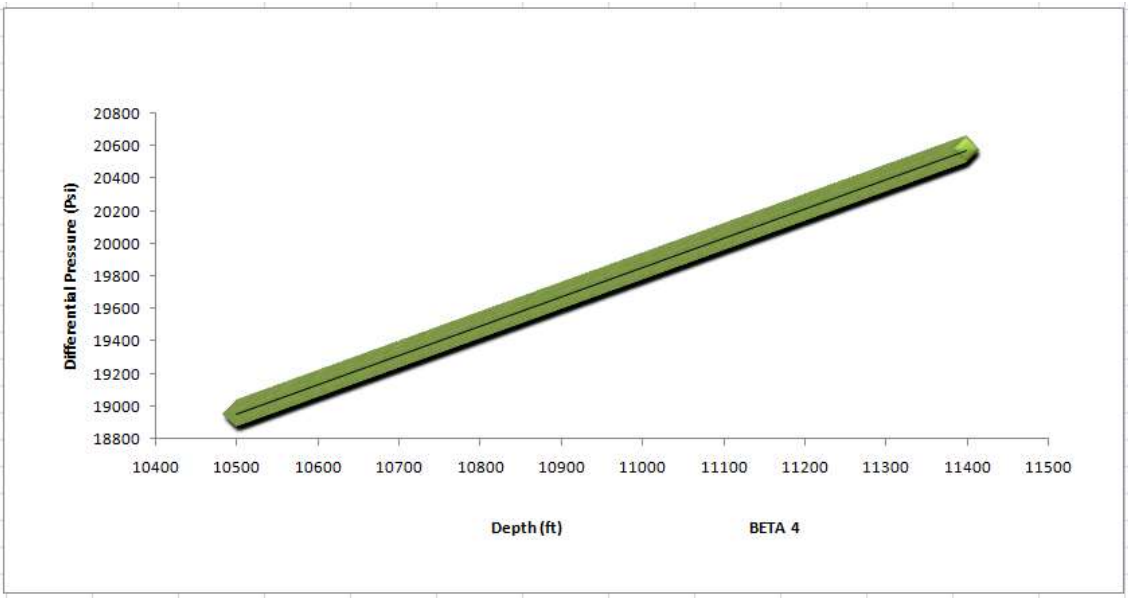


Fig. 4.8p: Cross plot showing trend line of Effective/differential pressure against measured depth for Beta 4 well.

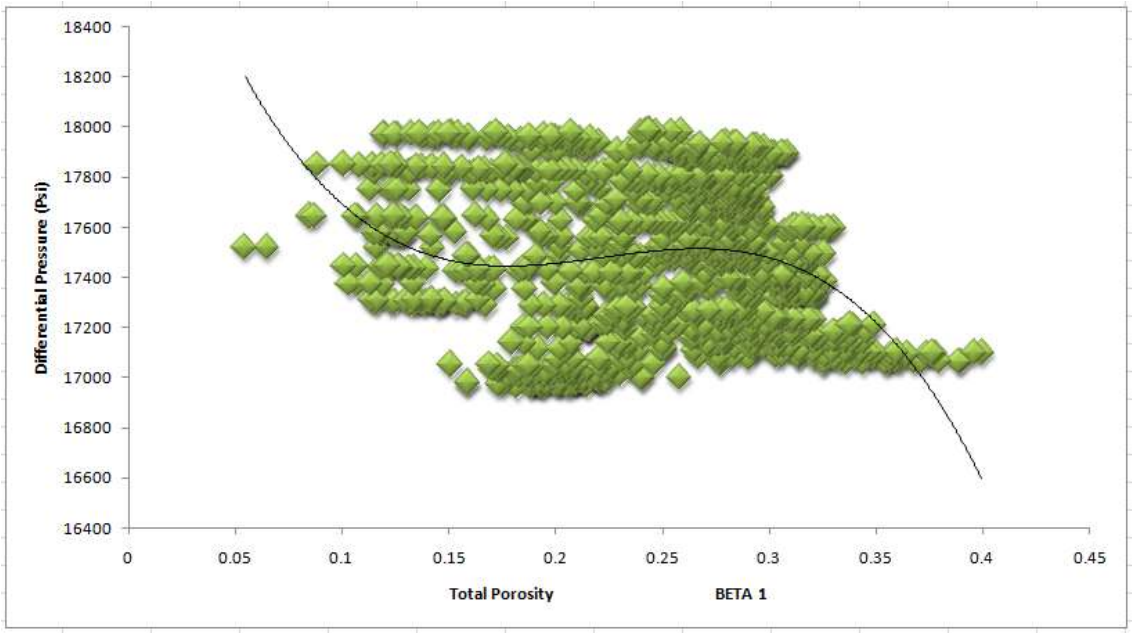


Fig. 4.8q: Cross plot showing trend line of Effective/differential pressure against total porosity for Beta 1 well.

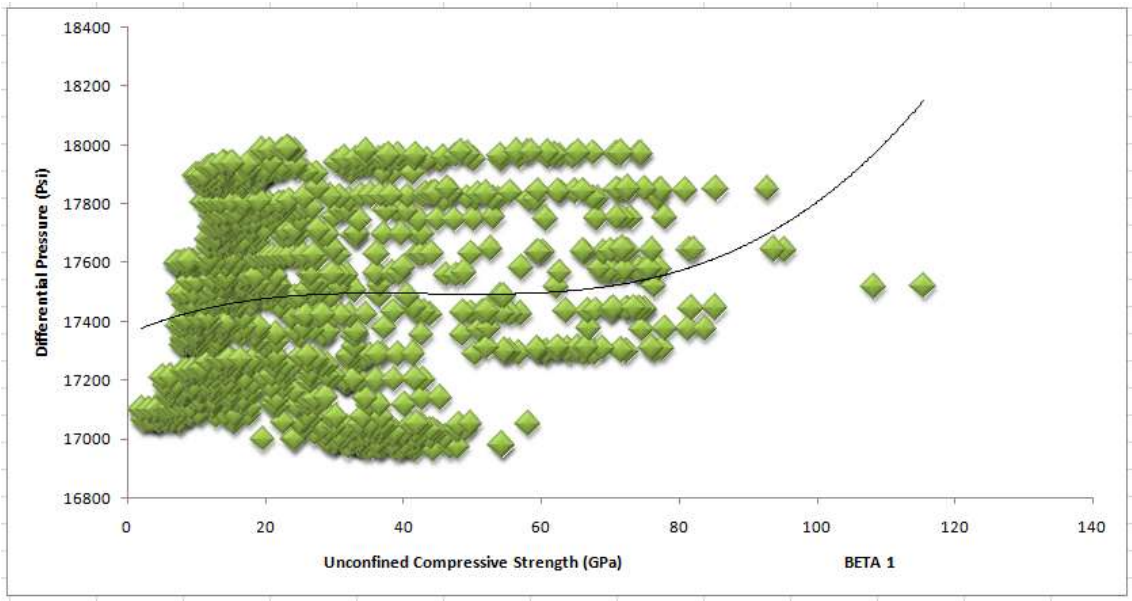


Fig. 4.8r: Cross plot showing trend line of Effective/differential pressure against unconfined compressive strength for Beta 1 well.

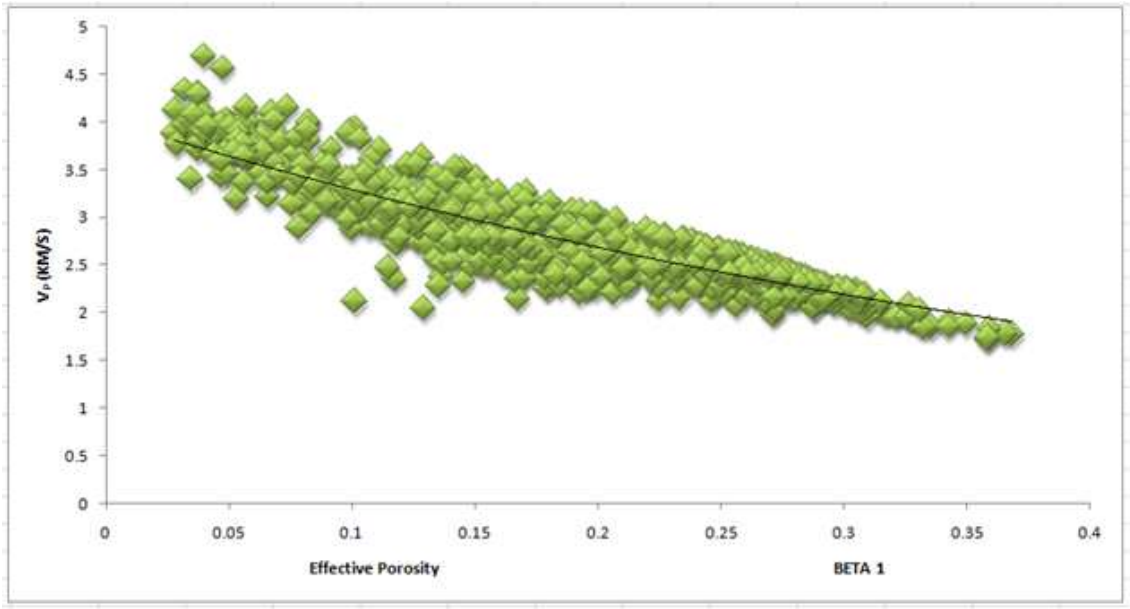


Fig. 4.8s: Cross plot showing trend line of compressional wave velocity against effective porosity for Beta 1 well.

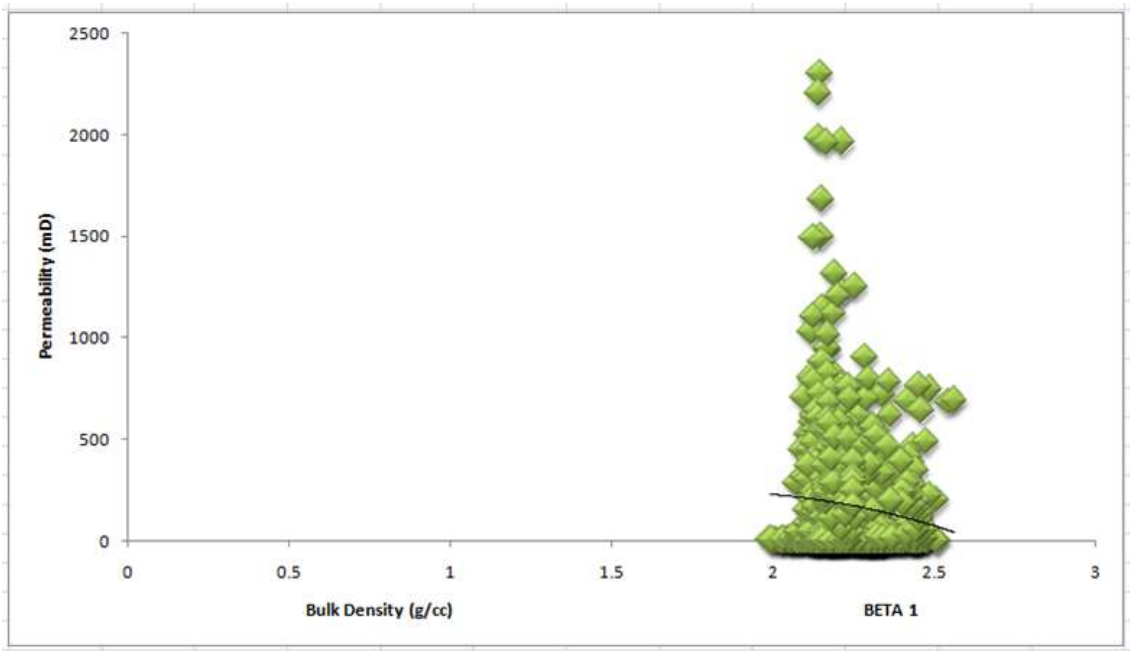


Fig. 4.8t: Cross plot showing trend line of permeability against bulk density for Beta 1 well.

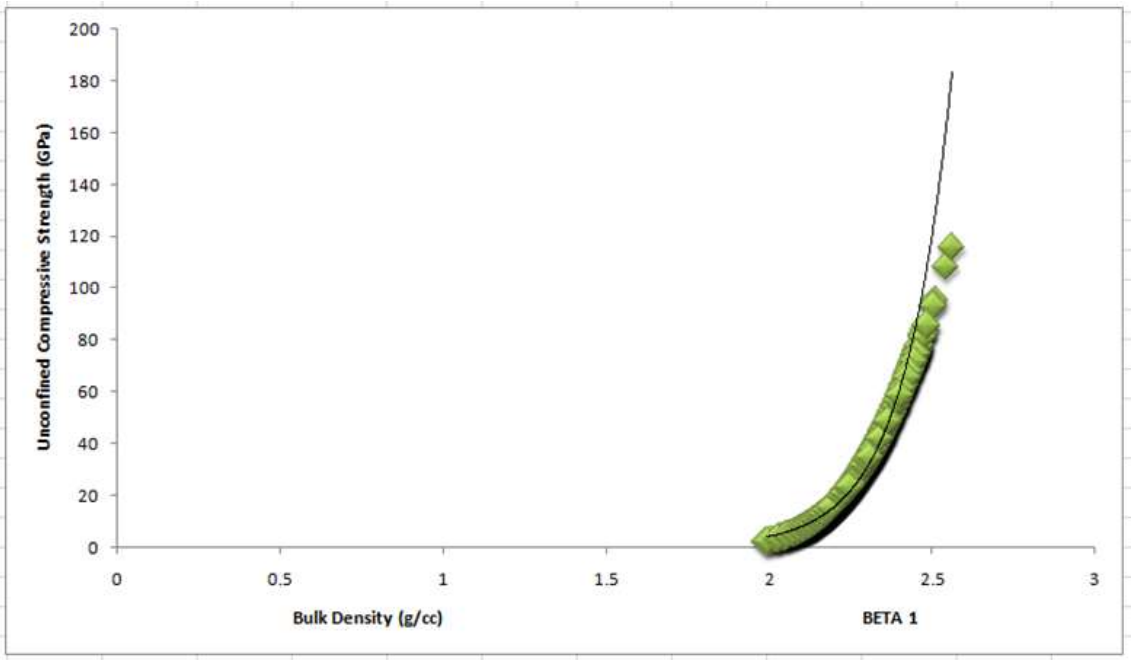


Fig. 4.8u: Cross plot showing trend line of unconfined compressive strength against bulk density for Beta 1 well.

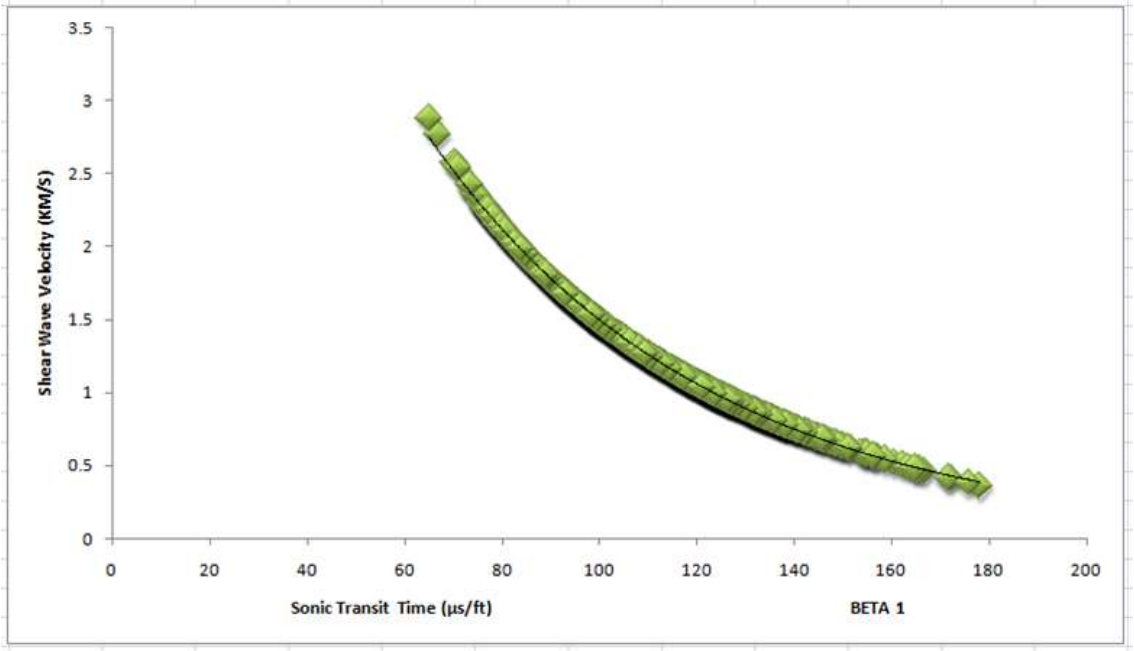


Fig. 4.8v: Cross plot showing trend line of shear wave velocity against sonic transit time for Beta 1 well.

From the cross plots between the elastic, inelastic and petrophysical rock properties of Beta Field, there is a conspicuous connection between these rock properties. There is a clear increase in unconfined compressive strength of the reservoir rock with the elastic properties,

depth and volume of shale, indicating that as the values of the elastic rock properties, rock depth, and shaliness increases the rock strength also increases. This implies that the elasticity of a rock and rock compaction plays a major and important role in determining the strength and ductility of that rock. As the elasticity and compaction of a rock increases, its strength and ductility also increases.

There is also a decrease in unconfined compressive strength and by extension the elastic rock properties with the petrophysical properties of total porosity, effective porosity and permeability. This implies that the presence of pore spaces within a rock unit (whether interconnected or not) decreases the overall strength of that rock and makes the rock highly susceptible to deformation and failure when subjected to stress. A highly porous rock unit will yield rapidly to deformation than a less porous rock when exposed to the same stress. These results therefore validate the assertion by Wong & David (1997) and Horsrud (2001) that there is a definite link between rock elastic parameters, depth, and unconfined compressive strength.

Results of the cross plots between effective pressure and unconfined compressive strength as well as effective pressure and depth show that effective pressure increases with increase in rock depth and increase in unconfined compressive strength. The increase in rock depth effectively decreases rock porosity due to compaction thereby decreasing the pore pressure within the rock unit (Okeke, 2010). This decrease in pore pressure increases the effective pressure within the rock unit from Terzaghi relationship and this explains the observed increase in effective pressure with rock depth in this field. Also, the increase in effective pressure with unconfined compressive strength is due to the fact that as rock depth increases, rock porosity decreases which effectively increases the strength and effective pressure of the rock unit. From the cross plots, the effective pressure was observed to decrease with increase

in porosity. This validates the assertion that an increase in pore pressure due to porosity increment reduces the effective pressure.

4.1.3.2 Fuja Field

Similarly, cross plots of rock elastic, inelastic and petrophysical properties as well as effective pressure for Fuja Field are shown in Figure 4.9(a-v) below. They also include cross plots between UCS and Poisson's ratio, UCS and shear modulus, UCS and sonic transit time, UCS and total porosity, UCS and measured depth, UCS and compressional wave velocity, UCS and shear wave velocity, UCS and volume of shale, UCS and Young's modulus, Young's modulus and depth, bulk modulus and compressional wave velocity, Poisson's ratio and total porosity, porosity and sonic transit time, UCS and effective porosity, UCS and permeability, effective pressure and depth, effective pressure and porosity, effective pressure and UCS, compressional wave velocity (V_P) and effective porosity, permeability and bulk density, UCS and bulk density, and finally shear wave velocity (V_S) and sonic transit time.

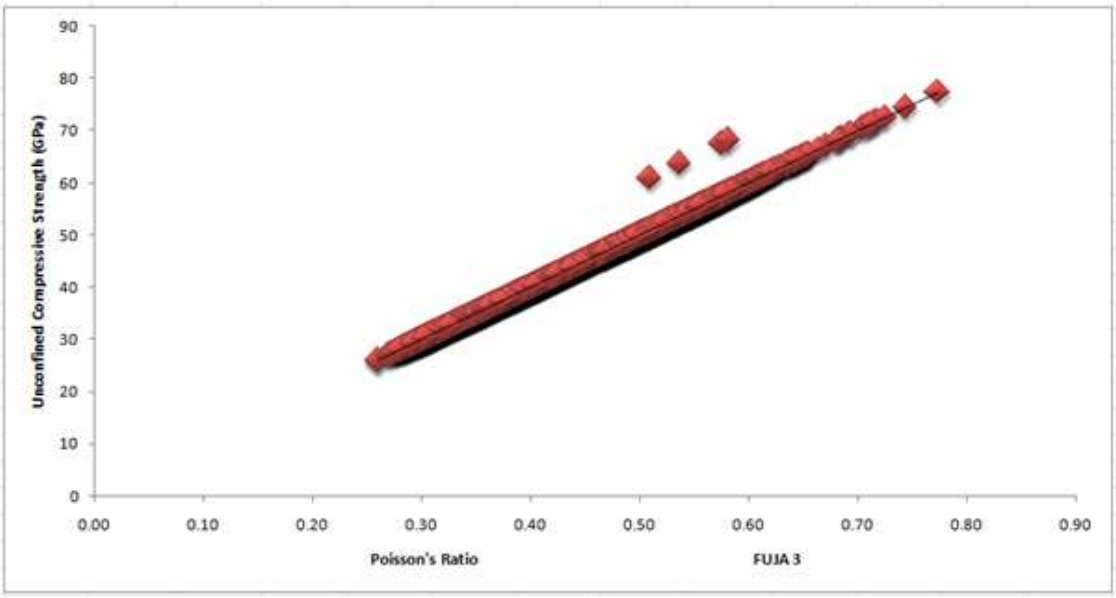


Fig. 4.9a: Cross plot showing trend line of unconfined compressive strength against Poisson's ratio for Fuja 3 well.

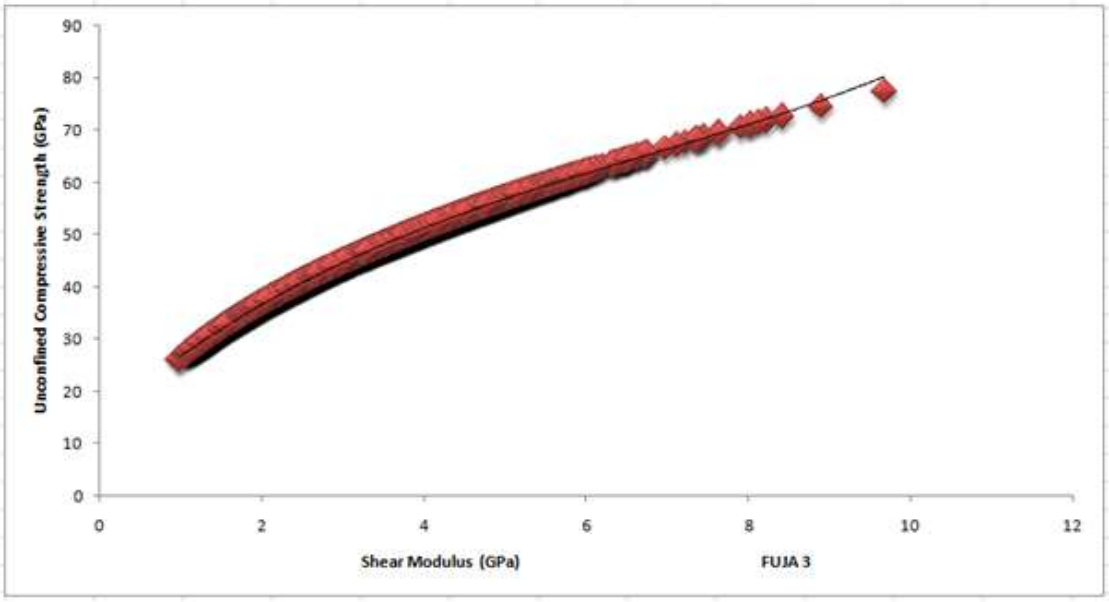


Fig. 4.9b: Cross plot showing trend line of unconfined compressive strength against shear modulus for Fuja 3 well.

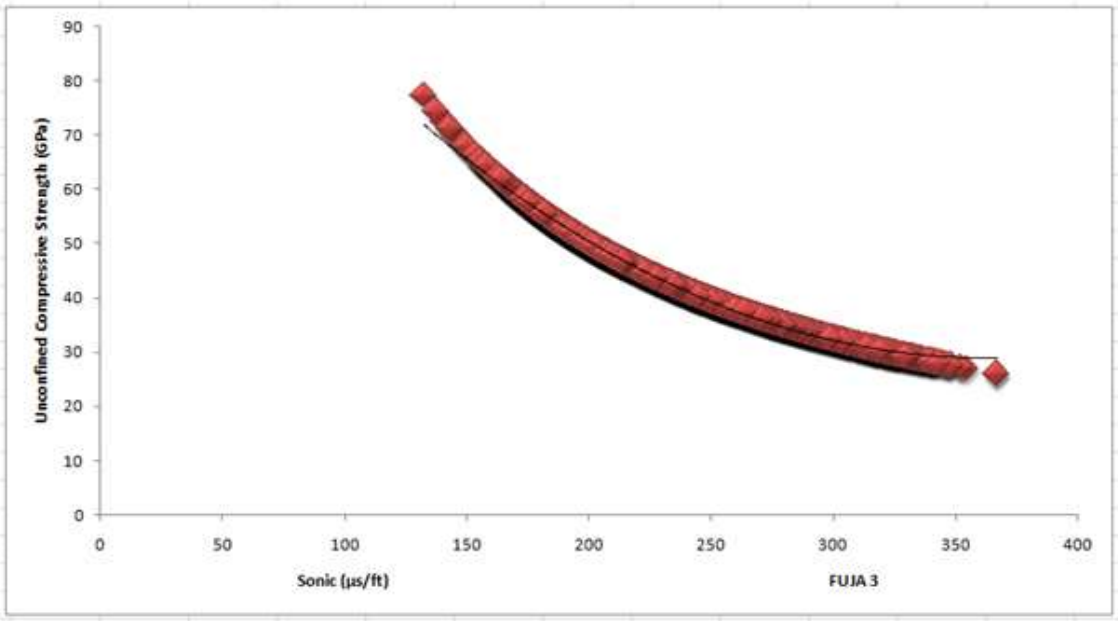


Fig. 4.9c: Cross plot showing trend line of unconfined compressive strength against sonic transit time for Fuja 3 well.

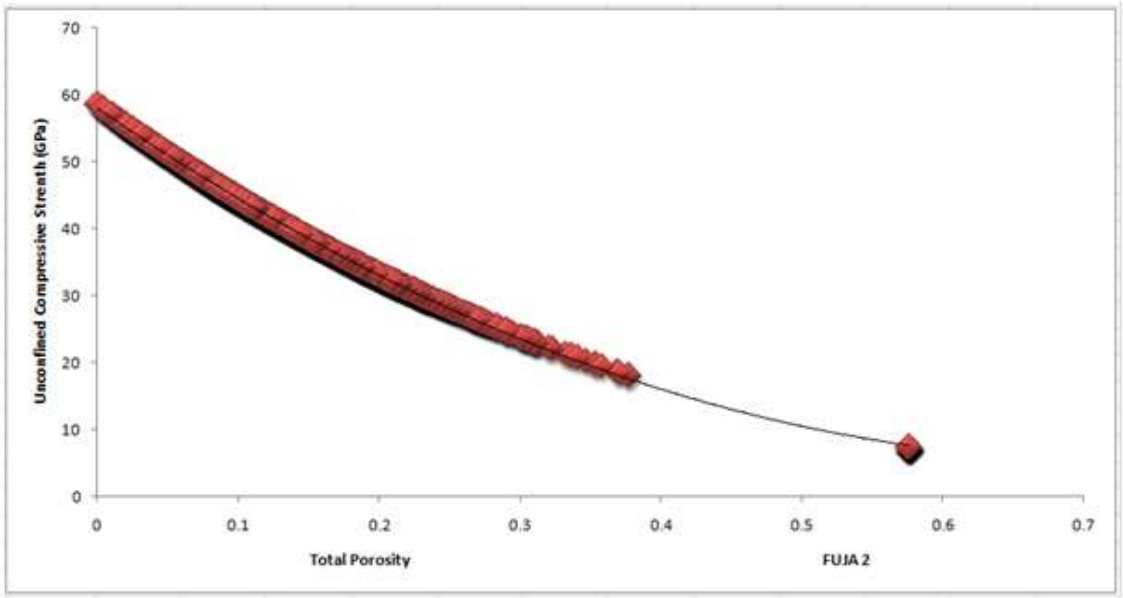


Fig. 4.9d: Cross plot showing trend line of unconfined compressive strength against total porosity for Fuja 2 well.

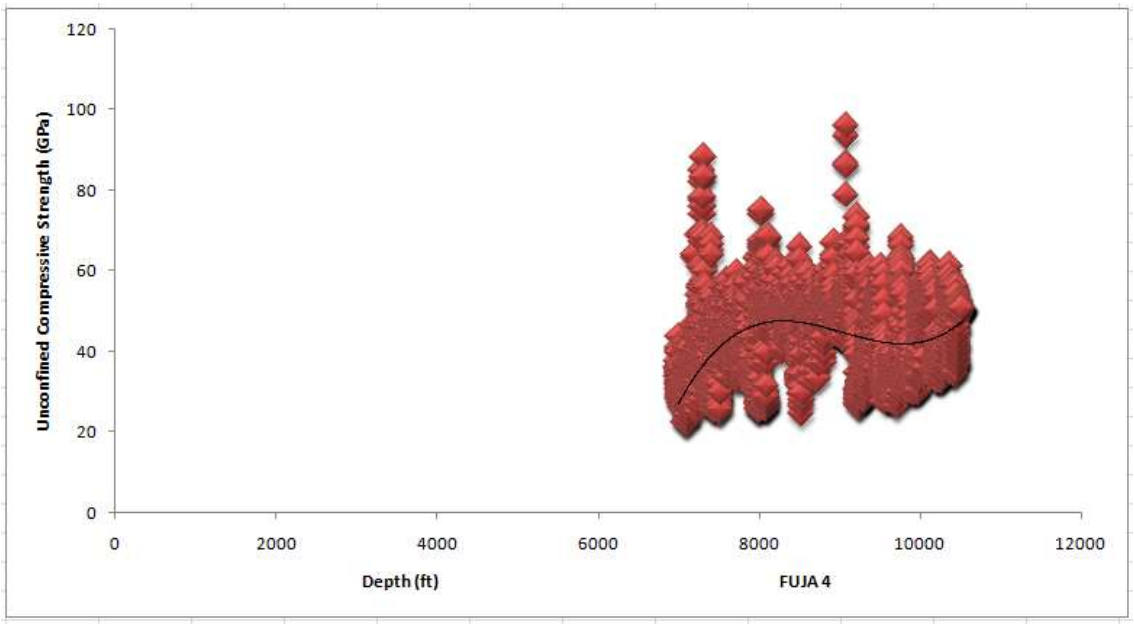


Fig. 4.9e: Cross plot showing trend line of unconfined compressive strength against measured depth for Fuja 4 well.

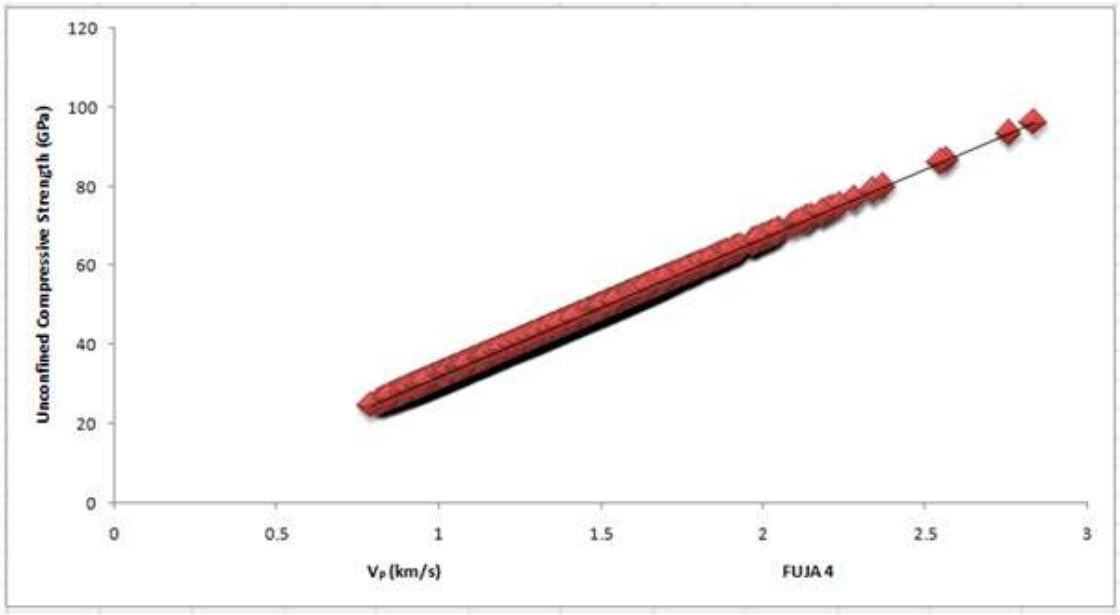


Fig. 4.9f: Cross plot showing trend line of unconfined compressive strength against compressional wave velocity (V_P) for Fuja 4 well.

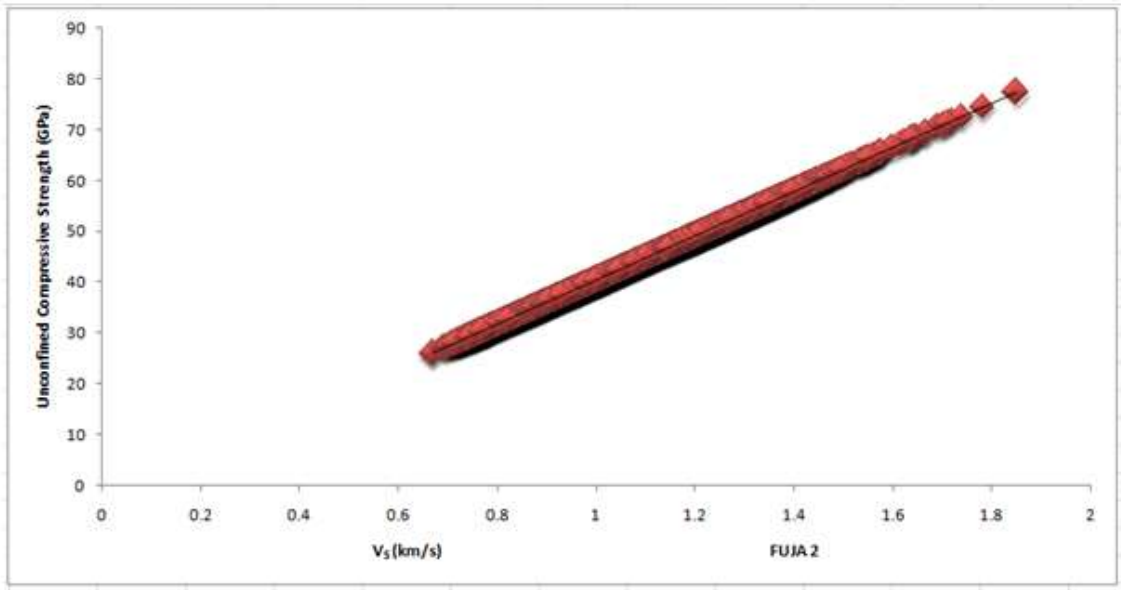


Fig. 4.9g: Cross plot showing trend line of unconfined compressive strength against shear wave velocity (V_S) for Fuja 2 well.

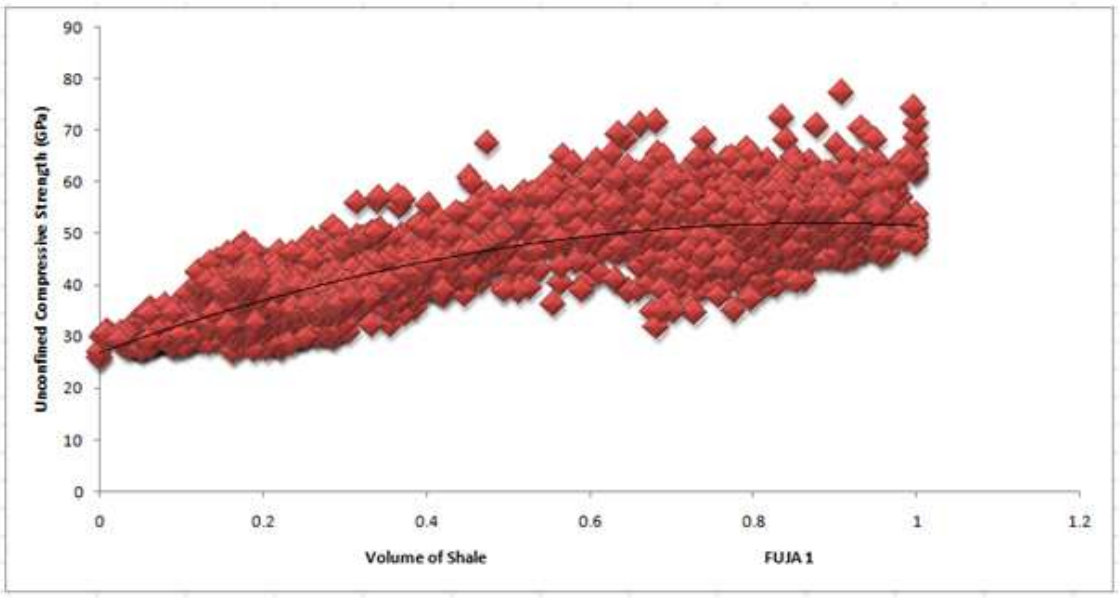


Fig. 4.9h: Cross plot showing trend line of unconfined compressive strength against volume of shale for Fuja 1 well.

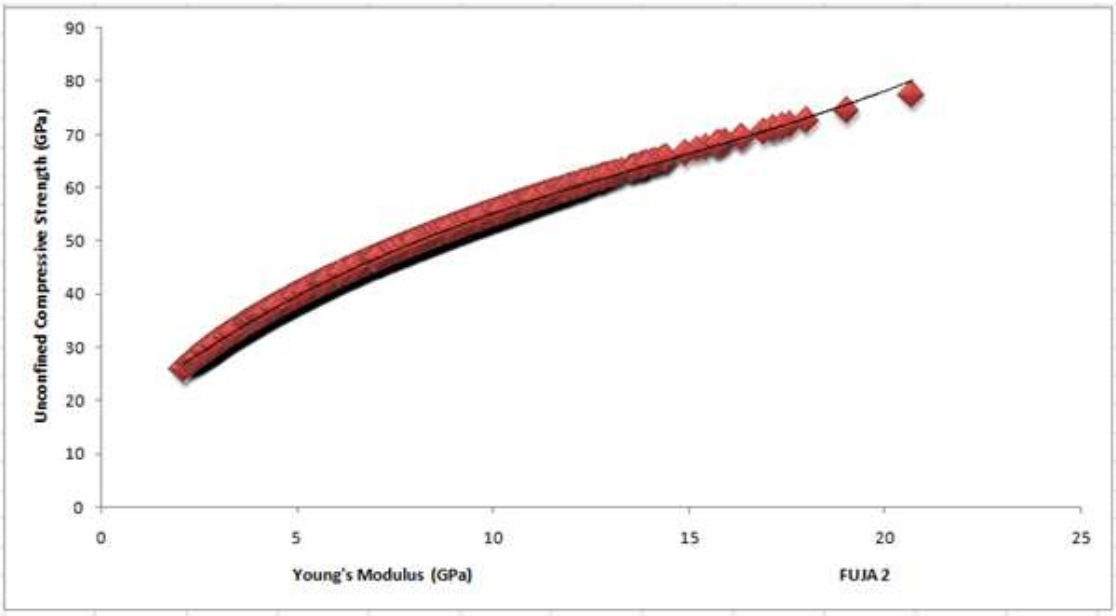


Fig. 4.9i: Cross plot showing trend line of unconfined compressive strength against Young's modulus for Fuja 2 well.

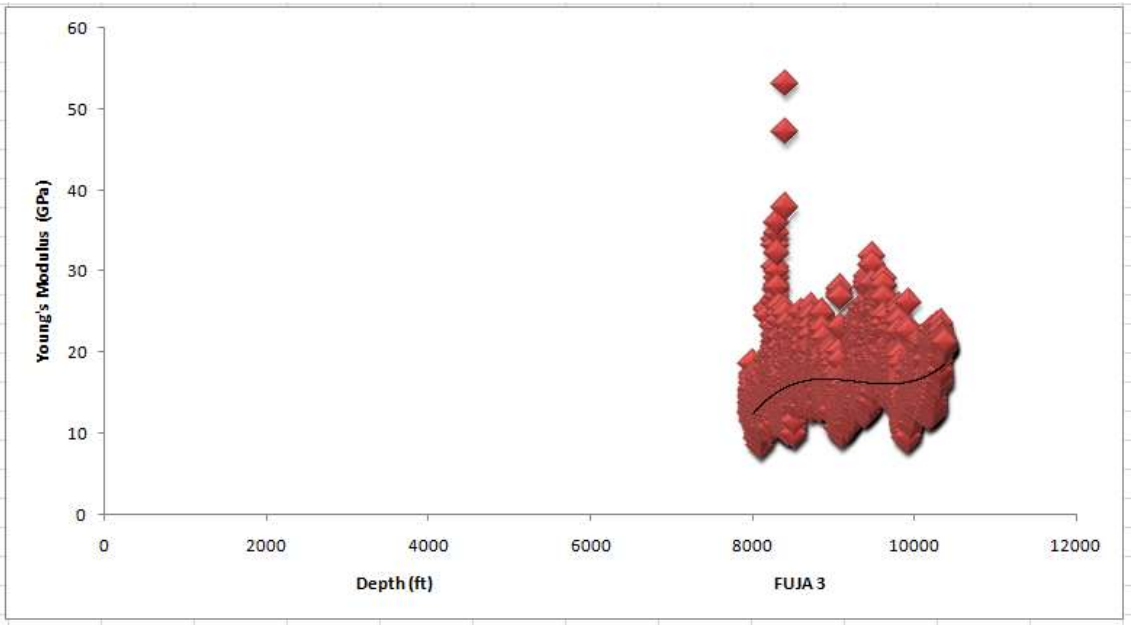


Fig. 4.9j: Cross plot showing trend line of Young's modulus against measured depth for Fuja 3 well.

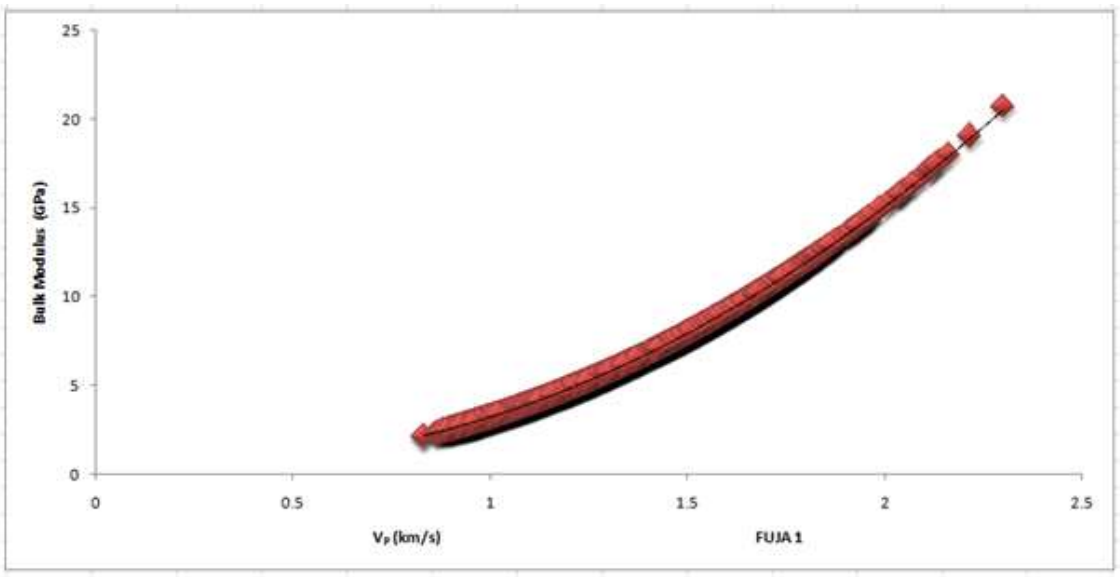


Fig. 4.9k: Cross plot showing trend line of bulk modulus against compressional wave velocity (V_P) for Fuja 1 well.

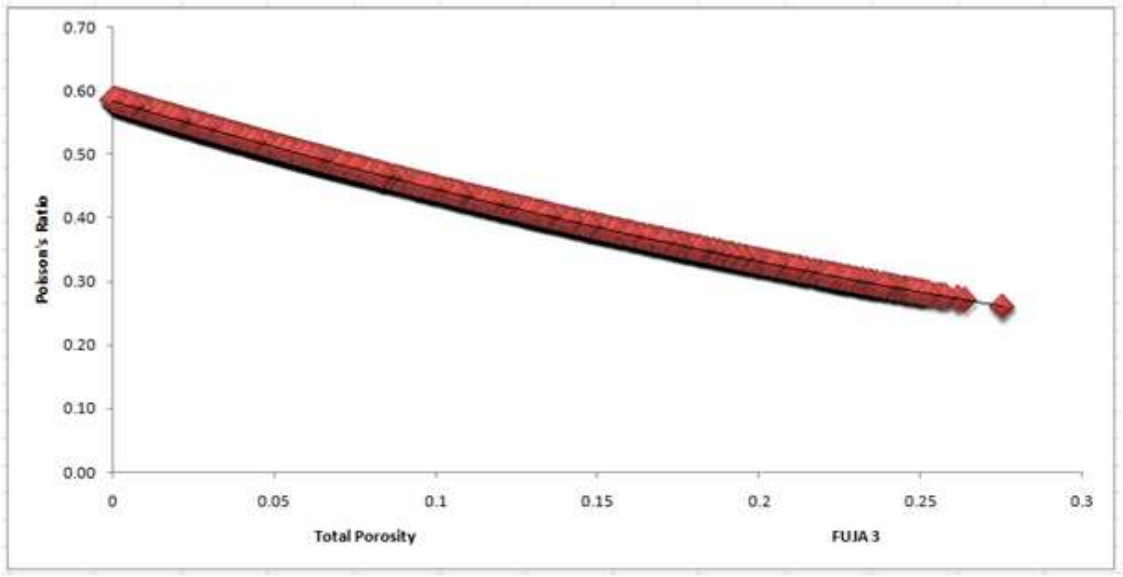


Fig. 4.9l: Cross plot showing trend line of Poisson's ratio against total porosity for Fuja 3 well.

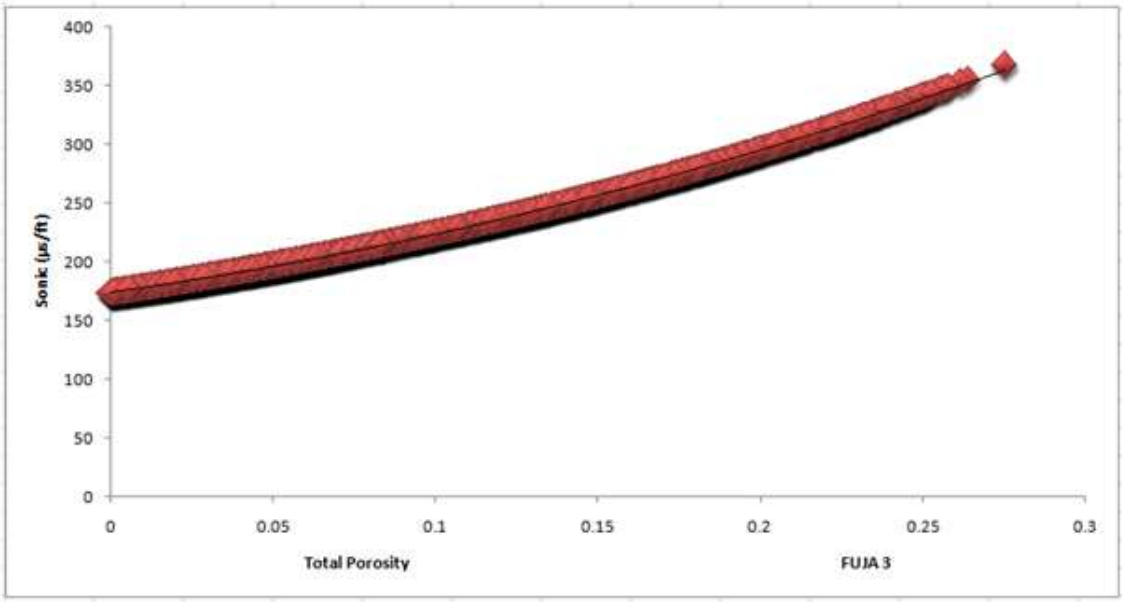


Fig. 4.9m: Cross plot showing trend line of sonic transit time against total porosity for Fuja 3 well.

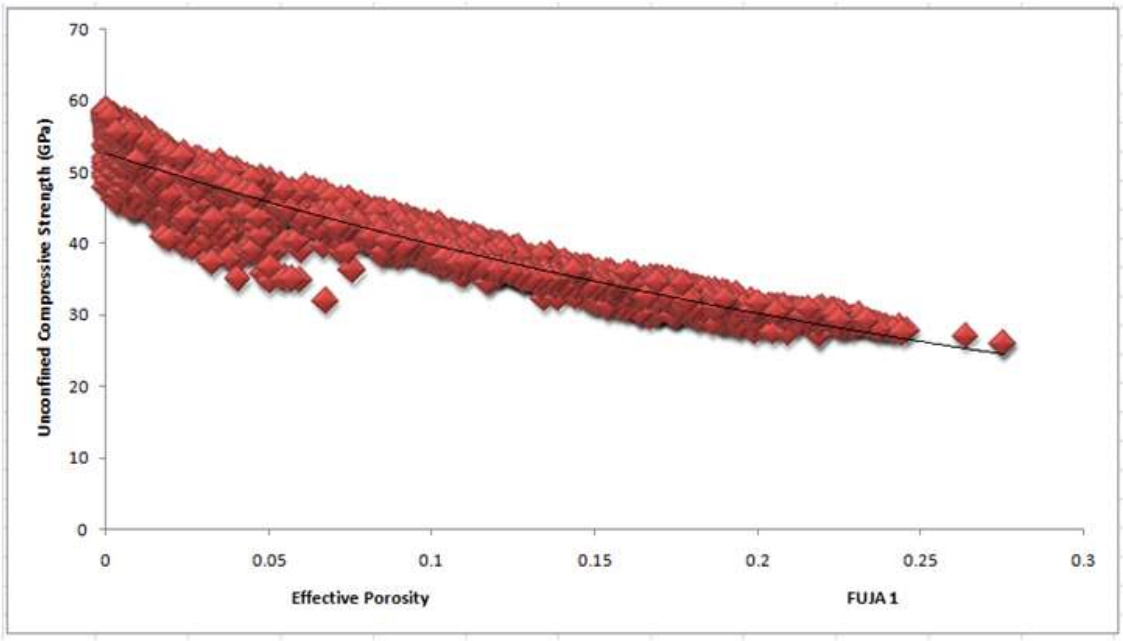


Fig. 4.9n: Cross plot showing trend line of unconfined compressive strength against effective porosity for Fuja 1 well.

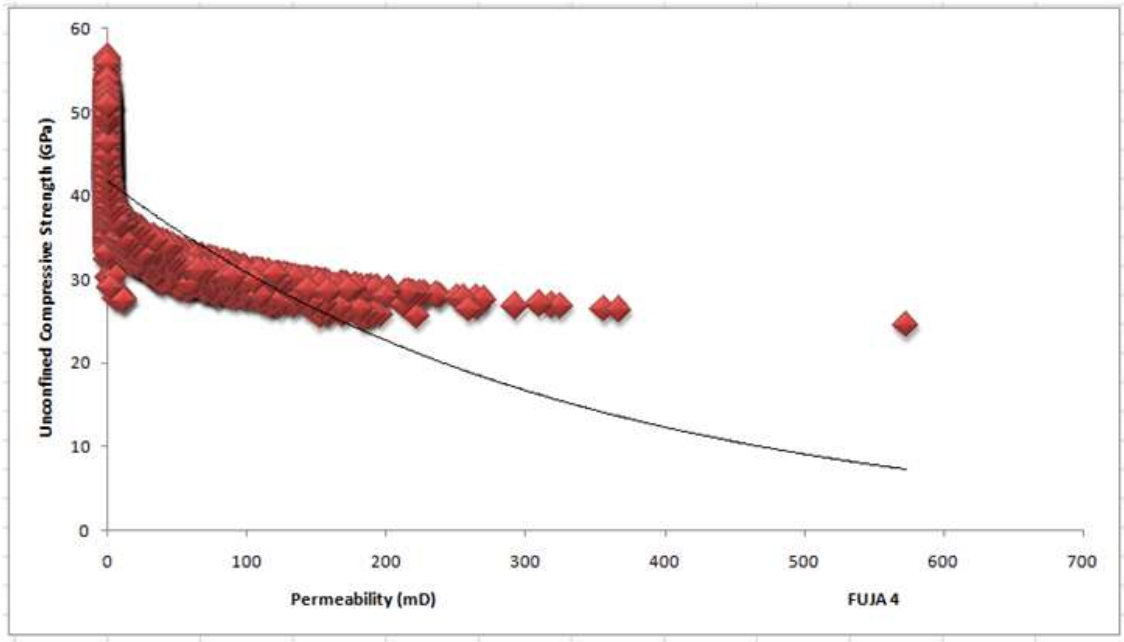


Fig. 4.9o: Cross plot showing trend line of unconfined compressive strength against permeability for Fuja 4 well.

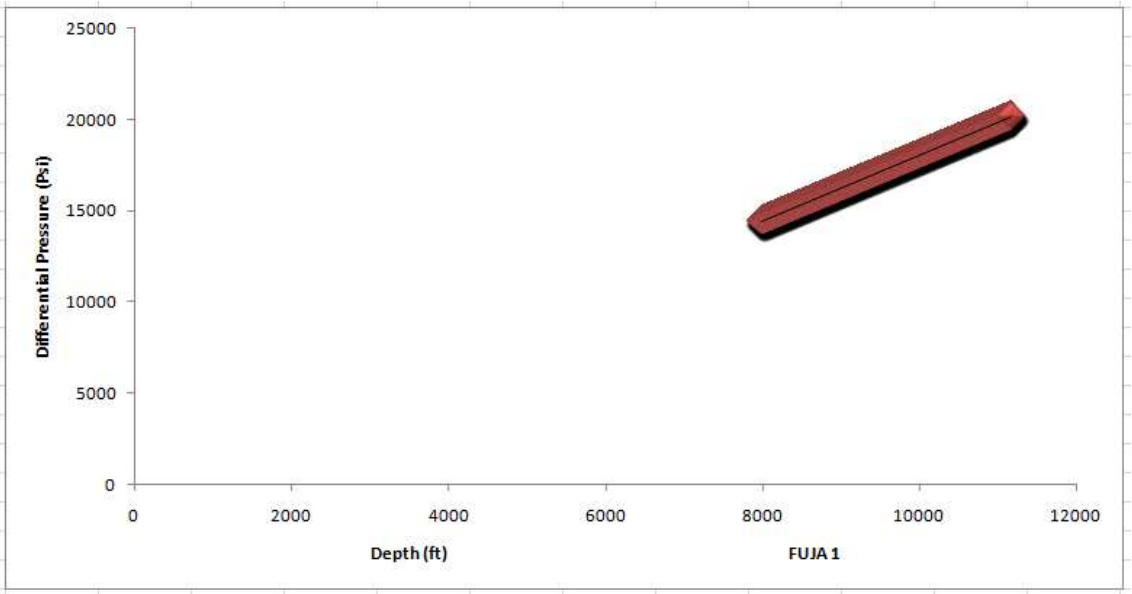


Fig. 4.9p: Cross plot showing trend line of Effective/differential pressure against measured depth for Fuja 1 well.

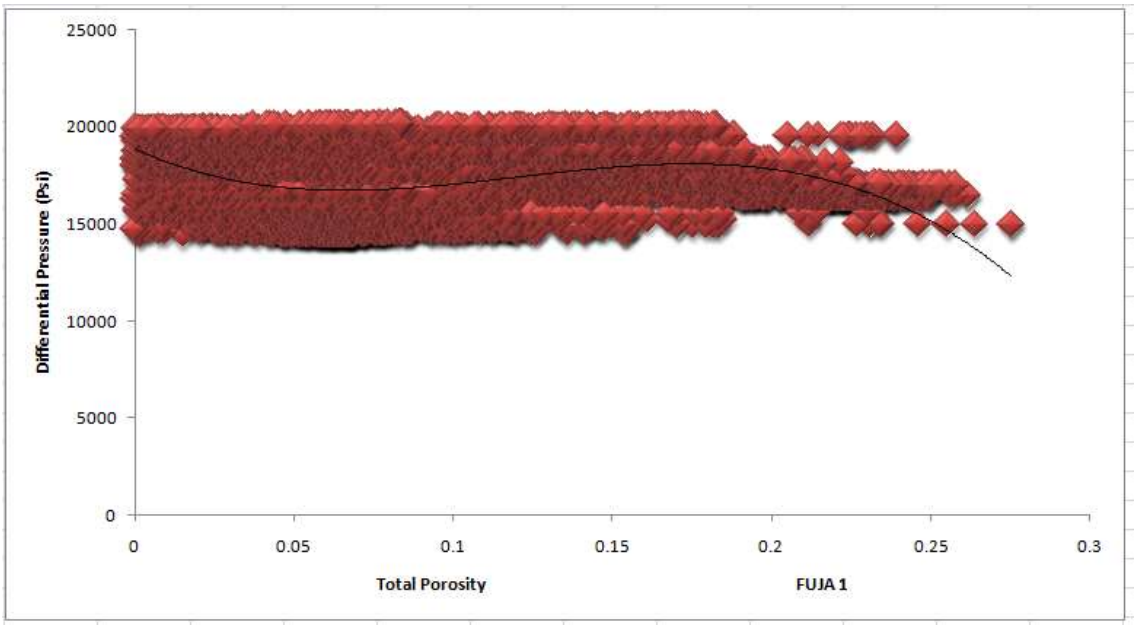


Fig. 4.9q: Cross plot showing trend line of Effective/differential pressure against total porosity for Fuja 1 well.

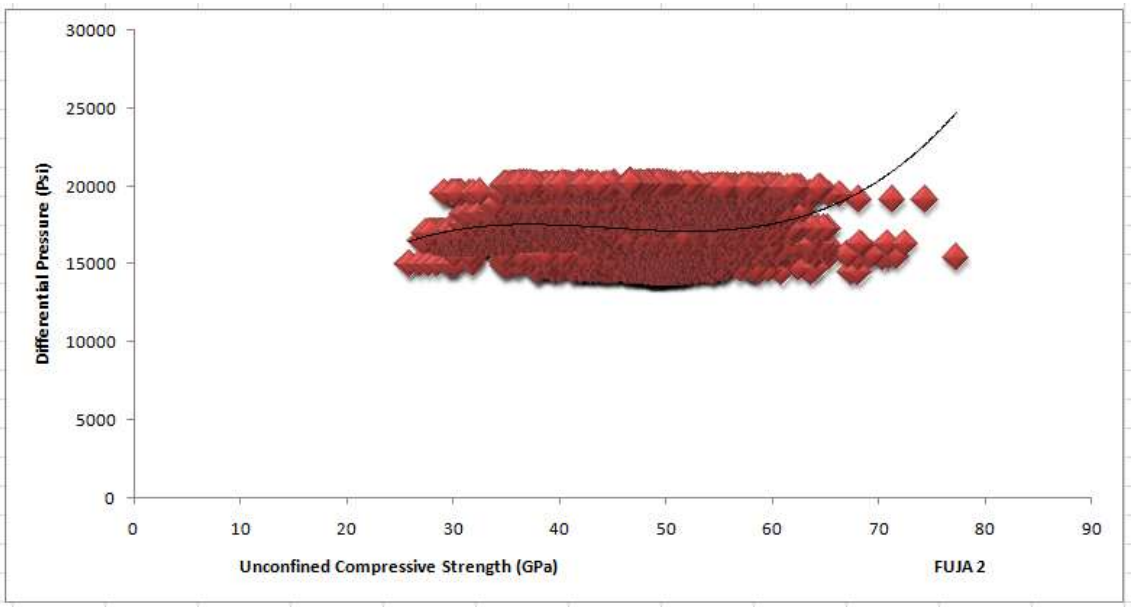


Fig. 4.9r: Cross plot showing trend line of Effective/differential pressure against unconfined compressive strength for Fuja 2 well.

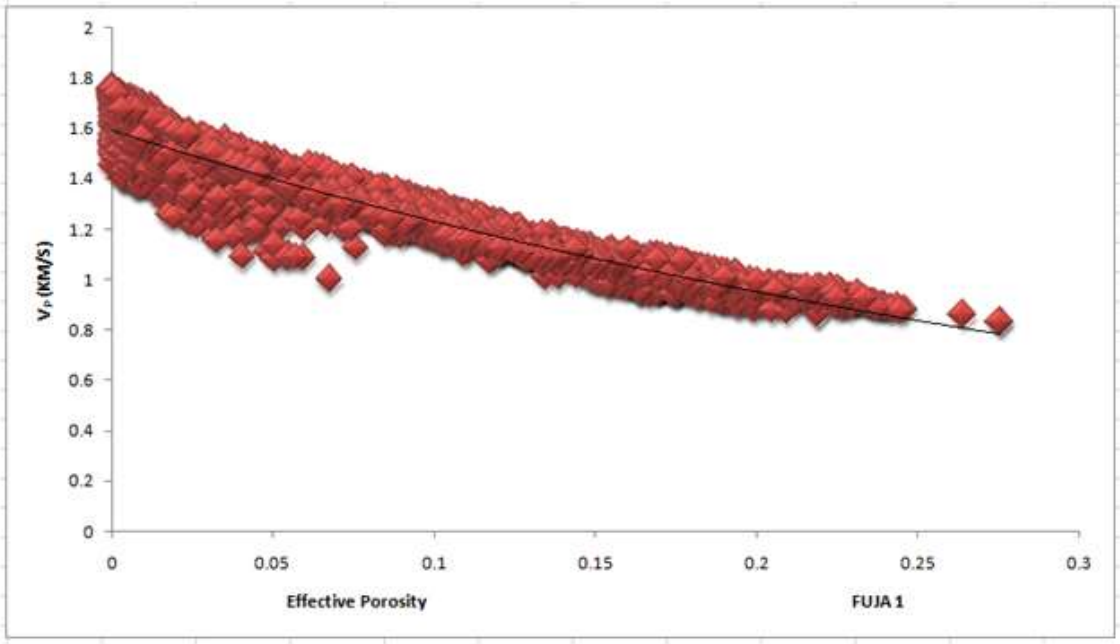


Fig. 4.9s: Cross plot showing trend line of compressional wave velocity against effective porosity for Fuja 1 well.

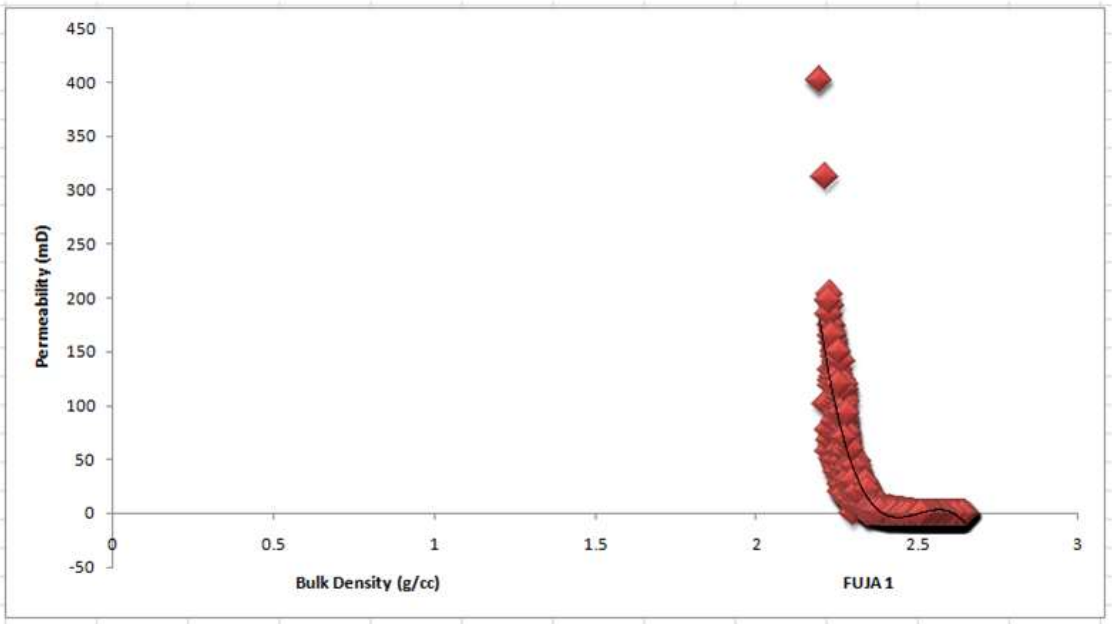


Fig. 4.9t: Cross plot showing trend line of permeability against bulk density for Fuja 1 well.

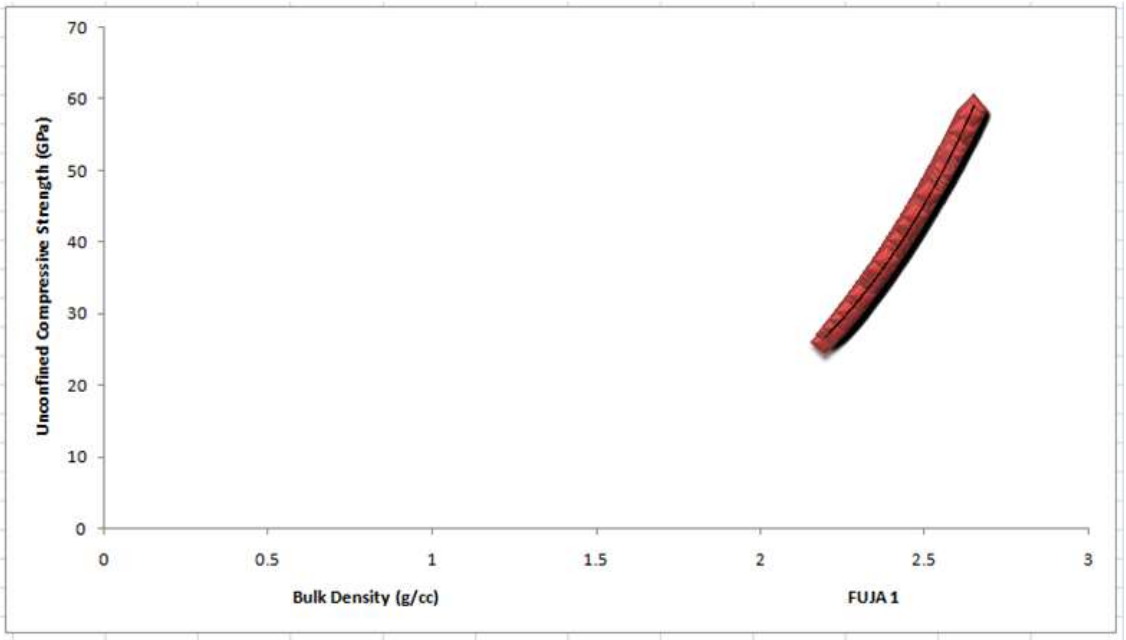


Fig. 4.9u: Cross plot showing trend line of unconfined compressive strength against bulk density for Fuja 1 well.

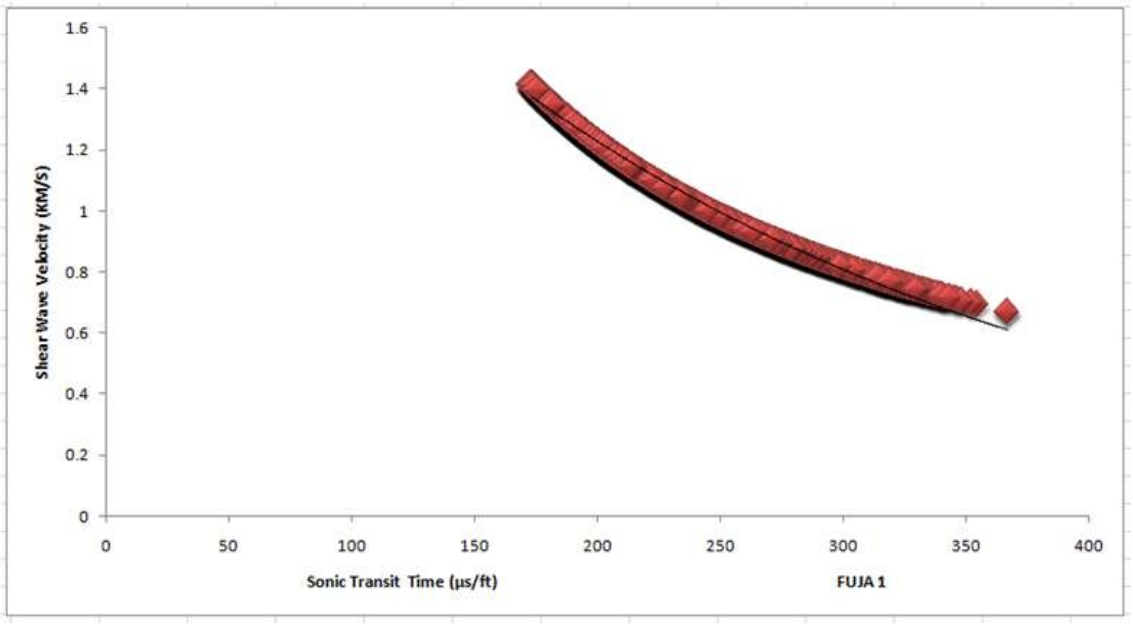


Fig. 4.9v: Cross plot showing trend line of shear wave velocity against sonic transit time for Fuja 1 well.

Results from the comparative analysis between the rock elastic, inelastic and petrophysical properties using cross plots in Fuja Field reveal a very strong connection between these rock properties. Just as observed in Beta Field, there is a clear increase in unconfined compressive strength of the reservoir rock with the elastic properties, depth and volume of shale which indicates that as the values of the elastic rock properties, rock depth, and shaliness increases the rock strength also increases. The overall implication of this is that the compaction and elasticity of a rock unit goes a long way in determining the strength and ductility of that rock. An increase in the compaction and elasticity of a rock increases its strength and ductility.

The cross plots also revealed that the unconfined compressive rock strength and by extension the elastic rock properties decreases with increase in petrophysical properties of total and effective porosity as well as permeability. This is clearly an indication that pore spaces contained within a rock unit reduces the overall strength of that rock thereby making the rock to be easily deformed and prone to failure when subjected to pressure. A rock unit characterized by very high porosity will yield rapidly to deformation than a rock unit

characterized by low porosity when exposed to the same stress condition. These results also validate the assertion that there is a connection between rock elastic parameters, depth, and unconfined compressive strength by Wong & David (1997) and Horsrud (2001).

Results of the cross plots between effective pressure and depth as well as effective pressure and unconfined compressive rock strength reveal that effective pressure increases with rock depth and unconfined compressive strength. As rock depth increases, porosity decreases thereby effectively decreasing the pore pressure within the rock unit (Okeke, 2010). From Terzaghi pressure relationship; this decrease in pore pressure increases the effective pressure within the rock and this explains the observed increase in effective pressure with depth in this field. Similarly, decrease in porosity of a rock increases the overall strength of that rock. This explains the increase in effective pressure with unconfined compressive strength. The cross plot also revealed that the effective pressure decreases with increase in porosity validating the assertion that an increase in pore pressure due to porosity increment reduces the effective pressure.

4.1.4 3D Geomechanical Models

3D geomechanical earth models representing the spatial distribution of the mechanical rock properties of the studied reservoir rocks were generated and variations in rock strength across the reservoir top were identified for the two fields under investigation. The models generated include Young's modulus model, Poisson's ratio model, bulk modulus model, shear modulus model, unconfined compressive strength model and bulk compressibility model.

4.1.4.1 Beta Field

The generated geomechanical earth models for Beta Field are presented in figure 4.10(a-f) below.

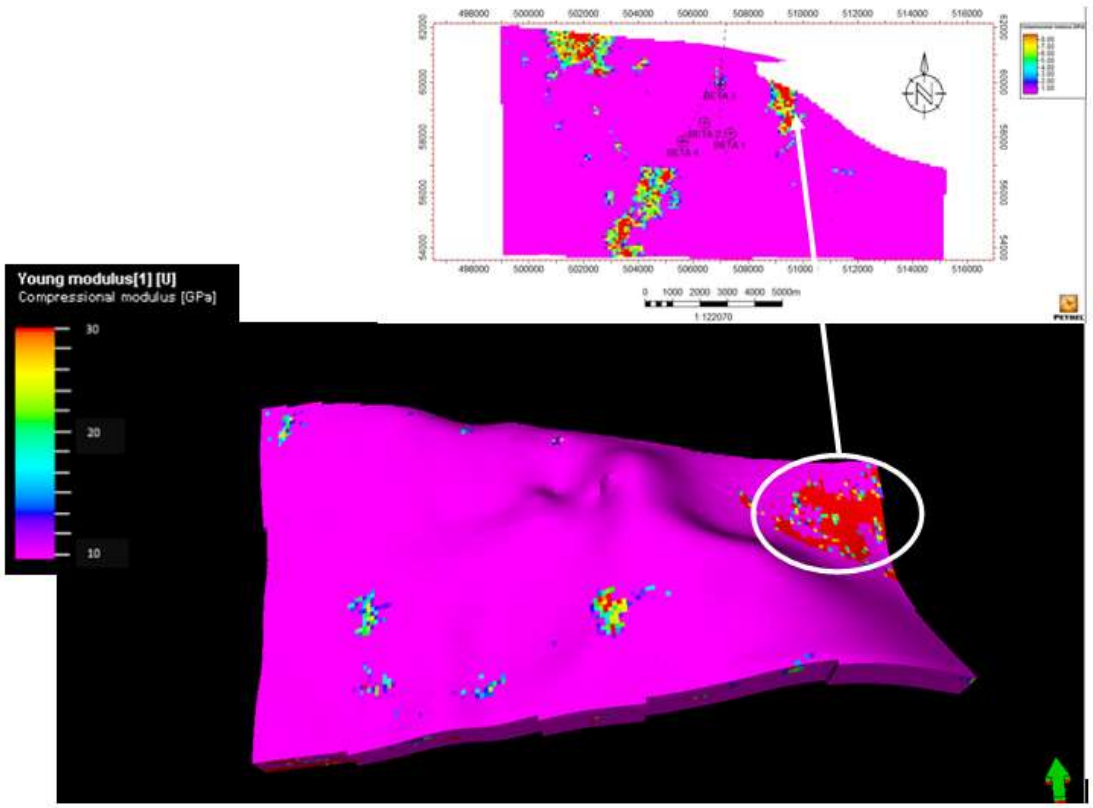


Fig. 4.10a: 3D geomechanical model with inserted map showing the spatial distribution of Young's modulus across the Beta reservoir top.

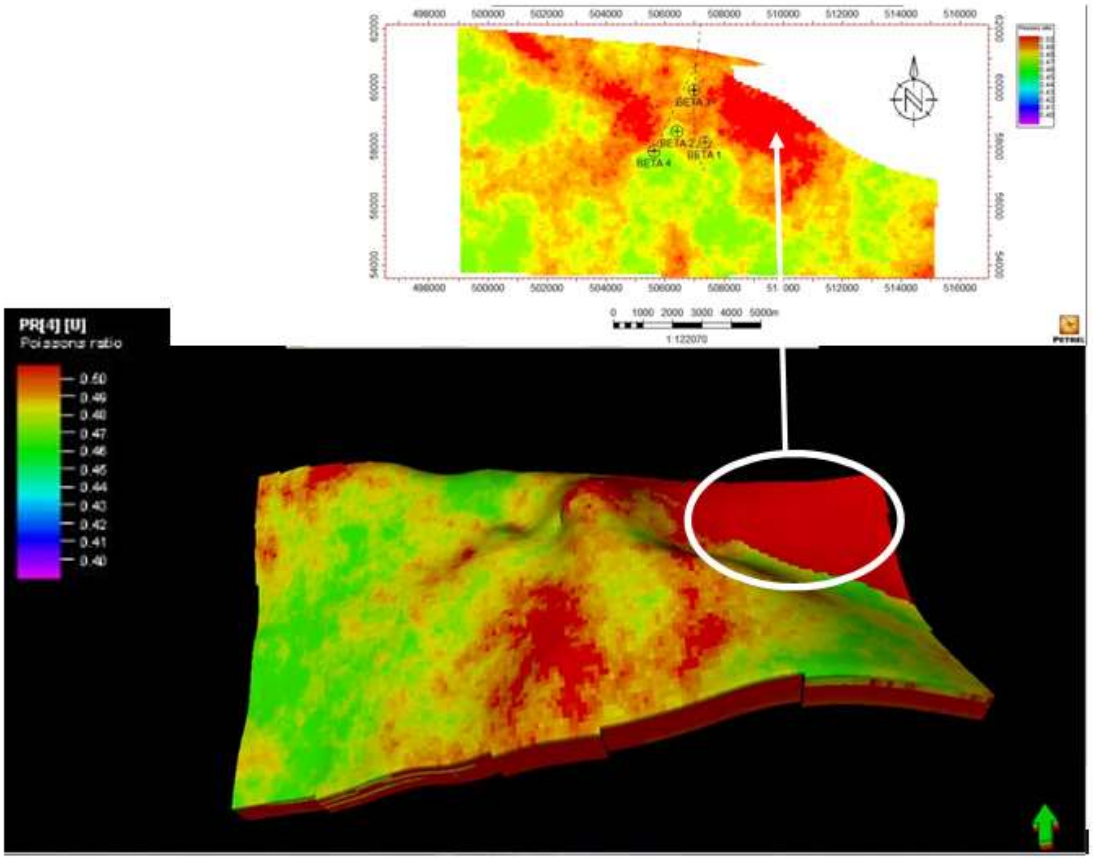


Fig. 4.10b: 3D geomechanical model with inserted map showing the spatial distribution of Poisson's ratio across the Beta reservoir top.

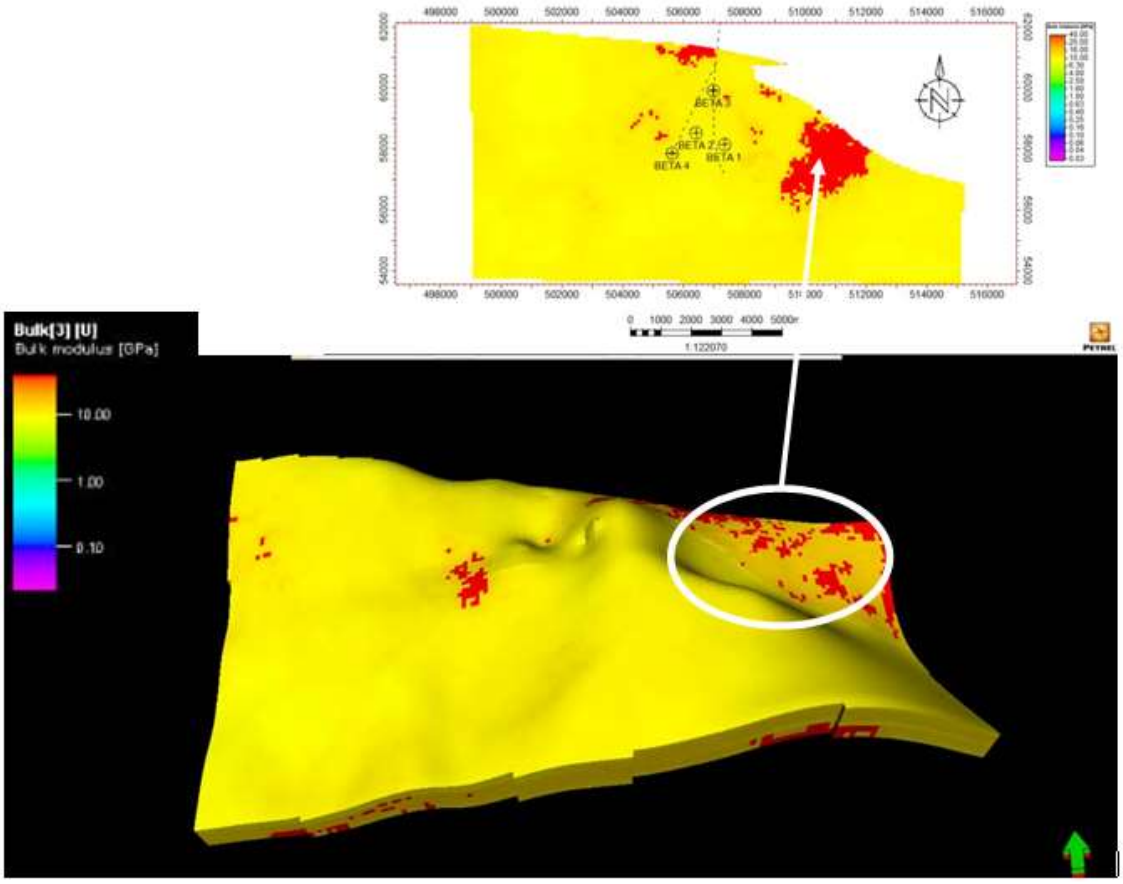


Fig. 4.10c: 3D geomechanical model with inserted map showing the spatial distribution of bulk modulus across the Beta reservoir top.

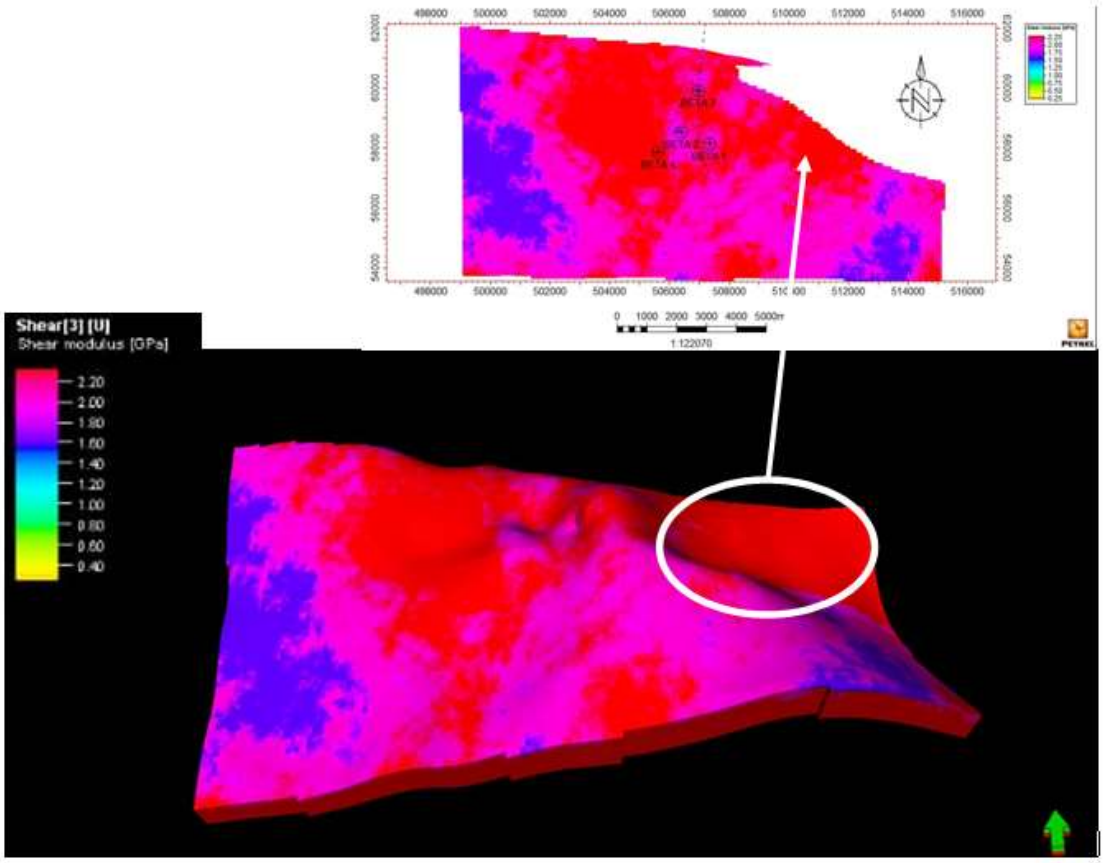


Fig. 4.10d: 3D geomechanical model with inserted map showing the spatial distribution of shear modulus across the Beta reservoir top.

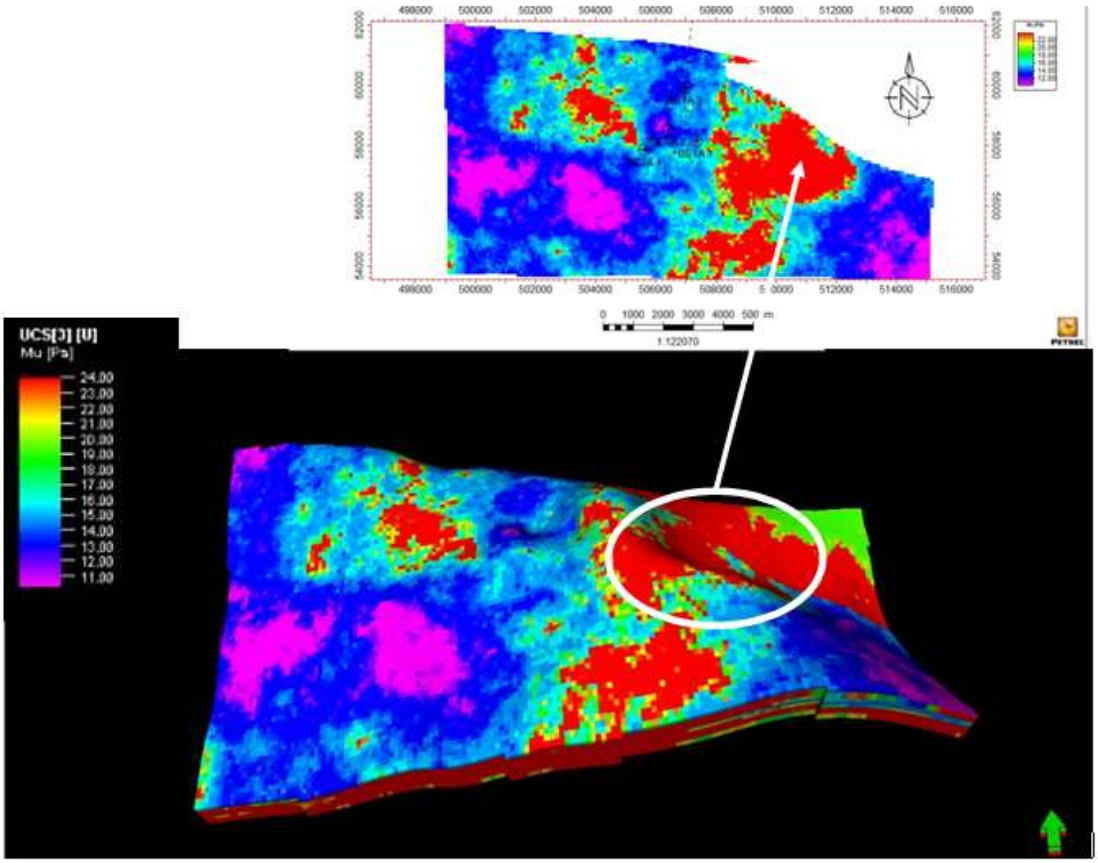


Fig. 4.10e: 3D geomechanical model with inserted map showing the spatial distribution of unconfined compressive strength across the Beta reservoir top.

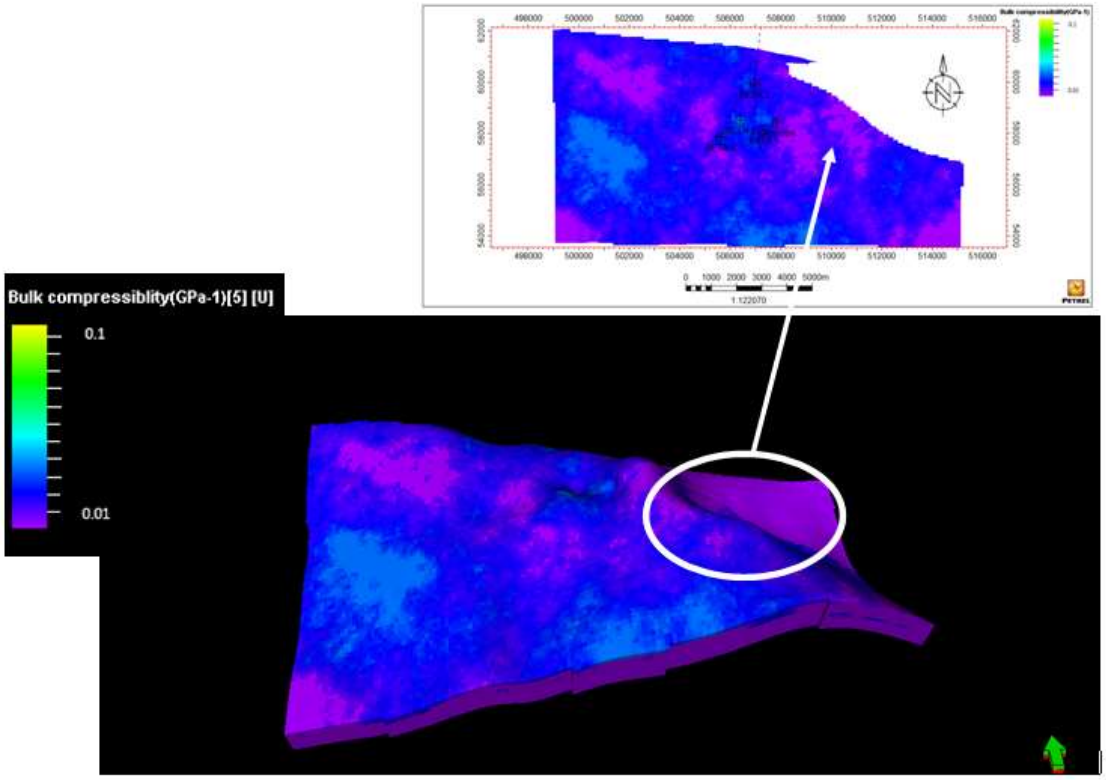


Fig. 4.10f: 3D geomechanical model with inserted map showing the spatial distribution of bulk compressibility across the Beta reservoir top.

3D geomechanical models were generated for rock elastic parameters of Young's modulus, bulk modulus, shear modulus, Poisson's ratio and bulk compressibility, and rock inelastic parameter of unconfined compressive strength. Considering the generated 3D geomechanical models of the studied reservoir, it can be observed from the inserted legends that all the rock elastic and inelastic parameters revealed higher values around the north-northeastern (NNE) portion of the field. This implies that mechanical rock deformation or failure during well drilling, exploitation, and hydraulic fracturing or fluid injection will be low in this section of the field compared to other sections. This section represents more stable rock units within Beta Field than other sections.

4.1.4.2 Fuja Field

The generated geomechanical earth models for Fuja Field are presented in figure 4.11(a-f) below.

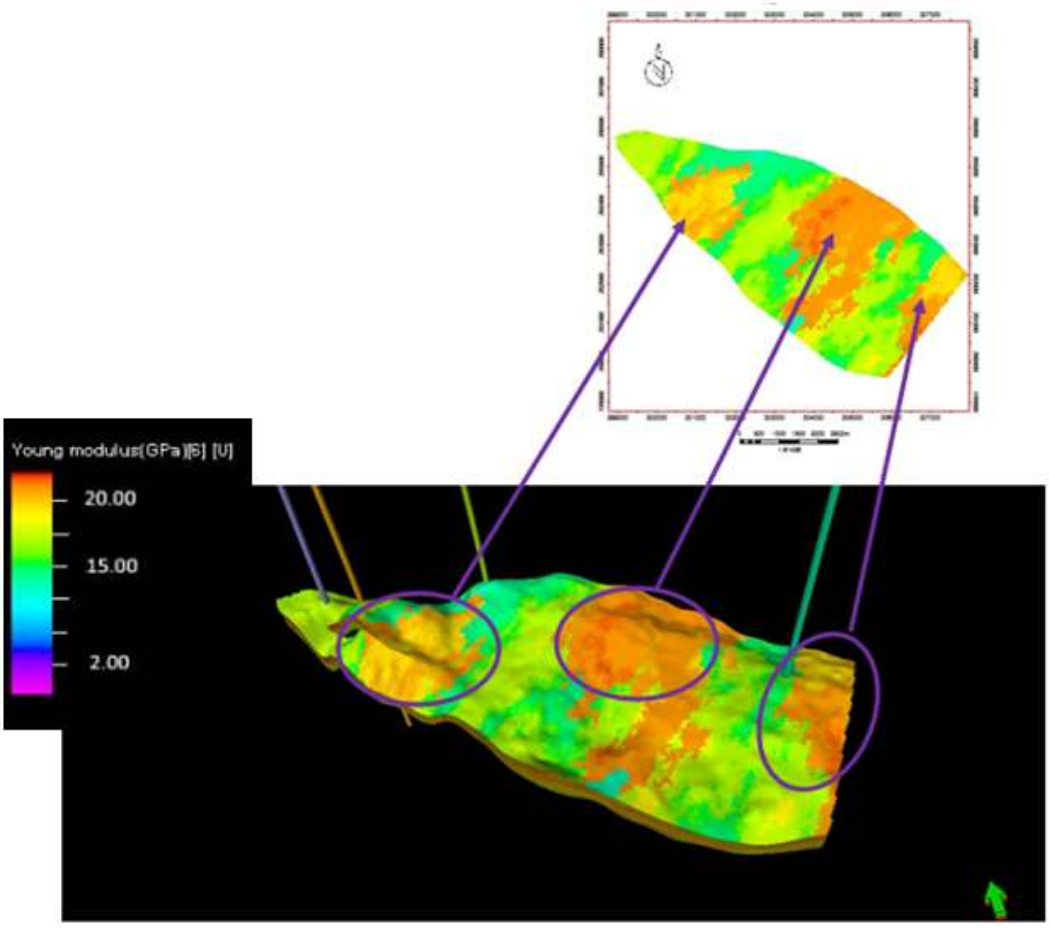


Fig. 4.11a: 3D geomechanical model with penetrated wells and inserted map showing the spatial distribution of Young's modulus across the Fuja reservoir top.

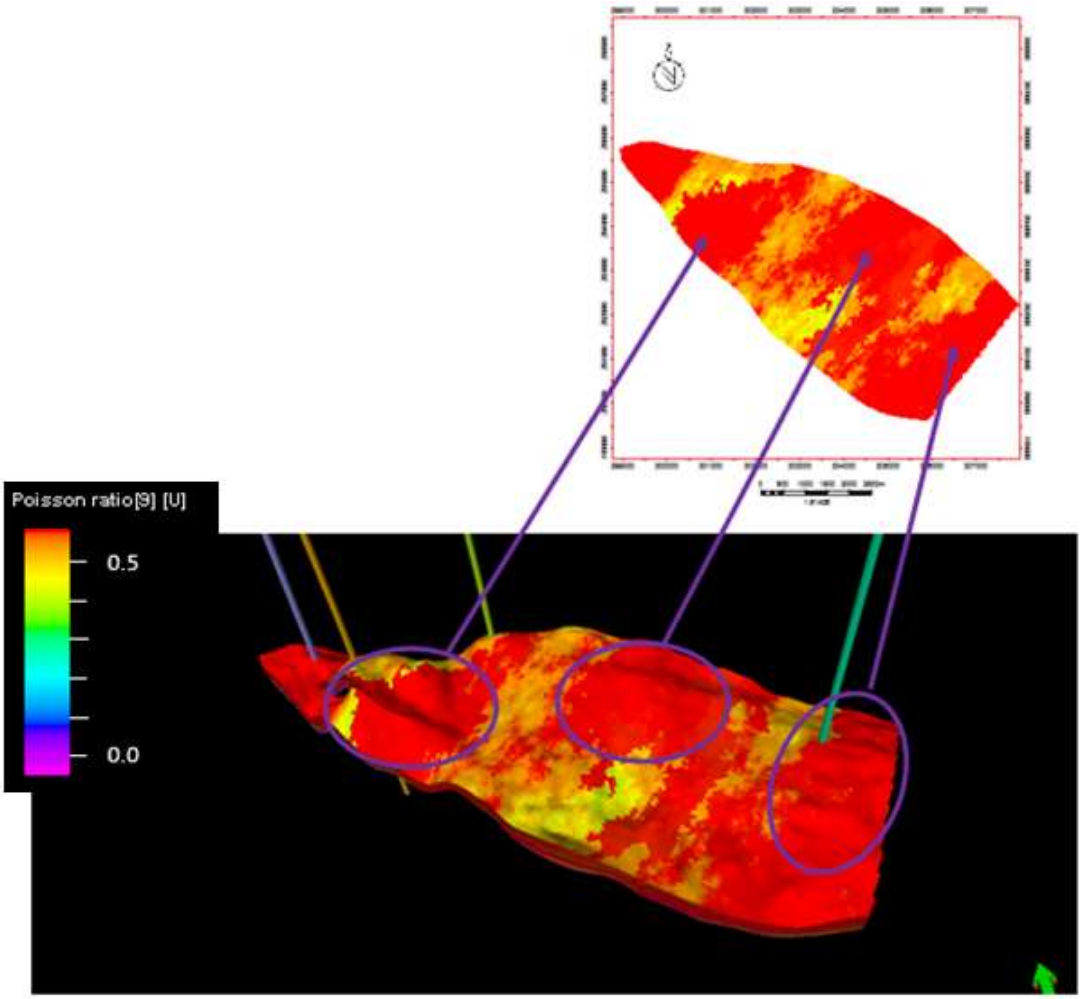


Fig. 4.11b: 3D geomechanical model with penetrated wells and inserted map showing the spatial distribution of Poisson's ratio across the Fuja reservoir top.

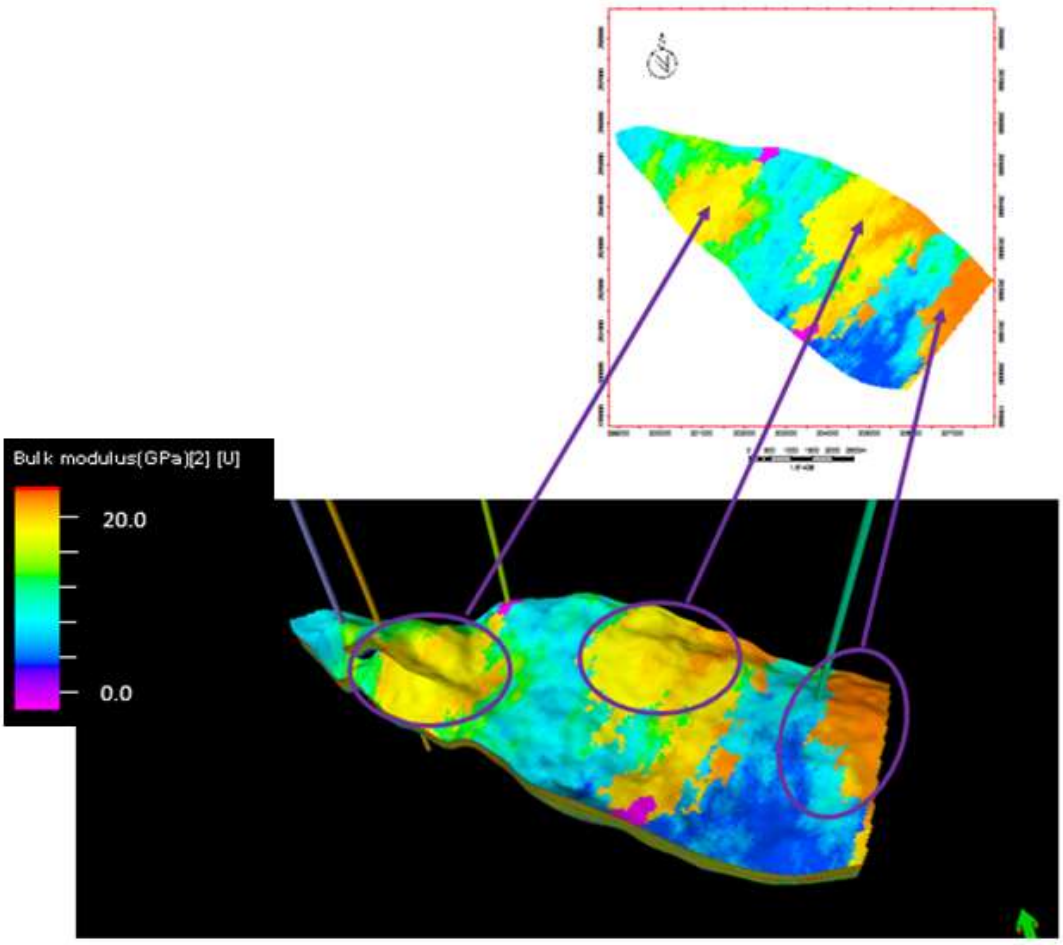


Fig. 4.11c: 3D geomechanical model with penetrated wells and inserted map showing the spatial distribution of bulk modulus across the Fuja reservoir top.

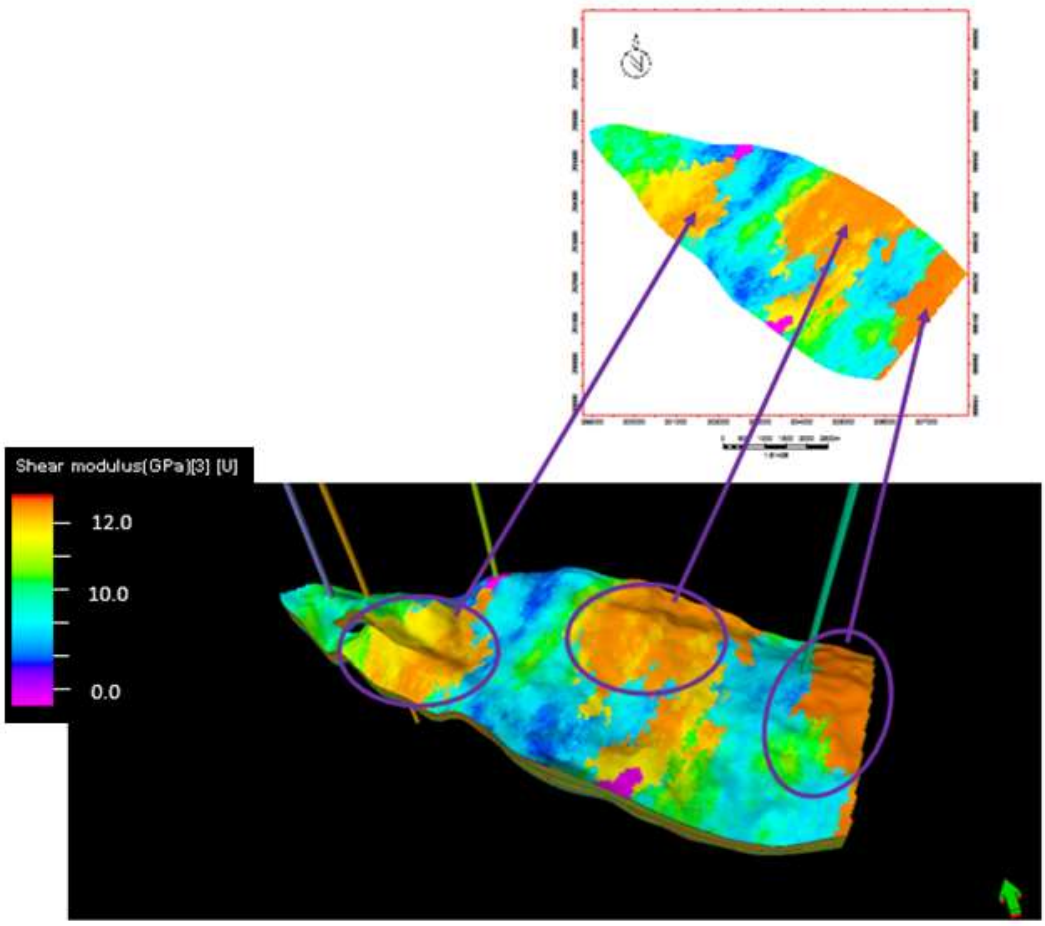


Fig. 4.11d: 3D geomechanical model with penetrated wells and inserted map showing the spatial distribution of shear modulus across the Fuja reservoir top.

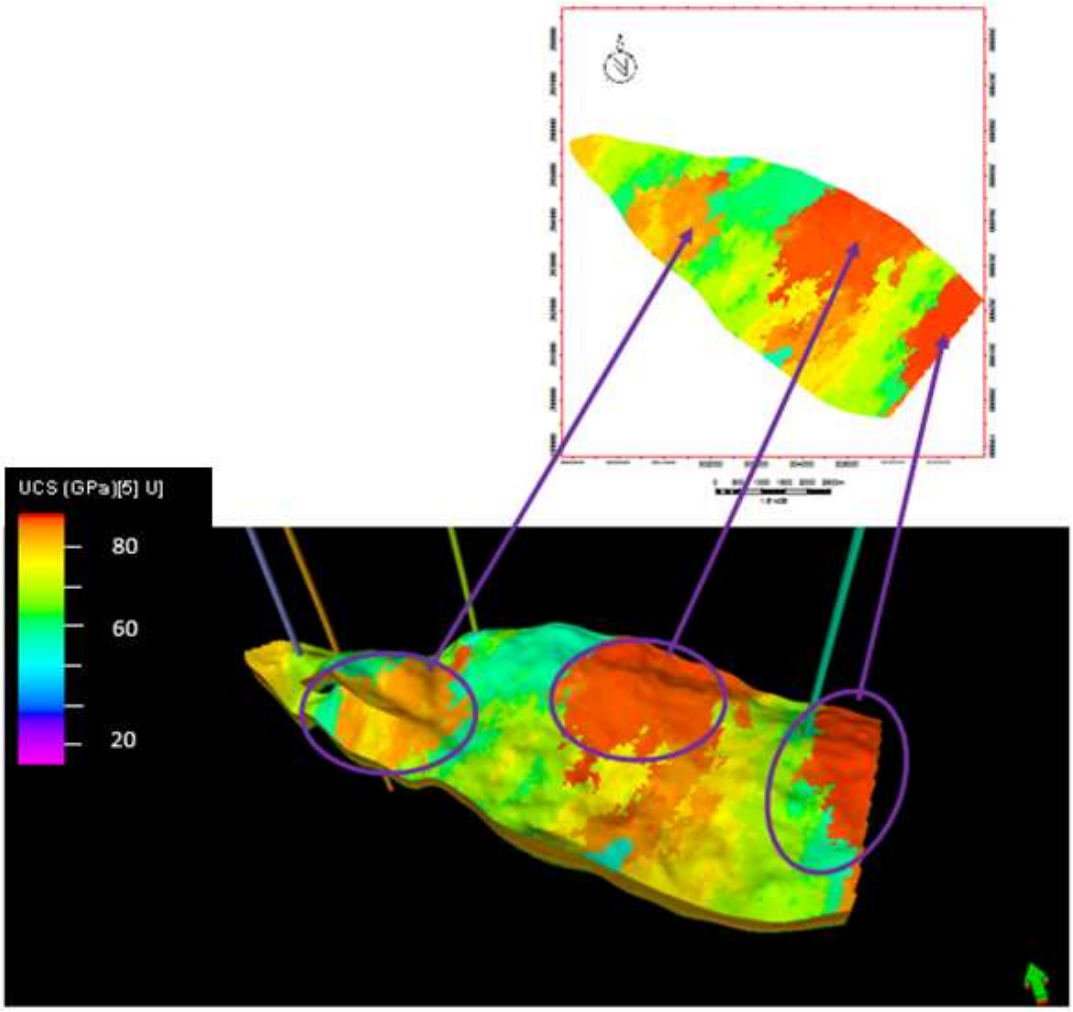


Fig. 4.11e: 3D geomechanical model with penetrated wells and inserted map showing the spatial distribution of unconfined compressive strength across the Fuja reservoir top.

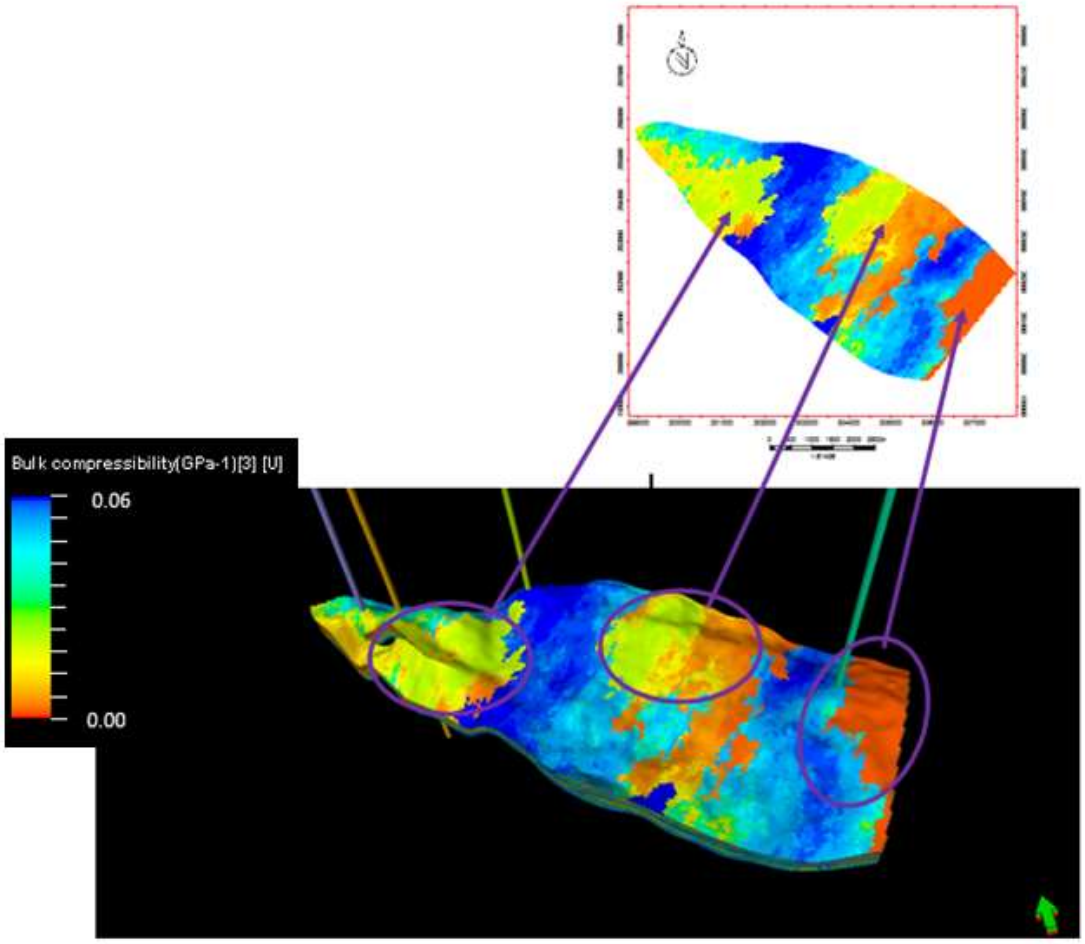


Fig. 4.11f: 3D geomechanical model with penetrated wells and inserted map showing the spatial distribution of bulk compressibility across the Fuja reservoir top.

For Fuja Field, 3D geomechanical models were also generated for rock elastic parameters of Young's modulus, bulk modulus, shear modulus, Poisson's ratio and bulk compressibility, and rock inelastic parameter of unconfined compressive strength. Considering the generated 3D geomechanical models of the studied reservoir, it can be observed from the inserted legends that all the rock elastic and inelastic parameters revealed higher values around the northeastern (NE) and parts of the eastern and western portions of the field. This implies that mechanical rock deformation or failure during well drilling, exploitation, and hydraulic fracturing or fluid injection will be minimized in these sections of the Field compared to other sections. These sections represent more stable rock units within the Fuja Field than other sections.

4.1.5 Comparative Assessment of Geomechanical Characteristics of Beta and Fuja Reservoirs

The comparative analysis of the geomechanical characteristics and other results, including rock elastic properties, inelastic properties, petrophysical properties, pore and effective pressures, interrelationship between these rock properties, and geomechanical models, obtained in the two fields under investigation are presented in this section. They are similarly presented under the subheadings of reservoir delineation; rock elastic and inelastic properties, petrophysical properties and effective pressure; cross plots of rock elastic properties, inelastic properties, petrophysical properties and effective pressure; and 3D geomechanical models.

4.1.5.1 Reservoir Delineation

By initially identifying surfaces of interest in the four Beta wells namely Beta 1, Beta 2, Beta 3 and Beta 4, and the four Fuja wells namely Fuja 1, Fuja 2, Fuja 3, and Fuja 4, reservoir delineation and correlation was done using gamma ray and sonic logs. Results of this delineation show that Beta reservoirs fell between a depth of 8,860ft and 10,220ft in the central part of the field while for Fuja Field, the reservoirs fell between 9,100ft and 9,860ft also around the central portion of the field. This shows that the reservoirs of Beta Field have a thickness of 1,360ft while those of Fuja Field have a thickness of 760ft implying that Beta Field reservoirs are thicker than Fuja Field reservoirs. Also, considering the litho-logs of the four Beta wells and those of the four Fuja wells as shown in figures 25 and 26, it can be seen that sand/shale ratio is higher in the reservoir of Beta Field than that of Fuja Field. This is possibly due to the fact that the fields are apart and as such cannot have exact profiles due to variations in sedimentation.

4.1.5.2 Rock Elastic, Inelastic and Petrophysical Properties, Pore and Effective Pressures, Total Vertical Stress, Maximum and Minimum Horizontal Stresses

Analysis of the values of rock elastic and inelastic properties obtained in this study for the two fields under investigation show that the values of Young's modulus, bulk modulus, shear modulus, and bulk compressibility are higher in the rock units (both sand and shale) of Beta reservoirs than the rock units of Fuja reservoirs. This is clearly shown by the obtained average values of these parameters from those fields as presented in tables 2 and 4. From these tables, the average values of Young's modulus in Beta and Fuja reservoir sands are 10.94 GPa and 5.11GPa respectively, while in Beta and Fuja reservoir shales it is respectively 13.70 GPa and 6.08 GPa. For bulk modulus, the average values are 12.76 GPa and 5.10 GPa for Beta and Fuja reservoir sands, while 13.30 GPa and 6.09 Gpa were recorded for Beta and Fuja shales respectively. For shear modulus, the average values are 4.11 GPa and 2.39 GPa for Beta and Fuja reservoir sands, while 5.12 GPa and 2.84Gpa were recorded for Beta and Fuja shales respectively. For bulk compressibility, the average values are 0.10$GPa^{-1}$and 0.023 $GPa^{-1}$for Beta and Fuja reservoir sands, while 0.07$GPa^{-1}$and 0.016 GPa^{-1}were recorded for Beta and Fuja shales respectively. This implies that the rock units of Beta reservoir are more plastic and ductile, and hence, more stable than those of the Fuja reservoir. The Beta reservoir rock units will resist deformation more than the Fuja reservoir rock units.

On the other hand, the values of Poisson's ratio and unconfined compressive strength are higher in the rock units (both sand and shale) of Fuja reservoir than the rock units of Beta reservoir. This is also clearly shown by the obtained average values of these parameters from those fields as presented in tables 2 and 4. From these tables, the average values of Poisson's ratio in Beta and Fuja reservoir sands are 0.30 and 0.39 respectively, while in Beta and Fuja reservoir shales it is respectively 0.33 and 0.42. For unconfined compressive strength, the

average values are 25.19 GPa and 39.00 GPa for Beta and Fuja reservoir sands, while 32.32 GPa and 42.30 GPa were recorded for Beta and Fuja shales respectively. The higher value of unconfined compressive strength observed in Fuja reservoir is attributable to the low total and effective porosity observed in this reservoir since the overall strength of a rock has a direct dependence on its porosity.

Results also revealed that the values of total porosity, effective porosity and permeability (petrophysical properties) are higher in the rock units of Beta reservoir than the rock units of Fuja reservoir. This is also shown by the obtained average values of these parameters from those fields as seen in tables 2 and 4. From these tables, the average values of total porosity in Beta and Fuja reservoir sands are 0.25 and 0.16 respectively, while in Beta and Fuja reservoir shales it is respectively 0.09 and 0.06. For rock effective porosity, the average values are 0.19 and 0.13 for Beta and Fuja reservoir sands, while 0.07 and 0.04 were recorded for Beta and Fuja shales respectively. From permeability results, the average values are 192.00 mD and 44.10 mD for Beta and Fuja reservoir sands, while 0.022 mD and 0.110 mD were recorded for Beta and Fuja shales respectively. This indicates that the reservoir rock units of Beta Field are more porous and permeable and hence, will be more prolific than the reservoir rock units of Fuja Field. This perhaps explains why the value of the unconfined compressive strength is higher in the rock units of Fuja reservoir than those of Beta reservoir.

From pore pressure estimations, it is observed that pore pressure is slightly higher in Beta reservoirs (both sand and shale units) than Fuja reservoirs as can be seen from mean pore pressure values presented in tables 4.1 and 4.3. Consequently, effective pressure is higher in Fuja reservoirs than Beta reservoirs. The higher value of pore pressure in Beta reservoirs compared to Fuja reservoirs is possibly as a result of the fact that Beta reservoirs sit deeper

and hence, more pressured by the thicker overlying fluid column than Fuja reservoirs. On the other hand, the higher value of effective pressure observed in Fuja reservoirs compared to Beta reservoirs is attributable to the fact that pore pressure is lower in Fuja Field and according to Terzaghi pressure relationship, this results in higher effective pressure. The parameters and their respective average values in sand and shale units of the reservoirs of both fields are presented in Table 4.5 below.

Table 4.5: The parameters and their respective average values in sand and shale units of the reservoirs of the two fields

S/N	PARAMETER	AVERAGE IN SAND		AVERAGE IN SHALE	
		BETA RESERVOIRS	**FUJA RESERVOIRS**	**BETA RESERVOIRS**	**FUJA RESERVOIRS**
1.0	Young's Modulus	10.94±1.52 GPa	5.11±1.53 GPa	13.70±1.90 GPa	6.08±1.96 GPa
2.0	Bulk Modulus	12.76±2.12 GPa	5.10±1.48 GPa	13.30±2.01 GPa	6.09±1.57 GPa
3.0	Shear Modulus	4.11±1.03 GPa	2.39±0.88 GPa	5.12±1.27 GPa	2.84±1.21GPa
4.0	Bulk Compressibility	0.10±0.03 GPa^{-1}	0.023±0.013 GPa^{-1}	0.07±0.014 GPa^{-1}	0.016±0.006 GPa^{-1}
5.0	Poisson's Ratio	0.30±0.02	0.39±0.08	0.33±0.03	0.42±0.07
6.0	UCS	25.19±14.15 GPa	39.0±5.30 GPa	32.32±17.52 GPa	42.3±8.70 GPa
7.0	Total Porosity	0.25±0.07	0.16±0.06	0.09±0.02	0.06±0.024
8.0	Effective Porosity	0.19±0.09	0.13±0.024	0.07±0.01	0.04±0.009
9.0	Permeability	192.00±53.9 mD	44.10±17.4 mD	0.022±0.016 mD	0.110±0.04 Md
10.0	Pore Pressure	13,683±360.3 psi	13,248±821.3 psi	15,662±119.5psi	15,220±746.2 psi
11.0	Effective Pressure	14,964±146.9 psi	14,945±891.2 psi	12,730±211.8 psi	12,973±608 psi

Analysis of the mean of the three principal stress components of total vertical stress, maximum horizontal stress and minimum horizontal stress operative within the reservoirs of both fields show that total vertical stress is slightly higher in Beta reservoirs (28,392psi) than Fuja reservoirs (28,193psi), maximum horizontal stress is higher in Fuja reservoirs (26,237psi) than Beta reservoirs (25,537psi), and minimum horizontal stress is also higher in Fuja reservoirs (21,532psi) than Beta reservoirs (20,781psi). This implies that the magnitude

of well breakouts will be higher in Fuja reservoirs than Beta reservoirs since minimum horizontal stress magnitudes, to a large extent, control well breakout magnitudes (Li et al, 2018). Also, hydraulic fracture growth and propagation will be slightly higher in Beta reservoirs than Fuja reservoirs since hydraulic fractures propagate easily in formations with low minimum horizontal stress (Zhang et al, 2021). Table 4.6 shows the respective average values of total vertical stress, maximum and minimum horizontal stresses within Beta and Fuja reservoirs.

Table 4.6: Mean values of total vertical stress, maximum and minimum horizontal stresses within Beta and Fuja reservoirs.

S/N	PARAMETER	AVERAGE IN BETA RESERVOIRS (psi)	AVERAGE IN FUJA RESERVOIRS (psi)
1.0	Total vertical stress (S_v)	28,392±629.0	28,193±1,682.5
2.0	Maximum horizontal stress (Sh_{max})	25,537±440.6	26,237±1,406.8
3.0	Minimum horizontal stress (Sh_{min})	20,781±330.5	21,532±1,225.7

4.1.5.3 Cross Plots of Rock Elastic and Inelastic Properties, Petrophysical Properties and Effective Pressure

The cross plots between rock elastic properties, inelastic properties, petrophysical properties, and effective pressure show exactly the same trends in both Fields; in other words, direct relationships between parameters in Beta Field gave direct relationships between those parameters in Fuja Field while inverse relationships in Beta Field also gave inverse relationships in Fuja Field. For instance, unconfined compressive strength decreases with increase in rock effective porosity in both Fields, unconfined compressive strength increases with increase in Young's modulus in both Fields, and effective pressure increases with increase in depth in both Fields as shown in figure 4.12(a-c).

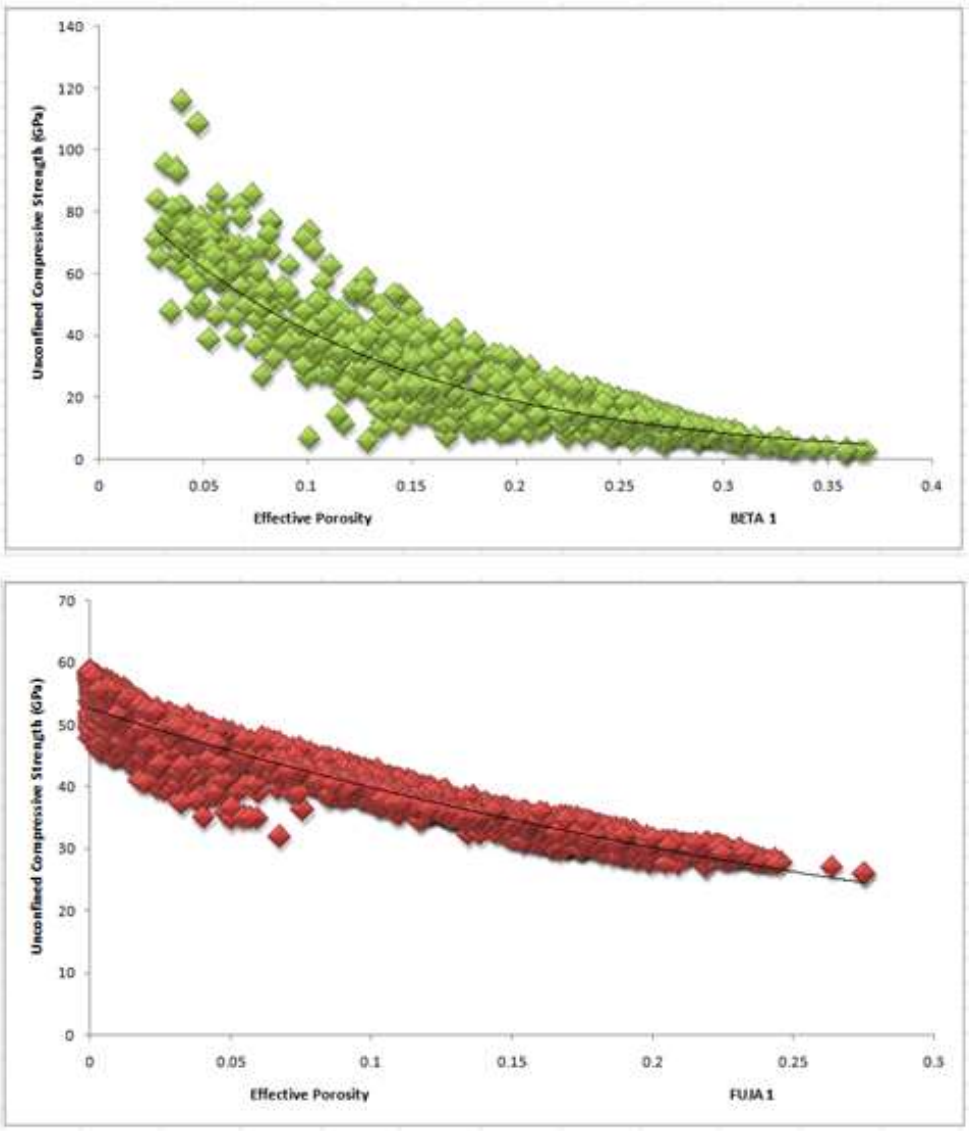


Fig. 4.12a: Relationship between unconfined compressive strength and effective porosity in Beta Field (green) and Fuja Field (red).

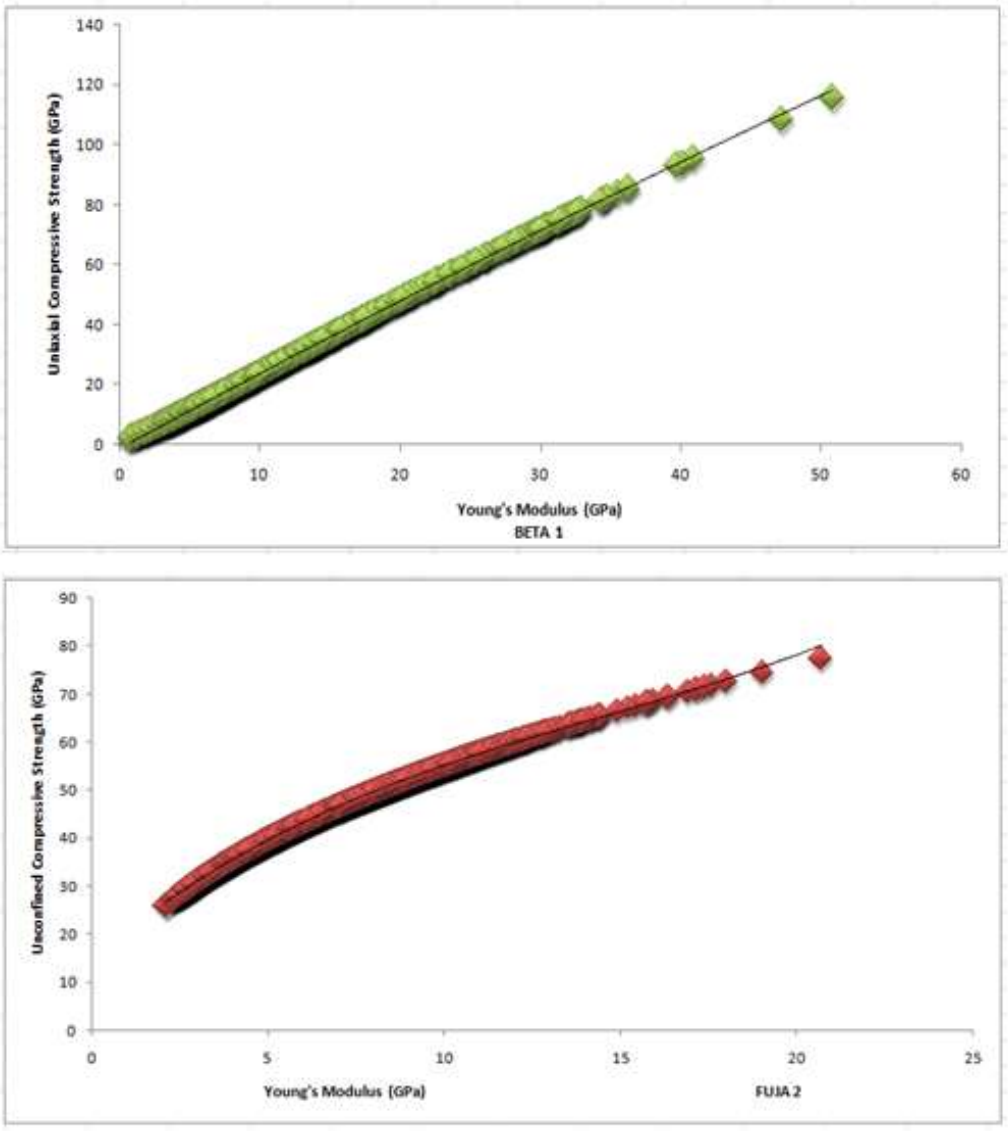


Fig. 4.12b: Relationship between unconfined compressive strength and Young's modulus in Beta Field (green) and Fuja Field (red).

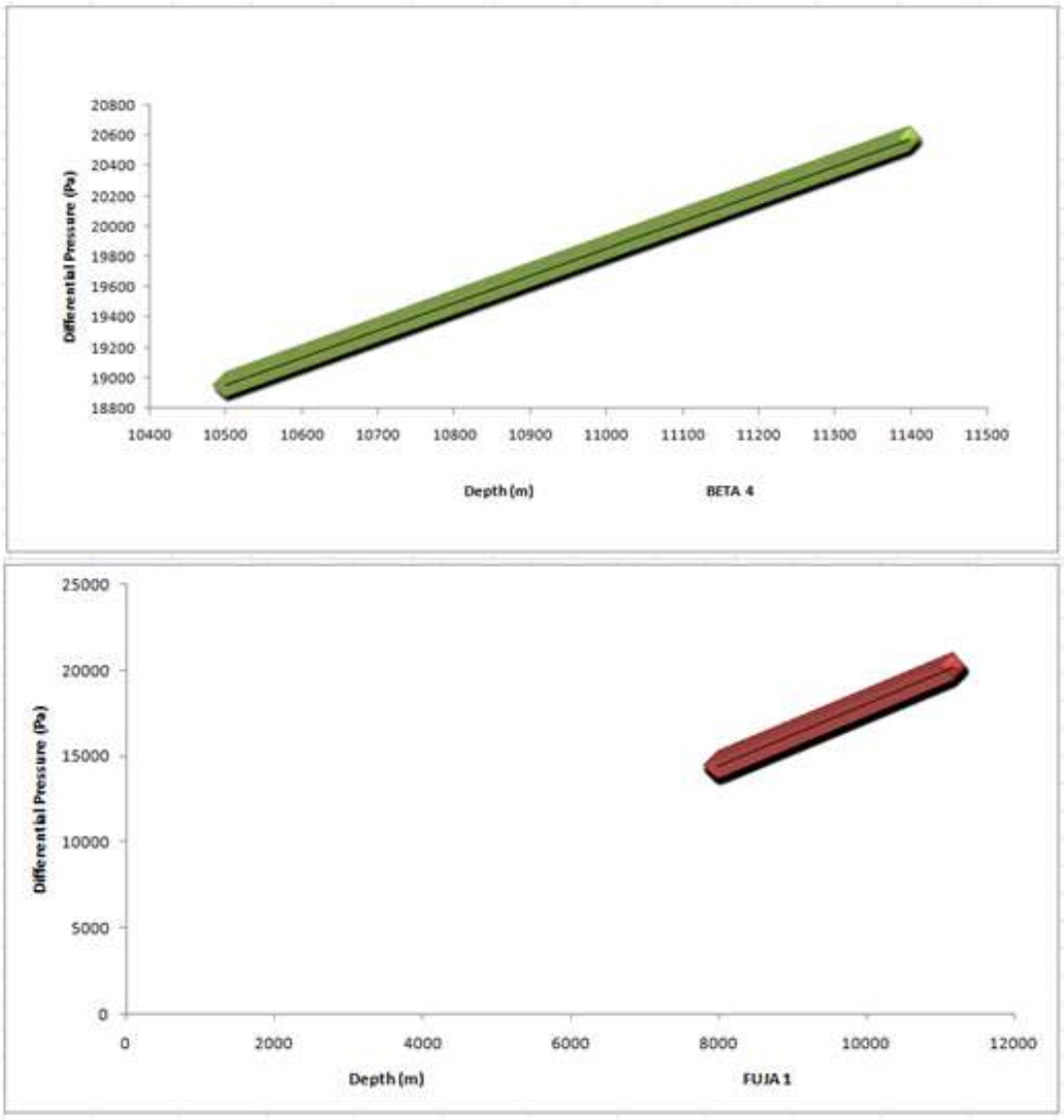


Fig. 4.12c: Relationship between effective/differential pressure and depth in Beta Field (green) and Fuja Field (red).

Results from cross plots of these rock parameters also show that the relationship between unconfined compressive strength and total porosity is stronger in Fuja Field than in Beta Field as shown in figure 4.13a. This implies that the UCS varies strongly with total porosity in Fuja Field but varies weakly with total porosity in Beta Field. On the other hand, the relationship between Young's modulus and depth is weak in Fuja Field but stronger in Beta Field as shown in figure 4.13b. This shows that the variation between the two parameters is stronger in Beta Field. Also, a weak relationship exists between unconfined compressive

strength and permeability in Beta Field but stronger in Fuja Field as shown in figure 4.13c. This suggests that the UCS varies weakly with permeability in Beta Field reservoir than in Fuja Field.

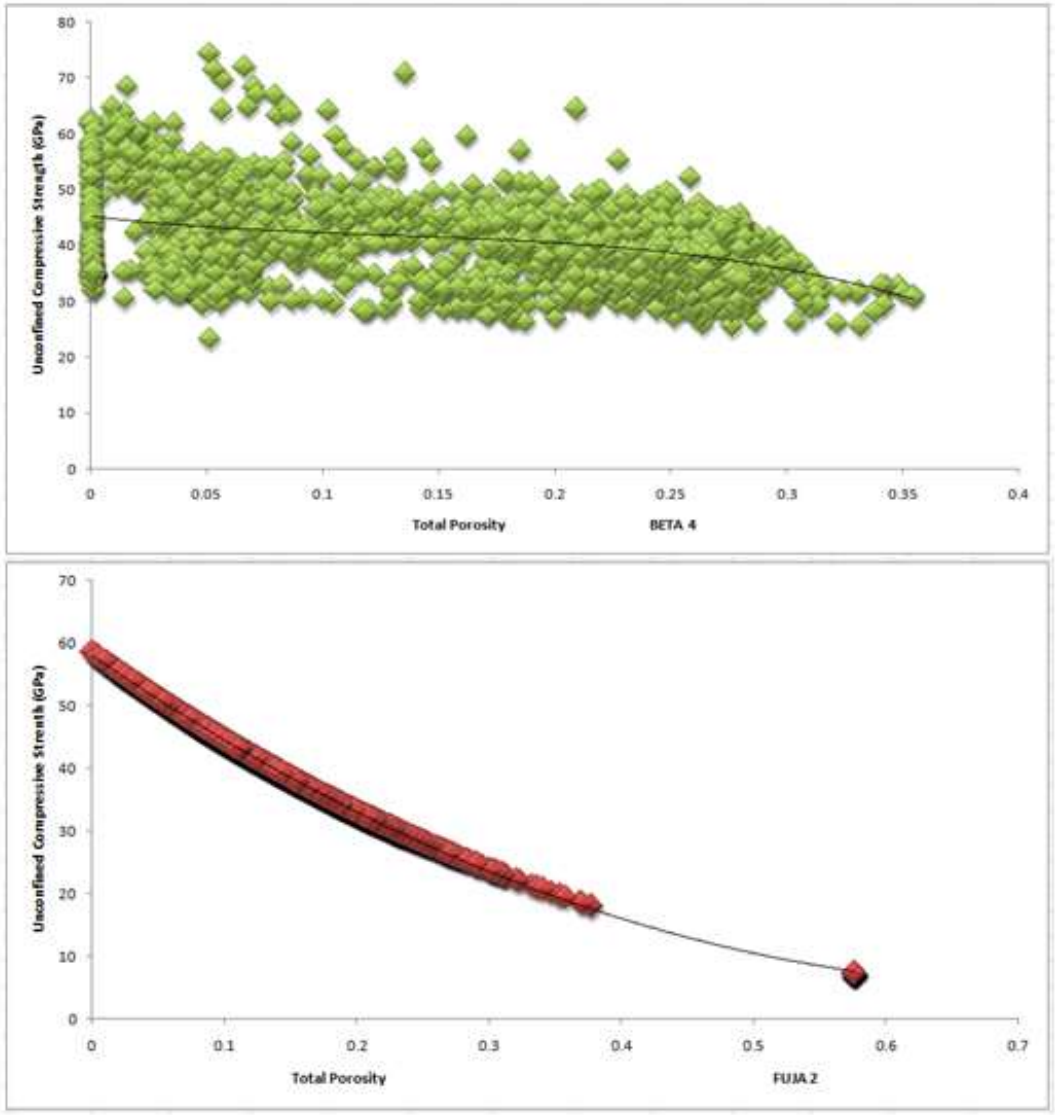


Fig. 4.13a: Relationship between unconfined compressive strength and total porosity for Beta Field (green) and Fuja Field (red).

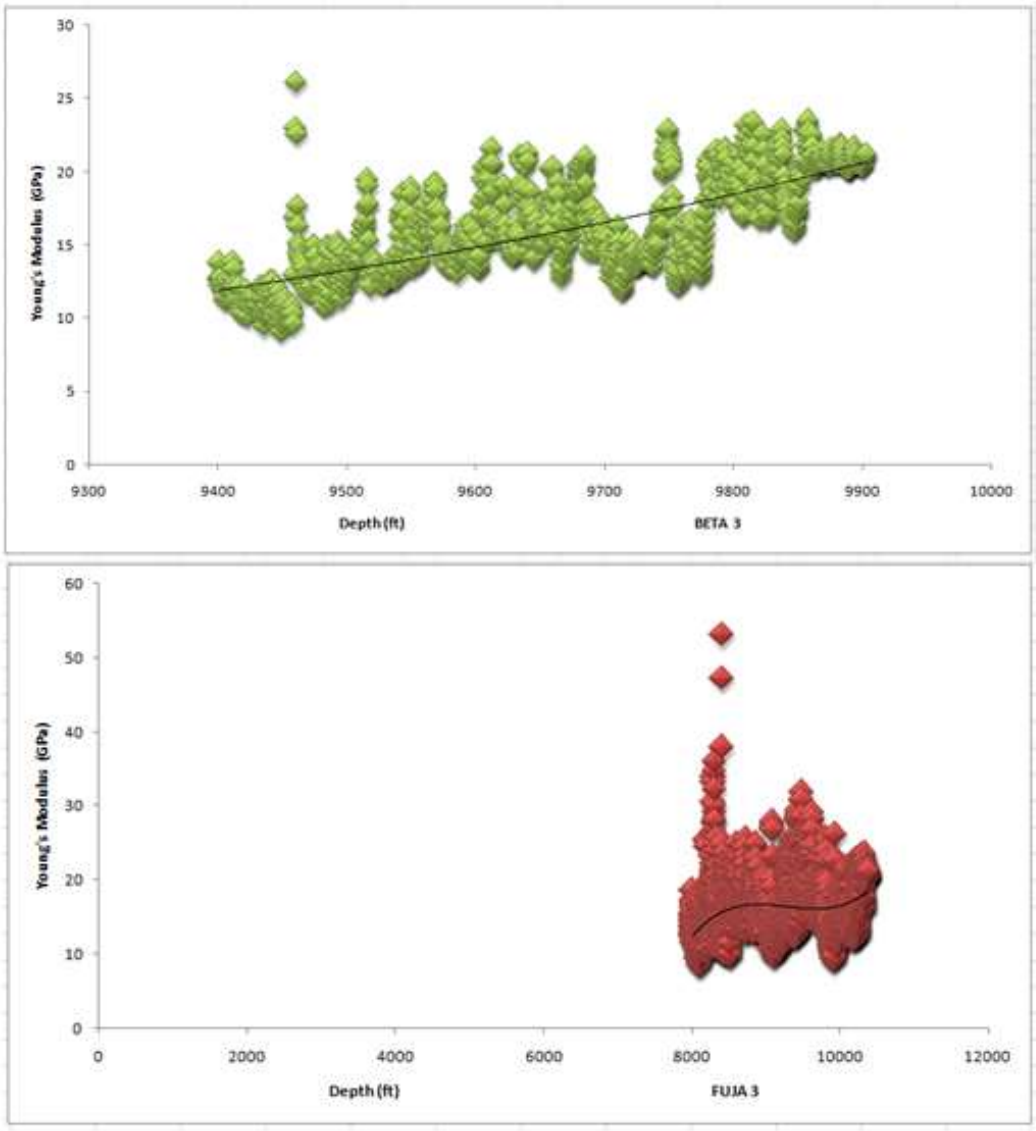


Fig. 4.13b: Relationship between Young's modulus and depth for Beta Field (green) and Fuja Field (red).

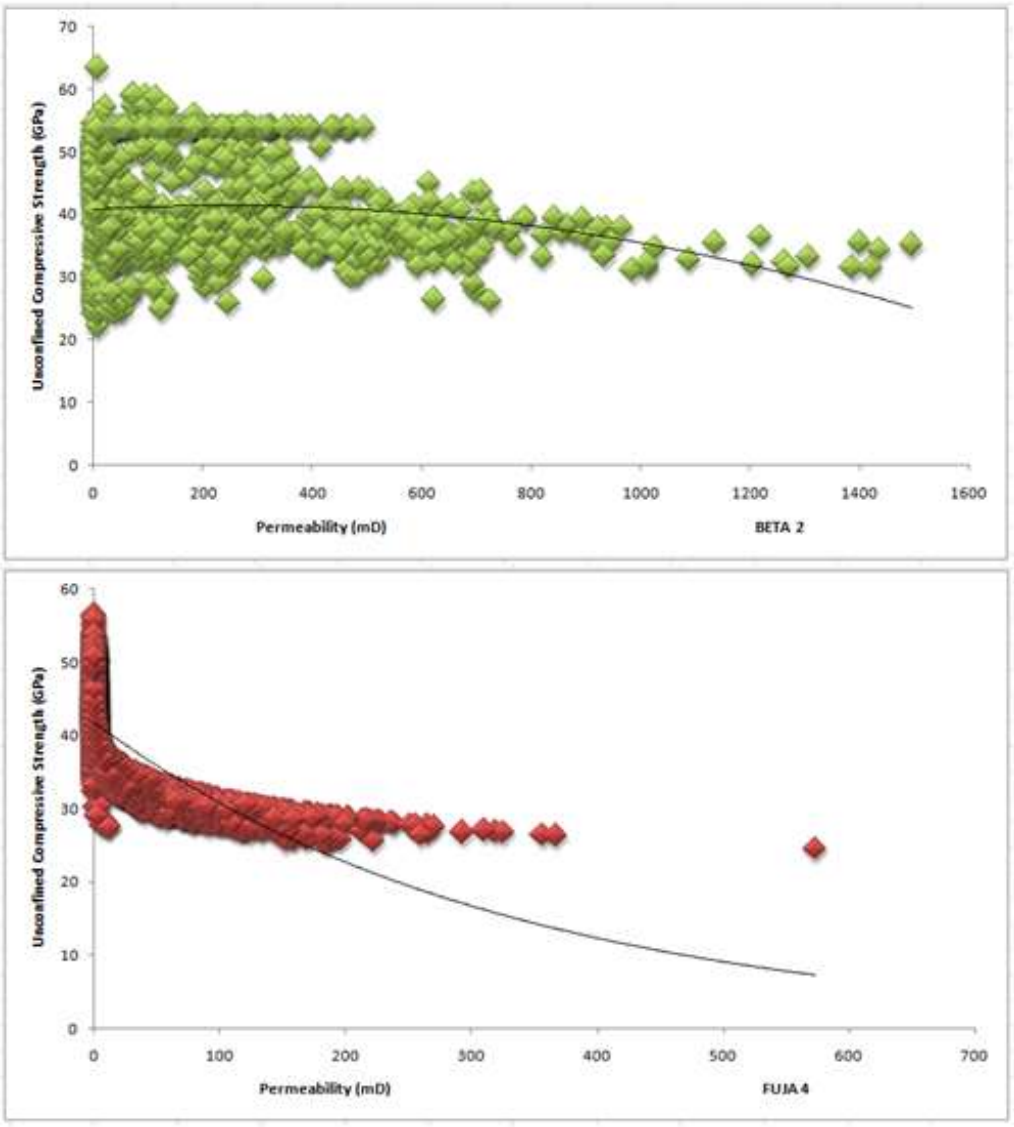


Fig. 4.13c: Relationship between unconfined compressive strength and permeability for Beta Field (green) and Fuja Field (red).

Further analysis of the cross plots also revealed that a weak relationship exists between effective pressure and total porosity and between pressure and unconfined compressive strength in both Fields as shown in figures 4.13d and 4.13e. This implies that effective pressure varies weakly with total porosity and unconfined compressive strength in the reservoirs of both Fields.

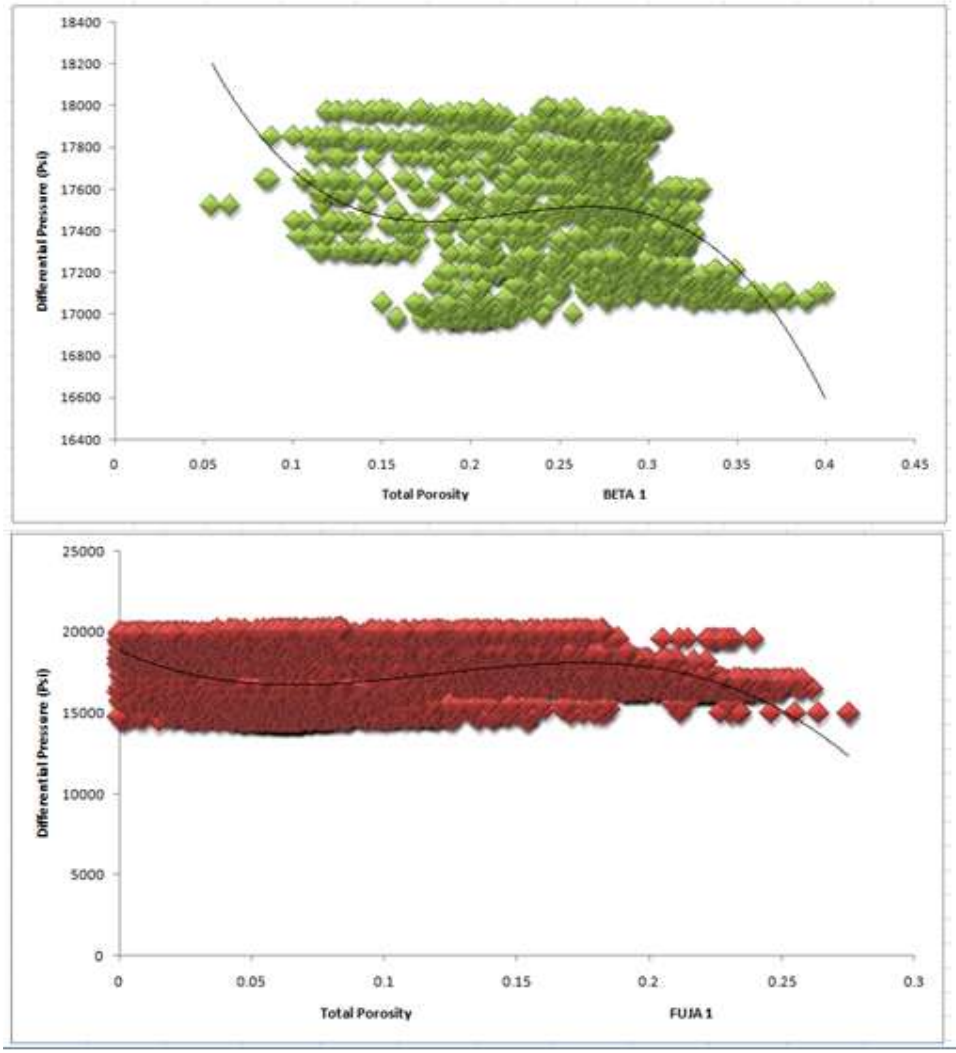


Fig. 4.13d: Relationship between effective pressure and total porosity in Beta Field (green) and Fuja Field (red).

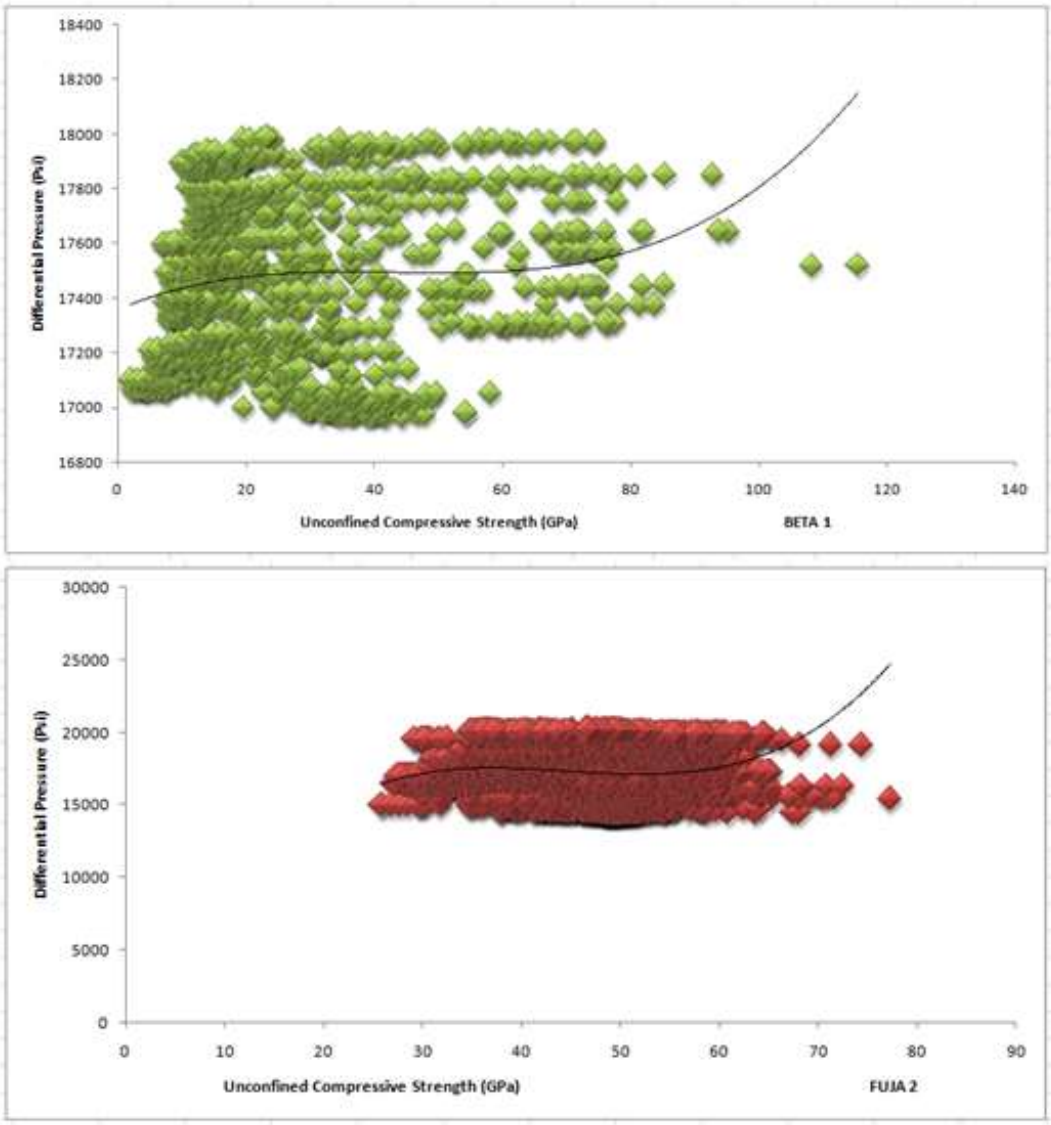


Fig. 4.13e: Relationship between effective pressure and unconfined compressive strength in Beta Field (green) and Fuja Field (red).

4.1.5.4 3D Geomechanical Models

From the generated 3D geomechanical models of the studied reservoirs, it can be observed from the inserted legends that all the rock elastic and inelastic parameters revealed highest values around the north-northeastern (NNE) portion of Beta Field compared to other portions of the field. In Fuja Field however, all the rock elastic and inelastic parameters revealed highest values around the northeastern (NE) and parts of the eastern and western portions of the field. This implies that the north-northeastern portion of Beta Field is more stable and can

resist mechanical rock deformation or failure during well drilling, exploitation, and hydraulic fracturing more than other sections of the Field while the northeastern (NE) and parts of the eastern and western portions of Fuja Field are more stable and can resist mechanical rock deformation or failure during well drilling, exploitation, and hydraulic fracturing more than other sections of the field. The comparison between the geomechanical models of unconfined compressive strength and Poisson's ratio for Beta and Fuja Fields are as shown in figures 4.14(a-b) below.

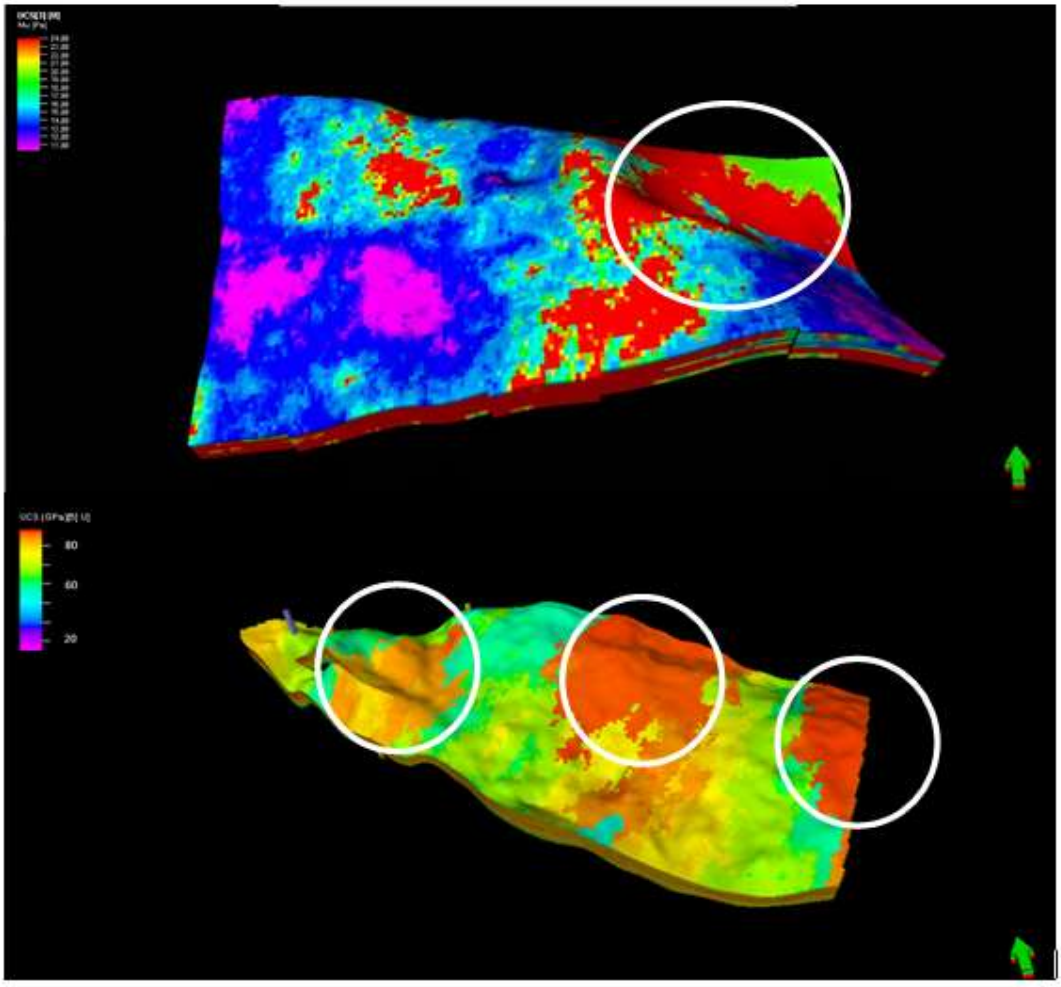


Fig. 4.14a: Comparison between the geomechanical models of unconfined compressive strength for Beta Field (top) and Fuja Field (bottom).

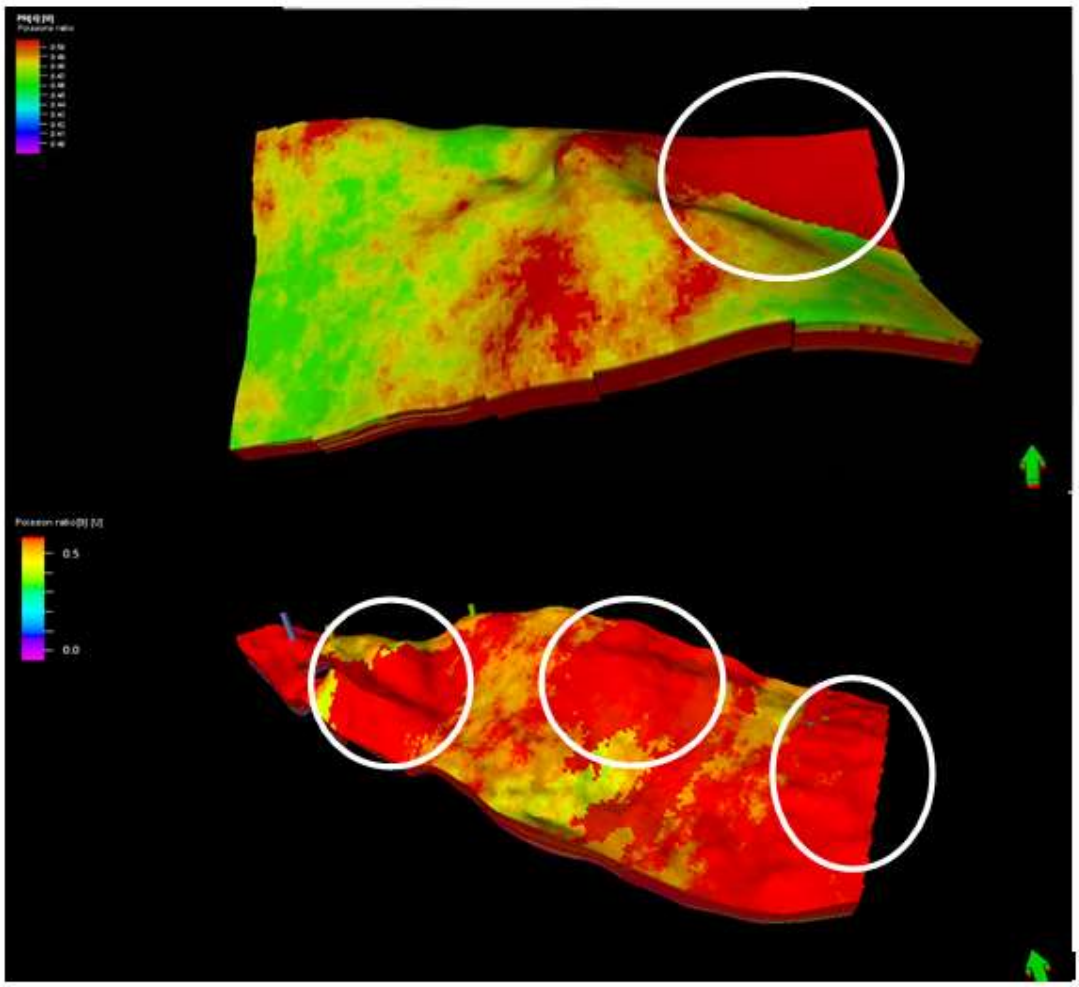


Fig. 4.14b: Comparison between the geomechanical models of Poisson's ratio for Beta Field (top) and Fuja Field (bottom).

4.1.6 Modeling with Empirical Linear and Non-Linear Methods

Relationships between unconfined compressive strength and bulk density, unconfined compressive strength and sonic transit time, permeability and bulk density, as well as shear wave velocity and sonic transit time were modelled with empirical linear and non-linear methods including linear model, quadratic model, power model, logarithmic model, and exponential model. The results of each of the models are as follows.

4.1.6.1 Linear and Quadratic Models

For UCS versus bulk density

The first degree linear model is given by equation 3.18, where y is the UCS and x is the bulk density with a_0 and a_1 being the regression coefficients to be obtained. Statistical table of the first degree linear model is shown in table 4.7.

Table 4.7: Statistical table of linear model of first degree for UCS versus bulk density

Regression coefficient		Other statistical parameters
a_0	-164.9	SSE = 155300
a_1	84.6	R-square = 0.8637
		Adjusted R-square = 0.8636
		RMSE = 4.623

Therefore, the linear model for UCS versus bulk density becomes:

$$UCS = -164.9 + 84.6\rho_b \quad (4.1)$$

Where ρ_b is the bulk density.

SSE signifies sum of square error, RMSE is root mean square error.

The Second degree linear model (quadratic model) is given by equation 3.19, where y is the UCS, x is the bulk density with a_0, a_1 and a_2 the regression coefficients to be obtained. The Statistical table of the second degree linear model (quadratic model) is shown in Table 4.8.

Table 4.8: Statistical table for linear model of second degree (quadratic model) for UCS versus bulk density

Regression coefficient		Other statistical parameters
a_0	-696.9	SSE = 131200
a_1	528.6	R-square = 0.8848
a_2	-92.29	Adjusted R-square = 0.8848
		RMSE = 4.249

Therefore, the quadratic model for UCS versus bulk density becomes:

$$UCS = -696.9 + 528.6\rho_b - 92.29{\rho_b}^2 \quad (4.2)$$

The comparative analysis of the actual and predicted output with linear and quadratic models is shown in figure 4.15.

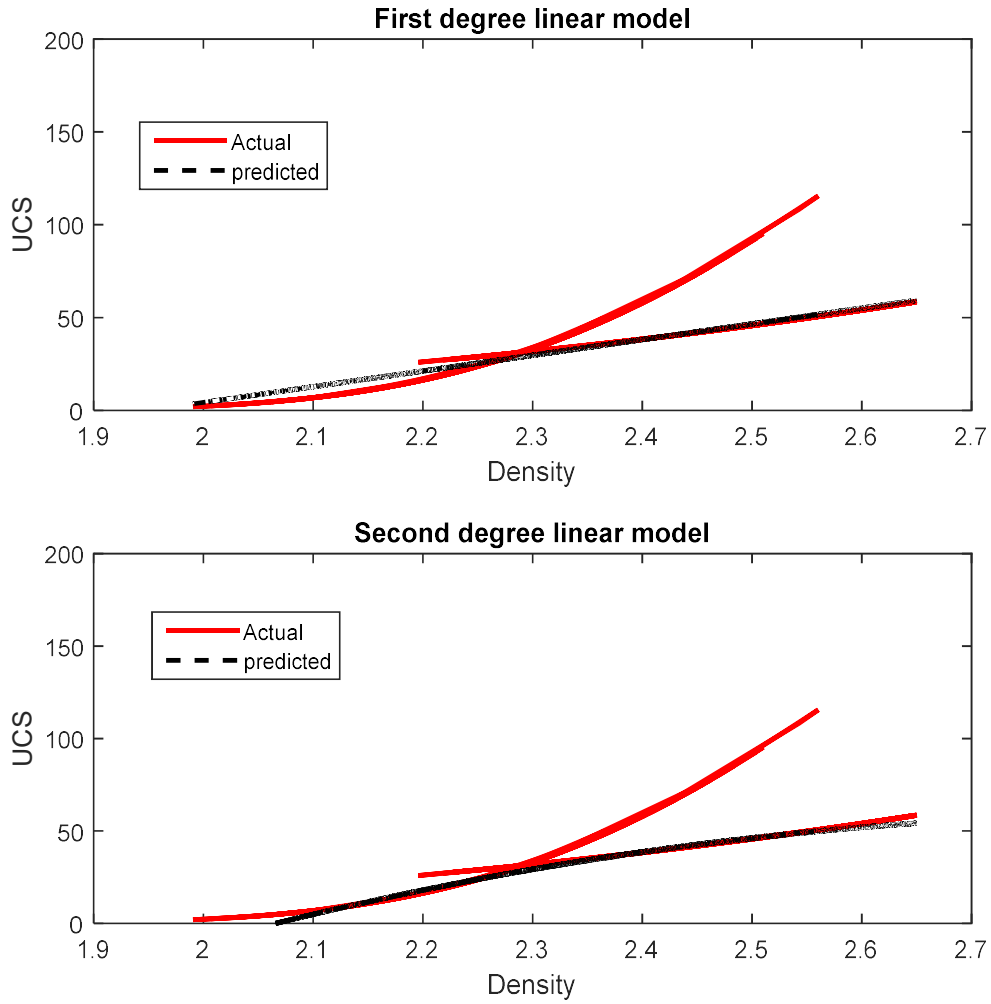


Fig. 4.15: Comparative analysis of actual and predicted output of UCS versus bulk density with linear and quadratic models

For UCS versus sonic

Statistical table of the first degree linear model is shown in Table 4.9. In this model, y remains UCS while x represents sonic transit time in equation 3.18.

Table 4.9: Statistical table of linear model of first degree for UCS versus sonic

Regression coefficient		Other statistical parameters
a_0	45.33	SSE = 1135000
a_1	-0.01327	R-square = 0.003559
		Adjusted R-square = 0.003422
		RMSE = 12.5

Where SSE signifies sum of square error, RMSE is root mean square error.

Statistical table of the second degree linear model (quadratic model) is shown in Table 4.10.

Table 4.10: Statistical table of linear model of second degree (quadratic model) for UCS versus sonic

Regression coefficient		Other statistical parameters
a_0	-0.001308	SSE = 893200
a_1	0.5216	R-square = 0.2159
a_2	-5.17	Adjusted R-square = 0.2157
		RMSE = 11.09

The comparative analysis of actual and predicted output with the linear and quadratic models is shown in figure 4.16.

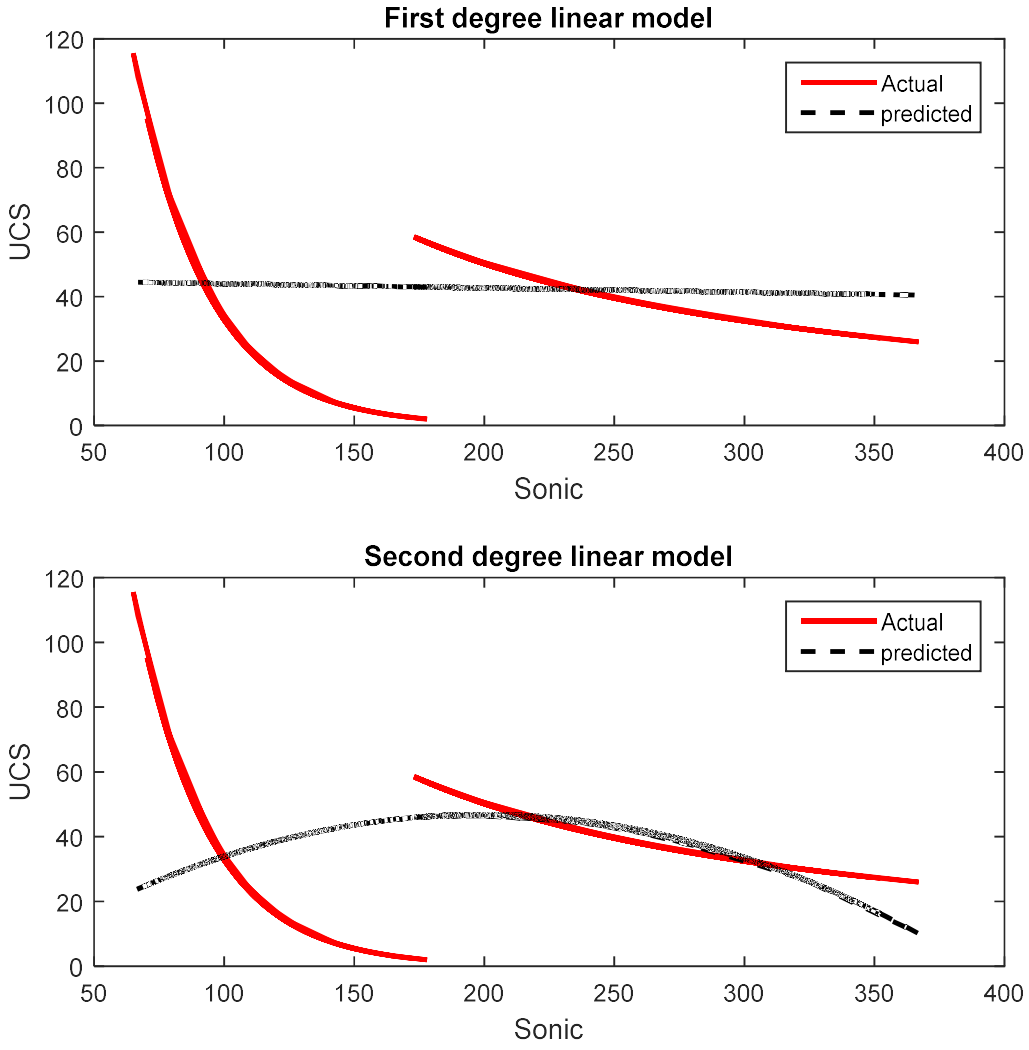


Fig. 4.16: Comparative analysis of actual and predicted output for UCS versus sonic with the linear and quadratic models

The comparative analysis of the R-square values obtained for UCS versus bulk density and UCS versus sonic for linear and quadratic models is shown in figure 4.17.

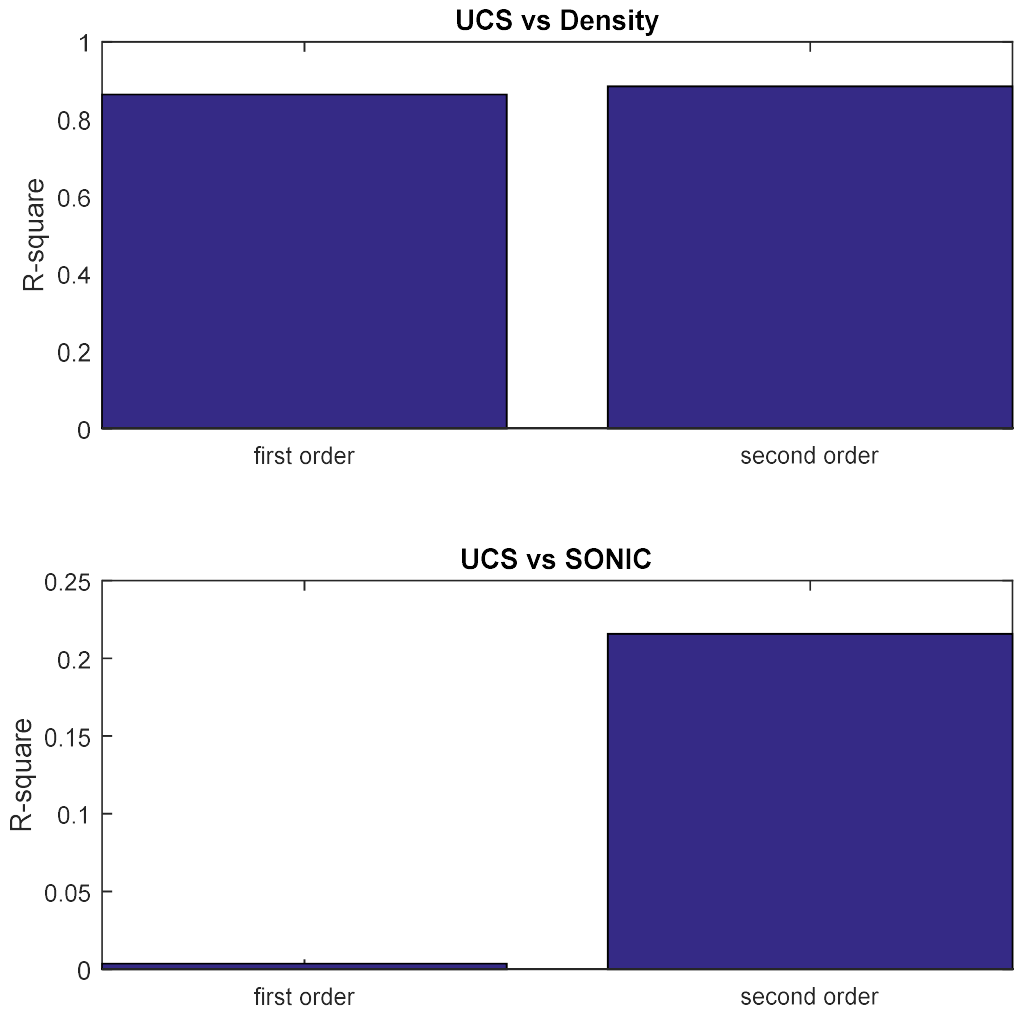


Fig. 4.17: R-square values for UCS versus bulk density and UCS versus sonic from linear and quadratic models

Figure 4.17 shows the bar chart of the R-square values obtained in the linear and quadratic models for UCS versus bulk density and UCS versus sonic. The bar chart of UCS versus bulk density has R-square value greater than 50% (0.8637 and 0.8848) for linear and quadratic models while the R-square values of UCS versus sonic is less than 50% (0.003559 and

0.2159) for both linear and quadratic models. This suggests that linear and quadratic models can be utilized in the modeling and analysis of UCS versus bulk density only.

For Permeability versus bulk density

Statistical table of the first degree linear model for permeability versus bulk density is shown in Table 4.11. In this model, y represents permeability while x represents bulk density in equation 3.18.

Table 4.11: Statistical table of linear model of first degree for permeability versus bulk density

Regression coefficient		Other statistical parameters
a_0	297.5	SSE = 1.553e+08
a_1	-55.66	R-square = 0.001263
		Adjusted R-square = 0.0008362
		RMSE = 257.7

Where SSE signifies sum of square error, RMSE is root mean square error.

Statistical table of the second degree linear model (quadratic model) for permeability versus bulk density is shown in Table 4.12.

Table 4.12: Statistical table of linear model of second degree (quadratic model) for permeability versus bulk density

Regression coefficient		Other statistical parameters
a_0	7074	SSE = 1.541e+08
a_1	-5825	R-square = 0.009212
a_2	1222	Adjusted R-square = 0.008364
		RMSE = 256.7

The comparative analysis of the actual and predicted output with the linear and quadratic models is shown in figure 4.18.

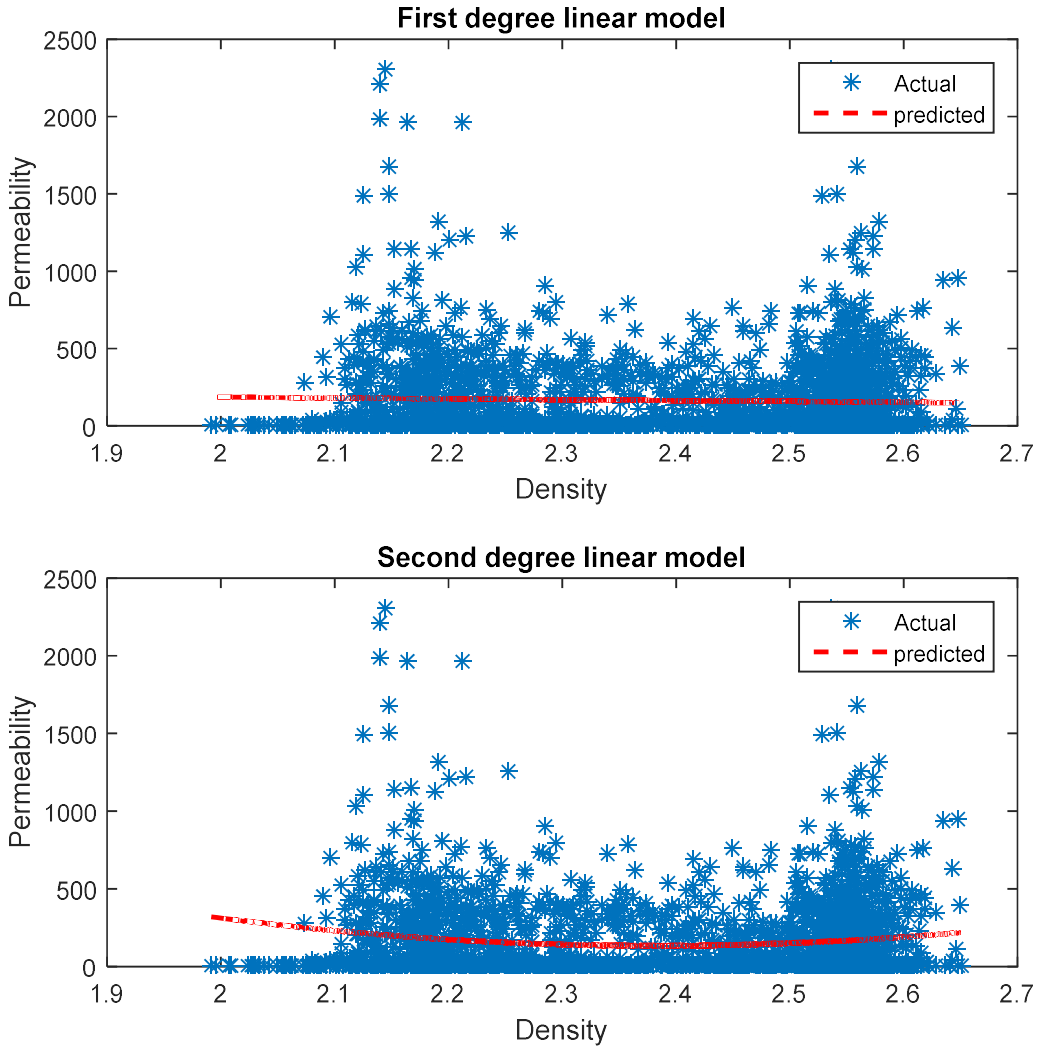


Fig. 4.18: Comparative analysis of the actual and predicted output for permeability versus bulk density with the linear and quadratic models

For shear wave velocity (V_s) versus sonic

Statistical table of the first degree linear model for V_s versus sonic is shown in Table 4.13. In this model, y represents shear wave velocity and x represents sonic transit time in equation 3.18.

Table 4.13: Statistical table of linear model of first degree for V_s versus sonic

Regression coefficient		Other statistical parameters
a_0	1.577	SSE = 421
a_1	-0.001829	R-square = 0.04606
		Adjusted R-square = 0.04564
		RMSE = 0.4307

Where SSE signifies sum of square error, RMSE is root mean square error.

Statistical table of the second degree linear model (quadratic model) for V_s versus sonic is shown in Table 4.14.

Table 4.14: Statistical table of linear model of second degree (quadratic model) for V_s versus sonic

Regression coefficient		Other statistical parameters
a_0	0.00004332	SSE = 387.8
a_1	-0.01594	R-square = 0.1214
a_2	2.61	Adjusted R-square = 0.1206
		RMSE = 0.4134

The comparative analysis of actual and predicted output with the linear and quadratic models is shown in figure 4.19.

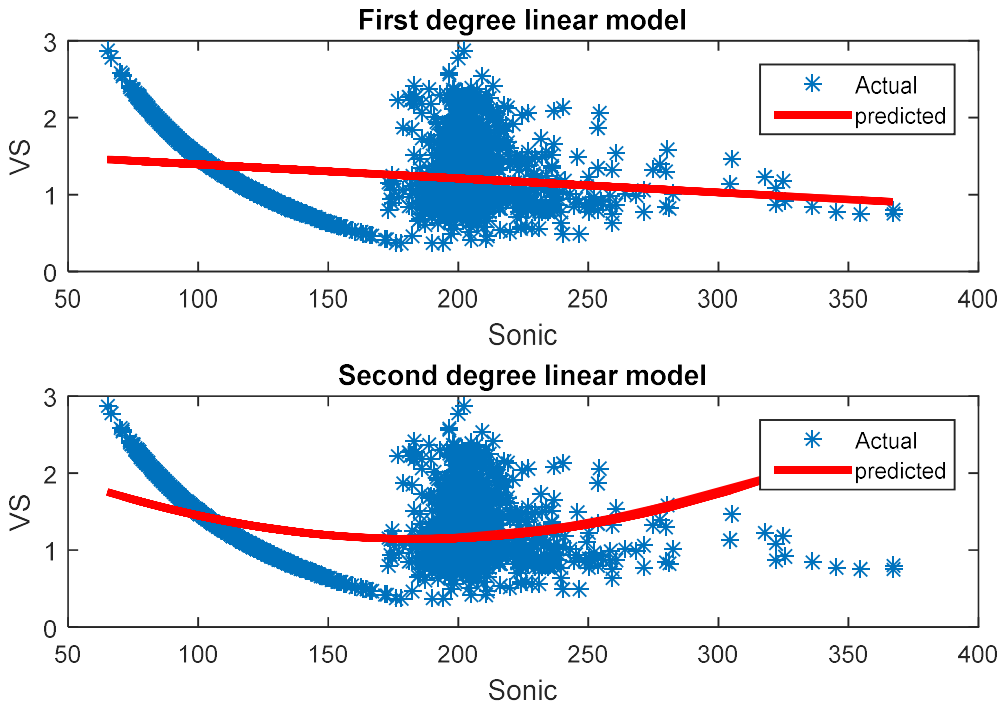


Fig. 4.19: Comparative analysis of actual and predicted output for shear wave velocity versus sonic with the linear and quadratic models

The comparative analysis of the R-square values obtained for permeability versus bulk density and shear wave velocity versus sonic for linear and quadratic models is shown in figure 4.20.

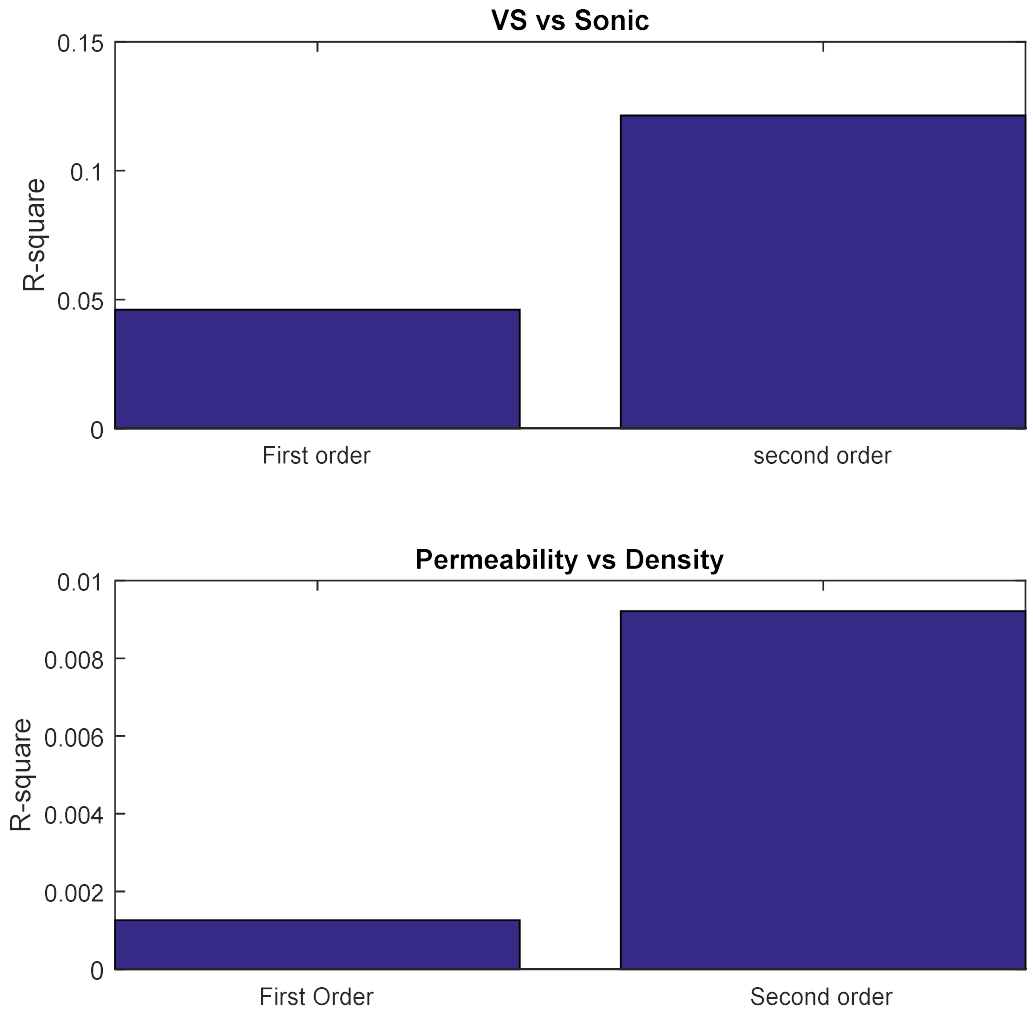


Fig. 4.20: R-square values for permeability versus bulk density and shear wave velocity versus sonic from linear and quadratic models

Figure 4.20 shows the bar chart of the R-square values obtained in the linear and quadratic models for permeability versus bulk density and shear wave velocity versus sonic. The figure shows that the R-square values of both models are very much less than 50% (0.001263, 0.009212, 0.04606 and 0.1214) hence, both models should not be utilized in the modeling and analysis of permeability versus bulk density and shear wave velocity versus sonic.

4.1.6.2 Power Models

For UCS versus bulk density

The power model is given by equation 3.20. Statistical table of the power model for UCS versus bulk density is shown in Table 4.15. In this model, y represents UCS while x represents bulk density.

Table 4.15: Statistical table of power model for UCS versus bulk density

Regression coefficient		Other statistical parameters
a_0	0.4845	SSE = 2.033e+05
a_1	4.96	R-square = 0.8216
		Adjusted R-square = 0.8215
		RMSE = 5.289

Where SSE signifies sum of square error, RMSE is root mean square error.

Therefore, the power model for UCS versus bulk density becomes:

$$UCS = 0.4845(\rho_b)^{4.96} \quad (4.3)$$

Where ρ_b is the bulk density.

The comparative analysis of the actual and predicted output for UCS versus bulk density with power model is shown in figure 4.21.

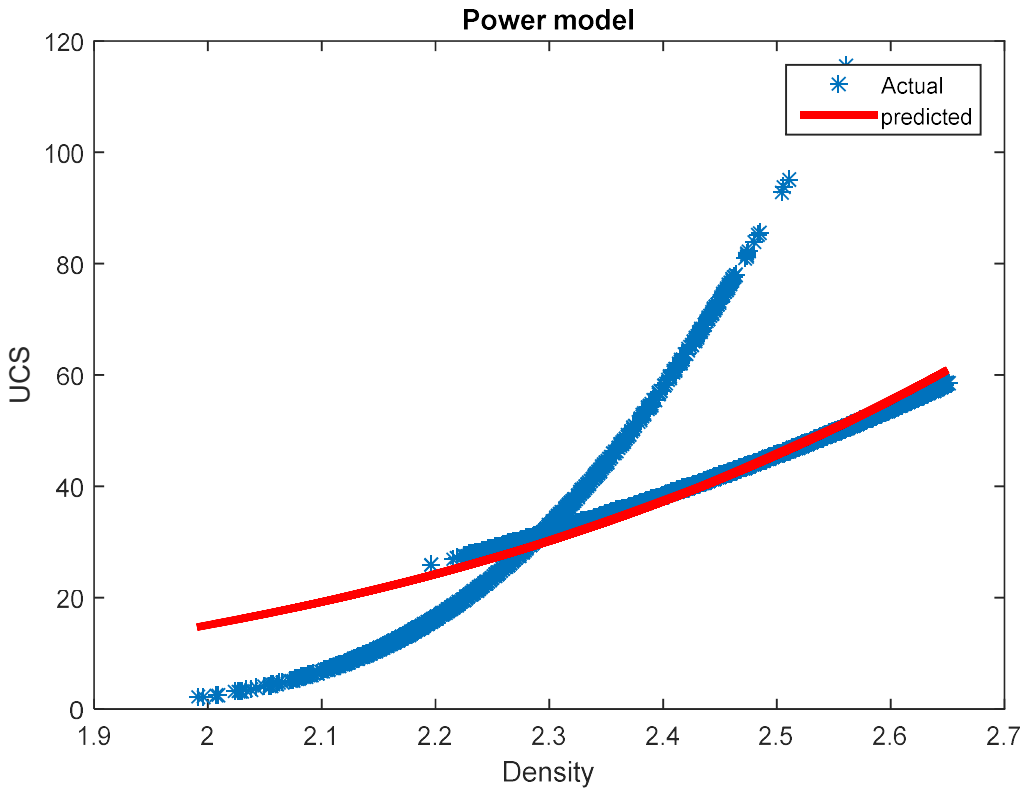


Fig. 4.21: Comparative analysis of actual and predicted output for UCS versus bulk density with power model

For UCS versus sonic

Statistical table of the power model for UCS versus sonic is shown in Table 4.16. In this model, y represents UCS while x represents sonic transit time in equation 3.20.

Table 4.16: Statistical table for power model for UCS versus sonic

Regression coefficient		Other statistical parameters
a_0	39.25	SSE = 1.139e+06
a_1	0.01535	R-square = 0.0002881
		Adjusted R-square = 0.0001505
		RMSE = 12.52

Where SSE signifies sum of square error, RMSE is root mean square error.

The comparative analysis of actual and predicted output for UCS versus sonic with power model is shown in figure 4.22.

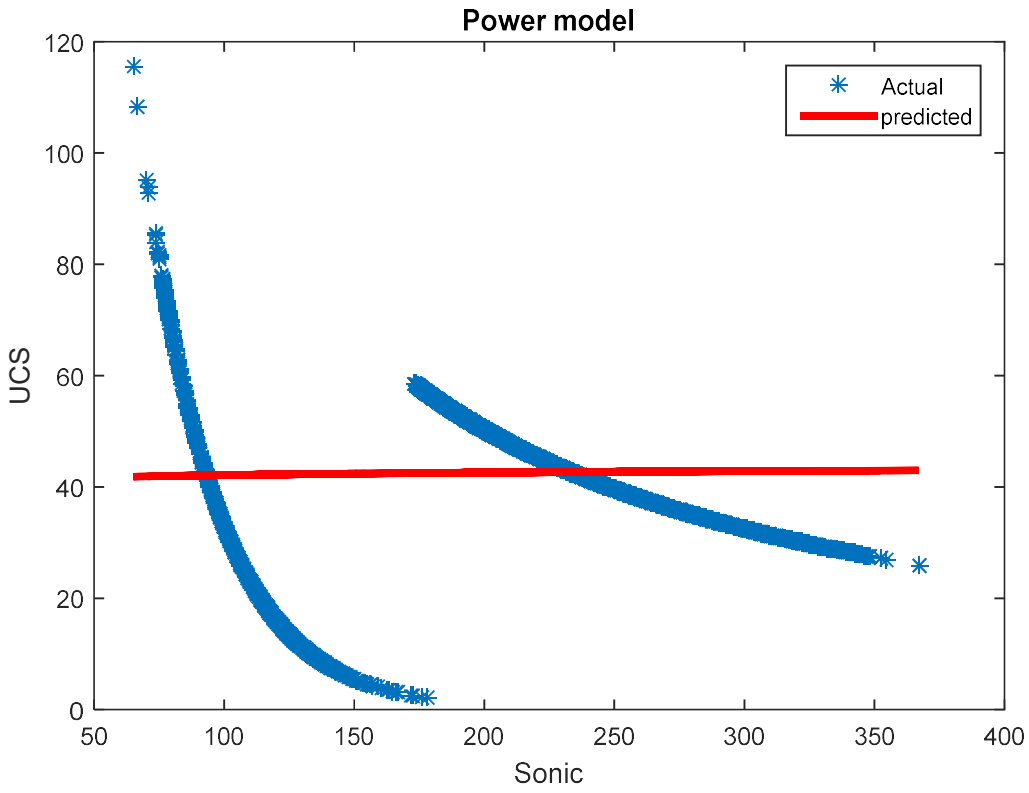


Fig. 4.22: Comparative analysis of actual and predicted output for UCS versus sonic with power model

The comparative analysis of the R-square values obtained for UCS versus bulk density and UCS versus sonic for power model is shown in figure 4.23.

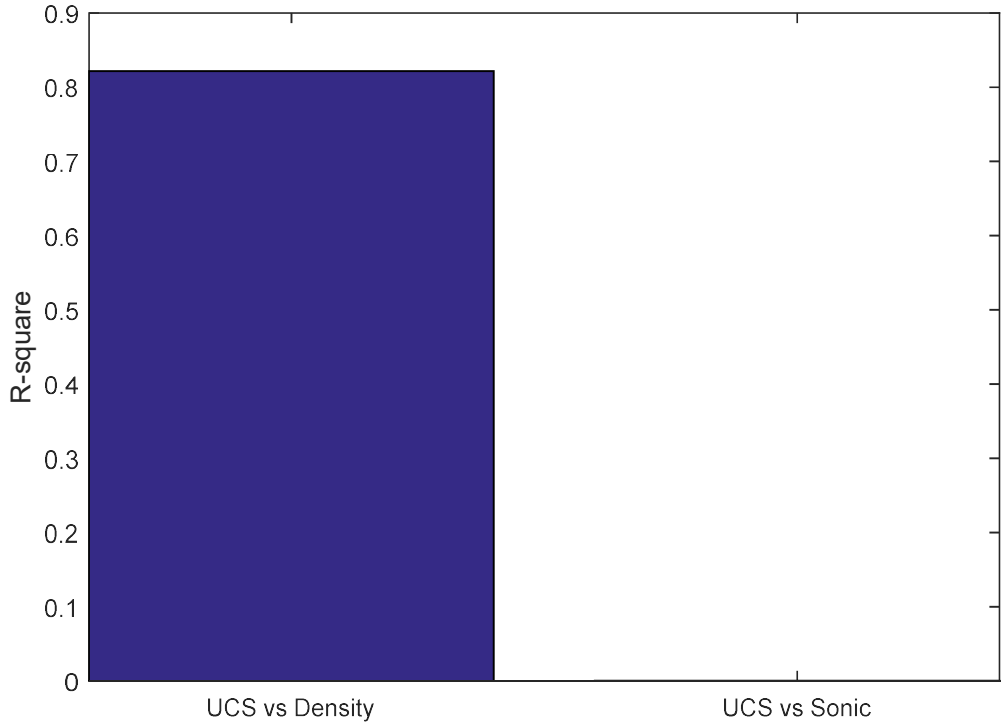


Fig. 4.23: R-square values for UCS versus bulk density and UCS versus sonic from power model

Figure 4.23 shows the bar chart of the R-square values obtained for UCS versus bulk density and UCS versus sonic from the power model. The bar chart of UCS versus bulk density has R-square value greater than 50% (0.8216) while the one of UCS versus sonic is less than 50% (0.0002881). This suggests that power model can be utilized in the modeling and analysis of UCS versus bulk density only.

For Permeability versus bulk density

Statistical table of the power model for permeability versus bulk density is shown in Table 4.17. In this model, y represents permeability while x represents bulk density in equation 3.20.

Table 4.17: Statistical table of power model for permeability versus bulk density

Regression coefficient		Other statistical parameters
a_0	361.7	SSE = 1.553e+08
a_1	-0.9089	R-square = 0.001547
		Adjusted R-square = 0.001121
		RMSE = 257.6

Where SSE signifies sum of square error, RMSE is root mean square error.

The comparative analysis of actual and predicted output for permeability versus bulk density with power model is shown in figure 4.24.

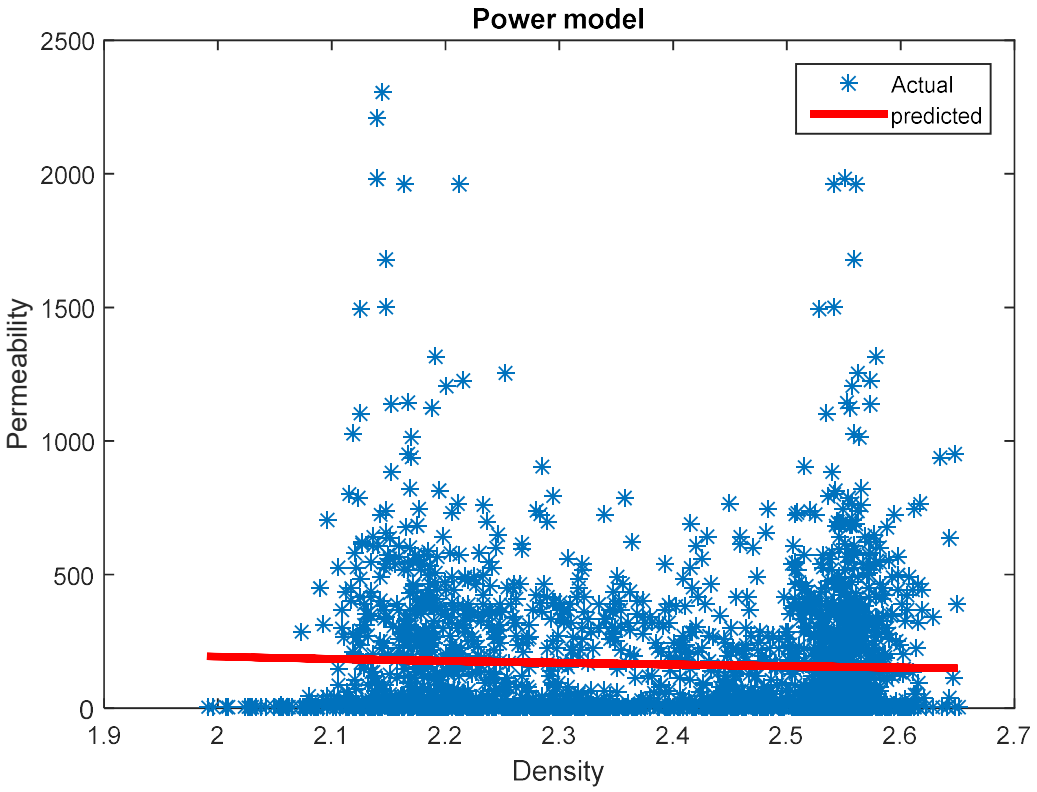


Figure 4.24: Comparative analysis of actual and predicted output for permeability versus bulk density with power model

For shear wave velocity (V_s) versus sonic

Statistical table of the power model for shear wave velocity versus sonic is shown in Table 4.18. In this model, y represents shear wave velocity while x represents sonic transit time in equation 3.20.

Table 4.18: Statistical table of power model for shear wave velocity versus sonic

Regression coefficient		Other statistical parameters
a_0	6.347	SSE = 401.5
a_1	-0.3197	R-square = 0.09036
		Adjusted R-square = 0.08996
		RMSE = 0.4205

Where SSE signifies sum of square error, RMSE is root mean square error.

The comparative analysis of actual and predicted output for shear wave velocity versus sonic with power model is shown in figure 4.25.

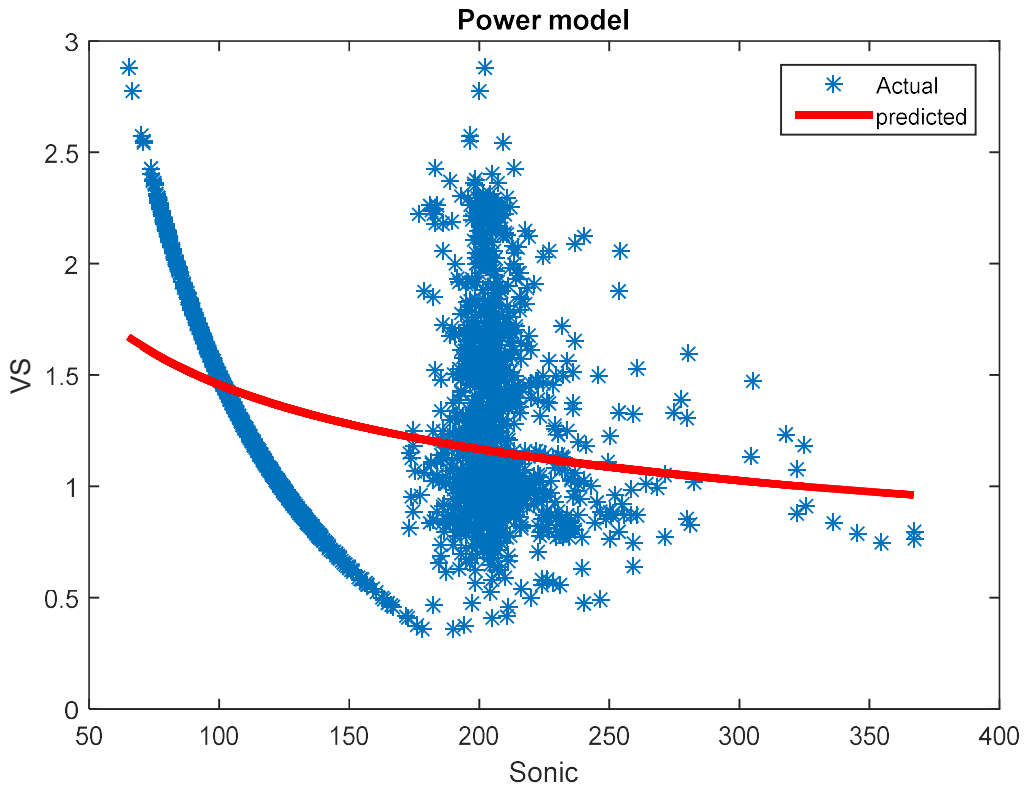


Fig. 4.25: Comparative analysis of actual and predicted output for shear wave velocity versus sonic with power model

The comparative analysis of the R-square values obtained for permeability versus bulk density and shear wave velocity versus sonic from power model is shown in figure 4.26.

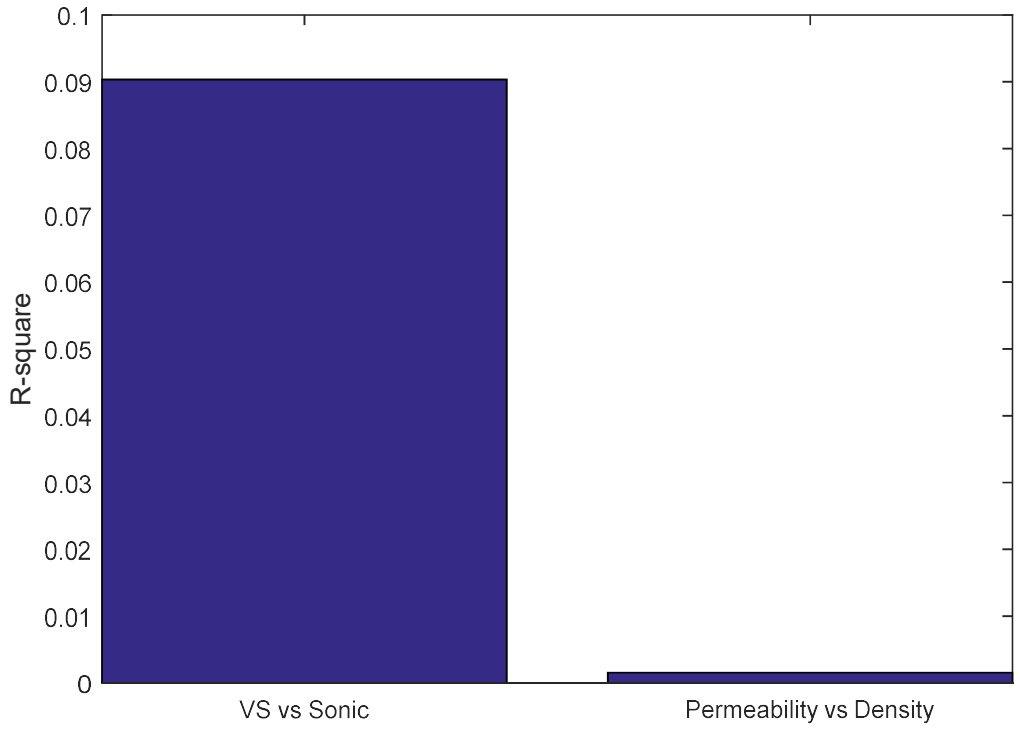


Fig. 4.26: R-square values obtained for permeability versus bulk density and shear wave velocity versus sonic from power model

Figure 4.26 shows the bar chart of the R-square values obtained for permeability versus bulk density and shear wave velocity versus sonic from the power model. This shows that the power model should not be utilized in the modeling and analysis of permeability versus bulk density and shear wave velocity versus sonic as their prediction performances are less than 50% (0.001547 and 0.09036).

4.1.6.3 Logarithmic Models

For UCS versus bulk density

The logarithmic model is given by equation 3.21. Statistical table of the logarithmic model for UCS versus bulk density is shown in Table 4.19. In this model, y represents UCS while x represents bulk density.

Table 4.19: Statistical table of logarithmic model for UCS versus bulk density

Regression coefficient		Other statistical parameters
a_0	453	SSE = 5060
a_1	4.96	R-square = 0.9956
		Adjusted R-square = 0.9956
		RMSE = 0.8345

Where SSE signifies sum of square error, RMSE is root mean square error.

Therefore, the logarithmic model for UCS versus bulk density becomes:

$$UCS = 453log\ (4.96\rho_b) \quad (4.4)$$

The comparative analysis of the actual and predicted output for UCS versus bulk density with logarithmic model is shown in figure 4.27.

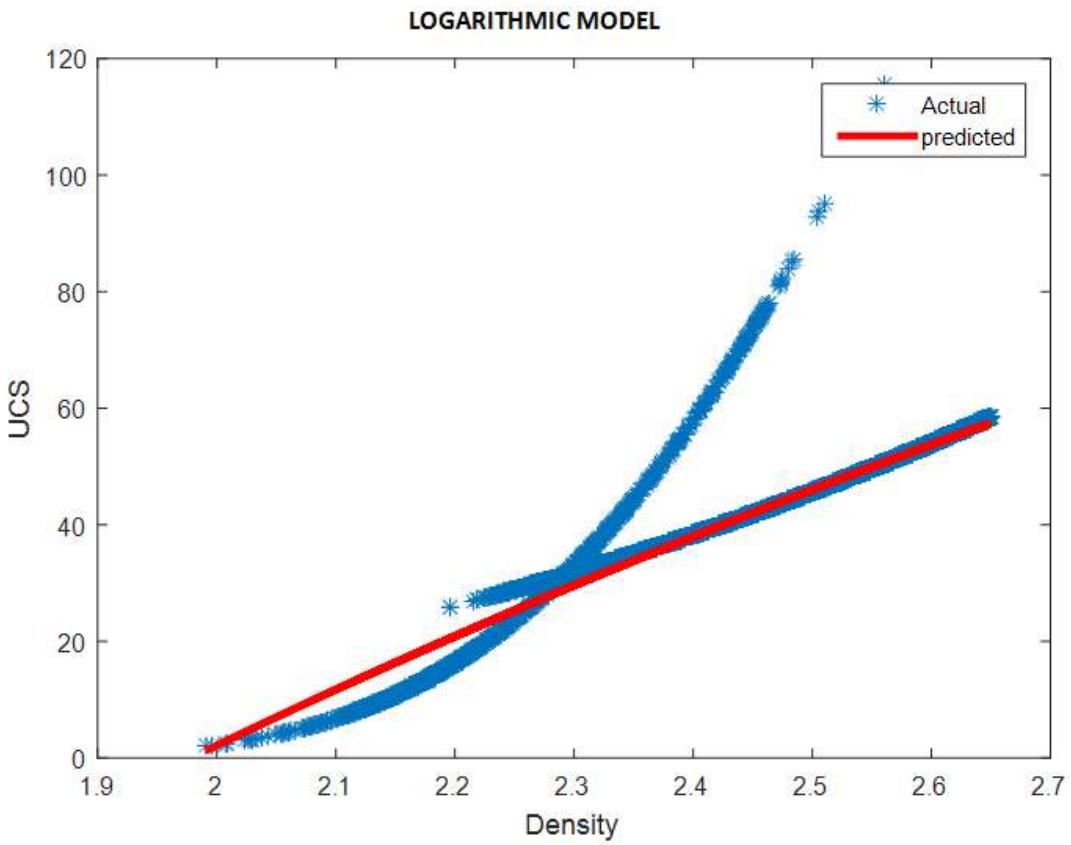


Figure 4.27: Comparative analysis of actual and predicted output for UCS versus bulk density with logarithmic model

For UCS versus sonic

Statistical table of the logarithmic model for UCS versus sonic transit time is shown in Table 4.20. In this model, y represents UCS while x represents sonic transit time in equation 3.21.

Table 4.20: Statistical table of logarithmic model for UCS versus sonic

Regression coefficient		Other statistical parameters
a_0	4.232	SSE = 2.655e+06
a_1	1.764e+08	R-square = 0.331
		Adjusted R-square = 0.331
		RMSE = 19.11

Where SSE signifies sum of square error, RMSE is root mean square error.

The comparative analysis of actual and predicted output for UCS versus sonic with logarithmic model is shown in figure 4.28.

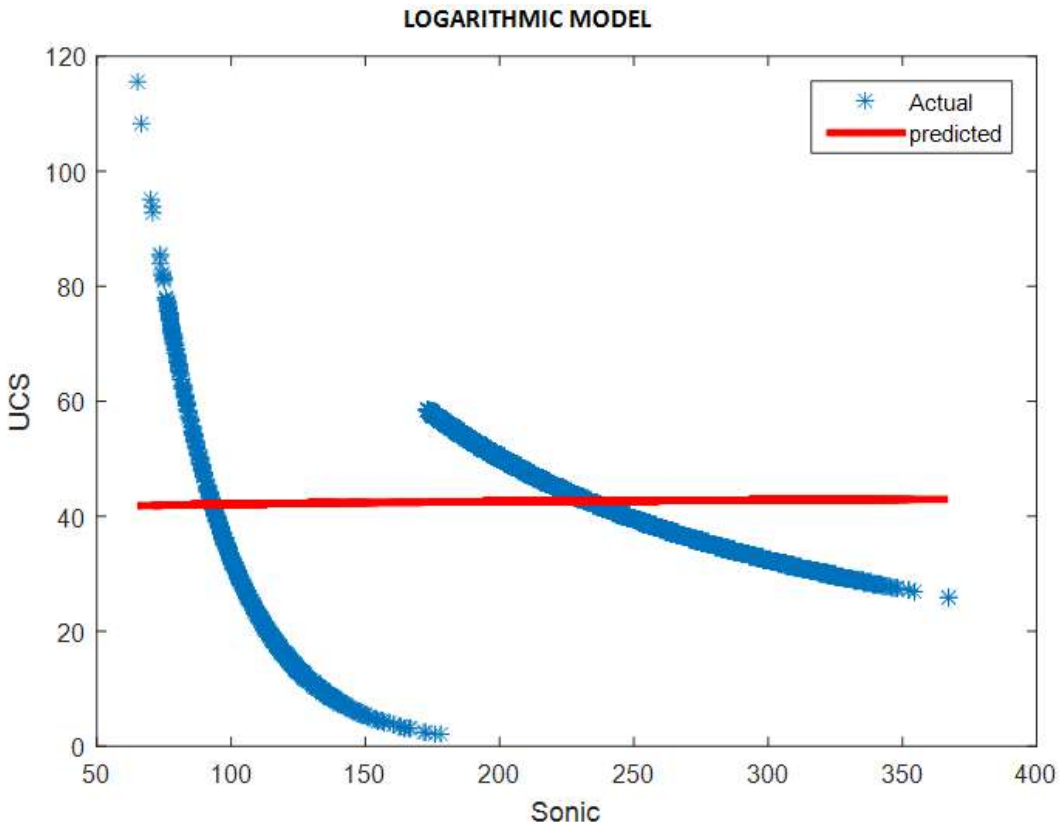


Fig. 4.28: Comparative analysis of actual and predicted output for UCS versus sonic with logarithmic model

The comparative analysis of the R-square values obtained for UCS versus bulk density and UCS versus sonic from logarithmic model is shown in figure 4.29.

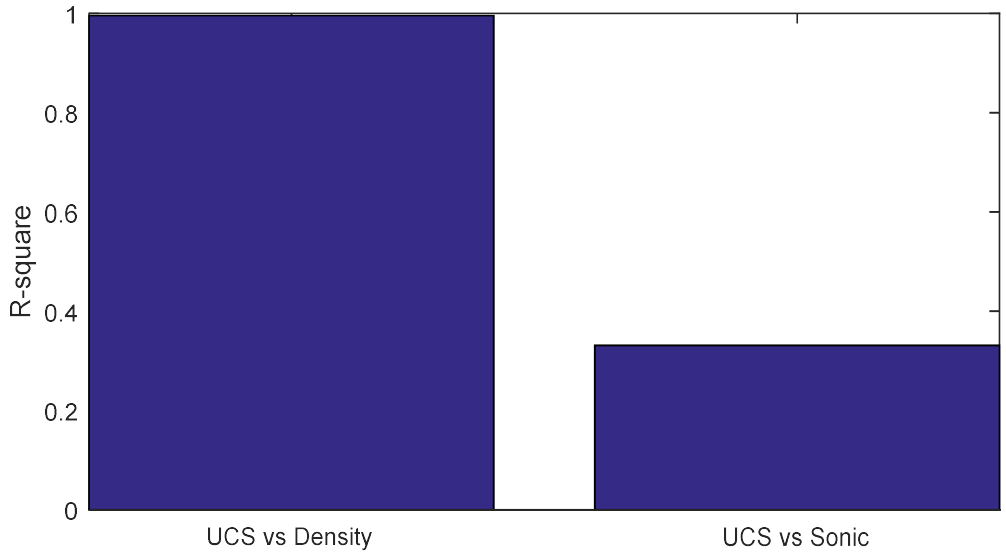


Fig. 4.29: R-square values obtained for UCS versus bulk density and UCS versus sonic from logarithmic model

Figure 4.29 shows the bar chart of the R-square values obtained for UCS versus bulk density and UCS versus sonic from logarithmic model. The bar chart of UCS versus bulk density has R-square value greater than 50% (0.9956) while that of UCS versus sonic is less than 50% (0.331). This implies that logarithmic model should be utilized in the modeling and analysis of UCS versus bulk density only.

Permeability versus bulk density

Statistical table of the logarithmic model for permeability versus bulk density is shown in Table 4.21. In this model, y represents permeability while x represents bulk density in equation 3.21.

Table 4.21: Statistical table of logarithmic model for permeability versus bulk density

Regression coefficient		Other statistical parameters
a_0	9.736	SSE = 1.513e+010
a_1	-0.9089	R-square = 0.00017
		Adjusted R-square = 0.00017
		RMSE = 357.6

Where SSE signifies sum of square error, RMSE is root mean square error.

The comparative analysis of the actual and predicted output for permeability versus bulk density with logarithmic model is shown in figure 4.30.

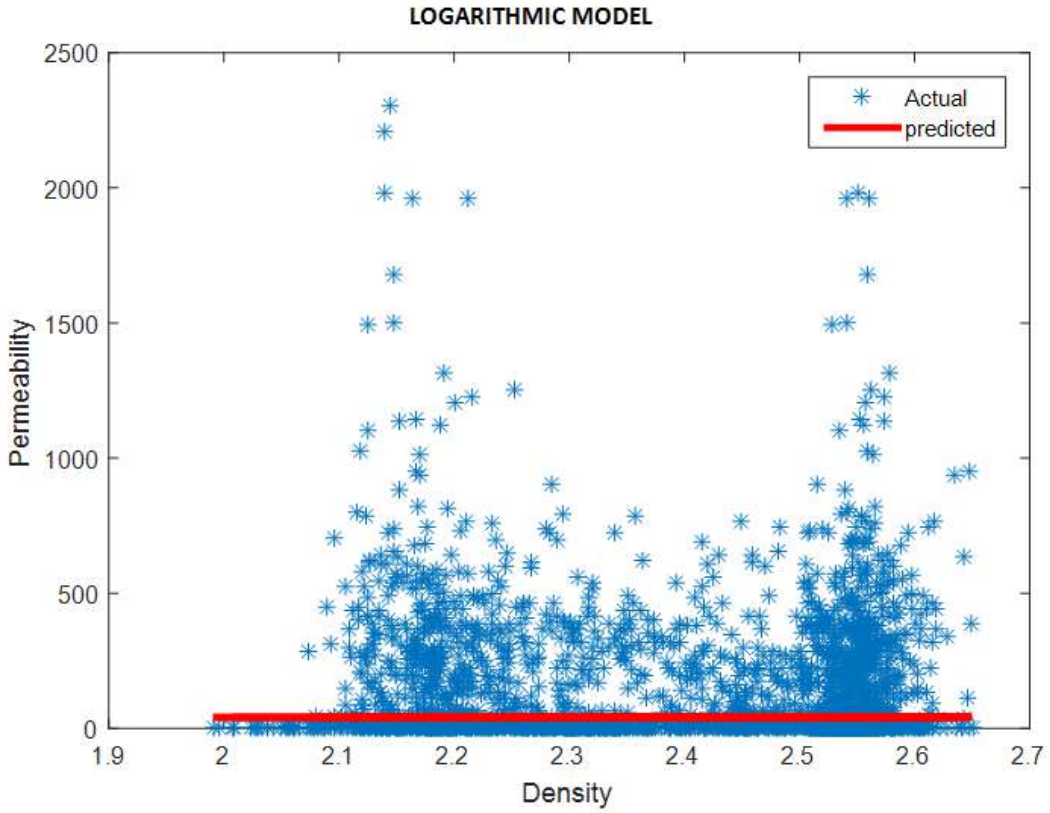


Figure 4.30: Comparative analysis of the actual and predicted output for permeability versus bulk density with logarithmic model

For shear wave velocity (V_s) versus sonic

Statistical table of the logarithmic model for shear wave velocity versus sonic transit time is shown in Table 4.22. In this model, y represents shear wave velocity while x represents sonic transit time in equation 3.21.

Table 4.22: Statistical table of logarithmic model for shear wave velocity versus sonic transit time

Regression coefficient		Other statistical parameters
a_0	486.2	SSE = 486.2
a_1	- 0.1017	R-square = 0.1017
		Adjusted R-square = 0.1022
		RMSE = 0.4628

Where SSE signifies sum of square error, RMSE is root mean square error.

The comparative analysis of actual and predicted output for shear wave velocity versus sonic transit time with logarithmic model is shown in figure 4.31.

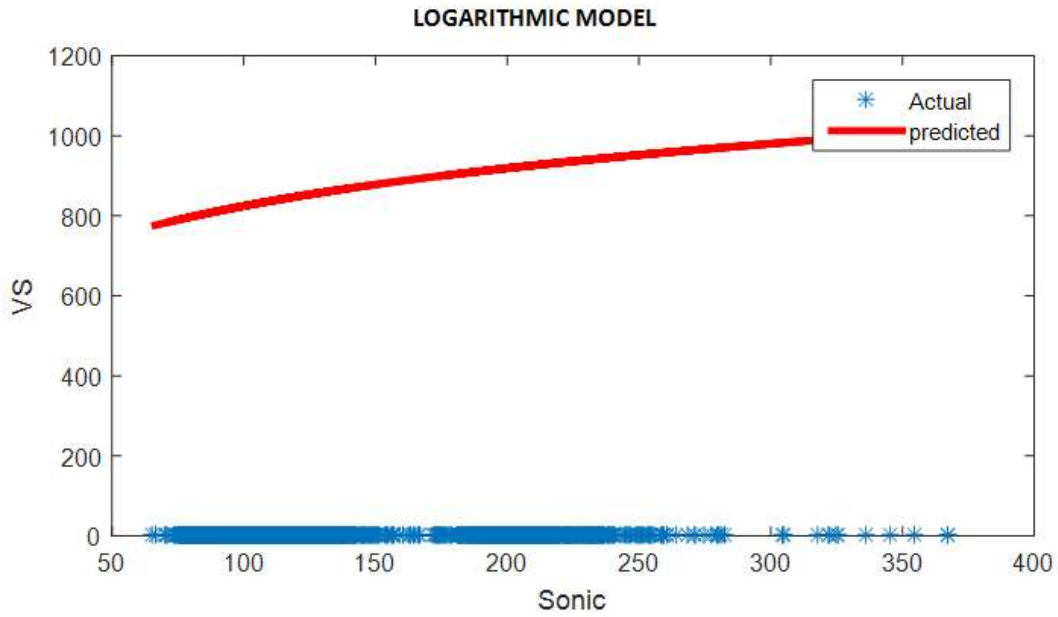


Fig. 4.31: Comparative analysis of actual and predicted output for shear wave velocity versus sonic transit time with logarithmic model

The comparative analysis of the R-square values obtained for permeability versus bulk density and shear wave velocity (V_s) versus sonic transit time from logarithmic model is shown in figure 4.32.

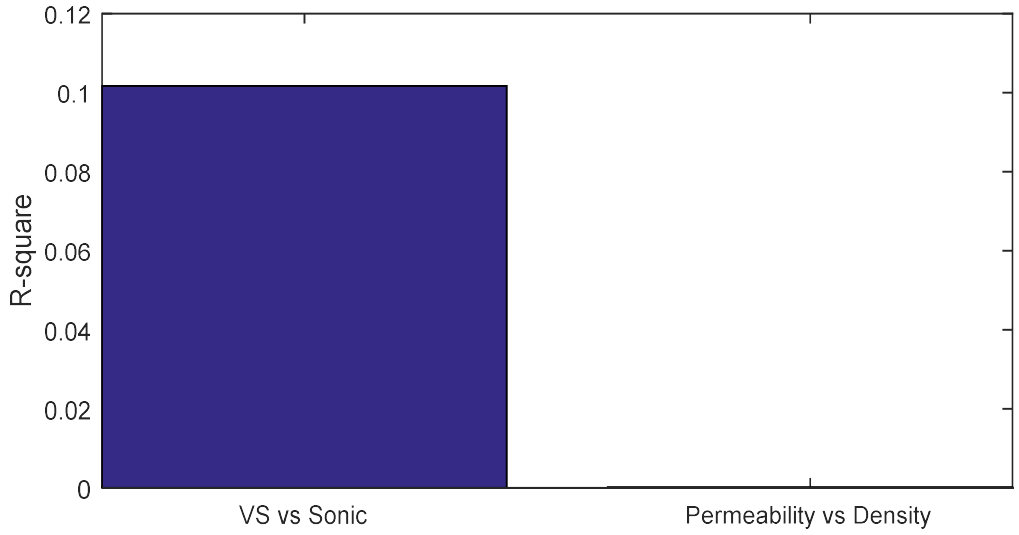


Fig. 4.32: R-square values obtained for permeability versus bulk density and shear wave velocity (V_s) versus sonic transit time from logarithmic model

Figure 4.32 shows the bar chart of the R-square values obtained for permeability versus bulk density and shear wave velocity (V_s) versus sonic transit time from logarithmic model. The figures show that the logarithmic model should not be utilized in the modeling and analysis of permeability versus bulk density and shear wave velocity (V_s) versus sonic transit time as the prediction performances of both are less than 50% (0.00017 and 0.1017).

4.1.6.4 Exponential Models

For UCS versus bulk density

The exponential model is given by equation 3.22. Statistical table of the exponential model for UCS versus bulk density is shown in Table 4.23. In this model, y represents UCS while x represents bulk density in equation 3.22.

Table 4.23: Statistical table of exponential model for UCS versus bulk density

Regression coefficient		Other statistical parameters
a_0	0.2876	SSE = 2.155e+05
a_1	2.024	R-square = 0.8108
		Adjusted R-square = 0.8108
		RMSE = 5.446

Where SSE signifies sum of square error, RMSE is root mean square error.

Therefore, the exponential model for UCS versus bulk density becomes:

$$UCS = 0.2876\exp(2.024\rho_b) \quad (4.5)$$

The comparative analysis of the actual and predicted output for UCS versus bulk density with exponential model is shown in figure 4.33.

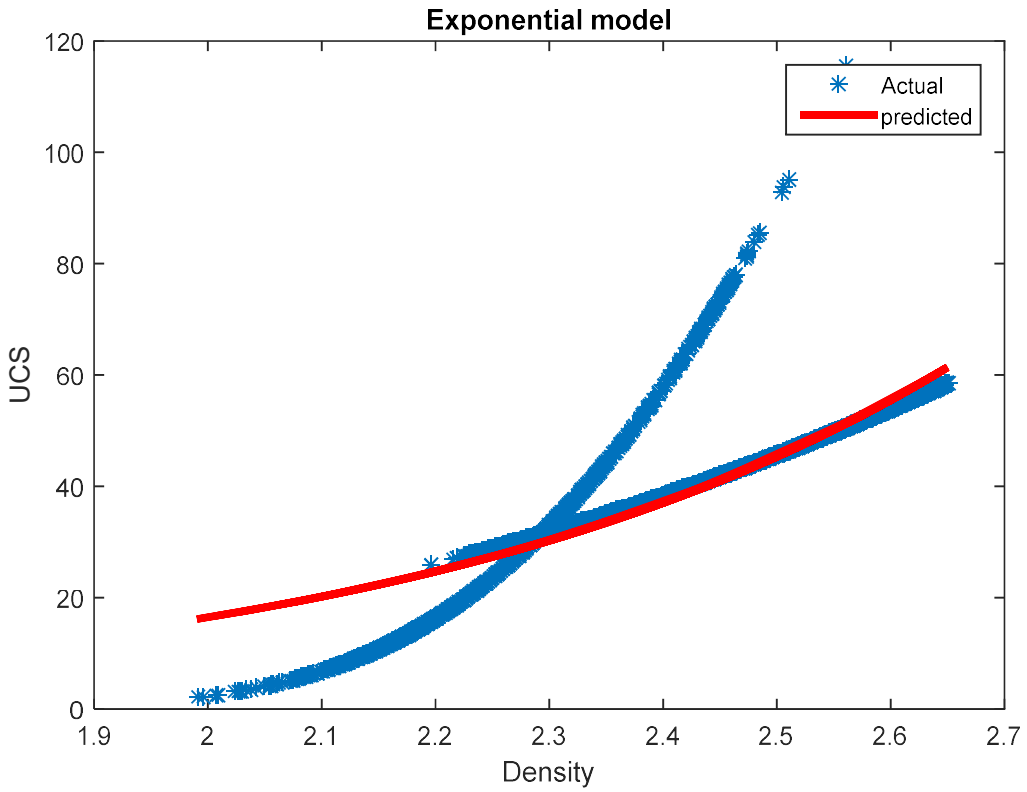


Fig. 4.33: Comparative analysis of the actual and predicted output for UCS versus bulk density with exponential model

For UCS versus sonic

Statistical table of the exponential model for UCS versus sonic transit time is shown in Table 4.24. In this model, y represents UCS while x represents sonic transit time in equation 3.22.

Table 4.24: Statistical table of exponential model for UCS versus sonic transit time

Regression coefficient		Other statistical parameters
a_0	44.96	SSE = 1.136e+06
a_1	-0.0002626	R-square = 0.002995
		Adjusted R-square = 0.002858
		RMSE = 12.5

Where SSE signifies sum of square error, RMSE is root mean square error.

The comparative analysis of actual and predicted output for UCS versus sonic transit time with exponential model is shown in figure 4.34.

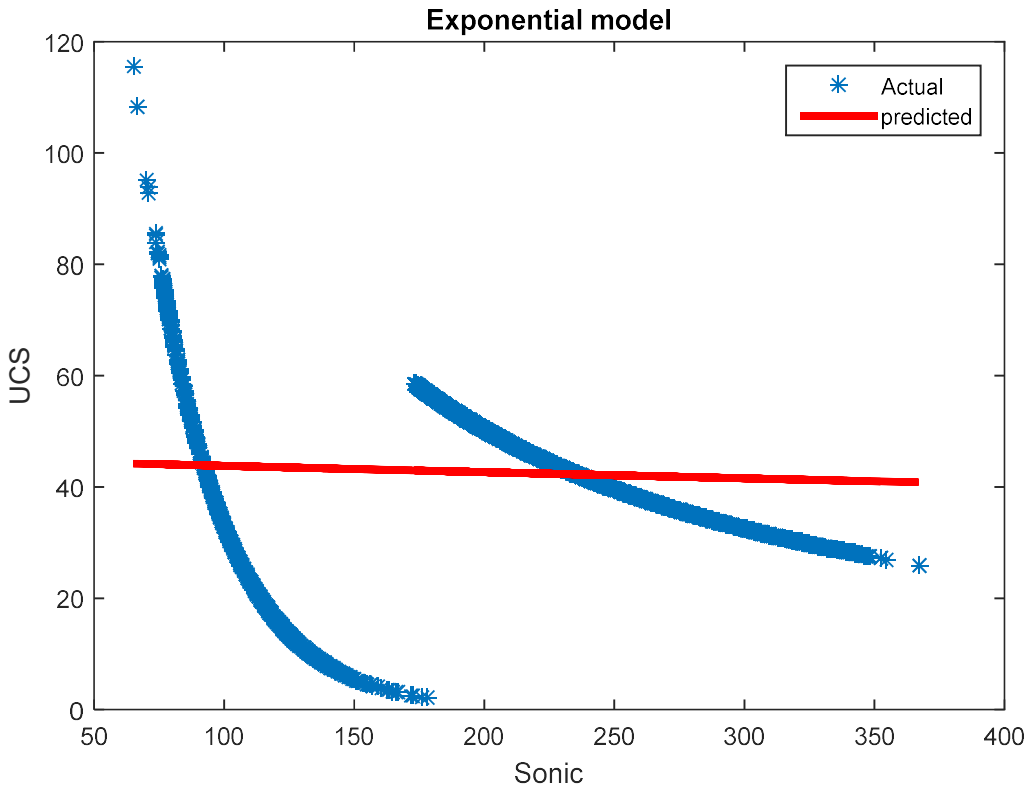


Fig. 4.34: Comparative analysis of actual and predicted output for UCS versus sonic transit time with exponential model

For the R-square values, the comparative analysis of the values obtained for UCS versus bulk density and UCS versus sonic transit time from exponential model is shown in figure 4.35.

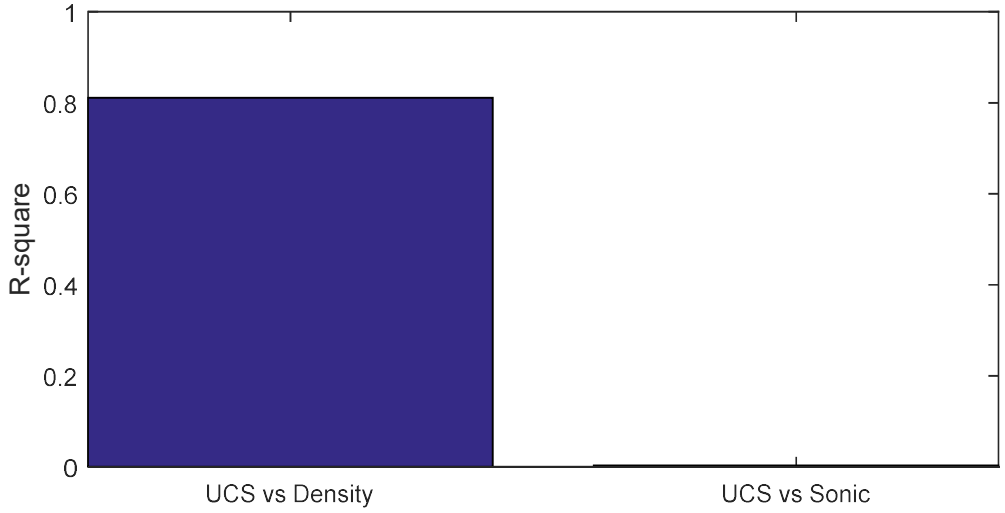


Fig. 4.35: R-square values obtained for UCS versus bulk density and UCS versus sonic transit time from exponential model

Figure 4.35 shows the bar chart of the R-square values obtained for UCS versus bulk density and UCS versus sonic transit time from exponential model. The bar chart of UCS versus bulk density has R-square value greater than 50% (0.8108) while the one of UCS versus sonic transit time is less than 50% (0.002995). This suggests that exponential model can be utilized in the modeling and analysis of UCS versus bulk density only.

For Permeability versus bulk density

Statistical table of the exponential model for permeability versus bulk density is shown in Table 4.25. In this model, y represents permeability while x represents bulk density in equation 3.22.

Table 4.25: Statistical table of exponential model for permeability versus bulk density

Regression coefficient		Other statistical parameters
a_0	396.3	SSE = 1.553e+08
a_1	-0.3686	R-square = 0.001394
		Adjusted R-square = 0.0009672
		RMSE = 257.7

Where SSE signifies sum of square error, RMSE is root mean square error.

The comparative analysis of the actual and predicted outputs for permeability versus bulk density with exponential model is shown in figure 4.36.

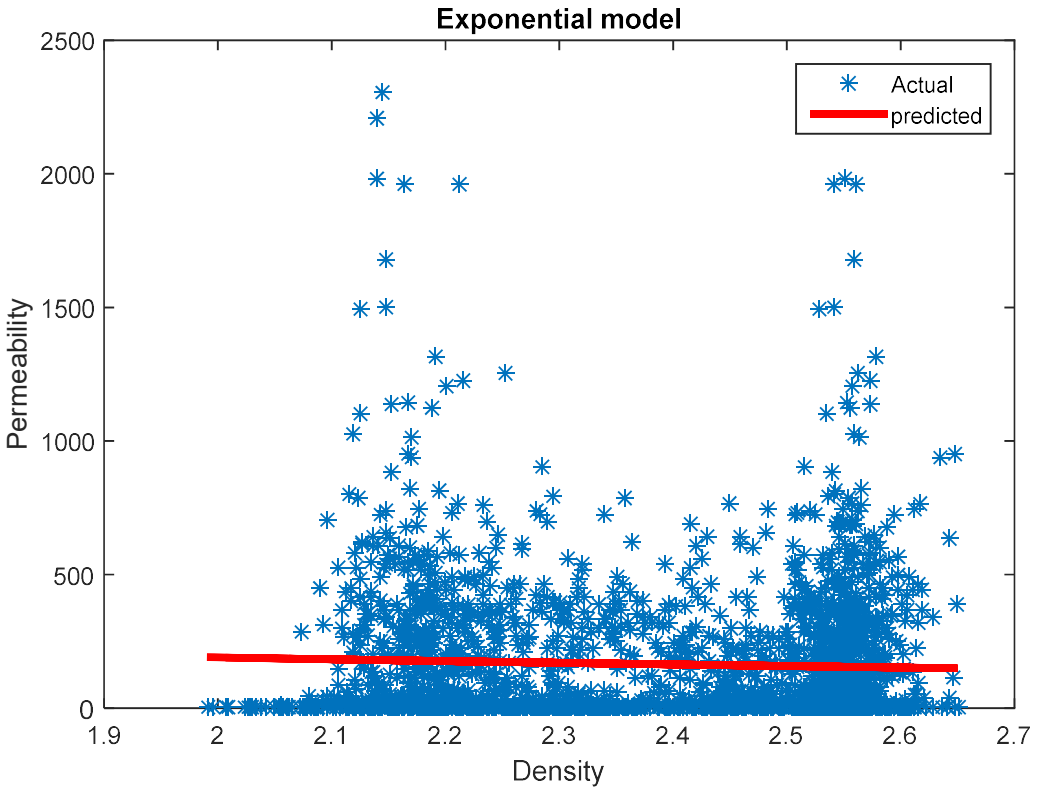


Fig. 4.36: Comparative analysis of the actual and predicted outputs for permeability versus bulk density with exponential model

For shear wave velocity (V_s) versus sonic

Statistical table of the exponential model for shear wave velocity versus sonic transit time is shown in Table 4.26. In this model, y represents shear wave velocity (V_s) while x represents sonic transit time in equation 3.22.

Table 4.26: Statistical table of exponential model for shear wave velocity versus sonic transit time

Regression coefficient		Other statistical parameters
a_0	1.652	SSE = 418.7
a_1	-0.001595	R-square = 0.05125
		Adjusted R-square = 0.05083
		RMSE = 0.4295

Where SSE signifies sum of square error, RMSE is root mean square error.

The comparative analysis of actual and predicted output for shear wave velocity versus sonic transit time with exponential model is shown in figure 4.37.

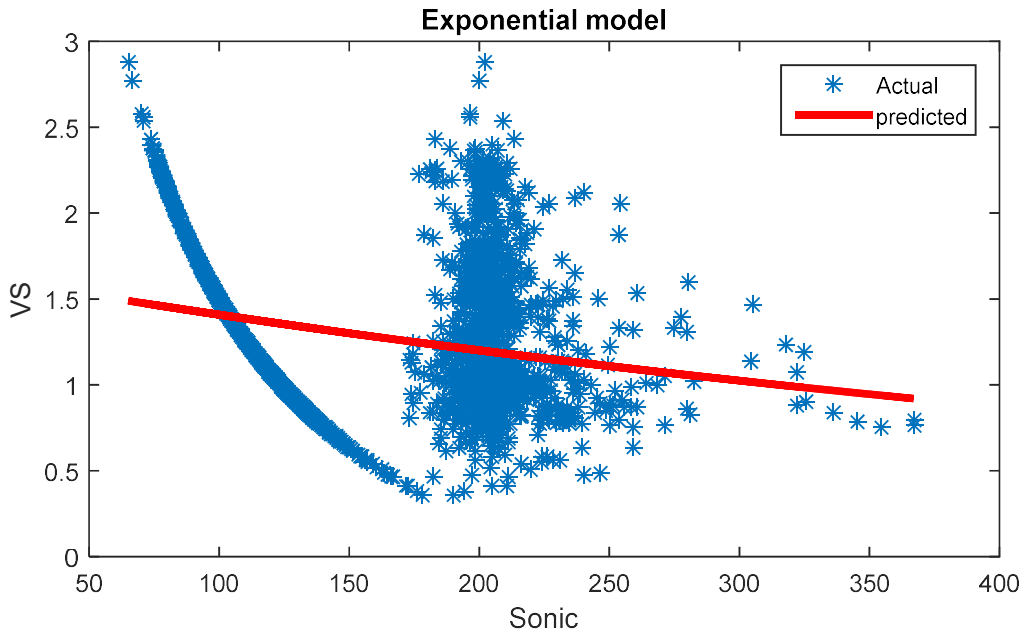


Fig. 4.37: Comparative analysis of actual and predicted output for shear wave velocity versus sonic transit time with exponential model

For the R-square values, the comparative analysis of the values obtained for permeability versus bulk density and shear wave velocity versus sonic transit time from exponential model is shown in figure 4.38.

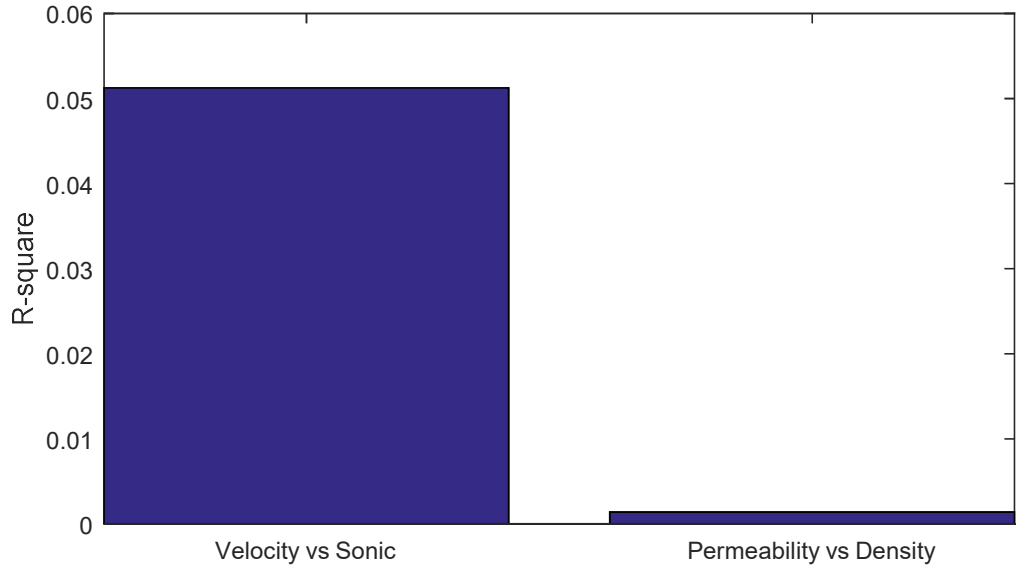


Fig. 4.38: R-square values obtained for permeability versus bulk density and shear wave velocity versus sonic transit time from exponential model

Figure 4.38 shows the bar chart of the R-square values obtained for permeability versus bulk density and shear wave velocity versus sonic transit time from exponential model. The figure shows that the exponential model should not be utilized in the modeling and analysis of permeability versus bulk density and shear wave velocity (V_S) versus sonic transit time as the prediction performances of both are less than 50% (0.001394 and 0.05125).

From the empirical linear and non-linear models, including linear, quadratic, power, logarithmic and exponential models carried out for UCS versus bulk density, UCS versus sonic transit time, permeability versus bulk density, and shear wave velocity versus sonic transit time, it is observed from the statistical parameters that for UCS versus bulk density, R-squared was greater than 50% for all the considered models (Linear 0.8637, quadratic 0.8848, power 0.8216, logarithmic 0.9956, and exponential 0.8108). This suggests that linear, quadratic, power, logarithmic and exponential models can be utilized in the modeling and analysis of UCS versus bulk density.

For UCS versus sonic transit time, it is observed from statistical parameters that R-squared is less than 50% for all the considered models (Linear 0.003559, quadratic 0.2159, power 0.0002881, logarithmic 0.331, and exponential 0.002995). This implies that linear, quadratic, power, logarithmic and exponential models cannot be utilized in the modeling and analysis of UCS versus sonic transit time.

For permeability versus bulk density, results from statistical parameters show that R-squared is less than 50% for all the considered models (Linear 0.001263, quadratic 0.009212, power 0.001547, logarithmic 0.00017, and exponential 0.001394). This implies that linear, quadratic, power, logarithmic and exponential models cannot be utilized in the modeling and analysis of permeability versus bulk density.

For shear wave velocity versus sonic transit time, results from statistical parameters show that R-squared is less than 50% for all the considered models (Linear 0.04606, quadratic 0.1214, power 0.09036, logarithmic 0.1017, and exponential 0.05125). This implies that linear, quadratic, power, logarithmic and exponential models cannot be utilized in the modeling and analysis of shear wave velocity versus sonic transit time.

4.1.7 Modeling with Artificial Neural Network (ANN)

In a similar manner to the empirical linear and non-linear models, relationships between unconfined compressive strength and bulk density, unconfined compressive strength and sonic transit time, permeability and bulk density, as well as shear wave velocity and sonic transit time were modelled with artificial neural network using the ANFIS artificial intelligence model. The results of each of the relationships are as follows.

For UCS versus bulk density

Statistical parameters including number of data samples, mean square error and R-square values for training, validation and testing and their respective values for UCS versus bulk

density are shown in figure 4.39. The structure and outcome of ANN simulation for UCS versus bulk density is shown in figure 4.40.

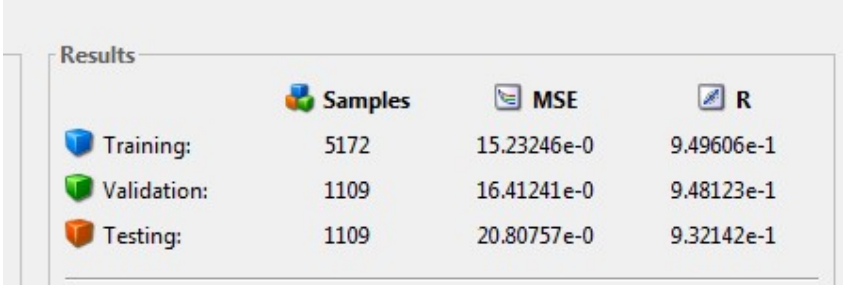


Fig. 4.39: Statistical parameters indicating degree of prediction for UCS versus bulk density

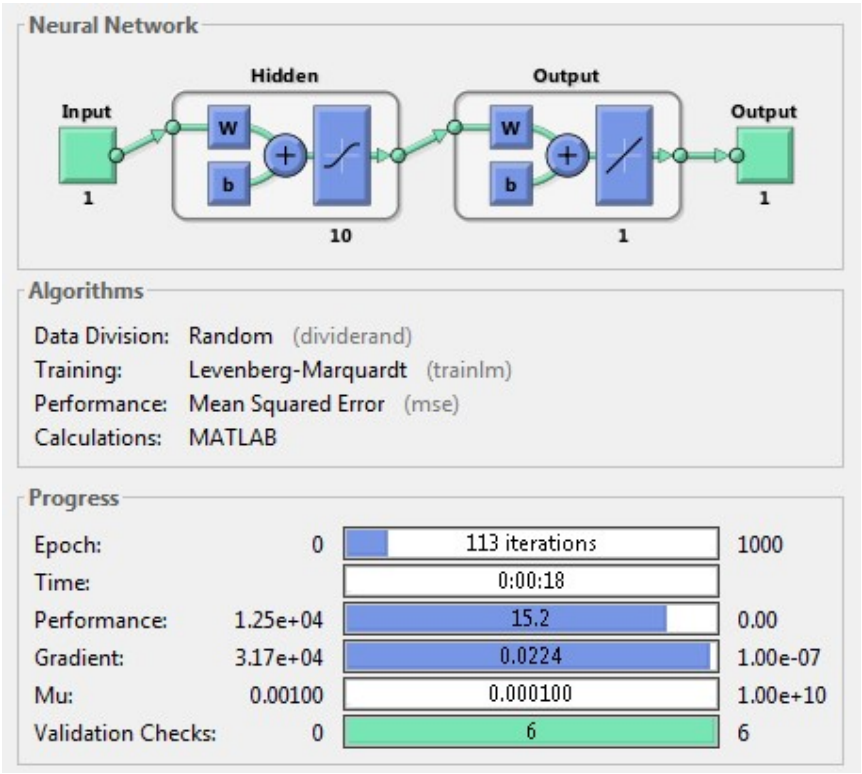


Fig. 4.40: ANN structure and outcome of ANN simulation for UCS versus bulk density

The training performance of artificial neural network for UCS versus bulk density is displayed in figure 4.41 while the R-square value of the various ANN segments (training, validation, testing and all) for UCS versus bulk density is shown in figure 4.42.

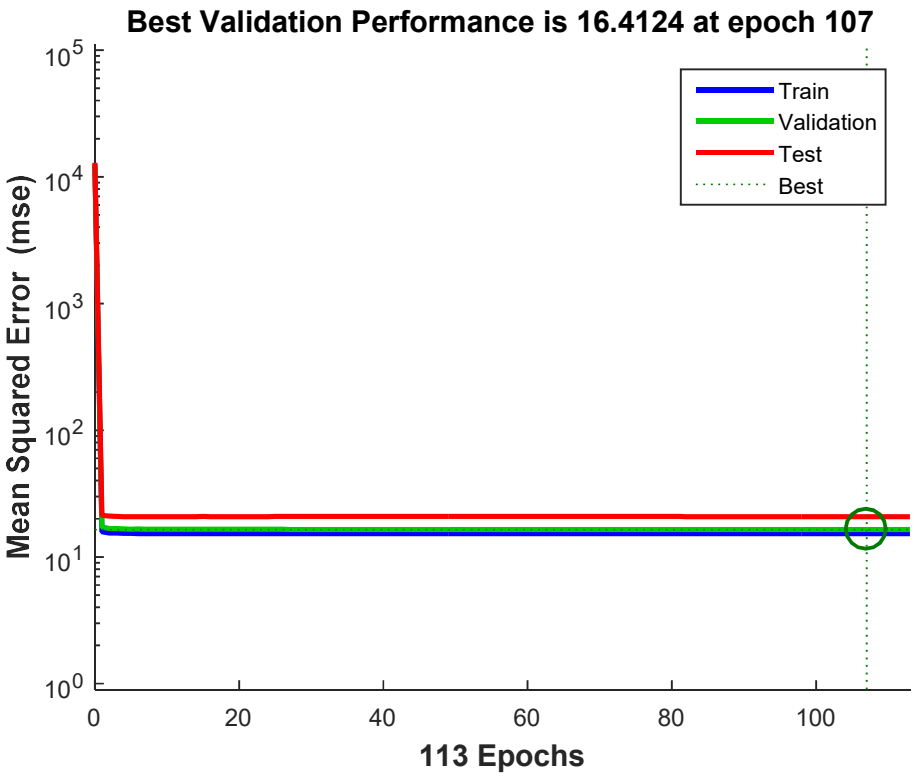


Fig. 4.41: Training performance of artificial neural network for UCS versus bulk density

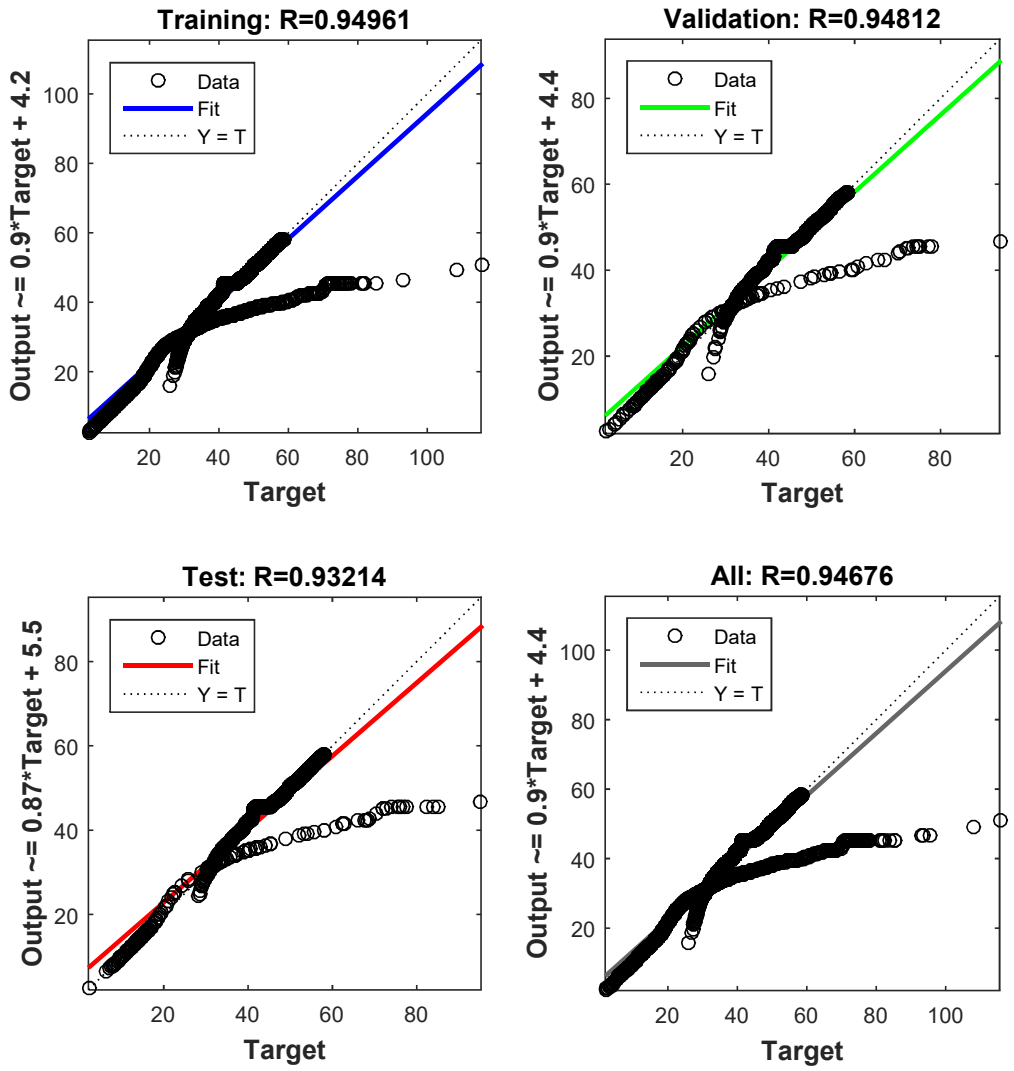


Fig. 4.42: R-square value of the various ANN segments for UCS versus bulk density

The comparative analysis of actual and predicted output for UCS versus bulk density with ANN model is shown in figure 4.43.

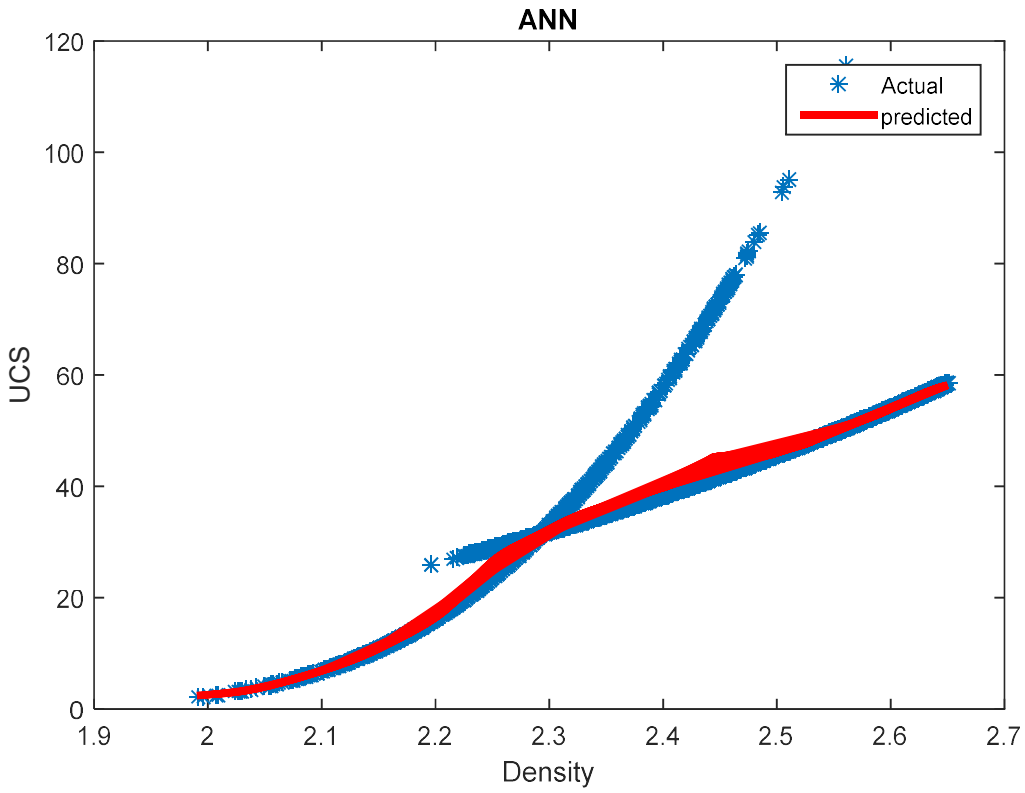


Fig. 4.43: Comparative analysis of actual and predicted output for UCS versus bulk density with ANN model

For UCS versus sonic

Statistical parameters including number of data samples, mean square error and R-square values for training, validation and testing and their respective values for UCS versus sonic transit time are shown in figure 4.44. The structure and outcome of ANN simulation for UCS versus sonic is shown in figure 4.45.

Results

	Samples	MSE	R
Training:	5172	1.20183e-0	9.96155e-1
Validation:	1109	8.88044e-1	9.97211e-1
Testing:	1109	1.47709e-1	9.99531e-1

Fig. 4.44: Statistical parameters indicating degree of prediction for UCS versus sonic

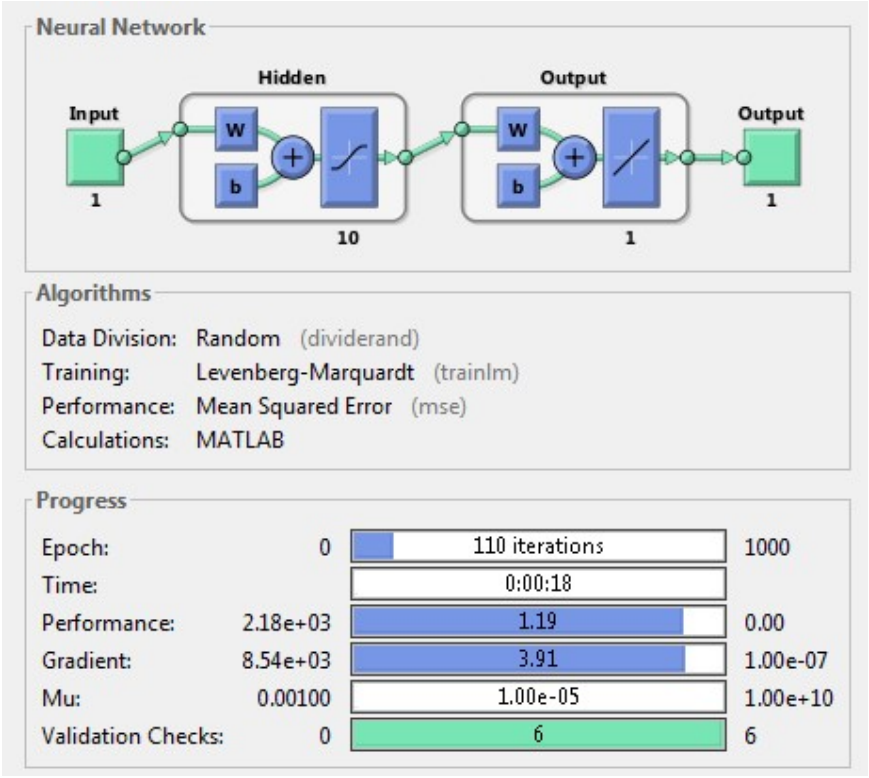


Fig. 4.45: ANN structure and outcome of ANN simulation for UCS versus sonic

The training performance of artificial neural network for UCS versus sonic transit time is displayed in figure 4.46 while the R-square value of the various ANN segments (training, validation, testing and all) for UCS versus sonic transit time is shown in figure 4.47.

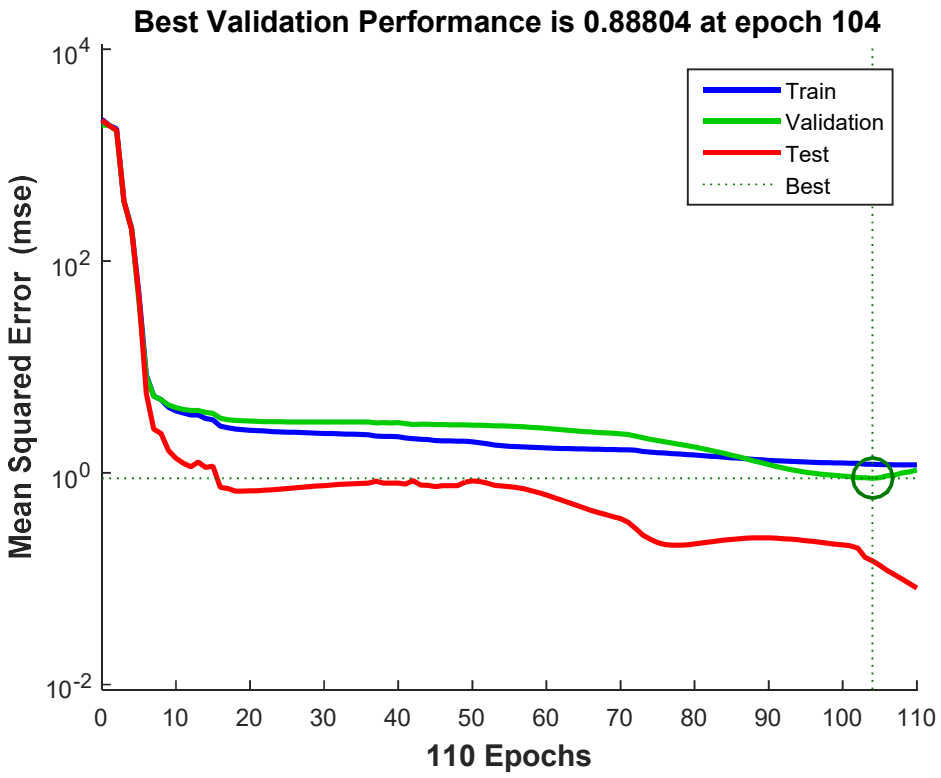


Fig. 4.46: Training performance of artificial neural network for UCS versus sonic transit time

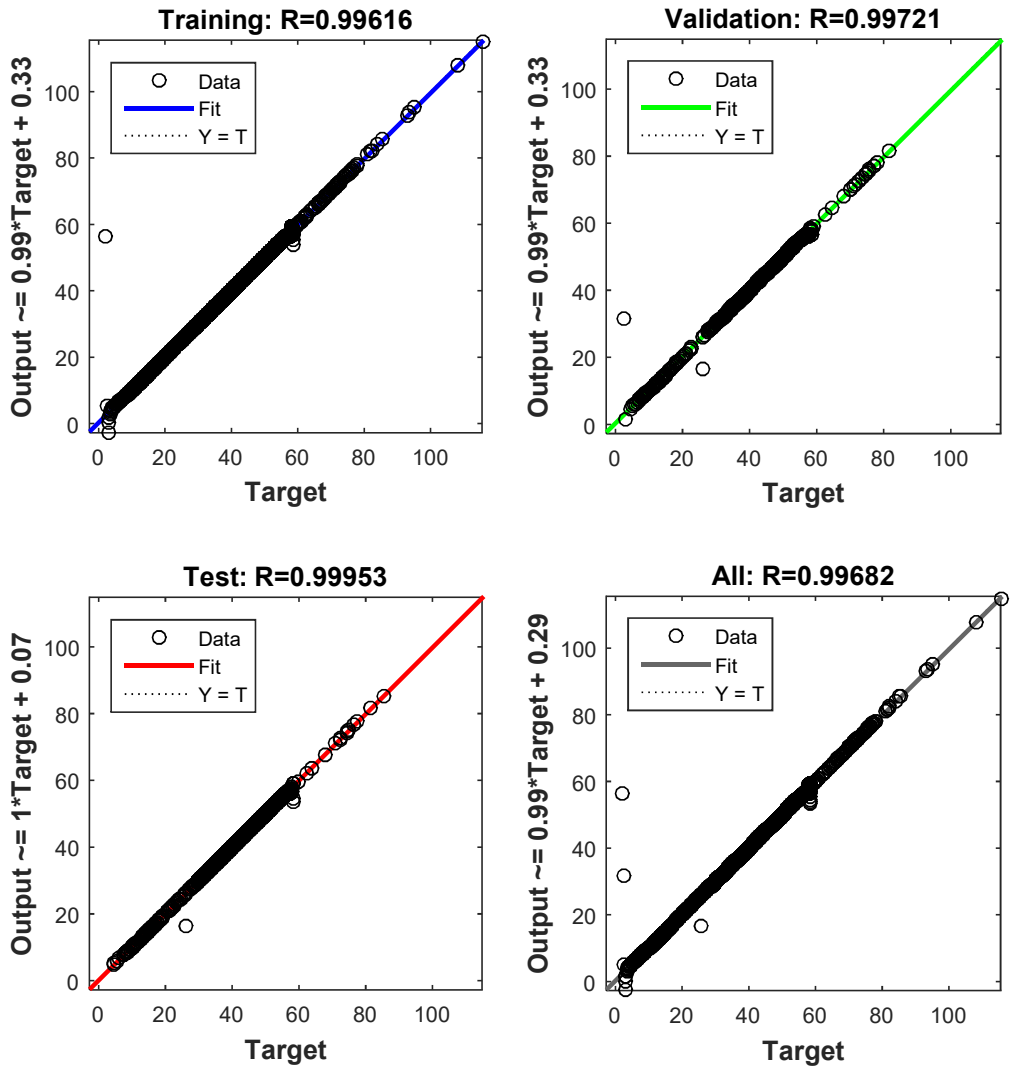


Fig. 4.47: R-square value of the various ANN segments for UCS versus sonic transit time

The comparative analysis of actual and predicted output for UCS versus sonic transit time with ANN model is shown in figure 4.48.

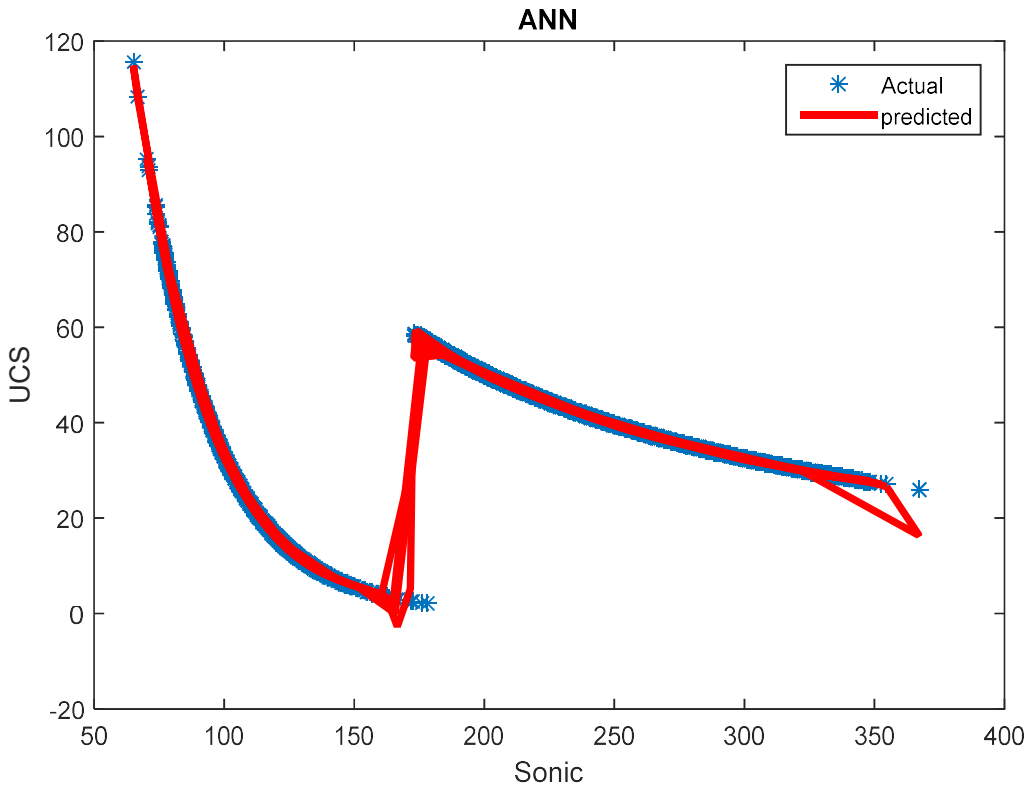


Fig. 4.48: Comparative analysis of actual and predicted output for UCS versus sonic transit time with ANN model

For the R-square values, the bar chart of values obtained for UCS versus bulk density and UCS versus sonic transit time from ANN model is shown in figure 4.49.

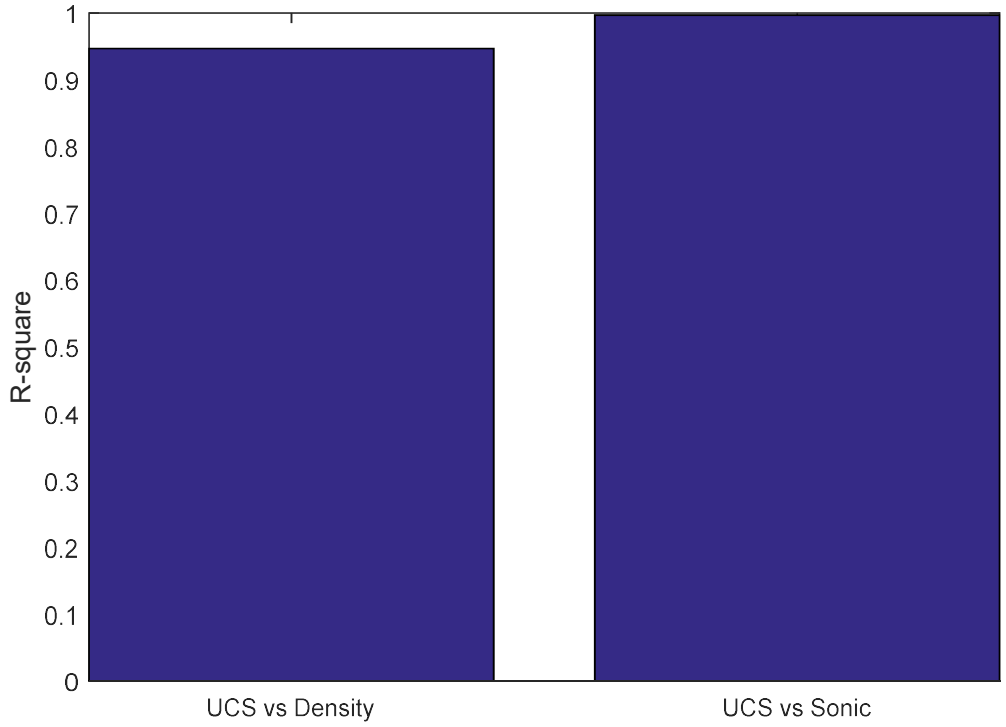


Fig. 4.49: R-square values obtained for UCS versus bulk density and UCS versus sonic transit time from ANN model

Figure 4.49 shows the bar chart of the R-square values obtained for UCS versus bulk density and UCS versus sonic transit time from ANN model. The bar chart of UCS versus bulk density and UCS versus sonic transit time has R-square values greater than 50% (0.93214 and 0.99953).This suggests that ANN model should be utilized in the modeling and analysis of both relationships.

For Permeability versus bulk density

Statistical parameters including number of data samples, mean square error and R-square values for training, validation and testing and their respective values for permeability versus bulk density are shown in figure 4.50. The structure and outcome of ANN simulation for permeability versus bulk density is shown in figure 4.51.

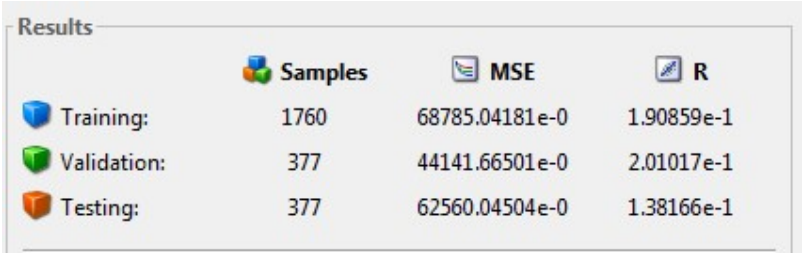


Fig. 4.50: Statistical parameters indicating degree of prediction for permeability versus bulk density

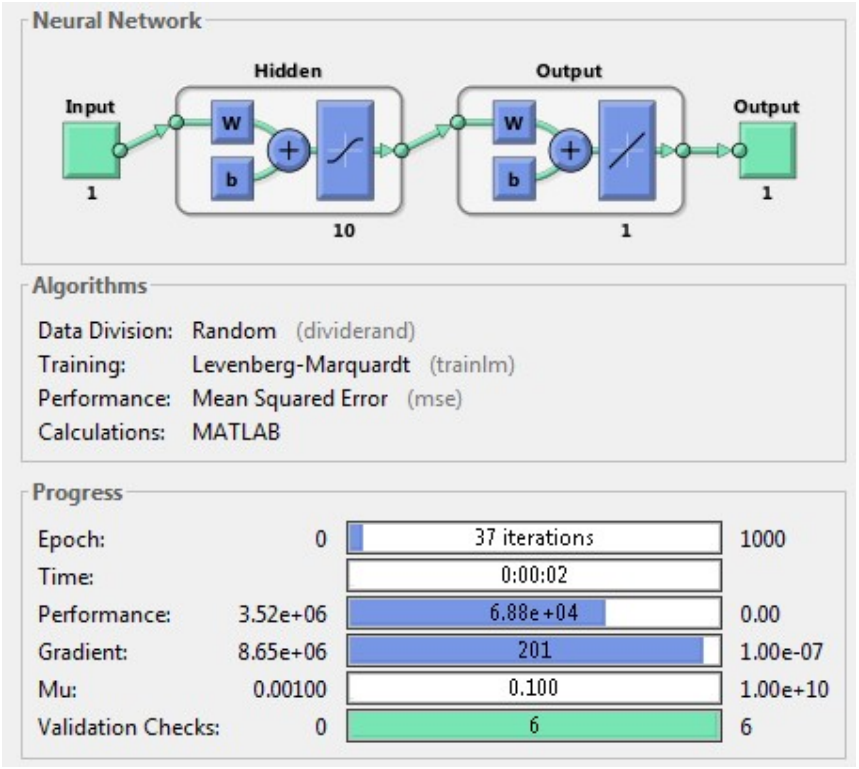


Fig. 4.51: ANN structure and outcome of ANN simulation for permeability versus bulk density

The training performance of artificial neural network for permeability versus bulk density is displayed in figure 4.52 while the R-square value of the various ANN segments (training, validation, testing and all) for permeability versus bulk density is shown in figure 4.53.

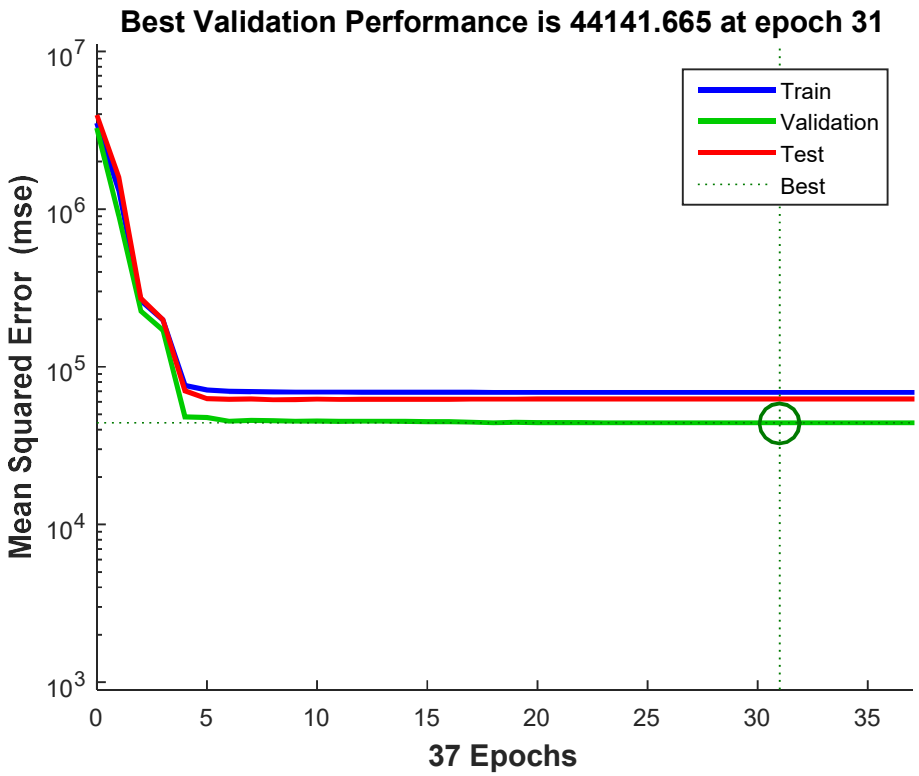


Fig. 4.52: Training performance of artificial neural network for permeability versus bulk density

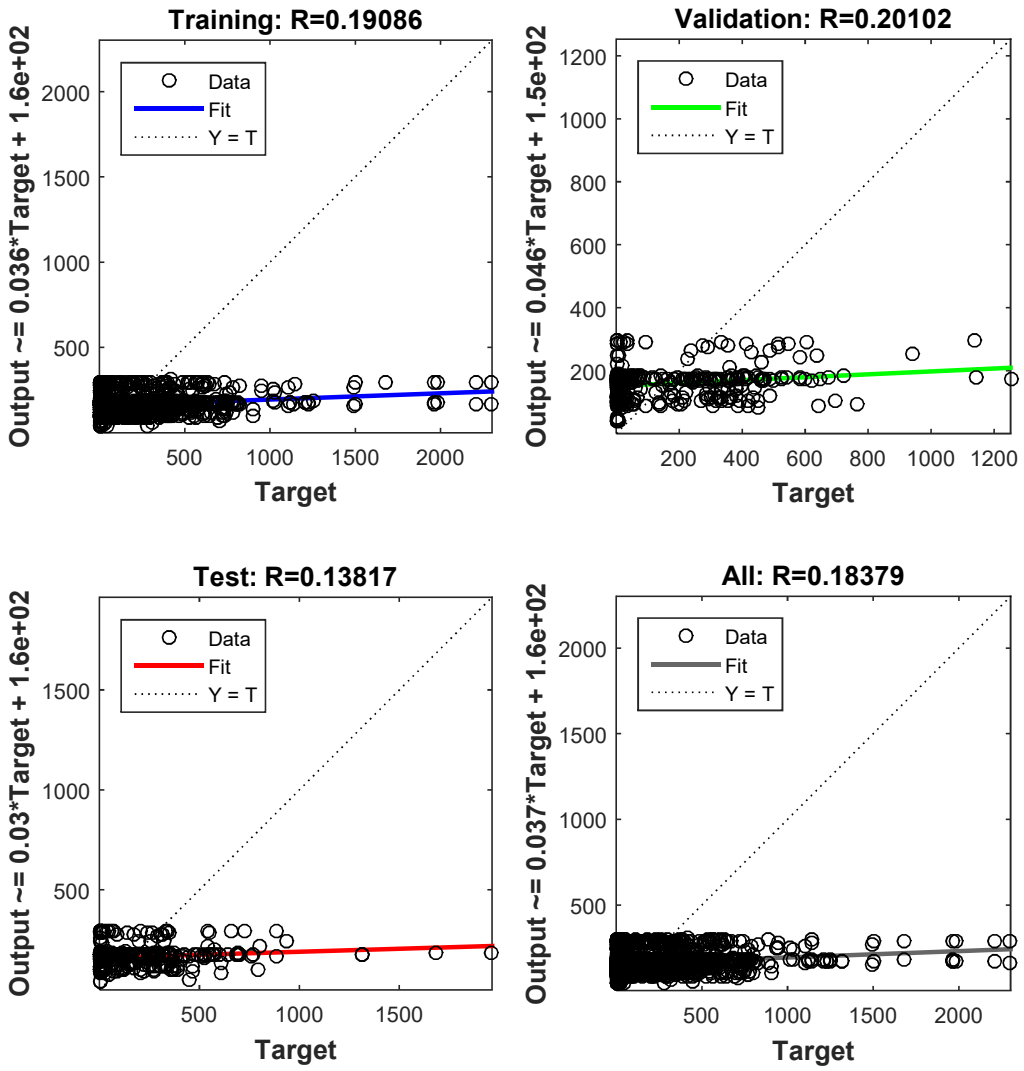


Fig. 4.53: R-square value of the various ANN segments for permeability versus bulk density

The comparative analysis of actual and predicted output for permeability versus bulk density with ANN model is shown in figure 4.54.

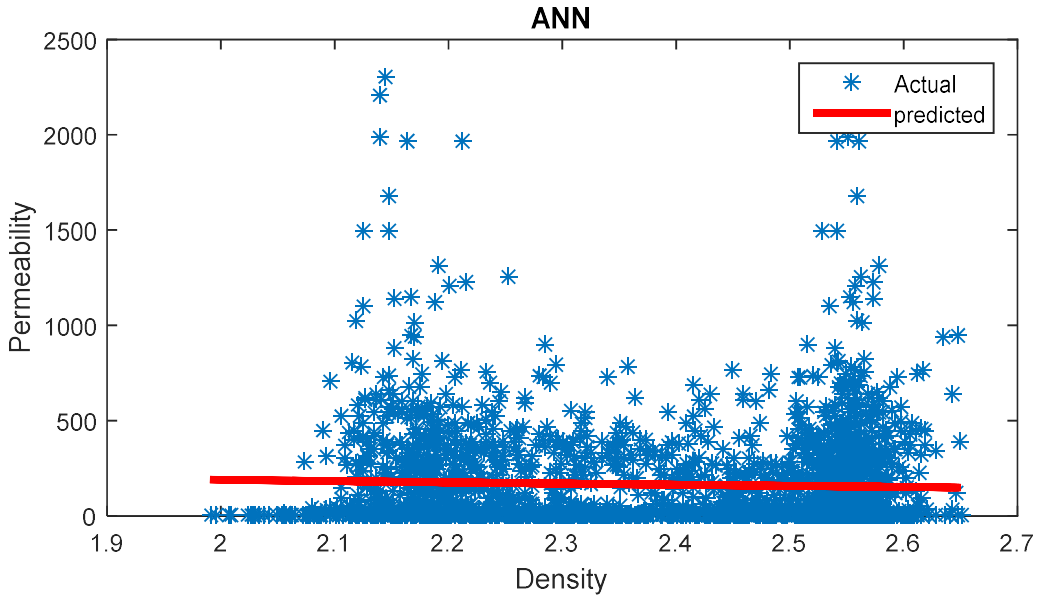


Fig. 4.54: Comparative analysis of actual and predicted output for permeability versus bulk density with ANN model

For shear wave velocity versus sonic

Statistical parameters including number of data samples, mean square error and R-square values for training, validation and testing and their respective values for shear wave velocity versus sonic transit time are shown in figure 4.55. The structure and outcome of ANN simulation for shear wave velocity versus sonic transit time is shown in figure 4.56.

Results

	Samples	MSE	R
Training:	1760	9.31841e-2	7.28092e-1
Validation:	377	8.07891e-2	7.42460e-1
Testing:	377	9.69061e-2	6.98539e-1

Fig. 4.55: Statistical parameters indicating degree of prediction for shear wave velocity versus sonic

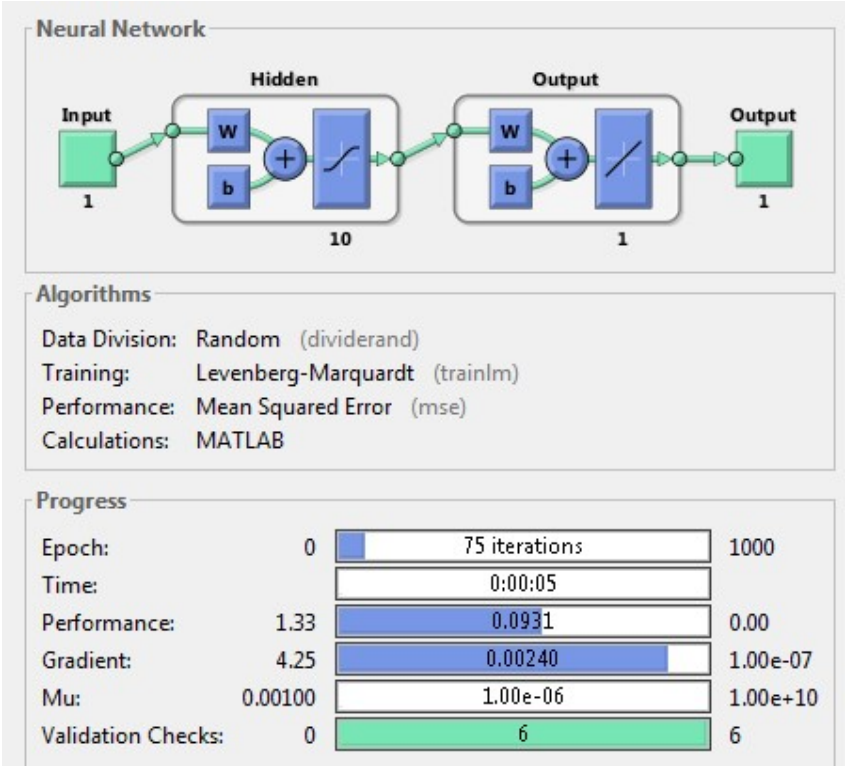


Fig. 4.56: ANN structure and outcome of ANN simulation for shear wave velocity versus sonic

The training performance of artificial neural network for shear wave velocity versus sonic transit time is displayed in figure 4.57 while the R-square value of the various ANN segments (training, validation, testing and all) for shear wave velocity versus sonic transit time is shown in figure 4.58.

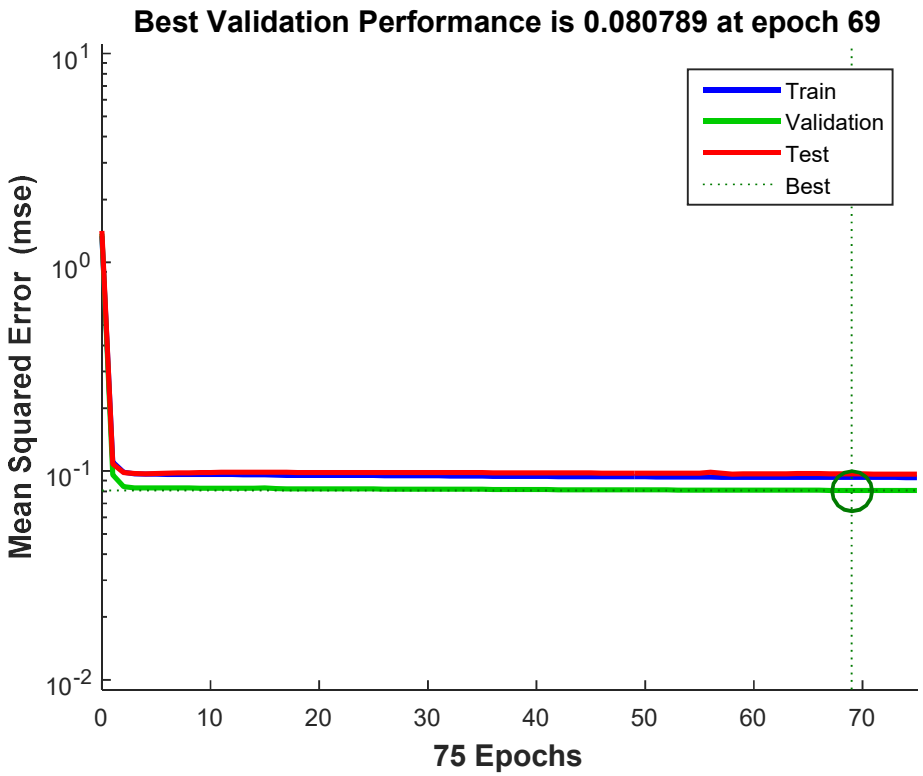


Fig. 4.57: Training performance of artificial neural network for shear wave velocity versus sonic

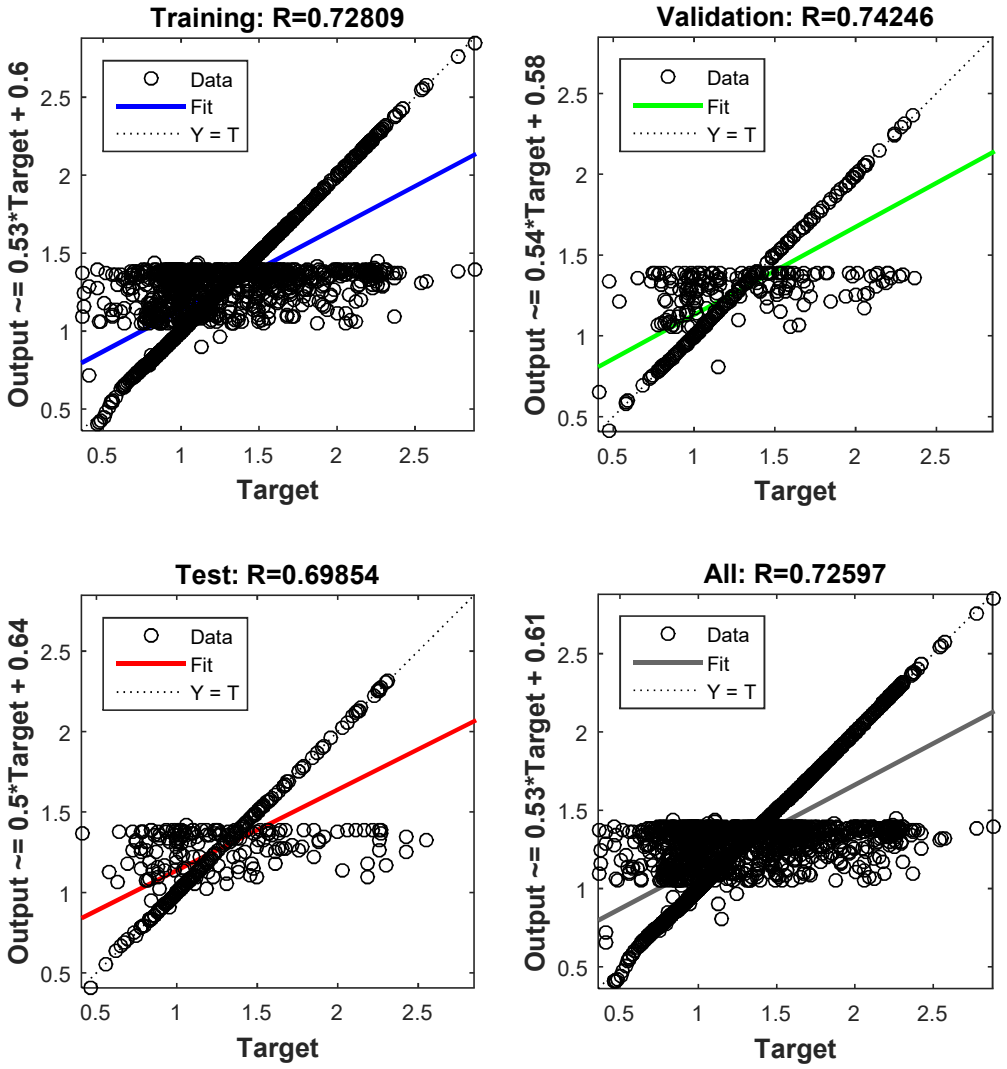


Fig. 4.58: R-square value of the various ANN segments for shear wave velocity versus sonic

The comparative analysis of actual and predicted output for shear wave velocity versus sonic transit time with ANN model is shown in figure 4.59.

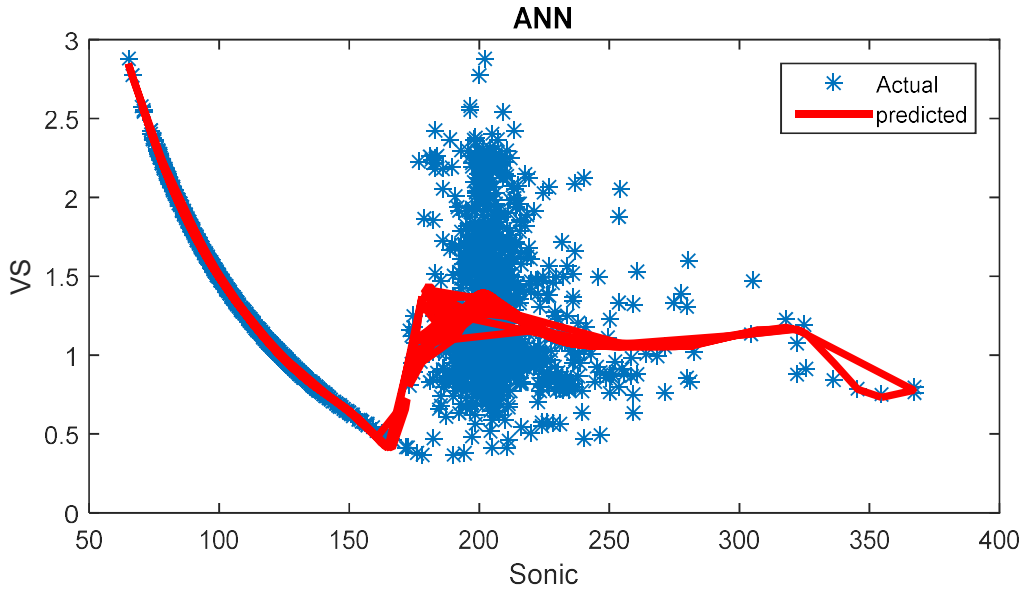


Fig. 4.59: Comparative analysis of actual and predicted output for shear wave velocity versus sonic with ANN model

For the R-square values, the bar chart of values obtained for permeability versus bulk density and shear wave velocity versus sonic transit time from ANN model is shown in figure 4.60.

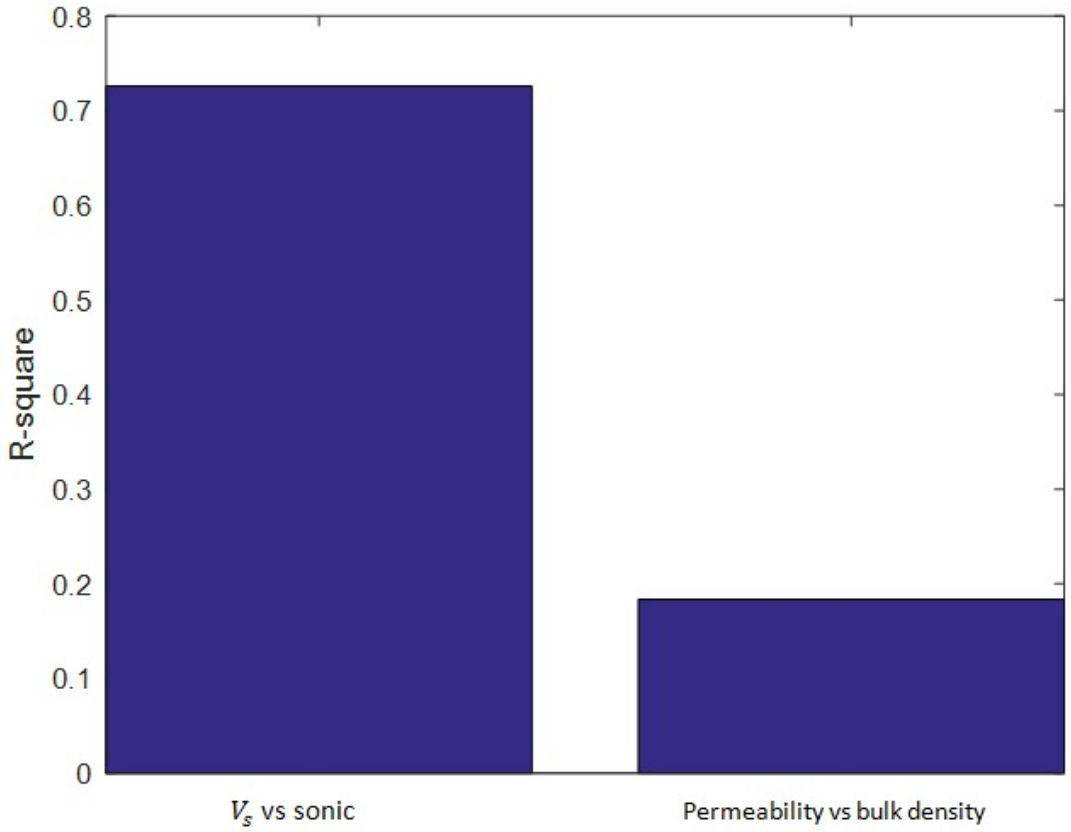


Fig. 4.60: R-square values obtained for permeability versus bulk density and shear wave velocity versus sonic from ANN model

Figure 4.60 shows the bar chart of the R-square values obtained for permeability versus bulk density and shear wave velocity versus sonic from ANN model. The bar chart of shear wave velocity versus sonic transit time has R-square values greater than 50% (0.69854) while that of permeability versus bulk density has R-square value less than 50% (0.13817). This suggests that ANN model should be utilized in the modeling and analysis of shear wave velocity versus sonic transit time only.

Artificial neural network using the adaptive-neuro fuzzy inference system (ANFIS) artificial intelligence model has been used to model the four parameter relationships including UCS versus bulk density, UCS versus sonic transit time, permeability versus bulk density, and shear wave velocity versus sonic transit time with a view to ascertaining their performance predictions using the various statistical parameters.

From the results observed for UCS versus bulk density, the best validation performance occurred at a mean square error of 16.4124 and the R-squared values for training, validation and testing data all exceeded 50% (0.94961, 0.94812 and 0.93214 respectively). This implies that artificial neural network model should be utilized in the modeling and analysis of UCS versus bulk density.

From the results of the modeling of UCS versus sonic transit time, the best validation performance occurred at a mean square error of 0.88804 and the R-squared values for training, validation and testing data all exceeded 50% (0.99616, 0.99721 and 0.99953 respectively). This implies that artificial neural network model should be utilized in the modeling and analysis of UCS versus sonic transit time.

From the observed results for permeability versus bulk density, the best validation performance occurred at a mean square error of 44141.665 and the R-squared values for training, validation and testing data did not exceed 50% (0.19086, 0.20102 and 0.13817 respectively). This low R-squared value could be as a result of pressure variations leading to irregular permeability information within the reservoirs. This result therefore implies that artificial neural network model cannot be utilized in the modeling and analysis of permeability versus bulk density.

Finally, for shear wave velocity (V_s) versus sonic transit time, the best validation performance occurred at a mean square error of 0.080789. Just like in UCS versus bulk density and UCS versus sonic transit time, the R-squared values for training, validation and testing data all exceeded 50% (0.72809, 0.74246 and 0.69854 respectively). This also implies that artificial neural network model should be utilized in the modeling and analysis of shear wave velocity (V_s) versus sonic transit time.

4.2 Discussion

The relationship between rock elastic, inelastic and petrophysical properties for sand and shale observed in this study for the two Fields show strong similarity with the results obtained by Chang et al, (2006) in the work ‘‘Empirical relations between rock strength and physical properties in sedimentary rocks’’. They Compared different empirical equations for the dependence of unconfined compressive strength of shale and sandstone on primary wave velocity (Vp), Young’s modulus and porosity and observed that unconfined compressive rock strength increased with Vp and Young’s modulus but decreased with increasing porosity which is similar to what is obtained in this study. In a similar study conducted for massive to medium to thickly bedded, red, coarse-grained and pebbly volcanic sandstone, and massive, unbedded, poorly sorted, lapilli tuff and matrix-to-clast-supported coarse breccias belonging to Borrowdale Volcanic Group, Sellafield, Entwisle, Hobbs, Jones, Gunn, & Raines (2005) obtained a result which agrees with the result of this study. They observed that unconfined compressive strength increased exponentially with increasing seismic velocity but decreased exponentially with increasing effective porosity, while seismic velocity decreased with increasing effective porosity. The only variation, however, is that in this work, the unconfined compressive strength increased linearly with increasing seismic velocity (V_P and V_S). The same can also be said of the results obtained by Horsrud (2001) in the estimation of mechanical properties of North Sea shale from empirical correlations. From his findings, Young’s modulus, shear modulus and unconfined compressive strength increased with increasing Vp while unconfined compressive strength decreased with increasing total porosity which are in agreement with the findings of this study in the two Fields. Furthermore, results of this work also show similarities with the findings of Garia, Pal, Ravi, and Nair (2019) who carried out comprehensive analysis on the relationships between static elastic wave velocities and petrophysical properties of sedimentary rocks. They observed that

both compressional and shear wave velocities decrease with increasing porosity in sedimentary rocks which agrees with the results of this study.

In this work, the generated 3D geomechanical models revealed areas of mechanical rock weakness within the reservoir top which will guide placement of future wells within the reservoir. This is in agreement with the findings of De Souza et al. (2014) who identified areas of higher and lower risk of mechanical rock failure within a reservoir through 3D geomechanical modeling and reservoir simulation in offshore Brazil. Another survey carried out to investigate the mechanical properties of reservoir rock in the Niger Delta by Osaki et al, (2019) shows average values of 0.28, 2.4GPa, 10.5GPa, 6.83GPa, 14.44MPa for sand and 0.35, 8.93GPa, 18.08GPa, 21.01GPa, 56.17MPa for shale representing Poisson ratio, Young, bulk, shear modulus and unconfined compressive strength respectively. This shows that the shale of that reservoir has higher strength and ductility than the sand which is also in total agreement with the findings of this work. Finally, the pore pressure gradient obtained in this study is in total agreement with the findings of Agbasi et al (2020) who obtained pore pressure gradients of 0.435psi/foot and 0.49psi/foot for lower Agbada sands and shales respectively while assessing pore pressure, wellbore failure and reservoir stability in Gabo Field, Niger Delta, Nigeria.

CHAPTER V

CONCLUSION AND RECOMMENDATIONS

5.1 Summary

The geomechanical characteristics of the reservoirs of ‘‘Beta’’ and ‘‘Fuja’’ Fields, offshore Niger Delta have been carefully studied and geomechanical models generated using well log information, 3D seismic volumes and core data from the two fields. Also, four different parameter relationships including UCS versus bulk density, UCS versus sonic transit time, permeability versus bulk density, and shear wave velocity versus sonic transit time from both fields have been modeled using empirical linear and non-linear models and artificial neural network. Stratigraphic correlation, well-to-seismic tie as well as horizon and fault picking were done using well log and 3D seismic data to delineate the reservoirs for both fields. The depth of the reservoir of Beta Field fell between 8,860ft and 10,220ft (thickness of 1,360ft) in the central part of the field, while the depth of the reservoir of Fuja Field fell between 9,100ft and 9,860ft (thickness of 760ft) also around the central portion of the field.

Estimation of the elastic, inelastic and petrophysical properties as well as effective pressure of the rocks of both reservoirs was done using empirical relationships after which logs of these properties were generated using Petrel software. Results revealed that the average values of the elastic and inelastic rock properties in addition to effective pressure are higher in shale than sand while the petrophysical properties and bulk compressibility are higher in sand than shale in both reservoirs. In Beta reservoir sand, the average Poisson’s ratio is 0.30, Young’s modulus is 10.94GPa, bulk modulus is 12.76GPa, shear modulus gave 4.11GPa, bulk compressibility is $0.10GPa^{-1}$, unconfined compressive strength is 25.19GPa, total porosity is 0.25, effective porosity is 0.19, permeability is 192.00mD, and effective pressure is 14,964psi whereas in Beta reservoir shale, the average Poisson’s ratio is 0.33, Young’s

modulus is 13.70GPa, bulk modulus is 13.30GPa, shear modulus is 5.12GPa, bulk compressibility is 0.07GPa^{-1}, unconfined compressive strength is 32.32GPa, total porosity is 0.21, effective porosity is 0.14, permeability is 0.022 mD, and effective pressure is 12,730psi as presented in table 2. On the other hand, in Fuja reservoir sand, the average Poisson's ratio is 0.39, Young's modulus is 5.11GPa, bulk modulus is 5.10 GPa, shear modulus is 2.39 GPa, bulk compressibility is 0.023 GPa^{-1}, unconfined compressive strength is 39.0 GPa, total porosity is 0.16, effective porosity is 0.13, permeability is 44.10 mD, and effective pressure is 14,945psi whereas in Fuja reservoir shale, the average Poisson's ratio is 0.42, Young's modulus is 6.08 GPa, bulk modulus is 6.09 GPa, shear modulus is 2.84GPa, bulk compressibility is 0.016 GPa^{-1}, unconfined compressive strength is 42.3 GPa, total porosity is 0.11, effective porosity is 0.09, permeability is 0.110 mD, and effective pressure is 12,973psi as presented in table 3. This implies that larger vertical stress would be required to achieve deformation in the compacted shale than the unconsolidated highly porous sand in both reservoirs.

The interrelationship between the rock elastic, inelastic and petrophysical properties was verified using cross plots and results from both reservoirs revealed that there is a definite link between these rock properties as asserted by Horsud (2001) and Wong et al. (1997). This was clearly shown by the increase in unconfined compressive strength with the elastic properties, depth and volume of shale; and a decrease in unconfined compressive strength and the elastic rock properties with total and effective porosity.

3D geomechanical models showing spatial variation of the rock elastic and inelastic properties across the reservoir top for the two fields were also generated. A careful study of the models and inserted legends for Beta Field revealed that the rock elastic and inelastic

parameters have higher values around the north-northeastern (NNE) portion of the field implying that mechanical rock failure during well drilling, exploitation, and hydraulic fracturing will be low in this section of the field compared to other sections. For Fuja Field, a study of the generated models and inserted legends revealed that all the rock elastic and inelastic parameters reported higher values around the northeastern (NE) and parts of the eastern and western portions of the field, implying that mechanical rock deformation or failure during well drilling and reserve exploitation will be minimized in these sections of the field compared to other sections. These sections represent more stable rock units within the field than other sections.

From the results of modeling with linear and non-linear empirical methods, it is observed from statistical parameters that the R-squared value of only UCS versus bulk density exceeded the required 50% in linear, quadratic, power, logarithmic, and exponential models considered. Hence, any of these models can be utilized in the modeling and analysis of UCS versus bulk density. The other tested relationships did not exceed 50% for the different models considered. Therefore, linear, quadratic, power, logarithmic and exponential models should not be utilized in the modeling and analysis of UCS versus sonic, permeability versus bulk density, and shear wave velocity versus sonic.

Finally, results of modeling with artificial neural network revealed from statistical parameters that UCS versus bulk density, UCS versus sonic transit time, and shear wave velocity versus sonic transit time all gave high performance predictions. This is due to the fact that their R-squared values exceeded 50%. However, permeability versus bulk density gave low performance prediction due to the fact that its R-squared value did not exceed 50%. Therefore, artificial neural network can be used in the modeling and analysis of UCS versus

bulk density, UCS versus sonic, and shear wave velocity versus sonic. However, it cannot be used in the modeling and analysis of permeability versus bulk density.

5.2 Conclusion

Results of this study have clearly shown that rock mechanical properties are central and very critical in determining the success or otherwise of hydrocarbon exploration and exploitation activities. It can therefore be concluded from the findings of this study that the geomechanical characterization of the rocks of a hydrocarbon reservoir goes a long way in mitigating the challenges often encountered by operators, including wellbore instability, sand production, casing collapse, perforation failure, bad hydraulic fracture initiation and fault reactivation, which are associated with rock mechanical properties. Robust knowledge of the reservoir geomechanics is vital for hitch-free hydrocarbon exploration and exploitation in conventional and unconventional plays and prospects in the Niger Delta and other hydrocarbon provinces like the North Sea and Gulf of Mexico. Rock strength estimation in relation to pore pressure and stress evaluations in these fields show that the reservoirs are stable and should not have issues with well stability, casing collapse, etc; however, production of hydrocarbon from these reservoirs may lead to subsidence and other challenges if stress is not properly managed. Rock strength has a direct and strong relationship with elastic rock parameters; hence, knowledge of these parameters is a pointer and gives an insight into the strength and competence of every formation. The magnitude of the principal stresses and their effect on the rock properties and wellbore are important parameters in the prediction and management of rock deformation via design, drilling and completion to avert possible drilling challenges.

It can also be concluded from the findings that empirical models including linear, quadratic, power, logarithmic, and exponential models can be used in the modeling and analysis of UCS

versus bulk density data only while artificial neural network model can be used in the modeling and analysis of UCS versus bulk density, UCS versus sonic transit time, and shear wave velocity versus sonic transit time data from these fields.

5.3 Recommendations

Based on the findings of this study, it is therefore recommended as follows:

1. Care should be taken when placing future exploratory wells within the sections of the fields with low mechanical and rock strength parameters. Adequate pressure management should be applied to prevent drilling and exploitation challenges.
2. The reservoirs of Beta Field should not be subjected to tensile stress, volume stress, shear stress and compressive stress (either during drilling, hydraulic fracturing or reserve exploitation) greater than or equal to 10.94 GPa, 12.76 GPa, 4.11 GPa, and 25.2GPa which are the average values of Young's modulus, bulk modulus, shear or rigidity modulus, and unconfined compressive strength respectively for sand, the weaker lithologic unit of the field.
3. Similarly, the reservoirs of Fuja Field should not be subjected to tensile stress, volume stress, shear stress and compressive stress greater than or equal to 5.11GPa, 5.10 GPa, 2.39 GPa, and 39.0 GPa which are the average values of Young's modulus, bulk modulus, shear modulus, and unconfined compressive strength respectively for sand which is the weaker lithologic unit of the field.
4. The generated empirical model equations can be used in the analysis and modeling of UCS versus bulk density for offshore Niger Delta and similar geologic environments.
5. Lastly, artificial neural network model should be used in the analysis and modeling of UCS versus bulk density, UCS versus sonic transit time and shear wave velocity versus sonic transit time.

5.4 Contribution to Knowledge

1. Using empirical equations including linear, quadratic, power, logarithmic and exponential models, as well as artificial neural network; models that can seamlessly estimate the following parameters for offshore Niger Delta and similar geologic environments without going to the field have been established:

   (i) Unconfined compressive strength (UCS) from bulk density data

   (ii) Unconfined compressive strength from sonic data, and

   (iv) Shear wave velocity from sonic data.

2. This work has also delineated sections of the fields with low mechanical and rock strength properties which were hitherto unknown, a result which will guide placement of future wells within the fields.

3. Robust and reliable information on the geomechanical characteristics of parts of offshore Niger Delta, particularly ‘‘Beta’’ and ‘‘Fuja’’ Fields have also been provided.

REFERENCES

Abijah, F.A., & Tse, A.C. (2016). Geomechanical Evaluation of an Onshore Oil Field in the Niger Delta, Nigeria. *IOSR Journal of Applied Geology and Geophysics*, e-ISSN: 2321-0990, p-ISSN: 2321-0982, 4(1), 99-111.

Adewole, E.O., & Healy, D. (2013). Quantifying in situ horizontal stress in the Niger Delta Basin, Nigeria. *GSTF Journal of Engineering Technology (JET), 2(3)*, DOI 10.7603/s40707-013-0006-7

Adiela, U.P., Ayodele, M., & Okafor, C.A. (2017). Petrophysical Attributes and Reservoir Productivity Index of Eta-1 Well, X-Field, Niger Delta, Nigeria. *International Journal of Advance Research and Innovative Ideas in Education, 3(4)*, 3292-3304, ISSN(0)-2395-4396.

Agbasi, O.E., Sen, S., Inyang, N., & Etuk, S.E. (2020). Assessment of Pore Pressure, Wellbore Failure and Reservoir Stability in the Gabo Field, Niger Delta, Nigeria-Implications for Drilling and Reservoir Management. *Journal of African Earth Sciences*. DOI: 10.1016/j.jafrearsci.2020.104038.

Agoha, C.C. (2018). Seismic Data Processing: Principles and Application (unpublished PhD seminar, Federal University of Technology, Owerri, Imo State, Nigeria).

Ahmed, U., Markley, M.E., Crary, S.F. (1991). Enhanced in-situ stress profiling with micro fracture, core and sonic logging data. *SPE Form. Eval*. *6(02)*. 243-251.

Ali, R.N., Mohammad, G., Gholam, R.L., & Mohammad, R.A. (2017). Reservoir Geomechanical Modeling: In-situ Stress, Pore Pressure, and Mud Design. *Journal of Petroleum Science and Engineering*. DOI 10.1016/j.petrol.2017.01.045.

Anderson, E.M. (1951). The dynamic of faulting and dyke formation with application of Britain. Edinburgh Oliver and Boyd.

Asquith, G.B., & Gibson, C.R. (1982). Basic Well Log Analysis for Geologists. *The American Association of Petroleum Geologists (AAPG)*, Tulsa.

Avbovbo, A. A. (1978). Tertiary lithostratigraphy of the Niger delta; *AAPG Bulletin, 62*, 295-300.

Beka, F. T., & Oti, M. N. (1995). The distal offshore Niger delta: frontier prospects of a mature petroleum province, in Oti, M.N., and Postma, G., eds., *Geology of Deltas: Rotterdam*, A. A. Balkema, 237-241.

Blyth, F.G.H., & Freitas, M.H. (2006). Geology for Engineers. *Elsevier Publishers Amsterdam, (7)*. ISBN: 0713128828 9780713128826.

Bowers, G.L. (1995). Pore Pressure Estimation from Velocity Data: Accounting for Overpressure Mechanisms Besides Undercompaction. *SPE Drill & Compl 10 (02)*, 89-95, SPE-27488-PA.

Burke, K.C., Dessauvagie, T.F.J., & Whiteman, A.J. (1972). Geological History of the Benue Valley and adjacent areas. In: Dessauvagie, T.F.J. and Whiteman, A.J. (Eds). African Geology, *University of Ibadan Press*. 187-218.

Bustin, R.M. (1988). Sedimentology and characteristics of dispersed organic matter in Tertiary Niger Delta: origin of source rocks in a deltaic environment: American Association of Petroleum Geologists Bulletin, 72, 277-298

Carmichael, R. S. (1982). Handbook of Physical Properties of Rocks. Boca Raton, FL, CRC Press. Carman, P. C. L‟´ecoulement des Gaz ´a Travers le MilieuxPoreux, Biblioth´eque des Sciences et Techniques Nucl´eaires, *Presses Universitaires de France*, Paris, 198.

Cerveny, K., Davis, R., Dudley, R.F., Kaufman, P., Knipe, R. & Krantz, B. (2004). Reducing uncertainty with fault seal analysis. Available from: *www.slb.com/2/media/file/.../04-faultsealanalysispdf.*

Chang, C., Zoback, M.D., & Khaksar, A. (2006). Empirical relations between rock strength and physical properties in sedimentary rocks. *Journal of Petroleum Science and Engineering*, 51, 223–237.

Choudhury, M.D., Atteya, W.A., Dahal, k., Chetia, P., Choudhury, K.D., & Paradkar, A. (2018). Virtual Screening of Phytochemicals – in Computational Phytochemistry. *Elsevier*, Pages 301-334, https://doi.org/10.1016/B978-0-12-812364-5.00011-0.

Codd, E.F. (1970). A Relational Model of Data for Large Shared Data Banks. *Communications of the ACM*, 13 (6), 377–387. doi:10.1145/362384.362685.

Cook, J. (2015). The Defining Series: Geomechanics. Schlumberger Oilfield Review Flagship Journal of Technology, Innovation, and the Science of E&P.

Cook, R.D., & Weisberg, S. (1982). Criticism and Influence Analysis in Regression. Wiley, 13, 313-361, https://doi.org/10.2307/270724, https://www.jstor.org/stable/270724

Coulomb, C.A. (1776). Essai Sur une application des regles des maximis et minimis a quelquels problemesde statique relatives, a la architecture. *Mem. Acad. Roy. Div. Sav.*, 7, 343-387.

Crain, E.R. (1986). The Log Analysis Hand Book. Penn-Well, Publishing Company, Tulsa.

Dayhoff, J.E., DeLeo, J.M. (2001). Artificial neural networks - opening the black box. Cancer, 91:1615-35. PMID: 11309760, DOI: 10.1002/10970142(20010415)91: 8+<1615:aid-cncr1175>3.0.co;2-1.

De Souza, A.L.S., De Souza, J.A.B., Meurer, G.B., Naveira, V.P., Chaves, R.A.P., Frydman, M., & Pastor, J. (2014). Integrated 3D Geomechanics and Reservoir Simulation; Optimize Performance, Avoid Fault Reactivation. *World Oil journal* published by Gulf Publishing Company, 55-58.

Devore, J.L. (2012). Probability and Statistics for Engineering and the Sciences, Eighth Edition. Brooks/Cole, Cengage Learning USA, ISBN-13: 978-0-538-73352-6

Doust, H. (1990). Petroleum Geology of the Niger Delta. *The Geological Society of London special publications, 50*, 365. ISSN 0305-8719.

Doust, H. (1989). The Niger Delta hydrocarbon potential, a major Tertiary Niger Delta Province; Proceedings of KNGMG Sympossium, Coastal Lowstands, Geology and Geotechnology, *The Hague, Kluver Acad. Publ*., Dordrecht; 22-25.

Doust, H., & Omatsola, E. (1990). Niger Delta, in Edwards, J. D., and Santogrossi, P. A., eds., Divergent/passive Margin Basins, AAPG Memoir 48: Tulsa, *American Association of Petroleum Geologists*, 239-248.

Dresser, A. (1982). Well logging and Interpretation Techniques. *Dresser Industries Incorporated*, 211.

Eaton, B.A. (1975). The Equation for Geopressure Prediction from Well Logs. Fall Meeting of the Society of Petroleum Engineers of AIME.

Economides, M.J. & Nolte, K. (2000). Reservoir Simulation. 3rd Edition. Chichester: John Wiley and Sons Ltd.

Edwards, J.D., & Santogrossi, P.A. (1990). Summary and Conclusions, in, Edwards, J.D. and Santogrossi, P.A., eds., Divergent/Passive Margin Basins, AAPG Memoir 48: Tusla, *American Association of Petroleum Geologists*, 239-248.

Ejedawe, J.E., Coker, S.J.L., Lambeth-Aikhionabare, D.O., Alofe, K.B., & Adoh, E.O. (1984). Evolution of oil-generative window and oil and gas occurrence in Tertiary Niger Delta Basin. *American Association of Petroleum Geologists Bulletin 68*, 1745-1754.

Ejedawe, J.E. (1981). Patterns of incidence of oil reserves in Niger Delta Basin: *American Association of Petroleum Geologists, 65*, 1574-1585.

Ekweozor, C.M., Okogun, J.I., Ekong, D.E.U., & Maxwell, J.R. (1979). Preliminary organic geochemical studies of samples from the Niger Delta, Nigeria: Part 1, analysis of crude oils for triterpanes: *Chemical Geology, 27*, 11-28.

Entwisle, D.C., Hobbs, P.R.N., Jones, L.D., Gunn, D., & Raines, M.G., 2005. The relationships between effective porosity, uniaxial compressive strength and sonic velocity of intact Borrowdale Volcanic Group core samples from Sellafield. British Geological Survey, Keyworth, Nottingham NG12 5GG. DOI: 10.1007/s10706-004-2143-x.

Evamy, B. D., Harembourne, J., Kamerling, P., Knaap, W. A., Molley, F. A. & Rowlands, P. H. (1978). Hydrocarbon habitat of the Tertiary Niger Delta; *AAPG bulletin; 62*, 1–39.

Finisha, B., Haris, A., & Ronoatmojo, I.S. (2018). Geomechanical Modeling of Reservoir Rock using 2D Seismic Inversion: Its Application to Wellbore Stability in the Onshore of Northwest Java Basin, Indonesia. *AIP Conference Proceedings* 2023, 020258. DOI: https://doi.org/10.1063/1.5064255.

Fjær, E., Holt, R. M., Horsud, P., & Raaen, A.M. (2008). Petroleum Related Rock Mechanics, Development in Petroleum Science, *Elsevier*, Amsterdam, ISBN 0-44488913-2.

Fredrich, J.T., Arguello, J.G., & Deitrick, G.L. (2000). Geomechanical Modeling of Reservoir Compaction, Surface Subsidence, and Casing Damage at the Belridge Diatomite Field, California. *Society of Petroleum Engineers, 3*, ID: SPE-65354-PA, DOI: https://doi.org/10.2118/65354-PA.

Gaarenstroom, L. (1984). The Value of 3D Seismic in Field Development. Paper presented at SPE Annual Conference and Exhibition, Houston Texas, SPE-13049-MS, https://doi.org/10.2118/13049-MS.

Gardner, G.H.F, Gardner, L.W., & Gregory, A.R. (1974). Formation Velocity and Density-The Diagnostic Basis of Stratigraphic Maps. *Geophysics, 39*, 770-780.

Garia, S., Pal, A.K., Ravi, K., and Nair, A.M. (2019). A comprehensive analysis on the relationships between elastic wave velocities and petrophysical properties of sedimentary rocks based on laboratory measurements. *J Petrol Explor Prod Technol 9*, 1869–1881. https://doi.org/10.1007/s13202-019-0675-0.

Glover, P. (1997). Petrophysics MSc Course Notes, Petroleum Geology, Department of Geology and Petroleum Geology, University of Aberdeen, Uk.

Grazulis, A. K. (2016). Analysis of stress and Geomechanical Properties in the Niobrara Formation of Wattenberg Field, Colorado USA. Unpublished thesis submitted to the Faculty and the Board of Trustees of the Colorado School of Mines in partial fulfillment of the requirements for the degree of Master of Science (Geophysics).

Greenberg ML, Castagna JP (1992) Shear wave velocity estimation in porous rocks: theoretical formulation, preliminary verification and applications 1. *Geophysical Prospecting*, 40(2), 195–209, **DOI:** https://doi.org/10.1111/j.1365-2478.1992.tb00371.x

Haack, R.C., Sundaraman, P., & Dahl, J. (1997). Niger Delta Petroleum System. Hedberg Research Symposium, ‘‘Petroleum Systems of the South Atlantic Margin’’, Rio de Janeiro, 16-19 November, extended abstract.

Harald, B. (2012). Wireline Depth Determination, Rev 3.3, available via Society of Professional Well Log Analysts web site, www.spwla.org.

Helmer, R & Hespanhol, I. (1997). Water Pollution Control - A Guide to the Use of Water Quality Management Principles. Edited by and Published on behalf of the United Nations Environment Programme, the Water Supply & Sanitation Collaborative Council and the World Health Organization by E. & F. Spon© 1997 WHO/UNEP, 110(3): 435-437. DOI:10.1023/A:1005024930548. ISBN 0419229108.

Hilchie, D.W. (1990). Wireline: A History of the Well Logging and Perforating Business in the Oil Fields. Boulder, Colorado: Privately Published, 74.

Holbrook, P.W., & Maggiori, D.A. (1993). Real time pore pressure and fracture gradient evaluation in all sedimentary lithologies. In: Proceedings of Offshore European Conference. Aberdeen, Scotland, SPE: 1993. Paper SPE 26791.

Horsrud, P. (2001). Estimating Mechanical Properties of Shale from Empirical Correlations. SPE Drilling and Completion, 16(2), 68–73.

Hospers, J. (1965). Gravity field and structure of the Niger Delta, Nigeria, West Africa: *Geological Society of American Bulletin, 76*, 407-422.

Hudson, J.A.,& Harrison, J.P. (1997). Engineering rock mechanics. An introduction to the principles. First edition. London: Elsevier.

Hunt, J.M. (1990). Generation and Migration of Petroleum from abnormally Pressured Fluid Compartments. *American Association of Petroleum Geologists Bulletin, 74*, 2-5.

Jaeger, J.C., Cook, N.G.W., & Zimmerman, R.W. (2007). Fundamentals of Rock Mechanics. Blackwell Science Limited, 4th edition, ISBN 13: 9780632057597.

Jones, M.E., Leddra, M.J., Goldsmith, A.S., & Edwards, D. (1992). The Geomechanical Characteristics of Reservoirs and Reservoir Rocks. Health and Safety Executive - Offshore Technology Report. London: HMSO Books.

Juvinal, R.C., & Marshek, K.M. (1991). Fundamentals of Machine Component Design. John Wiley, New York, (2) 283-288, ISBN: 0-471-62281-8.

Kamei, R., Nakata, N., & Lumley, D. (2015). Introduction to Microseismic Source Mechanisms, The Leading Edge, http://dx.doi.org/10.1190/tle34080876.1.

Kaplan, A., Lusser, C.U., and Norton, I.O. (1994). Tectonic Map of the World, panel 10: Tulsa, American Association of Petroleum Geologists, scale 1:10,000,000.

Kidambi, T., Kumar, G.S. (2016). Mechanical earth modeling for a vertical well drilled in a naturally fractured light carbonate gas reservoir in the Persian Gulf. *Journal of Petro. Sci. Eng., 141, 38-51.*

Kulke, H. (1995). Regional Petroleum Geology of the World. Part II: Africa, America, Australia and Antarctica: Berlin, Gebrüder Borntraeger, 143-172.

Kwasniewski, M. (1989). Laws of brittle failure and of B-D transition in sandstones, Rock at Great Depth. Proceedings ISRM-SPE International Symposium, Elf Aquitaine, Pau, France, A. A. Balkema.

Kumar, J. (1976). The Effect of Poisson's Ratio on Rock Properties: The 51st Annual Fall Technical Conference and Exhibition of the Society of Petroleum Engineering of AIME, SPE 6094.

Lal, M. (1999). Shale Stability: Drilling Fluid Interaction and Shale Strength. SPE Asia Pacific Oil and Gas Conference and Exhibition Paper, Jakarta, 20–22, SPE 54356.

Lama, R. & Vutukuri, V. 1978. Handbook on Mechanical Properties of Rock. Clausthal, Germany, Trans Tech Publications.

Lama, R.D. & Vutukuri, V.S. (1978). *Handbook on Mechanical Properties of Rocks*. 2nd Edition, Trans Tech Publications, Switzerland.

Larionov, V.V. (1969). Borehole Radiometry Moscow, USSR. In: Nedra, M.R.L. and Biggs, W.P., Eds., Using Log-Derived Values of Water Saturation and Porosity, Trans. SPWLA Ann. Logging Symp. Paper 10, 26.

Li, X., Jaffal, H., Feng, Y., elMohtar, C., & Gray, K. (2018). Wellbore breakouts:Mohr-Coulomb plastic rock deformation, fluid seepage and time-dependent mudcake buildup. *Journal of Natural Gas Science and Engineering, 52*, 515-528.

Mahmoud, A.A., Elkatatny, S., Ali, A., & Moussa, T. (2019). Estimation of Static Young's Modulus for Sandstone Formation Using Artificial Neural Networks. *MDPI Journal*, 12, 2125; 1-15 doi:10.3390/en12112125

Maiti, S., Tiwari, R.K. (2014). A comparative study of artificial neural networks, Bayesian neural networks and adaptive neuro-fuzzy inference system in groundwater level prediction. *Environmental Earth Sciences, 71(7)*, 3147–3160. https://doi.org/10.1007/s12665-013-2702-7

Maleki, S., Moradzadeh, A., Riabi, R.G., Sadaghzadeh, F. (2014). Comparison of several different methods of in situ stress determination. *International Journal of Rocks Mechanics and Mining Science*. 7, 395-404.

McNally,G.H. (1987). Estimation of coal measures rock strength using sonic and neutron logs. *Geoexploration, (24)*, 381 – 395.

Mehrdad, S. (2015). Application of Geophysical Data for Gemechanical Studies: A Critical Review, PetroGem Incorporated.

Nagel, N.B., & Meng, F. (2009). Wellbore Strengthening: The Effect of the Permeable Case. *A Publication of American Association of Drilling Engineers (AADE)*.

Nagham, J., Sameera, M.H., & Hazim, A. (2020). Evaluation of geomechanical properties for tight Reservoir using Uniaxial Compressive Test, Ultrasonic Test, and Well Logs Data. *Petroleum and Coal, 62(2)*: 329-340 ISSN 1337-7027.

Nton, M.E., & Esan, T.B. (2010). Sequence Stratigraphy of EMI Field, Offshore Eastern Niger Delta, Nigeria. *European Journal of Scientific Research, 44 (1)*, 115-132.

Nwachukwu, J.I., & Chukwura., P.I. (1986). Organic matter of Agbada Formation, Niger Delta, Nigeria; *AAPG Bulletin; 70*, 48 – 55.

Nwachukwu, S.O. (1972). The tectonic evolution of the southern portion of the Benue Trough, Nigeria: *Geology Magazine, 109*, 411-419.

Nygaard, R. (2010). Geomechanical Analysis of Wabamun Area Carbon Dioxide Sequestration Project (WASP). Energy and Environmental Systems Group, Institute for Sustainable Energy, Environment and Economy (ISEEE), University of Calgary, Colombia.

Obaje, N. G. (2009). Geology and Mineral Resources of Nigeria. Springer Berlin Heidelberg, Germany. ISBN: 978-3-540-92684-9.

Okeke, O.C. (2010). Influence of Pressure Gradients and Fracturing in Oilfield Rocks on Hydrocarbon Accumulation and Exploitation: A Review. *Global Journal of Geological Sciences, 8(1)*, 26-34. ISSN 1596-6798.

Okereke, C.N. (2012). Structural and tectonic analysis of the aeromagnetic and remote sensing data of the Niger Delta, Nigeria. Unpublished PhD Thesis, Federal University of Technology Owerri, Nigeria.

Omar, I. (2015). Reservoir geomechanics lecture slides. Stanford University. Available from: https://lagunita.Stanford.edu./Course v1…about.

Opara, A.I. (2010). Origin and generation mechanisms of geopressures in shale dominated settings worldwide: a review. *Global journal of pure and applied sciences, 16(4)*, 429-438.

Oresajo, B.S., Adekeye, A.O., and Haruna, K.A. (2015). Sequence Stratigraphy and Structural Analysis of the Emi Field, Offshore Depobelt, Eastern Niger Delta Basin, Nigeria. *Ife Journal of Science, 17(2)*, 395-408.

Osaki, L. J. (2019). Geomechanical Characterization of a Reservoir in Eastern Offshore Niger Delta, Nigeria (unpublished PhD thesis, Rivers State University of Science and Technology, Portharcourt, Rivers State, Nigeria).

Osaki, L. J., Uko, E.D., Iyeneomie, T.A., & Alabraba, M.A. (2019). Geomechanical Characterization of a Reservoir in Part of the Niger Delta, Nigeria. *Asian Journal of Applied Science and Technology, 3(1)*, 10-30.

Osaki, L. J., Uko, E.D., & Opara, A.I. (2018). 3D Geomechanical Reservoir Model for Appraisal and Development of Emi-003 Field in Niger Delta, Nigeria. *Asian Journal of Applied Science and Technology, 2(4)*, 276-294.

Ostadhassan, M., Zong, Z., & Zamrian, S. (2012). Geomechanical modeling of an anisotropic formation-Bakken: Case study. 46th US Rock 148 Mechanics/Geomechanics Symposium American Rock Mechanics Association.

Qiuguo, L., Zhang, X., Al-Ghammari, K., Mohsin, L., Jiroudi, F., & Al-Rawahi, A. (2013). 3D Geomechanical Modeling, Wellbore Stability Analysis, Improve Field's Performance.*World Oil journal published by Gulf Publishing Company*, 53-61.

Ranjbar A, Hassani H, & Shahriar K. (2017). 3D geomechanical modeling and estimating the compaction and subsidence of Fahlian reservoir formation (X-field in SW of Iran). *Arab J Geosci* 10:116. https://doi.org/10.1007/s12517-017-2906-3

Reed, K.J. (1969). Environment of deposition of source beds of high-wax oil: *American Association of Petroleum Geologists Bulletin, 53*, 1502-1506.

Reijers, T. J. A., Petters, S. W., & Nwajide, C. S. (1997). The Niger Delta Basin, in Selley, R. C., ed., African Basins--Sedimentary Basin of the World 3: Amsterdam, *Elsevier Science*, 151-172.

Reservoir Geomechanics Stanford Online (2016).

Reyment, R. A. (1965). Aspects of the Geology of Nigeria; University of Ibadan Press Ibadan Nigeria.

Rider, M.H. (1986). The Geological Interpretation of Well Logs. Wiley, New York, 175.

Schlumberger (1989). Log Interpretation Principles/Application. Schlumberger Wireline and Testing, 51.

Schlumberger (1987). Log Interpretation Principles. Schlumberger Educational Services, Houston.

Schlumberger (1985). Well Evaluation Conference. Nigeria.

Secci, R., Foddis, M.L., Mazzella, A., Montisci, A., & Uras, G. (2014). Artificial Neural Networks and Kriging Method for Slope Geomechanical Characterization. Conference Paper, DOI: 10.1007/978-3-319-09057-3_239.

Selemo, A.O.I. (2008). Basic Principles of Geophysical Logging: Open Hole Wireline Logs. MC Computer Press, Nnewi. ISBN: 978-978-48201-5-8.

Seyed, S.S., & Aghighi, M.A. (2015). Building and analyzing geomechanical model of Bangestan reservoir in Kopal oil field, Iranian. *Journal of Mining Engineering*, 10, 21-34.

Sheriff, R. E. & Geldart, L. P. (1995). Exploration Seismology Second Edition. Cambridge University Press, ISBN 0-521-46826-4, 209–210.

Short, K.C., & Stauble, A. J. (1967). Outline of Geology of Niger Delta. *The American Association of Petroleum Geologists Bulletin, 51(5)*, 761-779.

Son, T.P. (2020). Geomechanical Modelling Using Artificial Neural Networks Combined With Geostatistics. *Preprints* (www.preprints.org), doi: 10.20944/preprints202010.0036.v1.

Sorough, H. (2013). Discover a career in Geomechanics. Society of Petroleum Engineers. SPE-0313-015-TWA.

Stacher, P. (1995). Present understanding of the Niger Delta hydrocarbon habitat, in, Oti, M.N., and Postma, G., eds., Geology of Deltas: Rotterdam, A.A. Balkema, 257-267.

Telford, W. M., Geldart, L. P., & Sheriff, R. E. (1990). Applied Geophysics. Cambridge University Press, Cambridge.

Telford, W. M., Geldart, L. P., Sheriff, R. E., & Keys, D. A. (1976). Applied Geophysics. Cambridge University Press, Third Edition, 769.

Terzaghi, K. (1943). Theoretical Soil Mechanics. John Wiley and Sons, Inc.

Tiab, D., & Donaldson, E.C. (2012). Theory and practice of measuring reservoir rock and fluid transport properties, 3rd edition. Amsterdam: Gulf Professional Publishing.

Tingay, M. (2009). States and origin of present day stress fields in sedimentary basins. DOI: 10.1071/*ASEG* 2009ab 037.

Tingay, M.R.P., Muller, B., Reimaker, J., & Heidbach, O. (2005). State and original of the present day stress field in sedimentary basins. New results from the world stress map project. *American Rock Mechanics Association ARMA/USRMS*, 061048.

Tissot, B.P., & Welte, D.H. (1984). Petroleum Formation and Occurrence, 2, Springer-Verlag, Berlin, 699.

Tuttle, M. L. W., Charpentier, R. R & Brownfield, M. E. (1999). The Niger Delta Basin Petroleum System: Niger Delta Province, Nigeria, Cameroon, and Equatorial Guinea, Africa; Open- File Report 99-50-H, United States Geological Survey World Energy Report, 44.

Twiss, R.J., & Moores, E.M. (1992). Structural Geology. New York: W. H. Freeman and Company.

Ugwu, G.Z. (2015). Pore Pressure Prediction Using Seismic Data: Insight from Onshore Niger Delta Nigeria. *Journal of Geology and Mining Research, 7(8)*, 74-80, ISSN 2006 – 9766.

Weber, K.J. (1987). Hydrocarbon distribution patterns in Nigerian growth fault structures controlled by structural style and stratigraphy; *Journal of petroleum science and Engineering; 1*, 91-104.

Weber, K. J., & Daukoru, E. M. (1975). Petroleum Geology of the Niger Delta: Proceedings of the ninth World Petroleum Congress, 2, Geology: London, Applied Science Publishers, Ltd., 210-221.

Whaley, J. (2019). An Introduction to Geomechanics. Geoscience Magazine (GEOExPro), 6(2).

Whiteman, A. J. (1982). Nigeria: Its petroleum Geology, Resources and Potential, 1 and 2, Graham and Trottan, London, 394.

Wilson, G., & Cosgrove, J.W. (1982). Introduction to small scale geological structures. George Allen and Unwin Publishers Ltd.

Wong, T.F. & David, C. (1997). The Transition from Brittle Faulting to Cataclastic Flow in Porous Sandstones: Mechanical Deformation. *Journal of Geophysical Research, 102* (B2), 3009–3025.

Wyllie, M.R.J., & Rose, W.D. (1950). Some Theoretical Considerations Related to the Quantitative Evaluation of the Physical Characteristics of Reservoir Rock from Electrical Log Data. *Journal of Petroleum Technology*, 2, 04, DOI: https://doi.org/10.2118/950105-G.

Zhang, Y., Yin, S., & Zhang, J. (2021). In situ stress prediction in subsurface rocks: An overview and a new method. Geofluids, 2021, Article ID: 6639793, 11 pages, https://doi.org/10.1155/2021/6639793

Zoback, M.D. (2016). Reservoir Geomechanics: In situ stress and rock mechanics applied to reservoir process. Course overview. Standford University (online-lecture1-overview-2016%20Zoback. pdf.

Zoback, M.D. (2007). Reservoir Geomechanics, published in the United States of America by Cambridge University Press, New York.

Zoback, M.D. (1992). Stress-Field Constraints on Intraplate Seismicity in Eastern North American. *Journal of Geophysical Research-Solid Earth, 97*, B8, 11761-11782.

Zorasi, C.B., (2019). Petrophysical and Geomechanical Characterization of a Marginal (Wabi) Field Reservoir in North-Central Niger Delta. Robert Gordon University [online], MRes thesis. Available from: https://openair.rgu.ac.uk.

APPENDIX

Appendix A: Reservoir Elastic and Inelastic Parameters

	MD(ft)	GR(API)	Sonic(us/f	RHOB(g/cm3)	VP km/s	VS km/s	Young (Gpa)	Shear(Gpa)	Bulk(Gpa)	UCS(Gpa)	Bulk com(GPa-1)	Poissons ratio
2	9400	99.39	93.28	2.3394	3.268418	1.677081	17.387881	6.579800751	16.21769927	41.76241765	0.061661027	0.34
3	9400.5	99.11	91.61	2.35	3.327999	1.727487	18.4522383	7.012898759	16.67707706	44.35018303	0.059962546	0.34
4	9401	100.17	95.12	2.328	3.205193	1.623594	16.2920627	6.136739161	15.73384201	39.08570643	0.063557267	0.34
5	9401.5	90.94	98.5	2.3078	3.095208	1.530546	14.4687891	5.40618599	14.90119909	34.60772198	0.067108693	0.33
6	9402	88.39	97.97	2.3109	3.111953	1.544712	14.739504	5.514119264	15.02717251	35.27437698	0.066546118	0.32
7	9402.5	88.61	94.73	2.3304	3.218389	1.634757	16.5179617	6.227833317	15.83457171	39.63834016	0.063152955	0.32
8	9403	84.83	94.47	2.332	3.227247	1.642251	16.6703958	6.289374882	15.90223029	40.01109681	0.062884261	0.32
9	9403.5	84	96.92	2.3171	3.145667	1.573234	15.2919619	5.73497277	15.28157906	36.6332697	0.065438264	0.32
10	9404	86.56	100.62	2.2955	3.029994	1.475375	13.4371989	4.996686604	14.41242419	32.06473525	0.06938458	0.32
11	9404.5	90.72	96.49	2.3197	3.159685	1.585093	15.5248353	5.82829561	15.38791682	37.20476468	0.064986054	0.33
12	9405	90.5	90.08	2.3599	3.384525	1.775308	19.4900443	7.437740789	17.11568702	46.86151841	0.058425934	0.33
13	9405.5	90.11	89.43	2.3642	3.409124	1.796119	19.9505003	7.627014406	17.30768614	47.97100835	0.057777798	0.32
14	9406	90.94	93.65	2.3371	3.255505	1.666157	17.1613642	6.487973327	16.11867873	41.20983064	0.062039825	0.33
15	9406.5	96.39	96.77	2.318	3.150543	1.577359	15.3727318	5.767326176	15.31851014	36.83162443	0.0652805	0.34
16	9407	96.78	99.2	2.3037	3.073367	1.512068	14.1191256	5.267066636	14.73703708	33.7465043	0.067856245	0.34
17	9407.5	94.06	93.83	2.336	3.249259	1.660873	17.0524374	6.443856795	16.07094541	40.94365429	0.062224093	0.33
18	9408	89.89	85.96	2.3877	3.546743	1.912544	22.6205299	8.73379042	18.39074027	54.35392542	0.05437519	0.32
19	9408.5	93.39	85.96	2.3877	3.546743	1.912544	22.6205299	8.73379042	18.39074027	54.35392542	0.05437519	0.33
20	9409	95.72	93.28	2.3394	3.268418	1.677081	17.387881	6.579800751	16.21769927	41.76241765	0.061661027	0.33
21	9409.5	100.56	94.36	2.3327	3.231009	1.645434	16.7354994	6.315672127	15.93113542	40.16985488	0.062770165	0.34
22	9410	95.78	95.55	2.3254	3.190769	1.611391	16.0470828	6.038087623	15.62413317	38.48531869	0.064003551	0.33
23	9410.5	96.72	98.63	2.307	3.091128	1.527095	14.4029353	5.379965878	14.87027055	34.44613625	0.067248272	0.34
24	9411	92.89	102.54	2.2847	2.973259	1.427377	12.5704887	4.654861367	13.99088388	29.92328189	0.071475113	0.33

Appendix A1: Some calculated values of reservoir elastic and inelastic parameters from ‘‘Beta’’ 1 well.

	MD(ft)	GR(API)	Sonic(us/f	RHOB(g/cı	VP km/s	VS km/s	Young (Gp	Shear(Gpa	Bulk(Gpa)	UCS(Gpa)	Bulk com(	Poissons rati
2	9400	90.26	102.3	2.28	2.980235	1.433278	12.64205	4.683775	14.00547	30.18294	0.071401	0.3
3	9400.5	90.6	99.6	2.2714	3.061024	1.501626	13.74203	5.121739	14.45373	33.26404	0.069186	0.31
4	9401	94.62	101.7	2.2508	2.997817	1.448153	12.724	4.720261	13.93405	30.84198	0.071767	0.33
5	9401.5	95.43	102.2	2.2714	2.983151	1.435745	12.63504	4.682185	13.9707	30.29179	0.071578	0.33
6	9402	94.44	102.1	2.2864	2.986072	1.438217	12.75956	4.729348	14.08118	30.40104	0.071017	0.32
7	9402.5	93.22	104.1	2.3193	2.928703	1.389683	12.1357	4.479075	13.92124	28.28911	0.071833	0.32
8	9403	92.17	104.2	2.3209	2.925893	1.387305	12.10506	4.46684	13.91308	28.18745	0.071875	0.32
9	9403.5	92.23	103.6	2.3249	2.942838	1.401641	12.36232	4.567491	14.04433	28.80292	0.071203	0.33
10	9404	90.72	103.4	2.2919	2.94853	1.406456	12.26556	4.533652	13.88052	29.01105	0.072043	0.33
11	9404.5	96.19	103.5	2.264	2.945681	1.404046	12.07731	4.463127	13.69398	28.9068	0.073025	0.33
12	9405	96.65	102.5	2.221	2.97442	1.428359	12.23577	4.531305	13.60783	29.9664	0.073487	0.32
13	9405.5	98.57	105.3	2.2183	2.895328	1.361447	11.1679	4.111704	13.11356	27.09304	0.076257	0.33
14	9406	95.95	104	2.2126	2.931519	1.392065	11.6147	4.287677	13.29775	28.39113	0.075201	0.33
15	9406.5	95.49	105.1	2.2481	2.900837	1.366108	11.3909	4.195521	13.32341	27.28881	0.075056	0.33
16	9407	93.63	103.9	2.2602	2.934341	1.394452	11.90281	4.394952	13.60119	28.49352	0.073523	0.33
17	9407.5	92.99	102.2	2.2697	2.983151	1.435745	12.62558	4.67868	13.96025	30.29179	0.071632	0.32
18	9408	92.7	103	2.2571	2.959981	1.416144	12.23593	4.52653	13.74018	29.43183	0.072779	0.32
19	9408.5	90.55	99.8	2.263	3.05489	1.496437	13.60289	5.067588	14.36233	33.0254	0.069627	0.32
20	9409	90.78	102.8	2.2704	2.965739	1.421015	12.38759	4.584584	13.85677	29.64451	0.072167	0.32
21	9409.5	96.42	103.4	2.2587	2.94853	1.406456	12.08789	4.467979	13.67945	29.01105	0.073102	0.33
22	9410	101.59	102.7	2.2355	2.968627	1.423459	12.23653	4.529646	13.66137	29.75142	0.073199	0.32
23	9410.5	103.57	101.7	2.19	2.997817	1.448153	12.38029	4.592754	13.55766	30.84198	0.073759	0.31
24	9411	101.42	98.7	2.2168	3.088936	1.52524	13.80843	5.157068	14.27557	34.35944	0.07005	0.32

Appendix A2: Some calculated values of reservoir elastic and inelastic parameters from ‘‘Beta’’ 2 well.

1	MD(ft)	GR(API)	Sonic(us/f	RHOB(g/c	VP km/s	VS km/s	Young (Gp	Shear(Gpa)	Bulk(Gpa)	UCS(Gpa)	Bulk com(	Poissons ratio
2	10500	90.37	99.19	2.407	3.073677	1.512331	14.75702	5.505154922	15.3999	33.7586552	0.064935	0.33
3	10500.5	90.15	96.19	2.4066	3.169539	1.59343	16.26454	6.110406417	16.02945	37.6087537	0.062385	0.32
4	10501	91.35	97.38	2.3832	3.130807	1.560663	15.49473	5.804685219	15.62044	36.0316182	0.064019	0.33
5	10501.5	93.79	97.56	2.3522	3.125031	1.555776	15.204	5.693356635	15.38001	35.7988882	0.065019	0.33
6	10502	89.99	100.81	2.3244	3.024283	1.470544	13.5231	5.026511987	14.55762	31.8461608	0.068693	0.32
7	10502.5	89.17	100.31	2.3359	3.039358	1.483297	13.81139	5.139376108	14.72583	32.4245819	0.067908	0.32
8	10503	88.63	98.38	2.3557	3.098984	1.53374	14.82669	5.541451153	15.23483	34.7575507	0.065639	0.32
9	10503.5	93.68	98.44	2.398	3.097095	1.532142	15.06358	5.629207652	15.49599	34.6825555	0.064533	0.33
10	10504	93.41	98	2.4298	3.111	1.543906	15.48279	5.791782411	15.79401	35.2363012	0.063315	0.33
11	10504.5	92.22	94.44	2.4189	3.228272	1.643118	17.30858	6.530635487	16.50163	40.0543321	0.0606	0.33
12	10505	89.01	92	2.3948	3.313891	1.715552	18.56409	7.048180935	16.90182	43.7318573	0.059165	0.32
13	10505.5	92.92	97.81	2.3756	3.117043	1.549019	15.23109	5.70015381	15.48103	35.4781437	0.064595	0.33
14	10506	94.66	100.75	2.3587	3.026084	1.472067	13.74928	5.111261282	14.78404	31.9150229	0.067641	0.33
15	10506.5	95.86	103.44	2.3572	2.94739	1.405492	12.59879	4.656429609	14.26867	28.9693054	0.070084	0.33
16	10507	93.85	104.06	2.3596	2.929829	1.390635	12.36246	4.563151399	14.17036	28.3298731	0.07057	0.33
17	10507.5	88.2	99.06	2.362	3.07771	1.515743	14.54224	5.426640765	15.13806	33.917016	0.066059	0.32
18	10508	86.4	94.06	2.3473	3.241314	1.654152	17.00637	6.422724077	16.09738	40.6060405	0.062122	0.32
19	10508.5	84.61	93.81	2.2909	3.249952	1.661459	16.73417	6.323908943	15.76504	40.9731443	0.063431	0.32
20	10509	90.1	97.44	2.2775	3.128879	1.559032	14.77867	5.535646985	14.9156	35.9538739	0.067044	0.32
21	10509.5	91.13	94.75	2.2946	3.21771	1.634182	16.25358	6.12784933	15.58703	39.6098108	0.064156	0.33
22	10510	89.83	98.69	2.319	3.089249	1.525505	14.44972	5.39669534	14.93569	34.3718129	0.066954	0.32
23	10510.5	83.36	101.31	2.3013	3.009357	1.457916	13.17426	4.891459539	14.31916	31.2780582	0.069836	0.31
24	10511	83.58	98.44	2.2667	3.097095	1.532142	14.23879	5.320986232	14.64753	34.6825555	0.068271	0.32

Appendix A3: Some calculated values of reservoir elastic and inelastic parameters from ‘‘Beta’’ 3 well.

1	MD(ft)	GR(API)	Sonic(us/f	RHOB(g/c	VP km/s	VS km/s	Young (Gpa)	Shear(Gpa	Bulk(Gpa)	UCS(Gpa)	Bulk com(	Poissons ratio
2	10500	101.47	97.83	2.378	3.116406	1.548479	15.23657646	5.701942	15.49251	35.45260861	0.064547	0.35
3	10500.5	106.32	96.29	2.3996	3.166248	1.590646	16.1644999	6.071356	15.96115	37.47360565	0.062652	0.36
4	10501	103.37	96.69	2.4199	3.153149	1.579564	16.09035167	6.037707	16.00922	36.93785241	0.062464	0.35
5	10501.5	108.11	93.02	2.4322	3.277553	1.68481	18.23249155	6.904006	16.92221	42.15514899	0.059094	0.36
6	10502	103.24	90.53	2.4188	3.367701	1.761075	19.68142973	7.501633	17.43043	46.10847791	0.057371	0.35
7	10502.5	104.52	92.63	2.3899	3.291353	1.696484	18.14629586	6.878274	16.71876	42.75118164	0.059813	0.35
8	10503	102.34	91.7	2.3677	3.324733	1.724724	18.53618615	7.043133	16.78135	44.20672097	0.05959	0.35
9	10503.5	105.57	91.27	2.3713	3.340397	1.737976	18.82931196	7.162652	16.90936	44.89636509	0.059139	0.35
10	10504	102.71	89.83	2.3996	3.393944	1.783277	19.98260775	7.63091	17.4661	47.28517568	0.057254	0.35
11	10504.5	103.21	89.03	2.4073	3.424441	1.809077	20.58558648	7.878516	17.72523	48.66678847	0.056417	0.35
12	10505	103.38	88.29	2.329	3.453143	1.833359	20.41194318	7.828247	17.33379	49.98069525	0.057691	0.35
13	10505.5	107.63	91.3	2.2794	3.339299	1.737047	18.08168444	6.877707	16.24713	44.84790319	0.061549	0.36
14	10506	108.49	92.1	2.3052	3.310293	1.712508	17.81082518	6.760422	16.24658	43.57470562	0.061551	0.36
15	10506.5	110.1	91.13	2.3824	3.345528	1.742317	19.00500338	7.232177	17.02225	45.12321395	0.058747	0.37
16	10507	111.77	90.94	2.3862	3.352518	1.74823	19.15503307	7.292965	17.09545	45.4329147	0.058495	0.37
17	10507.5	112.58	91.81	2.3968	3.320749	1.721354	18.69615716	7.101861	16.96127	44.03200852	0.058958	0.37
18	10508	111.35	89.74	2.437	3.397348	1.786156	20.3546379	7.774894	17.76126	47.43862811	0.056302	0.37
19	10508.5	111.48	91	2.4269	3.350308	1.74636	19.44320951	7.401497	17.37223	45.33488551	0.057563	0.37
20	10509	112.17	92.87	2.3956	3.282847	1.689289	18.04676729	6.836314	16.7025	42.38340253	0.059871	0.37
21	10509.5	113.58	91.87	2.3865	3.318581	1.719519	18.57907596	7.056275	16.8741	43.93700202	0.059262	0.37
22	10510	109.37	91.46	2.4306	3.333457	1.732105	19.17967351	7.292255	17.28567	44.59032181	0.057851	0.36
23	10510.5	106.63	89.59	2.4535	3.403036	1.790969	20.59454868	7.869769	17.92011	47.6954896	0.055803	0.36
24	10511	105.98	89.61	2.4526	3.402277	1.790326	20.57335409	7.861238	17.90839	47.66116121	0.05584	0.36

Appendix A4: Some calculated values of reservoir elastic and inelastic parameters from ‘‘Beta’’ 4 well.

1	MD(ft)	GR(API)	Sonic(us/f	RHOB(g/c	Vp(km/s)	Vs(km/s)	Young (Gpa)	Shear (Gpa)	Bulk(Gpa)	UCS(Gpa)	Bulk com(GPa-	Poisson ratio
2	8000	85.05	190.5399	2.5868	1.600074	1.286374	9.155511	4.280529	9.154511	52.853	0.010923576	0.53
3	8003	98.72	185.5553	2.604	1.643057	1.320932	9.717924	4.543621	9.716924	54.357	0.010291323	0.54
4	8003.5	109.61	195.085	2.5716	1.562796	1.256402	8.682778	4.059391	8.681778	51.548	0.011518378	0.52
5	8004	106.27	201.9694	2.5494	1.509526	1.213573	8.031321	3.754656	8.030321	49.683	0.012452802	0.50
6	8004.5	107.31	203.4976	2.5446	1.49819	1.204459	7.896316	3.691505	7.895316	49.287	0.012665738	0.49
7	8005	102.93	203.7858	2.5437	1.496071	1.202755	7.87123	3.679769	7.87023	49.212	0.012706109	0.49
8	8005.5	107.14	201.5263	2.5508	1.512845	1.216242	8.071078	3.773255	8.070078	49.8	0.012391454	0.50
9	8006	108.44	200.9899	2.5525	1.516882	1.219487	8.11959	3.795948	8.11859	49.941	0.01231741	0.50
10	8006.5	107.71	200.4555	2.5542	1.520926	1.222739	8.168365	3.818762	8.167365	50.082	0.012243851	0.50
11	8007	103.33	204.2994	2.5421	1.49231	1.199732	7.826803	3.658988	7.825803	49.081	0.012778241	0.49
12	8007.5	105.68	204.2351	2.5423	1.49278	1.20011	7.832346	3.66158	7.831346	49.097	0.012769197	0.49
13	8008	113.03	202.891	2.5465	1.502669	1.20806	7.94951	3.716387	7.94851	49.443	0.012580974	0.49
14	8008.5	117.05	204.6211	2.5411	1.489964	1.197845	7.799151	3.646055	7.798151	48.999	0.012823553	0.49
15	8009	116.32	206.1745	2.5363	1.478738	1.188819	7.667626	3.584532	7.666626	48.606	0.013043547	0.49
16	8009.5	114.8	201.5896	2.5506	1.51237	1.21586	8.065388	3.770592	8.064388	49.783	0.012400197	0.50
17	8010	113.97	198.3039	2.5611	1.537428	1.236007	8.369019	3.912624	8.368019	50.66	0.01195026	0.51
18	8010.5	107.29	192.3777	2.5806	1.584789	1.274085	8.959987	4.189067	8.958987	52.318	0.011161976	0.52
19	8011	102.85	195.8454	2.5691	1.556728	1.251523	8.607134	4.024009	8.606134	51.335	0.011619619	0.51
20	8011.5	102.79	197.3159	2.5643	1.545126	1.242196	8.463557	3.956846	8.462557	50.929	0.011816759	0.51
21	8012	108.97	201.4631	2.551	1.513319	1.216623	8.076774	3.775919	8.075774	49.816	0.012382714	0.50
22	8012.5	107.15	197.5623	2.5635	1.543199	1.240646	8.43983	3.945747	8.43883	50.862	0.011849984	0.51
23	8013	103.32	194.449	2.5737	1.567907	1.260512	8.74677	4.089325	8.74577	51.727	0.011434099	0.52
24	8013.5	101.2	193.1249	2.5781	1.578657	1.269154	8.88221	4.152681	8.88121	52.103	0.011259727	0.52

Appendix A5: Some calculated values of reservoir elastic and inelastic parameters from ‘‘Fuja’’ 1 well.

1	MD(ft)	GR(API)	Sonic(us/f	RHOB(g/c	Vp(km/s)	Vs(km/s)	Young(Gp	Shear (Gp	Bulk(Gpa)	UCS(Gpa)	Bulk com(	Poisson ratio
2	8000	89.44	223.0152	2.487	1.367073	1.099041	6.426584	3.004027	6.425584	44.698	0.015563	0.45
3	8000.5	90.47	222.5137	2.4884	1.370154	1.101518	6.459203	3.019281	6.458203	44.805	0.015484	0.45
4	8001	92.1	221.5862	2.491	1.375889	1.106129	6.520158	3.047794	6.519158	45.006	0.015339	0.45
5	8001.5	93.07	220.5572	2.4939	1.382308	1.11129	6.588754	3.079881	6.587754	45.231	0.01518	0.45
6	8002	93.37	218.4124	2.5	1.395882	1.122204	6.735137	3.148352	6.734137	45.706	0.01485	0.46
7	8002.5	93.97	214.9867	2.5099	1.418125	1.140087	6.978874	3.262362	6.977874	46.484	0.014331	0.46
8	8003	95.39	212.5375	2.5171	1.434467	1.153226	7.161032	3.347567	7.160032	47.056	0.013966	0.47
9	8003.5	96.82	214.1324	2.5124	1.423783	1.144636	7.041652	3.291724	7.040652	46.682	0.014203	0.47
10	8004	96.26	219.4287	2.4971	1.389417	1.117005	6.665191	3.115634	6.664191	45.48	0.015006	0.45
11	8004.5	93.92	222.4778	2.4885	1.370375	1.101696	6.461536	3.020376	6.460536	44.813	0.015479	0.45
12	8005	92.86	220.805	2.4932	1.380757	1.110043	6.572143	3.072108	6.571143	45.176	0.015218	0.45
13	8005.5	93.8	220.2039	2.4949	1.384526	1.113074	6.612552	3.091014	6.611552	45.308	0.015125	0.45
14	8006	93.39	224.528	2.4828	1.357862	1.091635	6.329624	2.958673	6.328624	44.375	0.015801	0.44
15	8006.5	91.05	230.5971	2.4663	1.322124	1.062902	5.961166	2.78633	5.960166	43.124	0.016778	0.43
16	8007	89.11	234.8722	2.455	1.298059	1.043554	5.719952	2.673508	5.718952	42.282	0.017486	0.42
17	8007.5	88.8	236.3705	2.4511	1.289831	1.036939	5.638743	2.635525	5.637743	41.994	0.017738	0.42
18	8008	89.48	236.1777	2.4516	1.290884	1.037785	5.649096	2.640368	5.648096	42.031	0.017705	0.42
19	8008.5	90.51	236.6793	2.4503	1.288148	1.035585	5.622213	2.627791	5.621213	41.935	0.01779	0.42
20	8009	90.86	237.9198	2.4471	1.281432	1.030186	5.556512	2.597064	5.555512	41.7	0.018	0.42
21	8009.5	89.56	237.1049	2.4492	1.285836	1.033727	5.599549	2.617192	5.598549	41.854	0.017862	0.42
22	8010	87.97	233.2337	2.4593	1.307178	1.050886	5.810699	2.715954	5.809699	42.601	0.017213	0.43
23	8010.5	88.15	228.8846	2.4709	1.332016	1.070855	6.061921	2.833457	6.060921	43.471	0.016499	0.43
24	8011	89.08	225.3255	2.4806	1.353056	1.087771	6.279357	2.935161	6.278357	44.207	0.015928	0.44

Appendix A6: Some calculated values of reservoir elastic and inelastic parameters from ‘‘Fuja’’ 2 well.

	MD(ft)	GR(API)	Sonic(us/ft)	RHOB(g/cm	Vp km/s	Vs km/s	Young (Gpa	Shear(Gpa	Bulk(Gpa)	UCS(Gpa)	Bulk com(GPa	poisson ratio
2	8000	85.05	190.539938	2.5868	1.600074	1.286374	9.155511	4.280529	9.154511	52.853	0.010923576	0.53
3	8003	98.72	185.55534	2.604	1.643057	1.320932	9.717924	4.543621	9.716924	54.357	0.010291323	0.54
4	8003.5	109.61	195.084963	2.5716	1.562796	1.256402	8.682778	4.059391	8.681778	51.548	0.011518378	0.52
5	8004	106.27	201.96936	2.5494	1.509526	1.213573	8.031321	3.754656	8.030321	49.683	0.012452802	0.50
6	8004.5	107.31	203.497554	2.5446	1.49819	1.204459	7.896316	3.691505	7.895316	49.287	0.012665738	0.49
7	8005	102.93	203.785783	2.5437	1.496071	1.202755	7.87123	3.679769	7.87023	49.212	0.012706109	0.49
8	8005.5	107.14	201.526263	2.5508	1.512845	1.216242	8.071078	3.773255	8.070078	49.8	0.012391454	0.50
9	8006	108.44	200.989925	2.5525	1.516882	1.219487	8.11959	3.795948	8.11859	49.941	0.01231741	0.50
10	8006.5	107.71	200.455512	2.5542	1.520926	1.222739	8.168365	3.818762	8.167365	50.082	0.012243851	0.50
11	8007	103.33	204.299375	2.5421	1.49231	1.199732	7.826803	3.658988	7.825803	49.081	0.012778241	0.49
12	8007.5	105.68	204.235051	2.5423	1.49278	1.20011	7.832346	3.66158	7.831346	49.097	0.012769197	0.49
13	8008	113.03	202.890989	2.5465	1.502669	1.20806	7.94951	3.716387	7.94851	49.443	0.012580974	0.49
14	8008.5	117.05	204.621051	2.5411	1.489964	1.197845	7.799151	3.646055	7.798151	48.999	0.012823553	0.49
15	8009	116.32	206.174454	2.5363	1.478738	1.188819	7.667626	3.584532	7.666626	48.606	0.013043547	0.49
16	8009.5	114.8	201.589558	2.5506	1.51237	1.21586	8.065388	3.770592	8.064388	49.783	0.012400197	0.50
17	8010	113.97	198.303921	2.5611	1.537428	1.236007	8.369019	3.912624	8.368019	50.66	0.01195026	0.51
18	8010.5	107.29	192.37766	2.5806	1.584789	1.274085	8.959987	4.189067	8.958987	52.318	0.011161976	0.52
19	8011	102.85	195.845389	2.5691	1.556728	1.251523	8.607134	4.024009	8.606134	51.335	0.011619619	0.51
20	8011.5	102.79	197.315947	2.5643	1.545126	1.242196	8.463557	3.956846	8.462557	50.929	0.011816759	0.51
21	8012	108.97	201.463142	2.551	1.513319	1.216623	8.076774	3.775919	8.075774	49.816	0.012382714	0.50
22	8012.5	107.15	197.562336	2.5635	1.543199	1.240646	8.43983	3.945747	8.43883	50.862	0.011849984	0.51
23	8013	103.32	194.449033	2.5737	1.567907	1.260512	8.74677	4.089325	8.74577	51.727	0.011434099	0.52
24	8013.5	101.2	193.124916	2.5781	1.578657	1.269154	8.88221	4.152681	8.88121	52.103	0.011259727	0.52

Appendix A7: Some calculated values of reservoir elastic and inelastic parameters from ‘‘Fuja’’ 3 well.

	MD(ft)	GR(API)	Sonic(us/ft)	RHOB(g/cm	Vp km/s	Vs km/s	Young (Gpa)	Shear(Gpa	Bulk(Gpa)	UCS(Gpa)	Bulk com(GPa-1)	Poisson ratio
2	7000	104.04	231.797737	2.4631	1.315276	1.057396	5.891951	2.753959	5.890951	42.885	0.016975188	0.43
3	7000.5	100.76	224.347219	2.4833	1.358956	1.092515	6.341098	2.964039	6.340098	44.413	0.015772627	0.44
4	7001	98.96	220.451158	2.4942	1.382973	1.111825	6.595885	3.083216	6.594885	45.254	0.015163267	0.45
5	7001.5	98.03	221.372682	2.4916	1.377216	1.107196	6.534302	3.054409	6.533302	45.053	0.015306196	0.45
6	7002	96.18	225.325485	2.4806	1.353056	1.087771	6.279357	2.935161	6.278357	44.207	0.015927734	0.44
7	7002.5	92.06	224.274934	2.4835	1.359394	1.092867	6.345697	2.966189	6.344697	44.429	0.015761194	0.44
8	7003	92.68	224.419551	2.4831	1.358518	1.092163	6.336505	2.961891	6.335505	44.398	0.015784061	0.44
9	7003.5	94.21	225.725702	2.4795	1.350657	1.085843	6.254353	2.923466	6.253353	44.123	0.015991421	0.44
10	7004	94.12	231.496766	2.4639	1.316986	1.058771	5.909188	2.762022	5.908188	42.945	0.016925663	0.43
11	7004.5	92.16	237.027466	2.4494	1.286256	1.034064	5.603662	2.619117	5.602662	41.869	0.017848658	0.42
12	7005	92.34	246.997176	2.4243	1.234338	0.992322	5.10785	2.387216	5.10685	40.052	0.019581542	0.40
13	7005.5	91.9	250.243161	2.4164	1.218327	0.979449	4.960086	2.318104	4.959086	39.491	0.020165006	0.39
14	7006	94.18	249.210178	2.4189	1.223377	0.98351	5.00643	2.33978	5.00543	39.668	0.019978304	0.40
15	7006.5	93.42	238.114317	2.4466	1.280385	1.029344	5.54631	2.592292	5.54531	41.663	0.018033257	0.42
16	7007	94.47	233.575379	2.4584	1.305266	1.049348	5.791604	2.70702	5.790604	42.534	0.017269356	0.43
17	7007.5	95.15	232.023714	2.4625	1.313995	1.056366	5.87906	2.747928	5.87806	42.84	0.017012416	0.43
18	7008	93.87	235.331986	2.4538	1.295523	1.041515	5.694855	2.661769	5.693855	42.193	0.017562794	0.42
19	7008.5	93.13	238.816375	2.4448	1.276621	1.026317	5.509718	2.575175	5.508718	41.532	0.018153044	0.42
20	7009	88.28	241.571142	2.4378	1.262063	1.014613	5.369445	2.509566	5.368445	41.022	0.018627368	0.41
21	7009.5	90.2	248.428772	2.4208	1.227225	0.986603	5.04191	2.356374	5.04091	39.803	0.019837688	0.40
22	7010	89.17	243.203142	2.4337	1.253594	1.007804	5.28877	2.471833	5.28777	40.726	0.018911564	0.41
23	7010.5	88.21	239.677933	2.4426	1.272032	1.022628	5.465286	2.554394	5.464286	41.371	0.018300653	0.41
24	7011	89.98	232.363241	2.4616	1.312075	1.054823	5.859758	2.738901	5.858758	42.773	0.017068464	0.43

Appendix A8: Some calculated values of reservoir elastic and inelastic parameters from ‘‘Fuja’’ 4 well.

Appendix B: Reservoir Petrophysical Parameters, Core Sample Description and Effective Pressure

VShale	Effective Porosity	Total Porosity	CORE SAMPLE DESCRIPTION	GRAIN DENSITY gm/cc	Diff Pressure (Psi)	Pore Pressure (psi)	Perm (mD)
0.569	0.0811	0.1882	Sst, dk-brn,m-grn,lam, mica, pr srt, mod cmt, mod consol,	2.66	16963.99	15111.6	0.0858
0.5646	0.0792	0.1818	Sst, lt gry,f-m grn,lam, mica, carb, mod srt, mod cmt, mod consol,	2.65	16964.89	15112.3	0.0273
0.5815	0.0817	0.1952	Sst, brn,cr-m grn,lam, mica, carb, pr srt, mod cmt, mod consol,	2.64	16965.8	15113.2	0.0673
0.4475	0.1146	0.2074	Sst, brn, cr-mgrn ,mass, mica, carb, , wl consol, pr-srt, wl cmt,	2.67	16966.7	13417.5	0.0373
0.4154	0.1201	0.2055	Sst, brn, cr-mgrn ,mass, mica, mod consol, pr-srt, pr cmt, Vuggy	2.73	16967.6	13418.2	0.0985
0.4181	0.1127	0.1937	Sst, lt-brn,cr-mgrn,mass,mica,mod-consol,mod-cmt,pr-srt,	2.68	16968.5	13418.9	0.4349
0.3739	0.1207	0.1927	Sst, lt brn, m-crs grn ,mass, mica, carb, mod consol, mod srt, mod cmt,	2.65	16969.41	13419.6	0.8534
0.3647	0.1282	0.2018	Sst, lt-brn, m-crs grn, mass, mica, mod consol, pr srt, mod cmt,	2.64	16970.31	13420.4	1.0113
0.3936	0.1303	0.2148	Sst, lt-brn, m-fgrn, lam, mica, mod consol,wl srt, mod cmt, carb,	2.64	16971.21	13421.1	0.2631
0.4446	0.1112	0.2002	Sst, brn, m-grn, carb, mica, mod consol, wl srt, mod cmt,	2.66	16972.11	13421.9	0.0628
0.4418	0.0981	0.1758	Sst, brn, cr-mgrn, carb, mass, mod consol, pr srt, mod cmt, mica,	2.64	16973.02	13422.5	0.0354
0.4368	0.0976	0.1732	Sst, brn, crs-grn, mass,carb,mica, mod consol, pr srt, mod cmt,	2.67	16973.92	13423.2	0.0649
0.4475	0.1048	0.1896	Sst, brn, f-mgrn, thk lam,carb, mod consol, mod srt, mod cmt,	2.64	16974.82	13423.9	0.2191
0.5229	0.096	0.2012	Sst, brn, crs-mgrn, mass,mica, mod consol, pr srt, mod cmt,	2.64	16975.72	15121.9	0.373
0.5287	0.0989	0.2099	Sst, brn, m-crs grn, lam, carb, wl consol, pr srt, wl cmt,mica	2.67	16976.63	15122.8	1.5271
0.4894	0.0972	0.1903	Sst, brn, crs-m grn, lam, carb, mica,wl consol, pr srt, wl cmt,	2.64	16977.53	13426.1	1.149
0.434	0.09	0.159	Sst, lt-gry, f-grn, lam, carb, mica, wl consol, wl srt, wl cmt,	2.77	16978.43	13426.9	0.4103
0.4801	0.0826	0.159	Sst, lt-gry, f-grn, lam, carb, mica, wl consol, wl srt, wl cmt,	2.77	16979.33	13427.5	0.4299
0.5132	0.0916	0.1882	Slst, brn, vf-fgrn, mass, wl consol, wl srt, wl cmt,	2.76	16980.23	15126	0.5606
0.5879	0.0793	0.1923	Slst, brn, vf-fgrn, thk lam, wl consol, carb, wl srt, wl cmt,	2.65	16981.14	15126.8	0.1533
0.514	0.0956	0.1967	Slst, gry, vf-fgrn,lt lam, wl consol, wl srt, wl cmt,	2.67	16982.04	15127.6	0.0647
0.5279	0.0981	0.2079	Slst, gry, vf-fgrn, lt lam, carb, wl consol, wl srt, wl cmt,	2.68	16982.94	15128.4	0.0236
0.4733	0.1166	0.2214	Slst, gry, vf-f grn, lt lam, wl consol, wl cmt,wl srt,	2.69	16983.84	13431.1	0.0646

Appendix B1: Some calculated values of reservoir petrophysical parameters, effective and pore pressures as well as core sample description for ‘‘Beta’’ 1 well.

	1	VShale	Por,Eff,	Por,Tot,	CORE SAMPLE DESCRIPTION	GRAIN DENSITY gm/c	FOOT NOTE	Diff, Pressure (psi)	Perm (mD)
2		0.4386	0.2242	0.1259	Sst, dk-brn,m-grn,lam, mica, pr srt, mod cmt, mod consol,	2.62	(1)	16963.99	3.6787
3		0.4431	0.2295	0.1278	Sst, lt gry,f-m grn,lam, mica, carb, mod srt, mod cmt, mod consol,	2.65		16964.89	4.0249
4		0.4973	0.2419	0.1216	Sst, brn,cr-m grn,lam, mica, carb, pr srt, mod cmt, mod consol,	2.64		16965.8	2.9937
5		0.5089	0.2295	0.1127	Sst, brn, cr-mgrn ,mass, mica, carb, , wl consol, pr-srt, wl cmt,	2.67		16966.7	1.8926
6		0.4948	0.2204	0.1113	Sst, brn, cr-mgrn ,mass, mica, mod consol, pr-srt, pr cmt, Vuggy	2.73	(1), (4)	16967.6	1.7602
7		0.4778	0.2004	0.1047	Sst, lt-brn,cr-mgrn,mass,mica,mod-consol,mod-cmt,pr-srt,	2.68		16968.5	1.2149
8		0.4637	0.1995	0.107	Sst, lt brn, m-crs grn ,mass, mica, carb, mod consol, mod srt, mod cmt,	2.65		16969.41	1.3855
9		0.4644	0.197	0.1055	Sst, lt-brn, m-crs grn, mass, mica, mod consol, pr srt, mod cmt,	2.64		16970.31	1.2763
10		0.4446	0.217	0.1205	Sst, lt-brn, m-fgrn, lam, mica, mod consol,wl srt, mod cmt, carb,	2.64		16971.21	2.8359
11		0.5199	0.2339	0.1123	Sst, brn, m-grn, carb, mica, mod consol, wl srt, mod cmt,	2.66		16972.11	1.8548
12		0.5268	0.26	0.123	Sst, brn, cr-mgrn, carb, mass, mod consol, pr srt, mod cmt, mica,	2.64		16973.02	3.2052
13		0.5561	0.2616	0.1161	Sst, brn, crs-grn, mass,carb,mica, mod consol, pr srt, mod cmt,	2.67		16973.92	2.2692
14		0.5165	0.2651	0.1282	Sst, brn, f-mgrn, thk lam,carb, mod consol, mod srt, mod cmt,	2.64	(1)	16974.82	4.0975
15		0.5098	0.2436	0.1194	Sst, brn, crs-mgrn, mass,mica, mod consol, pr srt, mod cmt,	2.64		16975.72	2.6804
16		0.4834	0.2362	0.122	Sst, brn, m-crs grn, lam, carb, wl consol, pr srt, wl cmt,mica	2.67		16976.63	3.0541
17		0.4746	0.2305	0.1211	Sst, brn, crs-m grn, lam, carb, mica,wl consol, pr srt, wl cmt,	2.64		16977.53	2.9141
18		0.4707	0.2381	0.126	Sst, lt-gry, f-grn, lam, carb, mica, wl consol, wl srt, wl cmt,	2.77	(4)	16978.43	3.7063
19		0.4424	0.2345	0.1308	Sst, lt-gry, f-grn, lam, carb, mica, wl consol, wl srt, wl cmt,	2.77	(4)	16979.33	4.6284
20		0.4454	0.2301	0.1276	Slst, brn, vf-fgrn, mass, wl consol, wl srt, wl cmt,	2.76	(4)	16980.23	3.9912
21		0.5234	0.2372	0.113	Slst, brn, vf-fgrn, thk lam, wl consol, carb, wl srt, wl cmt,	2.65		16981.14	1.9281
22		0.6051	0.2512	0.0992	Slst, gry, vf-fgrn,lt lam, wl consol, wl srt, wl cmt,	2.67		16982.04	0.8816
23		0.6391	0.2788	0.1006	Slst, gry, vf-fgrn, lt lam, carb, wl consol, wl srt, wl cmt,	2.68		16982.94	0.9591
24		0.6021	0.2625	0.1045	Slst, gry, vf-f grn, lt lam, wl consol, wl cmt,wl srt,	2.69	(3)	16983.84	1.2009

Appendix B2: Some calculated values of reservoir petrophysical parameters and effective pressure as well as core sample description from ‘‘Beta’’ 2 well.

	VShale	Por,Eff,	Por,Tot,	CORE SAMPLE DESCRIPTION	GRAIN DENSITY gr	FOOT NOTE	Diff, Pressure (psi)	Perm (mD)
2	0.4401	0.1473	0.0825	Sst, dk-brn,m-grn,lam, mica, pr srt, mod cmt, mod consol,	2.64	(1)	18949.14	0.2906
3	0.4373	0.1475	0.083	Sst, lt gry,f-m grn,lam, mica, carb, mod srt, mod cmt, mod consol,	2.65		18950.04	0.3024
4	0.4527	0.1617	0.0885	Sst, brn,cr-m grn,lam, mica, carb, pr srt, mod cmt, mod consol,	2.64		18950.95	0.4439
5	0.4857	0.1805	0.0928	Sst, brn, cr-mgrn ,mass, mica, carb, , wl consol, pr-srt, wl cmt,	2.67		18951.85	0.5913
6	0.4353	0.1973	0.1114	Sst, brn, cr-mgrn ,mass, mica, mod consol, pr-srt, pr cmt, Vuggy	2.73	(1), (4)	18952.75	1.7712
7	0.425	0.1904	0.1095	Sst, lt-brn,cr-mgrn,mass,mica,mod-consol,mod-cmt,pr-srt,	2.68		18953.65	1.5896
8	0.4183	0.1784	0.1037	Sst, lt brn, m-crs grn ,mass, mica, carb, mod consol, mod srt, mod cmt,	2.65		18954.55	1.1529
9	0.4842	0.1527	0.0788	Sst, lt-brn, m-crs grn, mass, mica, mod consol, pr srt, mod cmt,	2.64		18955.46	0.2209
10	0.4805	0.1335	0.0693	Sst, lt-brn, m-fgrn, lam, mica, mod consol,wl srt, mod cmt, carb,	2.64		18956.36	0.1027
11	0.4642	0.1401	0.075	Sst, brn, m-grn, carb, mica, mod consol, wl srt, mod cmt,	2.66		18957.26	0.1651
12	0.423	0.1547	0.0892	Sst, brn, cr-mgrn, carb, mass, mod consol, pr srt, mod cmt, mica,	2.64		18958.16	0.467
13	0.4738	0.1663	0.0875	Sst, brn, crs-grn, mass,carb,mica, mod consol, pr srt, mod cmt,	2.67		18959.07	0.4153
14	0.4979	0.1765	0.0886	Sst, brn, f-mgrn, thk lam,carb, mod consol, mod srt, mod cmt,	2.64	(1)	18959.97	0.4484
15	0.5151	0.1775	0.086	Sst, brn, crs-mgrn, mass,mica, mod consol, pr srt, mod cmt,	2.64		18960.87	0.3751
16	0.4865	0.176	0.0904	Sst, brn, m-crs grn, lam, carb, wl consol, pr srt, wl cmt,mica	2.67		18961.77	0.5039
17	0.413	0.1745	0.1025	Sst, brn, crs-m grn, lam, carb, mica,wl consol, pr srt, wl cmt,	2.64		18962.68	1.0691
18	0.3918	0.1835	0.1116	Sst, lt-gry, f-grn, lam, carb, mica, wl consol, wl srt, wl cmt,	2.77	(4)	18963.58	1.7843
19	0.3714	0.2176	0.1368	Sst, lt-gry, f-grn, lam, carb, mica, wl consol, wl srt, wl cmt,	2.77	(4)	18964.48	6.0595
20	0.4366	0.2258	0.1272	Slst, brn, vf-fgrn, mass, wl consol, wl srt, wl cmt,	2.76	(4)	18965.38	3.9133
21	0.4499	0.2154	0.1185	Slst, brn, vf-fgrn, thk lam, wl consol, carb, wl srt, wl cmt,	2.65		18966.29	2.5584
22	0.4332	0.2006	0.1137	Slst, gry, vf-fgrn,lt lam, wl consol, wl srt, wl cmt,	2.67		18967.19	1.998
23	0.3578	0.2113	0.1357	Slst, gry, vf-fgrn, lt lam, carb, wl consol, wl srt, wl cmt,	2.68		18968.09	5.7796
24	0.3601	0.2323	0.1486	Slst, gry, vf-f grn, lt lam, wl consol, wl cmt,wl srt,	2.69	(3)	18968.99	9.9743

Appendix B3: Some calculated values of reservoir petrophysical parameters and effective pressure as well as core sample description from ‘‘Beta’’ 3 well.

	VShale	Por,Eff,	Por,Tot,	CORE SAMPLE DESCRIPTION	GRAIN DENSITY gm/	FOOT NOTE	Diff, Pressure (psi)	Perm (mD)
2	0.603	0.1648	0.0654	Sst, dk-brn,m-grn,lam, mica, pr srt, mod cmt, mod consol,	2.67	(1)	18950.04	0.0102
3	0.6892	0.1518	0.0472	Sst, lt gry,f-m grn,lam, mica, carb, mod srt, mod cmt, mod consol,	2.65		18950.95	0.0159
4	0.6355	0.1395	0.0508	Sst, brn,cr-m grn,lam, mica, carb, pr srt, mod cmt, mod consol,	2.64		18951.85	0.0022
5	0.7239	0.132	0.0364	Sst, brn, cr-mgrn ,mass, mica, carb, , wl consol, pr-srt, wl cmt,	2.67		18952.75	0.017
6	0.6334	0.1401	0.0514	Sst, brn, cr-mgrn ,mass, mica, mod consol, pr-srt, pr cmt, Vuggy	2.73	(1), (4)	18953.65	0.0235
7	0.656	0.1576	0.0542	Sst, lt-brn,cr-mgrn,mass,mica,mod-consol,mod-cmt,pr-srt,	2.68		18954.55	0.0723
8	0.6178	0.1711	0.0654	Sst, lt brn, m-crs grn ,mass, mica, carb, mod consol, mod srt, mod cmt,	2.65		18955.46	0.0252
9	0.6753	0.1689	0.0548	Sst, lt-brn, m-crs grn, mass, mica, mod consol, pr srt, mod cmt,	2.64		18956.36	0.0318
10	0.6241	0.1518	0.057	Sst, lt-brn, m-fgrn, lam, mica, mod consol,wl srt, mod cmt, carb,	2.64		18957.26	0.0229
11	0.6329	0.1471	0.054	Sst, brn, m-grn, carb, mica, mod consol, wl srt, mod cmt,	2.66		18958.16	0.1169
12	0.6358	0.1945	0.0708	Sst, brn, cr-mgrn, carb, mass, mod consol, pr srt, mod cmt, mica,	2.64		18959.07	0.0645
13	0.7143	0.2246	0.0642	Sst, brn, crs-grn, mass,carb,mica, mod consol, pr srt, mod cmt,	2.67		18959.97	0.0289
14	0.7314	0.209	0.0561	Sst, brn, f-mgrn, thk lam,carb, mod consol, mod srt, mod cmt,	2.64	(1)	18960.87	0.0029
15	0.764	0.1622	0.0383	Sst, brn, crs-mgrn, mass,mica, mod consol, pr srt, mod cmt,	2.64		18961.77	0.001
16	0.7992	0.1599	0.0321	Sst, brn, m-crs grn, lam, carb, wl consol, pr srt, wl cmt,mica	2.67		18962.68	0.0005
17	0.8169	0.1535	0.0281	Sst, brn, crs-m grn, lam, carb, mica,wl consol, pr srt, wl cmt,	2.64		18963.58	0.0004
18	0.7903	0.1291	0.0271	Sst, lt-gry, f-grn, lam, carb, mica, wl consol, wl srt, wl cmt,	2.77	(4)	18964.48	0.0004
19	0.793	0.1352	0.028	Sst, lt-gry, f-grn, lam, carb, mica, wl consol, wl srt, wl cmt,	2.77	(4)	18965.38	0.0006
20	0.8079	0.1542	0.0296	Slst, brn, vf-fgrn, mass, wl consol, wl srt, wl cmt,	2.76	(4)	18966.29	0.0003
21	0.8391	0.1597	0.0257	Slst, brn, vf-fgrn, thk lam, wl consol, carb, wl srt, wl cmt,	2.65		18967.19	0.0013
22	0.749	0.133	0.0334	Slst, gry, vf-fgrn,lt lam, wl consol, wl srt, wl cmt,	2.67		18968.09	0.0021
23	0.6952	0.1191	0.0363	Slst, gry, vf-fgrn, lt lam, carb, wl consol, wl srt, wl cmt,	2.68		18968.99	0.0028
24	0.6828	0.1196	0.0379	Slst, gry, vf-f grn, lt lam, wl consol, wl cmt,wl srt,	2.69	(3)	18969.89	0.0021

Appendix B4: Some calculated values of reservoir petrophysical parameters and effective pressure as well as core sample description from ‘‘Beta’’ 4 well.

	Vsh	Porot	Poreff	Perm	Diff_pressure(psi)	CORE SAMPLE DESCRIPTION
2	0.6548	0.0383	0.0132	0.0001	14437.44	Grey: fine to silt: with a few medium grains: moderately sorted and unconsolidated,
3	0.8892	0.0279	0.0031	0.0001	14442.85	Grey: fine to silt: well sorted and unconsolidated,
4	0.8781	0.0475	0.0058	0.0001	14443.76	Grey: very coarse to silt: poorly sorted and unconsolidated,
5	0.8688	0.061	0.008	0.0004	14444.66	Grey: fine to silt: Well sorted and loose,
6	0.8772	0.0639	0.0078	0.0006	14445.56	Grey: fine to silt: Well sorted and loose,
7	0.8696	0.0644	0.0084	0.002	14446.46	Grey: coarse to silt with a few very coarse grains: poorly sorted and unconsolidated,
8	0.8282	0.0601	0.0103	0.0027	14447.37	Grey: coarse to silt: moderately sorted and loose,
9	0.8234	0.0591	0.0104	0.0017	14448.27	Grey: very coarse to silt: poorly sorted and llose,
10	0.8203	0.0581	0.0104	0.0016	14449.17	Grey: coarse to silt: moderately sorted and loose,
11	0.8316	0.0654	0.011	0.0021	14450.07	Grey: very fine to silt: with a few scattered fine grains: well sorted and unconsolidated,
12	0.8386	0.0653	0.0105	0.0053	14450.98	Grey: coarse to silt: moderately sorted and loose,
13	0.8645	0.0627	0.0085	0.1055	14451.88	Grey: fine to silt: well sorted and unconsolidated,
14	0.8389	0.066	0.0106	0.5234	14452.78	Grey: fine to silt: with a few medium grains: moderately sorted and loose,
15	0.835	0.0689	0.0114	1.0385	14453.68	Grey: coarse to silt: with a few granules: poorly sorted and loose,
16	0.8613	0.0602	0.0084	0.9949	14454.58	Grey: coarse to silt with a few very coarse grains: poorly sorted and unconsolidated,
17	0.9016	0.0539	0.0053	0.4769	14455.49	Grey: coarse to silt with a few very coarse grains: poorly sorted and loose,
18	0.9441	0.0421	0.0024	0.0141	14456.39	Grey: very fine to silt: well sorted and loose,
19	0.9149	0.049	0.0042	0.0001	14457.29	Grey: very fine to silt: with a few fine grains: well sorted and unconsolidated,
20	0.8851	0.0519	0.006	0.0003	14458.19	Grey: very fine to silt: well sorted and loose,
21	0.8518	0.06	0.0089	0.0262	14459.1	Grey: very fine to silt: well sorted and loose,
22	0.8971	0.0524	0.0054	0.0485	14460	Grey: very fine to silt: well sorted and unconsolidated,
23	0.9566	0.0462	0.002	0.0008	14460.9	Grey: very fine to silt: well sorted and unconsolidated,
24	0.9803	0.0436	0.0009	0.0002	14461.8	Grey: very fine to silt: with a few fine grains: well sorted and loose,

Appendix B5: Some calculated values of reservoir petrophysical parameters and effective pressure as well as core sample description from ‘‘Fuja’’ 1 well.

	Vsh	Porot	Poreff	perm	Diff_pressure(psi)	CORE SAMPLE DESCRIPTION
2	0.9735	0.0988	0.0026	0.0001	14437.44	Dark grey; silty; frangible,
3	0.9886	0.0979	0.0011	0.0004	14438.34	Dark grey; silty; frangible,
4	1	0.0964	0	0.0022	14439.25	Dark grey; silty; frangible,
5	1	0.0946	0	0.0038	14440.15	Dark grey; silty; frangible,
6	1	0.0909	0	0.0028	14441.05	Dark grey; silty; frangible,
7	1	0.0849	0	0.0016	14441.95	Dark grey; silty; frangible,
8	1	0.0805	0	0.0011	14442.85	Dark grey; silty; frangible,
9	1	0.0834	0	0.0008	14443.76	Dark grey; silty; frangible,
10	1	0.0927	0	0.0009	14444.66	Dark grey; silty; frangible,
11	1	0.0979	0	0.001	14445.56	Dark grey; silty; frangible,
12	1	0.095	0	0.0009	14446.46	Dark grey; silty; frangible,
13	1	0.094	0	0.0006	14447.37	Dark grey; silty; frangible,
14	1	0.1013	0	0.001	14448.27	Dark grey; silty; frangible,
15	0.9973	0.1113	0.0003	0.0037	14449.17	Grey;V,fL-fL;very silty;very well sorted;clayey;slightly calcareous;loosely consolidated,
16	0.9688	0.1182	0.0037	0.0105	14450.07	Grey;V,fL-fU;very silty;very well sorted;slightly shaly and calcareous;loosely consolidated,
17	0.9642	0.1205	0.0043	0.0137	14450.98	Grey/dark grey;V,fL-fU;very silty;very well sorted;slightly calcareous;loosely consolidated,
18	0.9742	0.1202	0.0031	0.0128	14451.88	Dark grey;very silty;V,fL-fU grains;slightly calcareous;frangible,
19	0.9893	0.121	0.0013	0.0111	14452.78	Grey;V,fL-fU;very silty;very well sorted;calcareous;loosely consolidated,
20	0.9944	0.123	0.0007	0.0086	14453.68	Grey;V,fL-crsL;very silty;high sphericity;subrounded-subangular grains;well sorted;slightly shaly and calcareous;loosely consolidated,
21	0.9753	0.1217	0.003	0.0063	14454.58	Grey;V,fL-mU;very silty;very well sorted;clayey;slightly calcareous;loosely consolidated,
22	0.9519	0.1156	0.0056	0.003	14455.49	Grey;V,fL-fU;very silty;very well sorted;slightly clayey;calcareous;loosely consolidated,
23	0.9546	0.1085	0.0049	0.0005	14456.39	Grey;V,fU-mU;silty;very well sorted;slightly shaly and calcareous;loosely consolidated,
24	0.9683	0.1027	0.0033	0.003	14457.29	Grey;v,fL-mU;very silty;very well sorted;slightly shaly and calcareous;loosely consolidated,

Appendix B6: Some calculated values of reservoir petrophysical parameters and effective pressure as well as core sample description from ‘‘Fuja’’ 2 well.

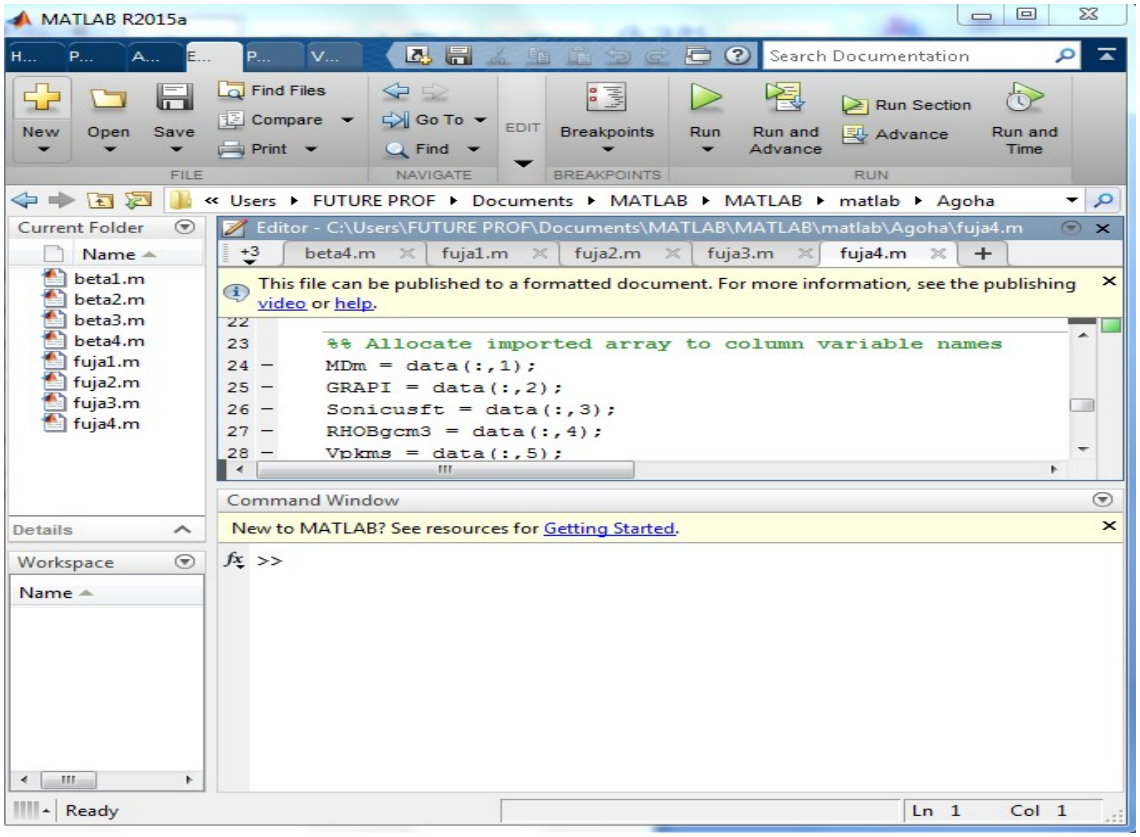
	Vsh	Porot	Poreff	Perm	Diff_pressure(psi)	CORE SAMPLE DESCRIPTION
2	0.6548	0.0383	0.0132	0.0001	14437.44	Grey: fine to silt: with a few medium grains: moderately sorted and unconsolidated,
3	0.8892	0.0279	0.0031	0.0001	14442.85	Grey: fine to silt: well sorted and unconsolidated,
4	0.8781	0.0475	0.0058	0.0001	14443.76	Grey: very coarse to silt: poorly sorted and unconsolidated,
5	0.8688	0.061	0.008	0.0004	14444.66	Grey: fine to silt: Well sorted and loose,
6	0.8772	0.0639	0.0078	0.0006	14445.56	Grey: fine to silt: Well sorted and loose,
7	0.8696	0.0644	0.0084	0.002	14446.46	Grey: coarse to silt with a few very coarse grains: poorly sorted and unconsolidated,
8	0.8282	0.0601	0.0103	0.0027	14447.37	Grey: coarse to silt: moderately sorted and loose,
9	0.8234	0.0591	0.0104	0.0017	14448.27	Grey: very coarse to silt: poorly sorted and llose,
10	0.8203	0.0581	0.0104	0.0016	14449.17	Grey: coarse to silt: moderately sorted and loose,
11	0.8316	0.0654	0.011	0.0021	14450.07	Grey: very fine to silt: with a few scattered fine grains: well sorted and unconsolidated,
12	0.8386	0.0653	0.0105	0.0053	14450.98	Grey: coarse to silt: moderately sorted and loose,
13	0.8645	0.0627	0.0085	0.1055	14451.88	Grey: fine to silt: well sorted and unconsolidated,
14	0.8389	0.066	0.0106	0.5234	14452.78	Grey: fine to silt: with a few medium grains: moderately sorted and loose,
15	0.835	0.0689	0.0114	1.0385	14453.68	Grey: coarse to silt: with a few granules: poorly sorted and loose,
16	0.8613	0.0602	0.0084	0.9949	14454.58	Grey: coarse to silt with a few very coarse grains: poorly sorted and unconsolidated,
17	0.9016	0.0539	0.0053	0.4769	14455.49	Grey: coarse to silt with a few very coarse grains: poorly sorted and loose,
18	0.9441	0.0421	0.0024	0.0141	14456.39	Grey: very fine to silt: well sorted and loose,
19	0.9149	0.049	0.0042	0.0001	14457.29	Grey: very fine to silt: with a few fine grains: well sorted and unconsolidated,
20	0.8851	0.0519	0.006	0.0003	14458.19	Grey: very fine to silt: well sorted and loose,
21	0.8518	0.06	0.0089	0.0262	14459.1	Grey: very fine to silt: well sorted and loose,
22	0.8971	0.0524	0.0054	0.0485	14460	Grey: very fine to silt: well sorted and unconsolidated,
23	0.9566	0.0462	0.002	0.0008	14460.9	Grey: very fine to silt: well sorted and unconsolidated,
24	0.9803	0.0436	0.0009	0.0021	14461.8	Grey: very fine to silt: with a few fine grains: well sorted and loose,

Appendix B7: Some calculated values of reservoir petrophysical parameters and effective pressure as well as core sample description from ‘‘Fuja’’ 3 well.

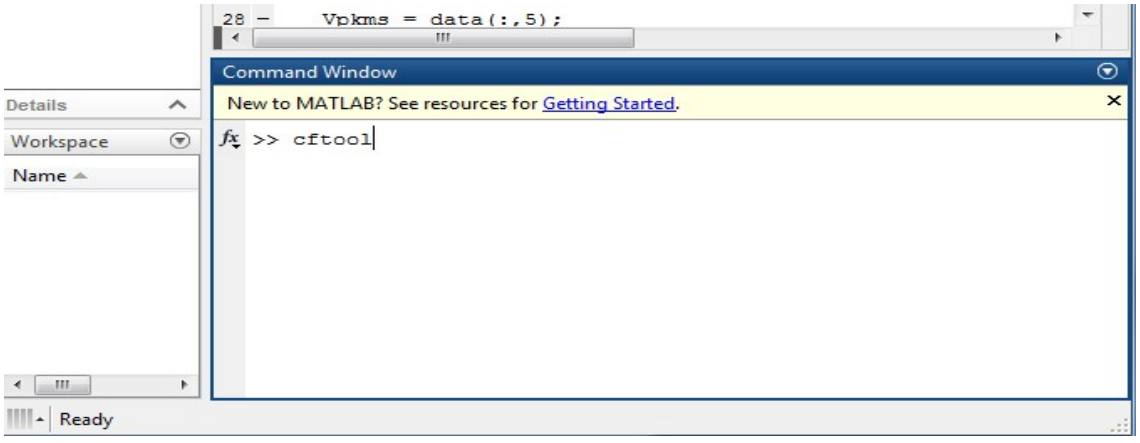
	Vsh	Porot	Poreff	Perm (mD)	Diff_pressure(psi)	Core Sample Description
2	0.6289	0.1133	0.042	0.0051	12632.76	Light yellowish grey; calcareous,
3	0.6419	0.101	0.0362	0.0021	12633.66	Brownish/ dark grey; partly calcareous; frangible,
4	0.6232	0.0944	0.0356	0.0019	12634.56	Dark grey; slightly silty; frangible,
5	0.6034	0.096	0.0381	0.0028	12635.47	Dark grey; silty; frangible,
6	0.623	0.1027	0.0387	0.0031	12636.37	Dark grey; silty; frangible,
7	0.6817	0.1009	0.0321	0.001	12637.27	Dark grey; silty; frangible,
8	0.7025	0.1012	0.0301	0.0007	12638.17	Dark grey; silty; frangible,
9	0.6666	0.1033	0.0345	0.0015	12639.08	Dark grey; silty; frangible,
10	0.6054	0.1128	0.0445	0.0072	12639.98	Dark grey; silty; frangible,
11	0.6017	0.1216	0.0484	0.0119	12640.88	Dark grey; silty; frangible,
12	0.6087	0.1368	0.0535	0.0217	12641.78	Dark brownish grey; silty; slightly calcareous; frangible,
13	0.6302	0.1416	0.0524	0.019	12642.69	Dark grey; silty; frangible,
14	0.6329	0.1401	0.0514	0.0171	12643.59	Dark grey; silty; slightly calcareous; frangible,
15	0.6934	0.1233	0.0378	0.0027	12644.49	Dark grey; silty; very slightly calcareous; frangible,
16	0.7053	0.1161	0.0342	0.0015	12645.39	Dark grey; silty; slightly calcareous; frangible,
17	0.7346	0.1136	0.0302	0.0007	12646.29	Dark grey; silty; frangible,
18	0.7085	0.1189	0.0347	0.0016	12647.2	Dark grey; silty; frangible,
19	0.6592	0.1244	0.0424	0.0054	12648.1	Dark grey; silty; frangible,
20	0.6362	0.1286	0.0468	0.0097	12649	Dark grey; silty; slightly calcareous; frangible,
21	0.6112	0.1389	0.054	0.0229	12649.9	Dark grey; silty; frangible,
22	0.6926	0.1311	0.0403	0.004	12650.81	Dark grey; silty; slightly calcareous; frangible,
23	0.7232	0.1257	0.0348	0.0016	12651.71	Dark grey; silty; slightly calcareous; frangible,
24	0.7698	0.1142	0.0263	0.0003	12652.61	Dark grey; silty; frangible,

Appendix B8: Some calculated values of reservoir petrophysical parameters and effective pressure as well as core sample description from ‘‘Fuja’’ 4 well.

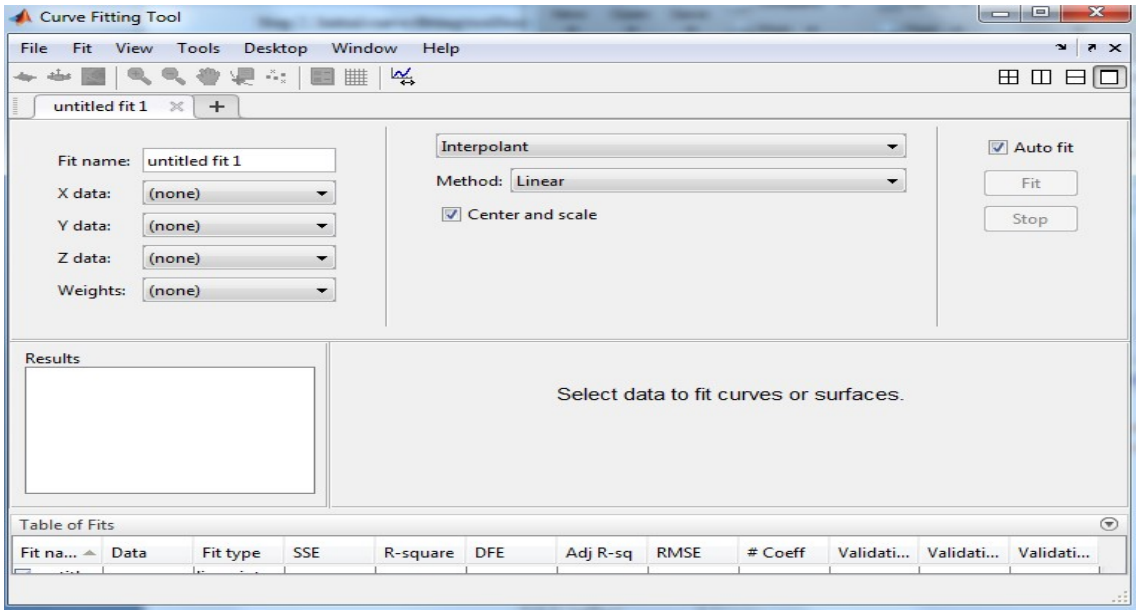
Appendix C: Empirical Linear and Non-Linear Modeling



Appendix C1: MATLAB environment with the imported data



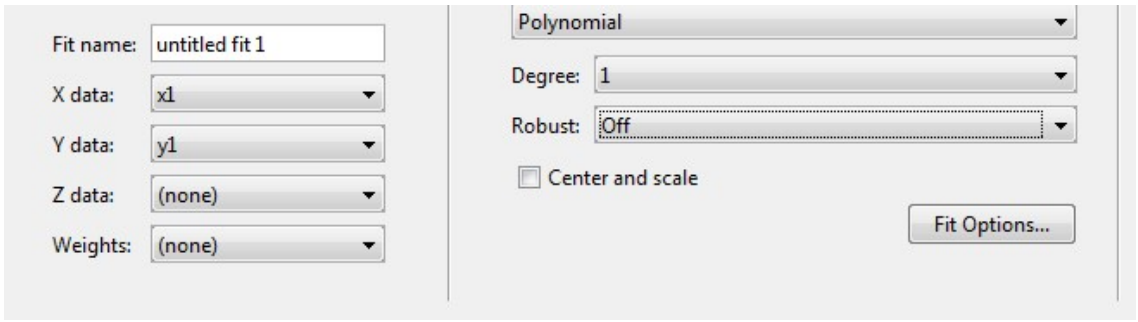
Appendix C2: Snapshot of the curve fitting tool command in MATLAB



Appendix C3: Graphic User Interface of curve fitting toolbox

```
1 -    beta1
2 -    x11 = RHOBgcm3;% density
3 -    x12 = Sonicusft;% sonic
4 -    y11 = UCSGpa;% UCS
5 -    y12 = VSkms;%VS
6 -    fuja1
7 -    x21 = RHOBgcm3;% density
8 -    x22 = Sonicusft;% sonic
9 -    y21 = UCSGpa;% UCS
10 -   y22 = VSkms;%VS
11
12 -   x1 = [x11;x21];% density
```

Appendix C4: Data codes for combining the data from different wells



Appendix C5: Snapshot of curve fitting tool with linear model

The linear model is given by: $y = a_o + a_1 x$ Where y is the dependent variable, x is the independent variable.				
RELATIONSHIP	**REGRESSION COEFFICIENTS**	**R-SQUARED**	**Equation**	**REMARK**
UCS versus bulk density	$a_0 =$ **-164.9** $a_1 =$ **84.6**	**0.8637**	**UCS = -164.9+ 84.6ρ_b**	**Can be used**
UCS versus Sonic	$a_0 =$ **45.33** $a_1 =$ **-0.01327**	**0.003559**		**Cannot be used**
Permeability versus bulk density	$a_0 =$ **297.5** $a_1 =$ **-55.66**	**0.001263**		**Cannot be used**
Shear wave velocity versus Sonic	$a_0 =$ **1.577** $a_1 =$ **-0.001829**	**0.04606**		**Cannot be used**

Appendix C6: Summary table for linear model

The quadratic model is given by: $y = a_o + a_1 x + a_2 x^2$ Where y is the dependent variable, x is the independent variable.				
RELATIONSHIP	**REGRESSION COEFFICIENTS**	**R-SQUARED**	**Equation**	**REMARK**
UCS versus bulk density	$a_0 =$ **-696.9** $a_1 =$ **528.6** $a_2 =$ **-92.29**	**0.8848**	$UCS = -696.9 + 528.6\rho_b - 92.29{\rho_b}^2$	**Can be used**
UCS versus Sonic	$a_0 =$ **-0.001308** $a_1 =$ **0.5216** $a_2 =$ **-5.17**	**0.2159**		**Cannot be used**
Permeability versus bulk density	$a_0 =$ **7074** $a_1 =$ **-5825** $a_2 =$ **1222**	**0.00921**		**Cannot be used**
Shear wave velocity versus Sonic	$a_0 =$ **0.00004332** $a_1 =$ **-0.01594** $a_2 =$ **2.61**	**0.1214**		**Cannot be used**

Appendix C7: Summary table for quadratic model

The power model is given by: $y = a_o x^{a_1}$ Where y is the dependent variable, x is the independent variable.				
RELATIONSHIP	**REGRESSION COEFFICIENTS**	**R-SQUARED**	**Equation**	**REMARK**
UCS versus bulk density	$a_0 = 0.4845$ $a_1 = 4.96$	0.8216	**UCS = 0.4845$(\rho_b)^{4.96}$**	**Can be used**
UCS versus Sonic	$a_0 = 39.25$ $a_1 = 0.01535$	0.00029		**Cannot be used**
Permeability versus bulk density	$a_0 = 361.7$ $a_1 = -0.9089$	0.00155		**Cannot be used**
Shear wave velocity versus Sonic	$a_0 = 6.347$ $a_1 = -0.3197$	0.09036		**Cannot be used**

Appendix C8: Summary table for power model

The logarithmic model is given by: $y = a_o \log(a_1 x)$ Where y is the dependent variable, x is the independent variable.				
RELATIONSHIP	**REGRESSION COEFFICIENTS**	**R-SQUARED**	**Equation**	**REMARK**
UCS versus bulk density	$a_0 = 453$ $a_1 = 4.96$	0.9956	$UCS = 453log\ (4.96\rho_b)$	**Can be used**
UCS versus Sonic	$a_0 = 4.232$ $a_1 = 1.764e+08$	0.331		**Cannot be used**
Permeability versus bulk density	$a_0 = 9.736$ $a_1 = -0.9089$	0.00017		**Cannot be used**
Shear wave velocity versus Sonic	$a_0 = 486.2$ $a_1 = -0.1017$	0.1017		**Cannot be used**

Appendix C9: Summary table for logarithmic model

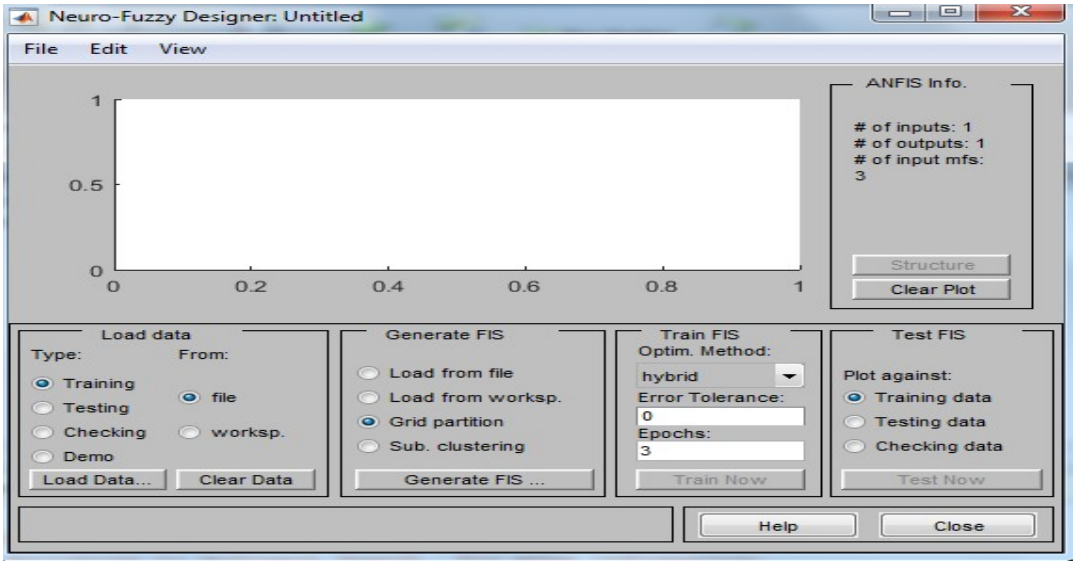
The exponential model is given by: $y = a_o \exp(a_1 x)$ Where y is the dependent variable, x is the independent variable.				
RELATIONSHIP	**REGRESSION COEFFICIENTS**	**R-SQUARED**	**Equation**	**REMARK**
UCS versus bulk density	$a_0 = 0.2876$ $a_1 = 2.024$	**0.8108**	$UCS = 0.2876\exp(2.02$	**Can be used**
UCS versus Sonic	$a_0 = 44.96$ $a_1 = -0.0002626$	**0.002995**		**Cannot be used**
Permeability versus bulk density	$a_0 = 396.3$ $a_1 = -0.3686$	**0.001394**		**Cannot be used**
Shear wave velocity versus Sonic	$a_0 = 1.652$ $a_1 = -0.001595$	**0.05125**		**Cannot be used**

Appendix C10: Summary table for exponential model

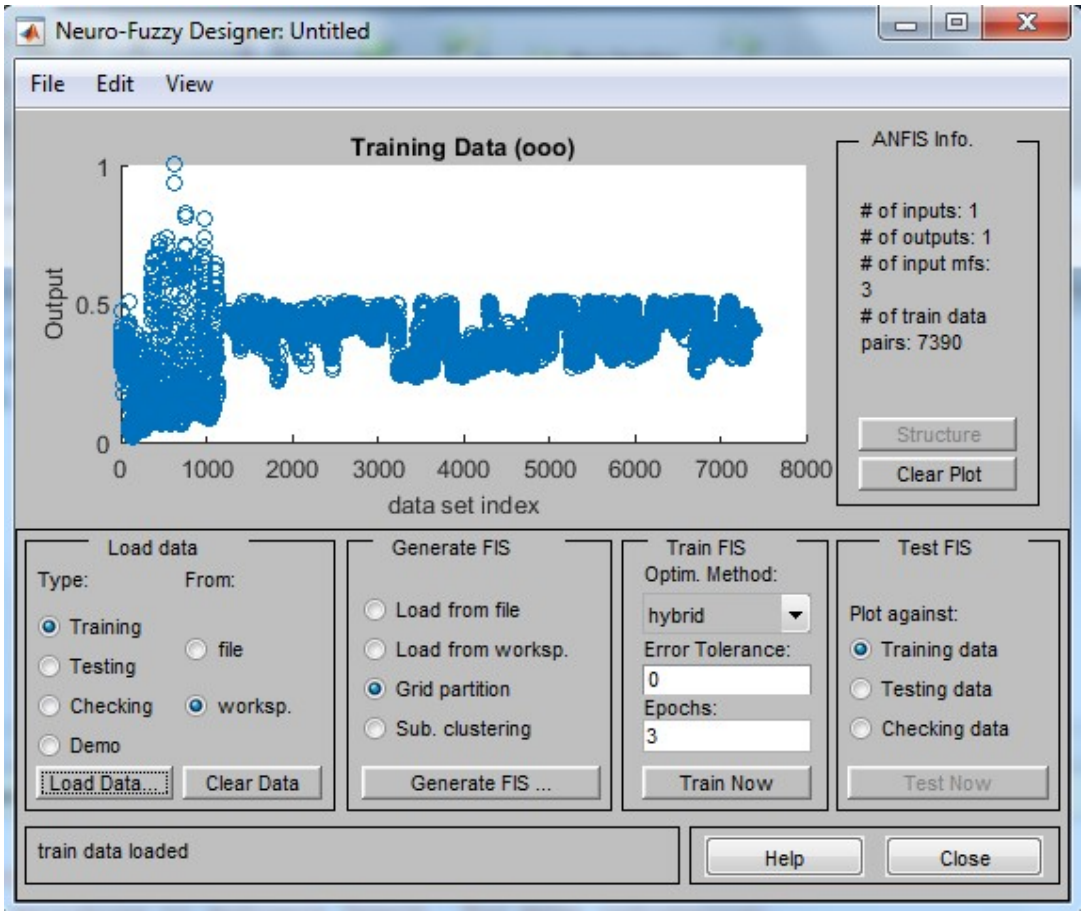
Appendix D: Modeling with Artificial Neural Network

```
1 -    X1 = x1/max(x1); % Normalization of density
2 -    Y1 = y1/max(y1); % Normalization of density
3
```

Appendix D1: Data normalization code



Appendix D2: ANFIS model environment



Appendix D3: Imported data to ANFIS model tool

Appendix E: Weights and Biases for ANN Model

1.0 For UCS Versus Bulk Density

Hidden Layer

Bias1=[-12.924070787817969; -5.5238815659793854; 1.795256886371168;-3.2463291041659557; -1.3388959929619653; -0.35436650838445671; -2.1006272773704713; 5.9111435367811582; 10.471825979153177; 13.95625672024545];

Weights1_1=[14.332874708457979; 7.8601852175834006;-15.78766367013454; 10.27997546345212; 8.9930710071809283; -6.4404895894805749; -7.3712417952231641; 10.858849884044835; 14.018825925234269; 14.013986875951467];

Output Layer

Bias2 = -0.52032498651842207;

Weights2_1 = [0.037934749060909385 0.068849812758166914 0.0050298082008995507 0.057628237487309254 0.030170458193256901 -0.060565852646096666 -0.15397685375703632 0.046698773375584084 0.031817810050832902 0.027162824523672698];

2.0 For UCS Versus Sonic Transit Time

Hidden Layer

Bias1=[12.065722846418147; -7.9132734565002609; -4.9554469376669221; 0.83989208634073531; 0.36770034084426761; 3.1652187624789572; 19.348897980815174; -23.242173622794855;-4.0165267590588423; 17.827136481533351];

Weights1_1=[-14.420267697597332; 11.867069580354995; 10.040811517677;-3.8714881589437953; 7.5731970833953497; 18.115247545288799; 64.965566498060895; -78.590590399379465; -2.9066034653603965; 12.243761017759903]

Output Layer

Bias2 = 4.3518003169195154;

Weights2_1 = [0.020945523537964722 -0.020063491784648405 -0.017829872856593553 0.1083118447648246 -0.055903614347807565 -0.026623294413529643 -3.2935449209540506 -3.7687516101144114 10.166997278531795 5.0237738614400165];

3.0 For Shear Wave Velocity Versus Sonic Transit Time

Hidden Layer

Bias1=[-14.012553434519038; 11.812126245357037; 1.3842333365647408;-4.2059355661312701; 1.4409623985981763; 1.7682292963115536; 3.7009477744311594; -12.156912317990363; 10.685155187819799; 29.778732979249227]

Weights1_1=[14.032485901273109; -14.965551222735508;-2.0548831800601559; 11.508338189006931; -10.398676697150343; 12.537550546065168; 14.195267628444153; -18.095141762455466; 14.094980089235776; 29.316759390586647];

Output Layer

Bias2 = 0.023830175467874234;

Weights2_1 = [0.12722984514626728 -0.12893415969647762 0.71558105898357172 0.24740079678005919 -0.036260848769319898 -0.025642535393042187 0.013910363600061586 -0.030043039672199449 0.026235673680799643 -1.0604698488937083]

4.0 For Permeability versus Bulk Density

Hidden Layer

Bias1=[14.234735241099816; 17.590014806028222; 7.6464205953541038; 3.1235610191799674; -0.70572737185239276; -2.7267375471128878; 7.7957585480650362; -10.636044844162234; -9.490391675219886;-8.2071590587739625];

Weights1_1=[13.048348572810156; -25.887305874048945; -14.912242233942111;-11.335175231947238; 16.069229833714196; -15.47160526587802; 16.022416560791864; -16.682330267079212; -10.61333463073667;-7.7220045020117887]

Output Layer

Bias2 = 0.13584928828250406;

Weights2_1 = [1.0907596582321044 -0.017940834374564476 -0.028618712365094938 0.033283819260466266 0.028139308312771293 0.04283336409767928 -0.064235927423973008 -0.15289329584906602 0.020879946952464933 -0.055825067816312537]